

## COVER SHEET FOR PROPOSAL TO THE NATIONAL SCIENCE FOUNDATION

PROGRAM ANNOUNCEMENT/SOLICITATION NO./CLOSING DATE/if not in response to a program announcement/solicitation enter NSF 11-1					<b>FOR NSF USE ONLY</b>	
<b>NSF 11-1</b>					<b>NSF PROPOSAL NUMBER</b>	
FOR CONSIDERATION BY NSF ORGANIZATION UNIT(S) (Indicate the most specific unit known, i.e. program, division, etc.)					<b>1239285</b>	
<b>EAR - SURFACE EARTH PROCESS SECTION</b>						
<b>DATE RECEIVED</b>	<b>NUMBER OF COPIES</b>	<b>DIVISION ASSIGNED</b>	<b>FUND CODE</b>	<b>DUNS# (Data Universal Numbering System)</b>	<b>FILE LOCATION</b>	
<b>03/15/2012</b>	<b>3</b>	<b>06030000 EAR</b>	<b>7570</b>	<b>003403953</b>	<b>03/15/2012 2:58pm</b>	
EMPLOYER IDENTIFICATION NUMBER (EIN) OR TAXPAYER IDENTIFICATION NUMBER (TIN)		SHOW PREVIOUS AWARD NO. IF THIS IS <input type="checkbox"/> A RENEWAL <input checked="" type="checkbox"/> AN ACCOMPLISHMENT-BASED RENEWAL		IS THIS PROPOSAL BEING SUBMITTED TO ANOTHER FEDERAL AGENCY? YES <input type="checkbox"/> NO <input checked="" type="checkbox"/> IF YES, LIST ACRONYM(S)		
<b>246000376</b>		<b>0725019</b>				
NAME OF ORGANIZATION TO WHICH AWARD SHOULD BE MADE			ADDRESS OF AWARDEE ORGANIZATION, INCLUDING 9 DIGIT ZIP CODE			
<b>Pennsylvania State Univ University Park</b>			<b>Pennsylvania State Univ University Park</b>			
AWARDEE ORGANIZATION CODE (IF KNOWN)			<b>110 Technology Center Building</b>			
<b>0033290000</b>			<b>UNIVERSITY PARK, PA. 168027000</b>			
NAME OF PRIMARY PLACE OF PERF			ADDRESS OF PRIMARY PLACE OF PERF, INCLUDING 9 DIGIT ZIP CODE			
<b>The Pennsylvania State University</b>			<b>The Pennsylvania State University</b>			
			<b>2217 Earth &amp; Engineering Bldg</b>			
			<b>University Park ,PA ,168025000 ,US.</b>			
IS AWARDEE ORGANIZATION (Check All That Apply) (See GPG II.C For Definitions)		<input type="checkbox"/> SMALL BUSINESS <input type="checkbox"/> FOR-PROFIT ORGANIZATION		<input type="checkbox"/> MINORITY BUSINESS <input type="checkbox"/> WOMAN-OWNED BUSINESS		<input type="checkbox"/> IF THIS IS A PRELIMINARY PROPOSAL THEN CHECK HERE
TITLE OF PROPOSED PROJECT <b>An Accomplishment-Based Request for Renewal of the Susquehanna-Shale Hills Critical Zone Observatory (SSHO)</b>						
REQUESTED AMOUNT \$ <b>1,000,000</b>	PROPOSED DURATION (1-60 MONTHS) <b>12 months</b>		REQUESTED STARTING DATE <b>11/01/12</b>		SHOW RELATED PRELIMINARY PROPOSAL NO. IF APPLICABLE	
CHECK APPROPRIATE BOX(ES) IF THIS PROPOSAL INCLUDES ANY OF THE ITEMS LISTED BELOW						
<input type="checkbox"/> BEGINNING INVESTIGATOR (GPG I.G.2)			<input type="checkbox"/> HUMAN SUBJECTS (GPG II.D.7) Human Subjects Assurance Number _____			
<input type="checkbox"/> DISCLOSURE OF LOBBYING ACTIVITIES (GPG II.C.1.e)			Exemption Subsection _____ or IRB App. Date _____			
<input type="checkbox"/> PROPRIETARY & PRIVILEGED INFORMATION (GPG I.D, II.C.1.d)			<input type="checkbox"/> INTERNATIONAL COOPERATIVE ACTIVITIES: COUNTRY/COUNTRIES INVOLVED (GPG II.C.2.j)			
<input type="checkbox"/> HISTORIC PLACES (GPG II.C.2.j)			_____			
<input type="checkbox"/> EAGER* (GPG II.D.2) <input type="checkbox"/> RAPID** (GPG II.D.1)			<input type="checkbox"/> HIGH RESOLUTION GRAPHICS/OTHER GRAPHICS WHERE EXACT COLOR REPRESENTATION IS REQUIRED FOR PROPER INTERPRETATION (GPG I.G.1)			
<input type="checkbox"/> VERTEBRATE ANIMALS (GPG II.D.6) IACUC App. Date _____ PHS Animal Welfare Assurance Number _____						
PI/PD DEPARTMENT <b>Earth &amp; Environmental Systems Institute</b>			PI/PD POSTAL ADDRESS <b>2217 Earth &amp; Engineering Sciences Bldg.</b>			
PI/PD FAX NUMBER <b>814-865-3191</b>			<b>University Park, PA 16802</b>			
			<b>United States</b>			
NAMES (TYPED)	High Degree	Yr of Degree	Telephone Number	Electronic Mail Address		
<b>Susan L Brantley</b>	<b>PhD</b>	<b>1987</b>	<b>814-865-1619</b>	<b>brantley@essc.psu.edu</b>		
<b>CO-PI/PD</b>	<b>Christopher J Duffy</b>	<b>Ph.D.</b>	<b>1982</b>	<b>814-863-4384</b>	<b>cxdl1@psu.edu</b>	
<b>CO-PI/PD</b>	<b>David M Eissenstat</b>	<b>PhD</b>	<b>1986</b>	<b>814-863-3371</b>	<b>dme9@psu.edu</b>	
<b>CO-PI/PD</b>	<b>Eric Kirby</b>	<b>PhD</b>	<b>2001</b>	<b>814-865-0732</b>	<b>ekirby@psu.edu</b>	
<b>CO-PI/PD</b>						

# CERTIFICATION PAGE

**Certification for Authorized Organizational Representative or Individual Applicant:**

By signing and submitting this proposal, the Authorized Organizational Representative or Individual Applicant is: (1) certifying that statements made herein are true and complete to the best of his/her knowledge; and (2) agreeing to accept the obligation to comply with NSF award terms and conditions if an award is made as a result of this application. Further, the applicant is hereby providing certifications regarding debarment and suspension, drug-free workplace, lobbying activities (see below), responsible conduct of research, nondiscrimination, and flood hazard insurance (when applicable) as set forth in the NSF Proposal & Award Policies & Procedures Guide, Part I: the Grant Proposal Guide (GPG) (NSF 11-1). Willful provision of false information in this application and its supporting documents or in reports required under an ensuing award is a criminal offense (U. S. Code, Title 18, Section 1001).

**Conflict of Interest Certification**

In addition, if the applicant institution employs more than fifty persons, by electronically signing the NSF Proposal Cover Sheet, the Authorized Organizational Representative of the applicant institution is certifying that the institution has implemented a written and enforced conflict of interest policy that is consistent with the provisions of the NSF Proposal & Award Policies & Procedures Guide, Part II, Award & Administration Guide (AAG) Chapter IV.A; that to the best of his/her knowledge, all financial disclosures required by that conflict of interest policy have been made; and that all identified conflicts of interest will have been satisfactorily managed, reduced or eliminated prior to the institution's expenditure of any funds under the award, in accordance with the institution's conflict of interest policy. Conflicts which cannot be satisfactorily managed, reduced or eliminated must be disclosed to NSF.

**Drug Free Work Place Certification**

By electronically signing the NSF Proposal Cover Sheet, the Authorized Organizational Representative or Individual Applicant is providing the Drug Free Work Place Certification contained in Exhibit II-3 of the Grant Proposal Guide.

**Debarment and Suspension Certification** (If answer "yes", please provide explanation.)

Is the organization or its principals presently debarred, suspended, proposed for debarment, declared ineligible, or voluntarily excluded from covered transactions by any Federal department or agency? Yes  No

By electronically signing the NSF Proposal Cover Sheet, the Authorized Organizational Representative or Individual Applicant is providing the Debarment and Suspension Certification contained in Exhibit II-4 of the Grant Proposal Guide.

**Certification Regarding Lobbying**

The following certification is required for an award of a Federal contract, grant, or cooperative agreement exceeding \$100,000 and for an award of a Federal loan or a commitment providing for the United States to insure or guarantee a loan exceeding \$150,000.

**Certification for Contracts, Grants, Loans and Cooperative Agreements**

The undersigned certifies, to the best of his or her knowledge and belief, that:

- (1) No federal appropriated funds have been paid or will be paid, by or on behalf of the undersigned, to any person for influencing or attempting to influence an officer or employee of any agency, a Member of Congress, an officer or employee of Congress, or an employee of a Member of Congress in connection with the awarding of any federal contract, the making of any Federal grant, the making of any Federal loan, the entering into of any cooperative agreement, and the extension, continuation, renewal, amendment, or modification of any Federal contract, grant, loan, or cooperative agreement.
- (2) If any funds other than Federal appropriated funds have been paid or will be paid to any person for influencing or attempting to influence an officer or employee of any agency, a Member of Congress, an officer or employee of Congress, or an employee of a Member of Congress in connection with this Federal contract, grant, loan, or cooperative agreement, the undersigned shall complete and submit Standard Form-LLL, "Disclosure of Lobbying Activities," in accordance with its instructions.
- (3) The undersigned shall require that the language of this certification be included in the award documents for all subawards at all tiers including subcontracts, subgrants, and contracts under grants, loans, and cooperative agreements and that all subrecipients shall certify and disclose accordingly.

This certification is a material representation of fact upon which reliance was placed when this transaction was made or entered into. Submission of this certification is a prerequisite for making or entering into this transaction imposed by section 1352, Title 31, U.S. Code. Any person who fails to file the required certification shall be subject to a civil penalty of not less than \$10,000 and not more than \$100,000 for each such failure.

**Certification Regarding Nondiscrimination**

By electronically signing the NSF Proposal Cover Sheet, the Authorized Organizational Representative is providing the Certification Regarding Nondiscrimination contained in Exhibit II-6 of the Grant Proposal Guide.

**Certification Regarding Flood Hazard Insurance**

Two sections of the National Flood Insurance Act of 1968 (42 USC §4012a and §4106) bar Federal agencies from giving financial assistance for acquisition or construction purposes in any area identified by the Federal Emergency Management Agency (FEMA) as having special flood hazards unless the:

- (1) community in which that area is located participates in the national flood insurance program; and
- (2) building (and any related equipment) is covered by adequate flood insurance.

By electronically signing the NSF Proposal Cover Sheet, the Authorized Organizational Representative or Individual Applicant located in FEMA-designated special flood hazard areas is certifying that adequate flood insurance has been or will be obtained in the following situations:

- (1) for NSF grants for the construction of a building or facility, regardless of the dollar amount of the grant; and
- (2) for other NSF Grants when more than \$25,000 has been budgeted in the proposal for repair, alteration or improvement (construction) of a building or facility.

**Certification Regarding Responsible Conduct of Research (RCR)  
(This certification is not applicable to proposals for conferences, symposia, and workshops.)**

By electronically signing the NSF Proposal Cover Sheet, the Authorized Organizational Representative of the applicant institution is certifying that, in accordance with the NSF Proposal & Award Policies & Procedures Guide, Part II, Award & Administration Guide (AAG) Chapter IV.B., the institution has a plan in place to provide appropriate training and oversight in the responsible and ethical conduct of research to undergraduates, graduate students and postdoctoral researchers who will be supported by NSF to conduct research. The undersigned shall require that the language of this certification be included in any award documents for all subawards at all tiers.

AUTHORIZED ORGANIZATIONAL REPRESENTATIVE		SIGNATURE	DATE
NAME			
TELEPHONE NUMBER	ELECTRONIC MAIL ADDRESS	FAX NUMBER	

\* EAGER - EARly-concept Grants for Exploratory Research  
\*\* RAPID - Grants for Rapid Response Research

## PROJECT SUMMARY: An Accomplishment-Based Request for Renewal of the Susquehanna - Shale Hills Critical Zone Observatory (SSHO)

*Intellectual merit.* Established originally for watershed research in the 1970s [1], Shale Hills was funded in 2007 as a Critical Zone Observatory (CZO). The CZO has implemented a wealth of experimental science to understand Critical Zone processes. SSHO researchers have published 20+ papers [2-24], submitted 7 papers for publication [25-31], spearheaded a special issue in the *Vadose Zone Journal* [32], and begun work on a special issue for *Earth Surface Processes and Landforms* [33]. The CZO team and the SSHO provide instrumentation, a real-time sensor network, an online dataset, a sample archive, and models – all of which continue to grow and are accessible to other scientists.

The 8-hectare Shale Hills catchment is a first-order watershed that was strategically chosen to entirely overlie shale of the Rose Hill Formation: building upon this, the SSHO team also developed a suite of satellite sites (Fig. 4, *Facilities*) on the same lithology but in different climate regimes, and one satellite site in the same climate zone but on organic-rich Marcellus shale. These satellite sites were established to understand regolith formation as a function of climate and composition and to establish collaborations with minority- or undergrad-serving institutions (Table 4, *Facilities*).

As examples of SSHO work, six papers are attached which describe i) new methodology to model water age [22]; ii) an extensive synthesis of measurements and models of soil moisture for the whole watershed [5]; iii) initial observations from the CZO team about the water-related controls on the distribution of tree species in temperate regimes such as Shale Hills [15]; iv) growing understanding of how soil forms on shale [23]; v) a novel use of U isotopes to measure soil formation rates [21]; and vi) observations of variations in permeability and fracture distribution in the Rose Hill Formation at the CZO [7]. The SSHO team is truly measuring and modeling the CZ across all timescales (Fig. 1).

*Broader impacts.* The SSHO team has collected, archived and distributed large datasets of stable isotopes, chemistry, soil moisture, eddy flux, cosmogenic isotopes, LiDAR, sapflux, and other observables. *Never before have Critical Zone researchers collected and published online such diverse datasets with such high-resolution spatial and temporal coverage for a single catchment.* During the 1-year transitional extension, SSHO will focus on cross-disciplinary synthesis and sharing of this data. Therefore, funding is sought for 4 postdoctoral and 2 graduate students to be mentored by several faculty to work on cross-cutting hypotheses that synthesize CZO data and models. Funding is also sought to provide \$50k in seed grants that will be subcontracted to outside participants to work at Shale Hills + satellites. Satellite-site colleagues will be especially encouraged from minority-serving and undergraduate-dominated colleges to apply for seed funding. The CZO + seed grant science will be managed by the Steering Committee: geochemist Brantley, hydrologist Duffy, geomorphologist Kirby, ecologist Eissenstat, and one rotating member derived from the rest of the team. All graduate and postdoctoral students will participate both in science and in outreach activities ranging from community education about natural gas development on shale to K-12 educational opportunities. SSHO will also participate in the cross-CZO initiative, *Drill-the-Ridge*, and in CUAHSI-hosted cyberseminars.

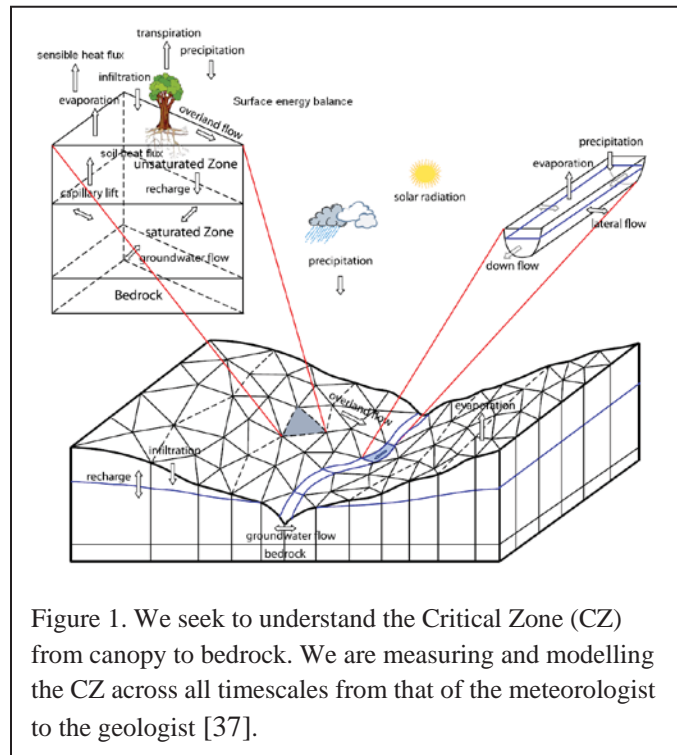


Figure 1. We seek to understand the Critical Zone (CZ) from canopy to bedrock. We are measuring and modelling the CZ across all timescales from that of the meteorologist to the geologist [37].

## TABLE OF CONTENTS

---

For font size and page formatting specifications, see GPG section II.B.2.

	<b>Total No. of Pages</b>	<b>Page No.* (Optional)*</b>
Cover Sheet for Proposal to the National Science Foundation		
Project Summary (not to exceed 1 page)	1	_____
Table of Contents	1	_____
Project Description (Including Results from Prior NSF Support) (not to exceed 15 pages) <b>(Exceed only if allowed by a specific program announcement/solicitation or if approved in advance by the appropriate NSF Assistant Director or designee)</b>	6	_____
References Cited	3	_____
Biographical Sketches (Not to exceed 2 pages each)	18	_____
Budget (Plus up to 3 pages of budget justification)	6	_____
Current and Pending Support	19	_____
Facilities, Equipment and Other Resources	5	_____
Special Information/Supplementary Documents (Data Management Plan, Mentoring Plan and Other Supplementary Documents)	3	_____
Appendix (List below. ) <b>(Include only if allowed by a specific program announcement/ solicitation or if approved in advance by the appropriate NSF Assistant Director or designee)</b>	_____	_____
Appendix Items:		

\*Proposers may select any numbering mechanism for the proposal. The entire proposal however, must be paginated. Complete both columns only if the proposal is numbered consecutively.

---

## PROJECT DESCRIPTION

### An Accomplishment-Based Request for Renewal of the Susquehanna-Shale Hills Critical Zone Observatory (SSHO)

#### Human resources development at the postdoctoral, graduate and undergraduate levels

*Education: Graduate students and postdoctoral fellows.* Seven postdoctoral fellows (Table 1) and 20 grad students (Table 2) were partially supported with CZO funds (Soil Science, Meteorology, Ecology, Geosciences, Civil & Environmental Engineering). Of these, 50% were female. We were also supplemented for CZO students to go abroad: 8 Penn State (PSU) and 36 non-PSU students participated.

Table 1. Postdoctoral scholars who completed research at SSHO (\* =salary from NSF, DOE & other sources)

Post Doctoral Scholar	Advisor	Research
K. Bazilevskaya *	Brantley	Regolith formation, porewater chemistry (DOE funded)
P. Chattopadhyay	Singha	Short and long term aquifer behavior
C. Graham	Lin/Duffy	Soil moisture at SSHO
L. Jin *	Brantley	Regolith formation, porewater chemistry
L. Ma *	Brantley	U-series isotope analysis during regolith formation
K. Naithani *	Eissenstat/Davis	Quantitative plant ecology at SSHO
Y. Zhao *	Lin	Spatial and temporal patterns of soil moisture

*Education: Undergraduate students, REUs, international CZO Field School, and satellite sites.* Our original grant provided funding for REU students -- especially from the institutions associated with our satellite sites (Fig. 4, *Facilities*) -- to work on shale. From 2008-2011, we funded 26 undergrads from PSU or satellite-site institutions: Univ. Puerto Rico, Alabama A&M, Univ. of Tenn., Washington & Lee, Juniata, and Colgate. Of the undergraduate participants, 14/26 were female, 4/26 self-reported as African-American, and 6/26 self-reported as Hispanic-American. Several undergrads have completed senior theses or given presentations at national meetings (Table 3). In addition, *Chemical Geology* will be publishing the first manuscript submitted by a lead author from a satellite institution on CZO work [2].

REU field work, organized by PSU scientist T. White and Ph.D. candidate A. Dere, targetted our Appalachian satellite sites (Fig. 4, *Facilities*). The work was combined in 2010 with a field school organized in coordination with the cross-European *SoilTrec* team. *SoilTrec* is a funded program of CZ scientists who work closely with all the U.S. CZOs: for example, White and Duffy are funded to build watershed models at 4 *SoilTrec* sites. In the international CZO Field School, we taught 10 students from 8 countries. Several international participants initiated collaborative research projects during the school. In addition, PSU students A. Dere and N. West are working on satellite site data with our satellite-site colleagues. Samples have also been shared with researchers at other universities (see Table 4, *Facilities*): for example, Lin Ma, Asst. Professor at University of Texas-El Paso, was funded by USGS to understand U/Th disequilibrium signatures and REEs in soils on shales using samples from our satellite sites.

*Education: K-12 students.* PSU graduate and postgraduate students participate in outreach. Students and the CZO watershed specialist (Colin Duffy) helped the local State College Area High School run a Summer Science, Technology, Engineering and Math (STEM) Academy for entering freshman. The academy emphasized hands-on activities by facilitating students building and deploying instruments, conducting experiments and analyzing data.

*Education: Beyond CZO.* One of the SSHO coIs, K. Singha, conducted three 3-week hydrogeophysics field camps from 2008-2010 using Shale Hills as a focus. Funding for this effort derived from Singha's CAREER grant: ~10 undergrads participated each year; half were from PSU and half from minority-serving institutions (Jackson State and Fort Valley State). In addition, the SSHO is developing a new generation of hydrologic models and experimental observations that are being implemented in

operational models. The models forecast drought, flood, water supply and water quality for a fully coupled approach to surface and groundwater systems. This hydrologic research is fundamental to management of land and water within the Chesapeake Bay watershed. A workshop was held in

Table 2. Grad students that have or will receive degrees for work at SSHO

Student	Discipline	Degree	Date
Andrews, D.M.	Soil Science	Ph.D.	2011
Baldwin, D.	Soil Science	M.S.	2011
Kumar, M.	Civil Eng.	Ph.D.	2009
Kuntz, B.	Geosciences	M.S.	2010
Wubbles, J.	Horticulture	M.S.	2010
Li, W.	Civil Engineering	M.S.	2010
Holmes III, G.H.	Civil Engineering	M.S.	2011
Zhang, J.	Soil Science	Ph.D.	2011
Takagi, K.	Soil Science	M.S.	2009
Berger, W.	Soil Science	M.S.	TBD
Dere, A.	Geosciences	Ph.D.	2013
Gaines, K.	Ecology	Ph.D.	2015
Herndon, E.	Geosciences	Ph.D.	2012
Shi, Y.	Meteorology	Ph.D.	2012
Smith, L.	Ecology	M.S.	2013
Thomas, E.	Civil Eng.	M.S.	2014
West, N.	Geosciences	Ph.D.	2014
Yesavage, T.	Geosciences	Ph.D.	2014
Yu, X.	Civil Engineering	Ph.D.	2013
Zhang, Y	Environ Engineering	Ph.D.	2015

Students received stipend, tuition, or research support at SSHO

State College for instruction on implementing the Penn State Integrated Hydrologic Model in Aug 2010: 27 participants (17/27 grad students) were taught to use PIHM, for terrestrial hydrologic simulation.

Table 3. Undergraduate senior theses or presentations at national meetings

Student	Institution	Presentation	Research topic
A. Carone	PSU	B.S. Thesis 2012	Weathering of Marcellus shale
Daniels, T.	PSU	B.S. Thesis, 2009	Lithologic controls on flow, SSHO
Twiest, B.	PSU	B.S. Thesis, 2012	Eddy flux data
L. Leidel	PSU	AGU Fall 2011	Soil geochemistry from satellites
E. Mann	Wash. And Lee	AGU Fall 2011	Tree throw in Appalachia
L. V. Albelo	Univ Puerto Rico	B.S. Thesis 2011	Shale Weathering in Puerto Rico
K. Downie	Juniata	GSA regional 2012	Metal isotopes in Marcellus soil
S. MacDonald	Colgate	Goldschmidt 2010	Clay mineral weathering in shale
D. Mizsei	PSU	B.S. Thesis 2010	Soil Carbon at SSHO
V. Prush	Juniata	GSA Annual 2009	Weathering of Marcellus shale
P. Giri	PSU	2009	Soil geochemistry on Rose Hill shale
J. Paul	Juniata	GSA Annual 2010	Weathering of Marcellus shale

## Proposed Research

We have collected extraordinary datasets at Shale Hills and the satellite sites as part of our CZO effort (see *Facilities, Data Management*) and we are beginning to use these datasets to test predictive modeling schemes for the Earth and environmental sciences. Our experimental and predictive capabilities developed at SSHO are now enabling a wide range of Earth Science. Specifically, we are providing the CZ community with the opportunity to tackle many long-standing problems in hydrogeology [8, 34], geomorphology [29, 35], soil science and ecology [31, 36]. In addition, the CZO led us to discover a previously unreported phenomenon -- widespread but patchy manganese addition to soils in industrialized areas in the U.S. and Europe [13, 18]. We see this one-year renewal as an exciting opportunity to synthesize and share our data and models across disciplines. To enable this, we seek funds for 2 senior graduate students already working with us at SSHO and 4 new postdocs.

With well-mentored postdoctoral scholars and senior grad students, we will test hypotheses that cross disciplines focused on the following areas: i) quantitative synthesis of measurements of soil moisture, eddy flux, precipitation, sapflux, leaf area index (LAI), groundwater levels, and stream flux; ii) calculation of water age and flowpath from water isotopes and weathering-derived solutes; iii) the effect of trees on water and regolith formation; iv) the effect of fractures and topographic aspect on water and regolith; v) the development of predictive models of regolith formation for Shale Hills and the satellites.

The CZO science, including the seed grants described below, will be managed by a Steering Committee consisting of a geochemist (PI Brantley), a hydrologist (C. Duffy), a geomorphologist (E. Kirby), an ecologist (D. Eissenstat), and one rotating member. This rotating member will be derived from the PSU team: K. Davis, meteorologist and specialist in eddy flux measurements; K. Singha, hydrogeophysicist and specialist in hydrogeologic modeling and resistivity measurements; J. Kaye, soil scientist and specialist in nutrients in soils; H. Lin, soil scientist and specialist in hydropedology. We anticipate that most graduate students already working at the CZO will complete their work using money from the first grant or PSU funds; furthermore, we will not recruit new grad students during this short transitional period. However, we seek funding for two senior graduate students (Dere, Zhang) to work on hypothesis 5. The nature of the hypotheses and the outreach activities that students will pursue are described below.

### **The five cross-cutting hypotheses to be tested by the postdoctoral and graduate students**

H1. Water-data integration hypothesis (Davis, Lin, Eissenstat, Duffy, postdoc). *Spatially intensive measurements of soil moisture, tree sap flux, sapwood area, LAI, ground water depth and physical properties can be synthesized with spatially integrated measures of eddy flux and landscape-level soil moisture (COSMOS) within a distributed modeling framework to understand and predict physical processes.*

This hypothesis targets the synthesis of our spatially intensive measurements of water and energy in the CZO through the use of the Penn State Integrated Hydrologic Model (PIHM). We will augment and use PIHM to project fluxes in Shale Hills [22, 37-43]. With the data we have collected, we have three outstanding questions: 1) Do the seasonal changes in the depths of uptake of water by different tree species affect transpiration across the watershed? 2) How can we best assimilate soil type and landform unit distribution to project spatial and temporal patterns of surface and subsurface soil moisture storage as well as stream flow and groundwater recharge? 3) What can we learn from these intensive data collection and modeling efforts so that in the future we can limit the number of measurements we need to make for any new location to project water and energy fluxes – in other words, can we go beyond “measure everything/everywhere” to determine the critical minimum datasets that should be used for watershed projections? To do this, we will explore an extensive modeling effort that will evaluate model performance after addition or removal of data within model assimilations.

By synthesizing our data, we are particularly well poised to promote fundamental understanding of the impact of trees on watershed hydrology. *We have mapped all trees greater than 10 cm in diameter in the watershed (see Facilities, Fig. 3).* In addition, we have two years of LAI, sap flux, partial data sets of sapwood area and depth of water use. We have also collected a spatially and temporally extensive

dataset of soil moisture across the Shale Hills at 100+ sites from the soil surface down to the shale bedrock (1.1 m depth) [3, 5, 6]. Intriguingly, our data show that tree species vary substantially in depth of water use, sap flux, sapwood depth, and seasonal leaf area [15, 30]. What we need to do now (with postdoc H1) is to synthesize and scale these measurements to assess how tree species influence watershed estimates of transpiration and spatial and temporal patterns of soil moisture under different drought scenarios and species composition.

H2. The water-age hypothesis (Duffy, Lin, Brantley, Kaye, postdoc). *Water isotopes and chemistry document the age and flow paths of water in Shale Hills.*

A major goal of the Shale Hills Critical Zone Observatory (SSHO) has been to carry out experiments that unravel the paths and timescales of hydrologic flow in the catchment. For H2, we seek to answer the question, how can we use water isotopes and chemistry to understand how macropores and fractures affect water flow in the catchment including soil- and ground-water? To date we have collected and analyzed more than 6000 water samples from the catchment for  $^2\text{H}$ ,  $^{18}\text{O}$  and major elemental solutes [8, 12, 44]. By intensive sampling over space and time in the catchment we have developed and quantified a conceptual model where transport of  $^2\text{H}$  and  $^{18}\text{O}$  are regulated by a quantitative soil-moisture threshold. For soil moisture below the threshold, pore water is largely immobile because it is held by surface tension. The solutes in this water increase in concentration due to weathering [8]: furthermore, this water is available for plants. Above the moisture threshold, soil water becomes mobile because macropores fill, allowing deep infiltration and recharge. This threshold controls the dynamics of fluid pathways, residence times, and water chemistry in the watershed. From these observations, we will implement a distributed model of  $^2\text{H}$  and  $^{18}\text{O}$  transport with unsteady flow at Shale Hills and/or a model quantifying weathering-derived solutes in soil-, ground-, and stream-waters. Transport parameters will be estimated with standard optimization tools [44]. As part of this effort, we have developed a new theory for “age” of water in watersheds that is based on data for concentrations of  $^2\text{H}$  and  $^{18}\text{O}$  [22] and this is being implemented in PIHM at Shale Hills.

H3. The tree-root hypothesis (Eissenstat, Kaye, Brantley, Kirby, one postdoc): *Tree roots and associated mycorrhizas are causing the soil thickness to deepen at rates of ~26 m/My on the ridgetops at SSHO as the catchment recovers from the periglacial conditions imposed during the last glacial maximum.*

When we started this project 4+ years ago, we did not know if the extent of geochemical reactions in the regolith would be significant or if the shale had simply physically disaggregated into augerable regolith. We have now mapped the more important geochemical reactions occurring as the Rose Hill shale forms soil [4, 8, 9, 11, 12, 23, 25, 28]. Furthermore, we have observed that the rate of formation of the regolith at the ridgetops on both sides of the catchment equal 40-45 m/My based on U series isotopes [21, 29]. In contrast, the rate of erosion at the southern ridgetop is only 19 m/My based on our  $^{10}\text{Be}$  measurements [45], suggesting that ridge-top soils could be deepening by as much as 26 m/My.

Postdoc H3 will investigate the mechanisms of regolith deepening at ridgetops. We know that just beneath the depth of augering refusal, illite and chlorite begin to weather measurably and we surmise that the clay reaction leads to or is driven by disaggregation of the bedrock [19]. Furthermore, we know that the rate of regolith production is slower at mid- and toe-slopes [21]. Because of soil volume limitations, we expect root density near the soil-rock interface to be highest for ridge-top soils and lowest for toe-slope soils. These latter observations lead us to hypothesize that rooting density and associated mycorrhizas may be a major driver of regolith thickening, especially at the ridge. Interestingly, we also suggest that this putative process of regolith thickening may set the ecological timescale of succession of maple-dominated forest along the ridge tops.

To test hypothesis H3 and learn about the mechanism of regolith thickening, we need to synthesize an extensive suite of water chemistry, regolith chemistry,  $\text{CO}_2$  soil flux chamber measurements, soil particle size, and soil gas chemistry measurements to understand regolith formation. Measurements of plant litterfall, trunk growth and leaf chemistry are also being completed by a PSU graduate student and this data will aid in estimating plant nutrient uptake and overall proton and mass balance. Postdoc H3 will help us synthesize this data and will work with PSU grad student K. Gaines to

examine root vertical distribution by profile wall mapping [46] and analyse organic acid concentrations in relation to slope position and aspect. We expect that organic + mineral acids from atmospheric SO<sub>2</sub> and NO<sub>x</sub> dominate weathering in topsoils and in shallow soils at the ridge tops, while organic + carbonic acids dominate weathering in deeper soils at midslope, in swales, and valley floor. By synthesizing the measured external acid inputs, CO<sub>2</sub> concentrations, and soil solution chemistry within key horizons, we will also calculate net proton balance, a key insight toward understand mechanisms of weathering.

H4. The fracture hypothesis (Singha, Kirby, Brantley, Duffy, one postdoctoral student):

*Feedbacks among frost shattering, weathering reactions, and the evolution of topography have resulted in an asymmetric distribution of fractures that in turn controls the observed differences in fluid flow in the subsurface between the sun-facing and shaded sides of the catchment.*

As inferred for water in most shales, fluids at depth at Shale Hills flow mostly through fractured bedrock. Five years ago, however, we did not know the permeabilities of the Rose Hill bedrock nor the regolith. Work led by K. Singha [7] and S. Brantley [19, 23] revealed that the upper 5-7 m of the shale is more highly fractured than shale at depth. Singha and grad student Kuntz [7] also quantified the permeability of bedrock and regolith. Singha's work led to a new stress model for the SSHO [26] that shows that fractures may be present at higher density beneath the valley compared to the ridgelines, potentially driving positive feedbacks that enhance relief [27]. Furthermore, PSU undergraduate M. Holleran (now matriculated as a grad student at the AZ CZO) completed a senior thesis that documented that fluid flow along fractures may have resulted in deep, nested subsurface chemical reaction fronts [28].

In addition to working on fractures, we have also collected a dataset of <sup>10</sup>Be and U series isotopic measurements – the first such dataset for these isotopic measurements in the same catchment from identical locations. These data document that the catchment is not in a geomorphological steady state [4, 23, 29]. For example, sediments stripped from the hillslopes during the last glacial maximum are still clogging the watershed. Furthermore, in comparison to the southern hillslope, the following characteristics are observed for the northern hillslope: 1) the extent of weathering is lower; 2) hydrologic response rates are faster; and 3) rates of regolith production and chemical weathering are greater [3, 21, 23, 29, 45, 47]. Despite this intriguing asymmetry, rates of regolith transport inferred from meteoric <sup>10</sup>Be appear similar on north and south slopes [45]. We attribute these observations to the fact that the southern, steeper, and shadier hillslope is mantled by a 1-2 m thick layer of fragmented colluvial rock which is largely lacking on the northern sunnier and less steep slope.

*We argue that our datasets for this monolithologic catchment provide the best opportunity to understand the interplay of fluid flow, sediment transport, and landscape evolution available today.* To substantiate and synthesize these observations, we will measure meteoric <sup>10</sup>Be and U-series isotopes to estimate rates of regolith production and transport on hillslopes of varying topographic gradient (~10° to 25°) that define the parallel watersheds to the north and south of the SSHO (also on Rose Hill shale). We will also furthermore closely with the Boulder Creek CZO to use models of fracture generation via frost shattering [e.g. 48] to explore the potential controls of topographic aspect on the evolution of rock damage and the role that frost shattering played during the last periglacial period [49].

As part of this hypothesis testing, SSHO will participate in a nucleating cross-CZO activity to “*Drill the Ridge.*” This initiative, engendered by discussions at a cross-CZO meeting held with our European *SoilTrec* colleagues at the Univ. of Delaware in fall 2011, will include mapping of fracture spacing in outcrop and drilled core. *Drill the Ridge* will be spearheaded within SSHO by K. Singha who will drill i) several 8-m deep wells to characterize subsurface lithology using a portable rotary drill, ii) several 2-m deep wells with a Geoprobe to collect core material, and 3) one deep ridge-top hole (tens of meters) with a wireline drill rig to recover core and characterize bedrock heterogeneity. This drilling will allow quantification of fracture distribution, rate and direction of groundwater movement, and recharge.

H5. Transect hypothesis (Brantley, Kirby, Eissenstat, Kaye, two graduate students): *Hillslopes become progressively less steep to the south along our Rose Hill shale climosequence because chemical weathering rates increase with increasing temperature and rainfall while erosion rates are relatively constant.*

When we began this project 4+ years ago, we did not yet have any satellite sites. Now, T. White (not seeking salary funding in the renewal), A. Dere, and students and faculty from satellite institutions have chosen our satellite sites on ridge tops on Rose Hill shale or its stratigraphic/compositional equivalent (Fig. 4, *Facilities*). From north to south along the Appalachian climosequence, we have observed that i) erosion rates are relatively constant, ii) chemical weathering rates increase; iii) regolith thickness on hillslopes stays relatively constant, iv) thickness of regolith on ridgetops increase, v) tree throw density decreases, and vi) tree plate volume increases. These data provide tantalizing clues to disentangle contributions of chemical, physical, and biological processes during weathering and erosion.

Two senior grad students will collect data and model ridgetop and hillslope evolution to understand these observations. In this endeavor, the two students will collaborate with PSU colleagues M. Lebedeva (funded by Dept. of Energy with PI Brantley) and R. Slingerland who are developing 1-dimensional and 2-dimensional models for ridgetops and hillslopes respectively. Lebedeva's model [50-52] couples chemistry (weathering) and physics (fluid  $\pm$  sediment flow) while Slingerland's model couples physics (sediment flux) and biology (tree throw). Although Slingerland desires no NSF salary after 2012, his graduate student, Y. Zhang, will be funded in this 1-year extension to test observations from SSHO and satellites using their newly developed tree-throw model. PhD student Dere will test the 1D and 2D models using constraints from data for climatic, biotic, and geological history, cosmogenic and uranium series isotopes, elevation, chemistry, regolith depth and chemistry. Data will be targeted mostly from the SSHO and the satellite sites along the climosequence, but if time allows, we can also compare sites on the organic-poor Rose Hill shale to those on black shale (Marcellus [2]).

### **Proposed SSHO-Focused Education and Outreach Activities**

*External seed grants.* One of our biggest goals, to stimulate science and education for those outside CZO, will be promoted by our participation in a cyberseminar series on CZ science to be facilitated by the Consortium of Universities for the Advancement of Hydrologic Sciences (CUAHSI, see attached letter from R. Hooper, Director of CUAHSI). In addition, we will provide \$50k in seed grants for non-PSU researchers or researchers who no longer have funding to work at SSHO. These seed grants will be awarded on a competitive basis and will be available to our original satellite-site members or to new researchers (see Table 4 in *Facilities* for summary of collaborators not explicitly included in this proposal – but we will also seek researchers not in Table 4). We anticipate grants will be used for activities such as: i) funding for a PSU graduate student to make new measurements, ii) funding to put novel sensors into SSHO, or iii) funding for non-PSU students to work at SSHO or a satellite site. We will particularly encourage seed grant proposals from undergraduate-only or minority-serving institutions near our satellite sites. To further our relationships with such groups, we have also included funding to host 2 undergraduates at PSU for summer research. Table 4 (*Facilities*) also summarizes the many inside-PSU collaborators whom we are facilitating at SSHO. An open solicitation for seed grants will be made using the SSHO website, email, and czen.org. Grantees will be chosen by the Steering Committee with input from the full SSHO team. Criteria for allocation will include diversity of personnel and science, novelty, record of productivity, student participation, and significance of proposed research.

*Local outreach.* The CZO will target two types of outreach in the year timeframe of the renewal. We already work with the State College Area High School to teach freshmen about wireless environmental sensors for measuring the Critical Zone. During the one year renewal, Duffy will work with the entire SSHO team to interface with high school teachers and students to use sensors. In addition, PI Brantley has been funded by NSF to develop a database of water quality measurements for PA for the area where shale is being developed for natural gas ([www.shalenet.org](http://www.shalenet.org)): Brantley will lead the CZO team to parlay its expertise in shale so that all postdoctoral students can participate in outreach concerning gas development for Marcellus shale. The rapid pace of development of the Marcellus has created significant concern among Pennsylvania stakeholders, as well as among citizens of the neighboring states.

## References

1. Lynch, J.A., *Effects of antecedent soil moisture on storm hydrographs*. 1976, Penn State University: University Park, PA.
2. Mathur, R., L. Jin, V. Prush, J. Paul, C. Ebersole, A. Fornadel, J.Z. Williams, and S.L. Brantley, *Insights into the weathering of black shale: Cu isotopes and concentrations in the Marcellus Formation shale, Huntingdon County, Pennsylvania (U.S.A.)*. *Chemical Geology*, 2012. in press.
3. Takagi, K. and H.S. Lin, *Changing controls of soil moisture spatial organization in the Shale Hills Catchment*. *Geoderma*, 2012(173-174): p. 289-302.
4. Ma, L., L. Jin, and S.L. Brantley, *How mineralogy and slope aspect affect REE release and fractionation during shale weathering in the Susquehanna/Shale Hills Critical Zone Observatory*. *Chemical Geology*, 2011. 290: p. 31-49.
5. Graham, C.B. and H.S. Lin, *Controls and frequency of preferential flow occurrence: A 175 event analysis*. *Vadose Zone Journal*. , 2011. 10.
6. Takagi, K. and H.S. Lin, *Temporal dynamics of soil moisture spatial variability in the Shale Hills Critical Zone Observatory*. *Vadose Zone Journal*, 2011. 10: p. 832-842.
7. Kuntz, B., S. Rubin, B. Berkowitz, and K. Singha, *Quantifying solute transport behavior at the Shale Hills Critical Zone Observatory*. *Vadose Zone Journal*, 2011. 10: p. 1-15, doi:10.2136/vzj2010.0130.
8. Jin, L., D.M. Andrews, G.H. Holmes, H. Lin, and S.L. Brantley, *Opening the "black box": water chemistry reveals hydrological controls on weathering in the Susquehanna Shale Hills Critical Zone Observatory*. *Vadose Zone Journal*, 2011. 10: p. 928-942, doi:10.2136/vzj2010.0133.
9. Andrews, D.M., H. Lin, Q. Zhu, L. Jin, and S.L. Brantley, *Hot spots and hot moments of dissolved organic carbon export and soil organic carbon storage in the Shale Hills catchment*. *Vadose Zone Journal*, 2011. 10: p. 943-954, doi: 10.2136/vzj2010.0149.
10. West, N., E. Kirby, P.R. Bierman, and D. Rood, *Preliminary estimates of regolith generation and mobility in the Susquehanna Shale Hills Critical Zone Observatory, Pennsylvania, using meteoric <sup>10</sup>Be*. *Applied Geochemistry*, 2011. 26: p. S146–S148.
11. Ma, L., L. Jin, and S.L. Brantley, *Geochemical behaviors of different element groups during shale weathering at the Susquehanna/Shale Hills Critical Zone Observatory*. *Applied Geochemistry*, 2011. 26: p. S89-S93.
12. Jin, L. and S.L. Brantley, *Soil chemistry and shale weathering on a hillslope influenced by convergent hydrologic flow regime at the Susquehanna/Shale Hills Critical Zone Observatory*. *Applied Geochemistry* 2011. 26: p. S51–S56.
13. Herndon, E.M. and S.L. Brantley, *Movement of manganese contamination through the Critical Zone*. *Applied Geochemistry*, 2011. 26: p. S40–S43.
14. Brantley, S.L., H. Buss, M. Lebedeva, R.C. Fletcher, and L. Ma, *Investigating the complex interface where bedrock transforms to regolith*. *Applied Geochemistry*, 2011: p. S12–S15, DOI:10.1016/j.apgeochem.2011.03.017
15. Johnson, D.M., K.A. McCulloh, F.C. Meinzer, D.R. Woodruff, and D.M. Eissenstat, *Hydraulic patterns and safety margins, from stem to stomata, in three eastern US tree species*. *Tree Physiology*, 2011. 31: p. 659-68.
16. Li, S. and C.J. Duffy, *Fully coupled approach to modeling shallow water flow, sediment transport, and bed evolution in rivers*. *Water Resource Research*, 2011. 47(W03508): p. 1-20, doi:10.1029/2010WR009751
17. Liermann, L.J., R. Mathur, L.E. Wasylenki, J. Nuester, A.D. Anbar, and S.L. Brantley, *Extent and isotopic composition of Fe and Mo release from two Pennsylvania shales in the presence of organic ligands and bacteria*. *Chemical Geology*, 2011. 281: p. 167-180.
18. Herndon, E.M., L. Jin, and S.L. Brantley, *Soils reveal widespread manganese enrichment from industrial inputs*. *Environmental Science & Technology*, 2011. 45(1): p. 241-247.

19. Jin, L., G. Rother, D.R. Cole, D.F.R. Mildner, C.J. Duffy, and S.L. Brantley, *Characterization of deep weathering and nanoporosity development in shale – a neutron study*. American Mineralogist, 2011. 96: p. 498-512, DOI:10.2138/am.2011.3598.
20. Lin, H.S., *Earth's Critical Zone and Hydrogeology: Concepts, characteristics and advances*. Hydrology and Earth System Science, 2010. 14: p. 25-45.
21. Ma, L., F. Chabaux, E. Pelt, E. Blaes, L. Jin, and S. Brantley, *Regolith production rates calculated with uranium-series isotopes at the Susquehanna/Shale Hills Critical Zone Observatory*. Earth and Planetary Science Letters, 2010. 297: p. 211-225.
22. Duffy, C.J., *Dynamical modeling of concentration-age-discharge in watersheds*. Hydrological Processes Journal, 2010. 24(12): p. 1711-1718.
23. Jin, L., R. Ravella, B. Ketchum, P.R. Bierman, P. Heaney, T. White, and S.L. Brantley, *Mineral weathering and elemental transport during hillslope evolution at the Susquehanna/Shale Hills Critical Zone Observatory*. Geochimica et Cosmochimica Acta, 2010. 74(13): p. 3669-3691.
24. Anderson, S.A., R.C. Bales, and C.J. Duffy, *Critical Zone Observatories: Building a network to advance interdisciplinary study of Earth surface processes*. Mineralogical Magazine, 2008. 72(1): p. 7-10.
25. Yesavage, T.A., M.S. Fantle, J. Vervoort, R. Mathur, L. Jin, L.J. Liermann, and S.L. Brantley, *Fe cycling in the Shale Hills Critical Zone Observatory, Pennsylvania: An analysis of microbiology, chemical weathering, and Fe isotope fractionation*. Geochimica et Cosmochimica Acta, 2012. subm.
26. Slim, M., J.T. Perron, S. Martel, and K. Singha, *Influence of topographic stress on rock fracture: A numerical model for arbitrary surface topography and comparisons with borehole observations*. Earth Surface Processes and Landforms, 2012. subm.
27. Singha, K., T. White, and J.T. Perron, *Fracture patterns and their relations to groundwater flow within the Shale Hills Critical Zone Observatory*. Earth Surface Processes and Landforms, 2012. subm.
28. Brantley, S.L., M. Holleran, and L. Jin, *Probing chemical reactions underlying the Shale Hills Critical Zone Observatory, Pennsylvania (U.S.A.): Nested weathering reaction fronts*. Earth Surface Processes and Landforms, 2012. subm.
29. Ma, L., F. Chabaux, L. Jin, N. West, E. Kirby, and S.L. Brantley, *Relationships between hill-slope aspect and regolith production: insights from U-series isotopes at Shale Hills*. Journal of Geophysical Research, 2012. subm.
30. Meinzer, R., D.R. Woodruff, D.M. Eissenstat, H.S. Lin, T. Adams, and K.A. McCulloh, *Above- and belowground controls on water use by trees of different wood types in an eastern United States deciduous forest*. Agricultural and Forest Meteorology 2012. subm.
31. Naithani, K.S., K.P. Gaines, D. Baldwin, H.S. Lin, and D.M. Eissenstat, *Spatial and temporal dynamics of vegetation and hydrological properties at Shale Hills Critical Zone Observatory in central Pennsylvania*. Journal of Hydrology, 2012. subm.
32. Lin, H., J.W. Hopmans, and D. deB. Richter, *Interdisciplinary Sciences in a Global Network of Critical Zone Observatories*. Vadose Zone Journal, 2011. 10: p. 5.
33. Riebe, C. and S.L. Brantley, *A Special Issue Probing the Deep Critical Zone*. Earth Surface Processes and Landforms, 2012. accepting manuscripts now.
34. Kirchner, J.W., *A double paradox in catchment hydrology and geochemistry*. Hydrological Processes, 2003. 17: p. 871-874.
35. Heimsath, A.M., W.E. Dietrich, K. Nishiizumi, and R.C. Finkel, *The soil production function and landscape equilibrium*. Nature, 1997. 388: p. 358-361.
36. Graham, R.C., A.M. Rossi, and K.R. Hubbert, *Rock to regolith conversion: Producing hospitable substrates for terrestrial ecosystems*. GSA Today, 2010. 20(2): p. 4-9.
37. Qu, Y. and C.J. Duffy, *A semidiscrete finite volume formulation for multi-process watershed simulation*. Water Resources Research, 2007. 43(W08419): p. doi:10.1029/2006WR005753.

38. Reed, P.M., R.B. Brooks, K.J. Davis, D.R. DeWalle, K.A. Dressler, C.J. Duffy, H. Lin, D.A. Miller, R.G. Najjar, K.M. Salvage, T. Wagener, and B. Yarnal, *Bridging river basin scales and processes to assess human-climate impacts and the terrestrial hydrologic system*. Water Resource Research, 2006. 42(W07418): p. 11.
39. Kumar, M., C.J. Duffy, and K.M. Salvage, *A second-order accurate, finite volume-based, integrated hydrologic modeling (FIHM) framework for simulation of surface and subsurface flow*. Vadose Zone Journal, 2009. 8: p. 873-890.
40. Kumar, M., G. Bhatt, and C.J. Duffy, *An object-oriented shared data model for GIS and distributed hydrologic models*. International Journal of Geographical Information Science, 2010. 24(7): p. 1061-1079.
41. Kumar, M., G. Bhatt, and C.J. Duffy, *Domain partitioning for parallelization of fully-coupled, distributed hydrologic models: A theoretical analysis based on PIHM*. Advances in Water Resources, 2012. in preparation.
42. Kumar, M., G. Bhatt, and C.J. Duffy, *Optimal domain partitioning for increased efficiency of parallel distributed hydrologic model simulations: A case study*. Computers in Geoscience, 2012. in preparation.
43. Shi, Y., K.J. Davis, C.J. Duffy, and X. Yu, *A watershed scale groundwater-land-surface model*. Journal of Hydrometeorology, 2012. in preparation.
44. Holmes, G.H.I., *Using  $\delta^2H$  and  $\delta^{18}O$  to Determine the Flowpaths and Timescales of Water at the Susquehanna Shale Hills Critical Zone Observatory*, in *Civil and Environmental Engineering*. 2011, Pennsylvania State University.
45. West, N., E. Kirby, P. Bierman, D. Rood, R. Slingerland, and S.L. Brantley, *Regolith evolution at the Susquehanna Shale Hills Critical Zone Observatory: constraints from shallow subsurface stratigraphy and meteoric  $^{10}Be$* . Journal of Geophysical Research, 2012: p. in prep.
46. Dauer, J.M., J.M. Withington, J. Oleksyn, J. Chorover, O.A. Chadwick, P.B. Reich, and D.M. Eissenstat, *A scanner-based approach to soil profile-wall mapping of root distribution*. Dendrobiology, 2009. 62: p. 35-40.
47. Lin, H.S., *Temporal stability of soil moisture spatial pattern and subsurface preferential flow pathways in the Shale Hills Catchment*. Vadose Zone Journal, 2006. 5: p. 317-340.
48. Anderson, S.P., R.S. Anderson, E.S. Hinckley, P. Kelly, and A.E. Blum, *Exploring weathering and regolith transport controls on critical zone development with models and natural experiments*. Applied Geochemistry, 2011. 26(S1): p. S3-S5.
49. Gardner, T.W., J.B. Ritter, C.A. Shuman, J.C. Bell, K.C. Sasowsky, and N. Pinter, *A periglacial stratified slope deposit in the valley and ridge province of central Pennsylvania, USA: Sedimentology, stratigraphy, and geomorphic evolution*. Permafrost and Periglacial Processes, 1991. 2: p. 141-162.
50. Lebedeva, M.I., R.C. Fletcher, V.N. Balashov, and S.L. Brantley, *A reactive diffusion model describing transformation of bedrock to saprolite*. Chemical Geology, 2007. 244(3-4): p. 624-645.
51. Lebedeva, M.I., R.C. Fletcher, and S.L. Brantley, *A mathematical model for steady-state regolith production at constant erosion rate*. Earth Surface Processes and Landforms, 2010. 35(5): p. 508-524.
52. Lebedeva, M. and S.L. Brantley, *Why ridgetops have thicker soil than hillslopes*. Earth Surface Processes and Landforms, 2011, under revision.

**Susan L. Brantley**

Earth & Environmental Systems Institute and Department of Geosciences  
Pennsylvania State University, University Park, PA

**(a) Professional Preparation**

Princeton University	Chemistry, Magna cum Laude	B.A.	1980
Princeton University	Geological and Geophysical Sciences	M.A.	1983
Princeton University	Geological and Geophysical Sciences	Ph.D.	1987

**(b) Appointments and Awards**

2008-present	Distinguished Professor, Penn State
2004-present	Director, Center for Environmental Kinetics Analysis
2003-present	Director, Earth & Environmental Systems Institute, Penn State
1997-present	Full Professor of Geosciences, Penn State
2011	Arthur L. Day Medal, The Geological Society of America
2011	Docteur Honoris Causa de l'Universite Toulouse III – Paul Sabatier', French Ministry of Education Award from the University Paul-Sabatier' of Toulouse
2011	Elected Fellow, Geological Society of America
2007	Elected Fellow, American Geophysical Union
1/08-1/10	Past-President, Geochemical Society
1/06-1/08	President, Geochemical Society
1/04-1/06	Vice-President, Geochemical Society
6/02-11/05	Member, Advisory Committee to the Geosciences Directorate, NSF
1/03-7/03	Visiting Scientist, U.S. Geological Survey Menlo Center
8/99-4/03	Director, Biogeochemical Research Initiative for Education, Penn State
7/98-04/03	Director, Center for Environmental Chemistry and Geochemistry, Penn State
1/95-7/95	Visiting Scientist, Stanford University, Visiting Scientist, U.S.G.S. Menlo Pk
6/91-7/97	Associate Professor of Geosciences, Penn State
1988-93	David and Lucile Packard Fellow
1987-92	NSF Presidential Young Investigator
9/86-6/91	Assistant Professor of Geosciences, Penn State

**(c) Publications (from more than 140 peer-reviewed publications)**

*(i) Five Publications Closely Related to the Proposed Project*

- Jin, L., Andrews, D. M., Holmes, G. H., Lin, H., and Brantley, S. L., 2011a. Opening the "black box": water chemistry reveals hydrological controls on weathering in the Susquehanna Shale Hills Critical Zone Observatory. *Vadose Zone Journal* 10, 928-942, doi:10.2136/vzj2010.0133.
- Jin, L., Rother, G., Cole, D. R., Mildner, D. F. R., Duffy, C. J., and Brantley, S. L., 2011b. Characterization of deep weathering and nanoporosity development in shale – a neutron study. *American Mineralogist* 96, 498-512, DOI:10.2138/am.2011.3598.
- Ma, L., Jin, L., and Brantley, S. L., 2011. How mineralogy and slope aspect affect REE release and fractionation during shale weathering in the Susquehanna/Shale Hills Critical Zone Observatory. *Chemical Geology* 290, 31-49.
- Brantley, S. L. and Lebedeva, M., 2011. Learning to read the chemistry of regolith to understand the Critical Zone. *Annual Review Earth Planetary Science* 39, 387-416.
- Jin, L., Ravella, R., Ketchum, B., Bierman, P. R., Heaney, P., White, T., and Brantley, S. L., 2010. Mineral weathering and elemental transport during hillslope evolution at the Susquehanna/Shale Hills Critical Zone Observatory. *Geochimica et Cosmochimica Acta* 74, 3669-3691.

*(ii) Five Other Significant Publications*

- Mathur, R., Jin, L., Prush, V., Paul, J., Ebersole, C., Fornadel, A., Williams, J. Z., and Brantley, S. L., 2012. Insights into the weathering of black shale: Cu isotopes and concentrations in the Marcellus Formation shale, Huntingdon County, Pennsylvania (U.S.A.). *Chemical Geology* in press.

- Herndon, E. M., Jin, L., and Brantley, S. L., 2011. Soils Reveal Widespread Manganese Enrichment from Industrial Inputs. *Environmental Science & Technology* 45, 241-247.
- Ma, L., Chabaux, F., Pelt, E., Blaes, E., Jin, L., and Brantley, S., 2010. Regolith production rates calculated with uranium-series isotopes at the Susquehanna/Shale Hills Critical Zone Observatory. *Earth and Planetary Science Letters* 297, 211-225.
- Brantley, S., Kubicki, J., and White, A. F., 2008. *Kinetics of Water-Rock Interaction*. Springer, New York.
- Brantley, S. L., 2008. Understanding soil time. *Science* 321, 1454-1455.

#### **(d) Synergistic Activities**

- Director, Earth and Environmental Systems Institute, an interdisciplinary research center, College of Earth and Mineral Sciences.
- Member, Earth Science Council, Dept. of Energy Office of Basic Energy Sciences.
- Member, Critical Zone Exploration Network, a working group organizing Critical Zone Scientists internationally.
- Member, NRC Space Studies Board Panel, Astrobiology Strategy for the Exploration of Mars 2005-2007.
- Vice-chair of the Earth Sciences Policy and Research in Space Solid-Earth Panel established to write the Solid-Earth Contribution to the “Earth Science Applications from Space: A Community Assessment and Strategy for the Future” (Decadal Study), 2005-2007.

#### **(e) Collaborators and Co-editors**

A.D. Anbar (AZ State), Z. Balogh-Brunstad (Hartwick Coll), R. T. Barnes (U Colorado), M. A. Bruns (PSU), W. D. Burgos (PSU), H.L. Buss (USGS), P. van Cappellen (Georgia Tech), J. Chorover (U. AZ), L.J. Criscenti (Sandia Nat. Lab), K. Dontsova (U of AZ), S. Driese (Baylor U.), R. Fletcher (New Mexico), Y. Godderis (CNRS, France), K. Goyne (Univ MI), H. Hartnett (AZ State), T. Hartshorn (James Madison U), E. M. Hausrath (Univ NV), A. Heimsath (AZ State), C. K. Keller (Washington State U), B. Kimball (USGS), J. R. Leake (U of Sheffield), M. Lebedeva (PSU), J.L. Lewicki (Lawrence Berkely L), P. Lichtne (Los Alamos Nat Lab), L. Liermann (PSU), R. Mathur (Juniata Coll), W. H. McDowell (U of New Hampshire), J. P. Megonigal (Smithsonian), F. C. Meinzer (USDA Forest Service), J. Moore (Northwestern U), T. J. Mozdzer (Smithsonian), M. Pavich (USGS), S. Petsch (U Mass), J. Pett-Ridge (Oregon State), K. S. Pregitzer (U of Idaho), P. Raymond (Yale), C. S. Riebe (U Wyoming), P. Sak (Dickinson Coll), F. N. Scatena (Penn), K. Shumaker (U West Alabama), A. Sitchler-Navarre (CO School of Mines), A. Sutton-Grier (Smithsonian), M. Tien (PSU), Robert Walter (Franklin & Marshall), A.F. White (USGS), A. Zimmerman (Univ Fla)

#### **Dissertations Directed/Graduate and Postgraduate Students Advised:**

*Post Doctoral Scholars:* J. Bandstra (St. Francis), E. Bazilevskaya (PSU), M. Bhatt (PSU), C. Conrad (unknown), L. Criscenti (Sandia Nat. Lab), G. Icopini (Bureau Land Management), J. Jang (Sandia), L. Jin (PSU), L. Ma (PSU), A. Neaman (U. Chile), J. Nuester (Bigelow Lab for Ocean Sciences), A. Olsen (U of Maine), A. Zimmerman (Univ of Fla). Total: 13

*Students supervised:* A. Agustsdottir (Soil Conservation Survey, Iceland), A. Barnes (3M), H. Buss (USGS), M. Carter (PSU), Y. Chen, M. Everett (Los Alamos Nat Lab), E. Hausrath (UNLV), E. Herndon (PSU), B. Kimball (PSU), K. Koepenick (Hydrologist-Baltimore), V. Lee (unknown), J. Lewicki (Lawrence Berkeley Natl. Lab.), I. MacInnis (unknown), N. Mellott (Alfred Univ.), J. Moore (Northwestern U.), S. Murphy (USGS Boulder CO), A. Sitchler-Navarre (Colo. School Mines), M. Nugent (unknown), A. Regberg (PSU), G. Rowe (USGS Denver), S. Ruebush (Montana State U), L. Stillings (USGS Reno NV), N. Tsomaia (Brown U), B. Turner (PSU DuBois), C. Werner (USGS Cascades Volc. Obs.), J. Williams (PSU), S. Yau (unknown), T. Yesavage (PSU). Total: 28

**Thesis Advisor:** D. A. Crerar (deceased)

**Post Graduate Advisor:** None

## **Christopher J. Duffy**

Professor of Civil and Environmental Engineering  
The Pennsylvania State University  
212 Sackett Building  
University Park, PA 16802  
Phone: (814) 863-4384  
Email: [cxdl1@psu.edu](mailto:cxdl1@psu.edu)

### **Education**

B.S. (1975) Environmental Engineering, New Mexico Institute of Mining and Tech.

M.S. (1977) Hydrology, New Mexico Institute of Mining and Technology

Ph.D. (1982) Hydrology/Geoscience, New Mexico Institute of Mining and Tech.

### **Appointments**

1999-present Professor, The Pennsylvania State Univ., Dept. of Civil & Environ. Engrg.

2006-2007 Visiting Professor, Ecole Polytechnique Federale Lausanne, Fluid Dynamics Lab

2007-2008 Senior Fellow Smithsonian Institution, Smithsonian Environmental Research Center

1997-1998 Visiting Scientist, Los Alamos National Laboratory, Earth & Environmental Sciences

1981-1989 Assist.-Assoc. Prof., Utah State University, Civil Environmental Engineering Dept.

1987-1988 Visiting Assoc. Prof., Cornell University, Civil & Environmental Engrg Dept.

### **Five Recent Publications**

Li, S, C.J. Duffy, 2011, Fully coupled approach to modeling shallow water flow, sediment transport, and bed evolution in rivers, *Water Resources Research*, 47, W03508, doi:10.1029/2010WR009751

Duffy, C. J., 2010, Dynamical modeling of concentration–age–discharge in watersheds, *Hydrological Processes*, 24(12), 1711–1718, doi: 10.1002/hyp.7691

Kumar, M. C. C. Duffy and K. Salvage, 2009, A Second-Order Accurate, Finite Volume–Based, Integrated Hydrologic Modeling (FIHM) Framework for Simulation of Surface and Subsurface Flow, *Vadose Zone Journal*, doi:10.2136/vzj2009.0014.

Kumar, M., G. Bhatt, and C.J. Duffy, 2008, An efficient domain decomposition framework for accurate representation of geodata in distributed hydrologic models, *International Journal of Geographical Information Science*, 23(12), 1569-1596.

Qu Y., C. J. Duffy (2007), A semi-discrete finite volume formulation for multiprocess watershed simulation, *Water Resour. Res.*, 43, W08419, doi:10.1029/2006WR005752.

### **Five Other Publications**

Reed P. M., R. P. Brooks, K. J. Davis, D. R. DeWalle, K. A. Dressler, C. J. Duffy, H. Lin, D. A. Miller, R. G. Najjar, K. M. Salvage, T. Wagener, and B. Yarnal (2006), Bridging river basin scales and processes to assess human-climate impacts and the terrestrial hydrologic system, *Water Resources Research*, 42, W07418, doi:10.1029/2005WR004153.

Newman B. D., B. P. Wilcox, S. R. Archer, D. D. Breshears, C. N. Dahm, C. J. Duffy, N. G. McDowell, F. M. Phillips, B. R. Scanlon, E. R. Vivoni (2006), Ecohydrology of water-limited environments: A scientific vision, *Water Resources Research*, 42, W06302, doi:10.1029/2005WR004141.

Entekhabi, E., G. R. Asrar, A.K. Betts, K.J. Beven, R.L. Bras, C.J. Duffy, T. Dunne, R.D. Koster, D.P. Lettenmaier, D.B. McLaughlin, W. J. Shuttleworth, M.T. van Genuchten, M. Wei, E.F. Wood (1999), An Agenda for Land-Surface Hydrology Research and a Call for the Second International Hydrological Decade, *Bulletin of the American Meteorological Society*, 80(10). Pp. 2043-2058.

Shun, T. and C. J. Duffy (1998), Low Frequency Oscillations in Precipitation, Temperature and Runoff Across a West-Facing Mountain Front: A Hydrogeologic Interpretation, *Water Resources Research*, 35(1), 191-201.

Brandes, D., C.J. Duffy and J.P. Cusumano (1998), Instability and Self-Excited Oscillations in a Two-State Variable Dynamical Model of Hillslope Soil Moisture, *Water Resources Research*, 34(12), 3303-3313.

### **Synergistic Activities**

- PI Chesapeake Bay Watershed Modeling Technical Support to the EPA Chesapeake Bay Program, 2011-2017.
- The Susquehanna/Shale Hills Critical Zone Observatory, Principal Investigator and leading the modeling and stable isotope groups.
- Funded by the European Commission through the SoilTrEC Critical Zone Observatory program for integrated modeling at 4 EC sites located in Greece, Wales, Switzerland and Czech Republic, Co-PI Duffy and T. White level:\$250,000.
- Hydrologic Forecasting for Characterization of nonlinear responses of freshwater wetlands to climatic and landuse change in the Susquehanna River Basin. With Kevin Dressler, Ray Najaar and Denice Wardrop.
- Lead development of eKo multi-hop wireless sensor network team with Colin Duffy, Ken Davis, Lorne Leonard and Gopal Bhatt.

### **Collaborators and Co-Authors in Last 48 Months**

Suzanne Anderson (UC Boulder), Roger Bales (UC Merced), Cliff Dahm (Univ. of New Mexico), Michael Dettinger (USGS), Jeff Dozier (UCSB), Upmanu Lall (Columbia U.), Peter Lichtner (Los Alamos National Lab), Danny Marks (USDA\_NRCS), Brent Newman (IAEA, Vienna), Fred Phillips (NMIMT), Karen Salvage, (Univ. of Binghamton), Laura Toran (Temple), Larry Winters (Univ. of Arizona),

### **Graduate Advisors**

Lynn Gelhar, (New Mexico Institute of Mining and Technology), Allan Gutjahr (New Mexico Institute of Mining and Technology) Peter Wierenga (New Mexico State University)

**Former PhD Students** (12 total) Peter Beeson (scientist, USDA), David Brandes (Prof. Lafayette U.), Flavio DeRezende (CH2M-Hill), Minghui Jin (consultant), Mukesh Kumar (Assist. Prof. Duke U.), Umesh Lalwani, (indep. consultant), D. H. Li (Prof. Kyung Hee U.), Shuangcai Li (Risk Management Strategies Inc), Yizhong Qu (AIR-Worldwide), Ying Fan Rhinefelter (Prof. Rutgers), Tongying Shun (scientist, U. Pittsburgh), Marcel Tchaou (United Nations).

## **Biographical Sketch- David M. Eissenstat**

*Department of Horticulture  
The Pennsylvania State University  
218 Tyson Building  
University Park, PA 16802-4200*

*Phone: (814) 863-3371*

*FAX: (814) 863-6139*

*Email: dme9@psu.edu*

*Web site: <http://rootecology.psu.edu>*

### **PROFESSIONAL PREPARATION**

CORNELL UNIVERSITY	Agriculture	B.S. 1978
UNIVERSITY OF IDAHO	Range Science	M.S. 1980
UTAH STATE UNIVERSITY	Range Ecology	Ph.D. 1987

### **APPOINTMENTS**

2001 to present	Professor, The Pennsylvania State University Department of Horticulture. Woody plant physiology.
Aug 1994 to 2000	Associate Professor, The Pennsylvania State University,
1988 to Aug 1994	Asst. and Assoc. Professor, University of Florida, IFAS, Citrus Research and Education Center. Root biology, physiology and ecology.
1987	Postdoctoral Fellow, Department of Botany, University of Bristol. Nutrient transfer among interconnected plants. Advisor: Dr. E. I. Newman.

### **FIVE MOST RELEVANT PUBLICATIONS :** \*denotes graduate student or postdoc.

- \*Mueller, K.E., Eissenstat, D.M, Hobbie, S.E., Oleksyn, J., Jagodzinski, A.M., Reich, P.B., Chadwick, O.A., and Chorover, J. 2012. Tree species effects on coupled cycles of carbon, nitrogen, and acidity in mineral soils at common garden experiment. *Biogeochemistry* (in press)
- \*Dauer, J.M., Withington, J.M., Chorover, J., Chadwick, O.A., Oleksyn, J., Reich, P.B. and Eissenstat, D.M. 2009. A scanner-based approach to soil profile-wall mapping of root distribution. *Dendrobiology* 62: 35-40
- \*Goebel, M., Hobbie, S.E., Bulaj, B., Zadworny, M., Archibald, D.D., Oleksyn, J., Reich, P.B., and D.M. Eissenstat. 2011. Decomposition of the finest root branching orders: Linking carbon and nutrient dynamics belowground to fine root function and structure. *Ecological Monographs* 81:89-102
- \*Bauerle T.L., Richards J.H., Smart D.R. & Eissenstat D.M. 2008. Importance of internal hydraulic redistribution for prolonging lifespan of roots in dry soil. *Plant Cell & Environment* 31:171-186
- Johnson DM, McCulloh KA, Meinzer FC, Woodruff DR, and D.M. Eissenstat. 2011. Hydraulic patterns and safety margins, from stem to stomata, in three eastern US tree species. *Tree Physiology* 31:659-68

### **FIVE OTHER SIGNIFICANT PUBLICATIONS**

- Eissenstat DM, Yanai RD. 1997. The ecology of root lifespan. *Advances in Ecological Research*, 27:1-60.
- \*Mueller, K.E., Diefendorf, A.F., Freeman, K.H., and D.M. Eissenstat. 2010. Appraising the roles of nutrient availability, global change, and functional traits during the angiosperm rise to dominance. *Ecology Letters* 13:E1-E6

\*Dauer J.M., Chorover J., Chadwick O.A., Oleksyn J., Tjoelker M.G., Hobbie S.E., Reich P.B., Eissenstat D.M. 2007. Controls over leaf and litter calcium concentrations among temperate trees. *Biogeochemistry* 86:175-187

Zadworny, M. and D.M. Eissenstat. 2011. Contrasting the morphology, anatomy and fungal colonization of new pioneer and fibrous roots. *New Phytologist* 190:213-221

Eissenstat DM, \*Wells CE, Yanai RD, \*Whitbeck JL. 2000. Building roots in a changing environment: implications for root longevity. *New Phytol.* 147: 33-42.

#### **SYNERGISTIC ACTIVITIES**

- Chair: Penn State Intercollege Graduate Program in Ecology
- Panel member, Ecological & Evol. Physiology Program, NSF, (1995-97, 2004, 2009)
- Scientific Advisor: *New Phytol.*(1995 to present), *Tree Physiol.* (2002 to present)

**COLLABORATORS AND CO-EDITORS:** Laurel Anderson (Ohio Wesleyan College), Elena Baldi (Univ. of Bologna), William Bauerle (Colorado State Univ.), Arnold Bloom (UC –Davis), Sue Brantley (PSU), David Bryla (USDA-ARS), Oliver Chadwick (UC -Santa Barbara), Jon Chorover (Univ. Arizona), Justin Derner (USDA-ARS ), Chris Duffy (PSU), Kate Freeman (PSU), Dali Guo (Chinese Academy of Sciences), Sarah Hobbie (Univ. Minnesota), Rob Jackson (Duke University), Roger Koide (PSU), Alan Lakso (Cornell University), Glenna Malcolm (PSU), Jacek Oleksyn (Polish Academy of Sciences), Wayne Polley (USDA ARS), Eric Post (PSU), Peter Reich (Univ. Minnesota), Jim Richards (UC –Davis), David Smart (UC –Davis), Erica Smithwick (PSU), Astrid Volder (Texas A& M Univ.),

#### **ADVISORS**

M.S. Advisor: J.E. Mitchell

Ph.D. Advisor: M. M. Caldwell

#### **ADVISEES**

*Graduate Students:* Tom Adams (Ph.D. in progress), Taryn Bauerle (Ph.D., 2007), Louise Comas (Ph.D, 2001), Quanying Du (M.S. 2011), Jenny Edwards (M.S., 2005), Javier Espeleta (M.S. 1995), Maria Fisher (M.S., 2000), Katie Gaines (Ph.D. in progress), Marc Goebel (Ph.D., in progress), M. Luke McCormack (Ph.D. in progress), Kevin Mueller (Ph.D., 2011), Luis Valenzuela (Ph.D., 2008), Christina Wells (Ph.D., 1999), Eric Whaley (M.S. 1995), Jennifer Withington (Ph.D., 2005), Jane Wubbels (M.S., 2010), Huining Xu (M.S., 2007),

*Postdoctoral Fellows:* Laurel Anderson (Ohio Wesleyan Univ), Tjeerd Bouma (NIOO-CEMO, The Netherlands), David Bryla (USDA/ARS, Corvallis), Omer Falik (Beersheva Univ, Israel); Kevin Kosola (Univ Wisconsin, Madison), Shaobing Peng (IRRI, Philippines), Lidia Trocha (Inst. of Dendrology, Kornik, Poland), Astrid Volder (Texas A&M), Julie Whitbeck (Univ New Orleans, LA)

*Visiting Scientists:* Christian Ceccon (University of Bolzano), Tracy Gartner (UC Irvine), Xuming Huang (South China Agricultural University), Serena Polverigiani (Università Politecnica delle Marche), Marcin Zadworny (Inst. of Dendrology, Kornik, Poland),

Total students: 17

Total postdocs: 9

**Eric Kirby**  
Department of Geosciences  
Pennsylvania State University  
University Park, PA 16802  
ekirby@psu.edu

---

**Professional Preparation:**

B.A. Geology (1992)	Hamilton College
M.S. Geology (1994)	University of New Mexico
Ph.D. Geology (2001)	Massachusetts Institute of Technology
NSF Post-Doctoral Fellow	UC, Santa Barbara (2001 – 2002)

**Appointments:**

2008 – present	Associate Professor – The Pennsylvania State University
2010 – 2011	Humboldt Fellow – University of Potsdam, Germany
2002 – 2008	Assistant Professor – The Pennsylvania State University

---

**PUBLICATIONS** (\*denotes student author)

**Relevant to current proposal**

- \*Hu, X., **Kirby, E.**, Pan, B., Ganger, D., and Su, H., 2011, Cosmogenic burial ages reveal sediment reservoir dynamics along the Yellow River, China: *Geology*, v. 39, p. 839-842, doi:10.1130/G32030.1.
- \*Craddock, W., **Kirby, E.**, Harkins, N., Zhang, H., and Shi, X., 2010, Rapid fluvial incision along the Yellow River during headward basin integration: *Nature Geoscience*, v. 3, p. 209-213, doi:10.1038/ngeo777.
- Kirby, E.**, Johnson, C., Furlong, K., and Heimsath, A., 2007, Transient channel incision along Bolinas Ridge, California: Evidence for differential rock uplift adjacent to the San Andreas fault: *Journal of Geophysical Research, Earth Surface*, 112, F03S07, doi: 10.1029/2006JF000559.
- \*Harkins, N., **Kirby, E.**, Heimsath, A., Robinson, R., and Reiser, U., Transient fluvial incision in the headwaters of the Yellow River, northeastern Tibet, China: *Journal of Geophysical Research, Earth Surface*, 112, F03S04, doi:10.1029/2006JF000570.
- \*Duvall, A., **Kirby, E.**, and Burbank, D., Tectonic and lithologic controls on channel profiles and processes in coastal California: *Journal of Geophysical Research: Earth Surface*, v. 109, F03002, doi:10.1029/2003JF000086.

**Other recent publications**

- Kirby, E.** and Ouimet, W., 2011, Tectonic geomorphology along the eastern margin of Tibet: Insights into the pattern and processes of active deformation adjacent to the Sichuan Basin, in, Gloaguen, R. and Ratschbacher, L., eds., *Growth and Collapse of the Tibetan Plateau*: Geological Society, London, Special Publications, v. 353, p. 165-168. doi: 10.1144/SP353.9.
- \*Craddock, W., **Kirby, E.**, and Zhang, H., 2011, Late Miocene – Pliocene range growth in the interior of the northeastern Tibetan Plateau: *Lithosphere*, v. 3, no. 6, p. 420-438.
- \*Wang, W., Zhang, P., **Kirby, E.**, Wang, L., Zhang, G., Zheng, D., and Chia, C., 2011, A revised chronology for Tertiary sedimentation in the Sikouzi basin: Implications for the tectonic evolution of the northeastern corner of the Tibetan Plateau: *Tectonophysics*, v. 505, p. 100-114.
- \*Harkins, N.W., **Kirby, E.**, Shi, X., Wang, E., Burbank, D., and Chun, F., 2010, Millennial slip-rates along the eastern Kunlun fault: Implications for the dynamics of intracontinental

deformation in Asia: *Lithosphere*, v.2, p. 247-266., doi: 10.1130/L85.1.  
\*Regalla, C., Fisher, D., and Kirby, E., 2010, Timing and magnitude of shortening within the inner fore arc of the Japan Trench: *Journal of Geophysical Research*, v. 115, doi:10.1029/2009JB006603.

## **SYNERGISTIC ACTIVITIES**

I have been intimately involved in the development of an ArcGIS-based tool for analysis of river gradients and topographic data. We hosted a short course at 2007 GSA Annual Meeting entitled *New tools for Quantitative Geomorphology: Extraction and interpretation of stream profiles from digital topographic data*. The tool has been made freely available to colleagues at other institutions for use in research and instructional environments (<http://www.geomorphtools.org>).

I have just begun a position as Science Editor for *Lithosphere* (2012-2016), and I continue to serve as Associate Editor for *GSA Bulletin* (2007-2015). I co-lead of a GSA field trip in Eastern California (2008), co-organized a recent NSF workshop on Future Directions in Research in Tibet (2010), and I have been an invited participant in recent science planning workshops (Earthscope, 2009; MARGINS, 2010).

## **COLLABORATORS**

Paul Bierman (UVM), Sue Brantley (PSU), Doug Burbank (UCSB), Clark Burchfiel (MIT), Marin Clark (Michigan), Nancye Dawers (Tulane), Ken Deuker (Wyoming), Ken Farley (Caltech), Kevin Furlong (PSU), Carmala Garzione (Rochester), John Gosse (Dalhousie), Arjun Heimsath (ASU), Matt Heizler (NMT), Kip Hodges (ASU), Chen Jie (UCSB), Karl Karlstrom (UNM), Eric McDonald (DRI), Peter Molnar (Colorado), Tom Parsons (USGS), Fred Phillips (NMT), Marith Reheis (USGS), Pete Reiners (Yale), Gerard Roe (Washington), Wiki Royden (MIT), Kamini Singha (PSU), Rudy Slingerland (PSU), J. Doug Walker (Kansas), Kelin Whipple (ASU).

## **GRADUATE AND POSTDOCTORAL ADVISORS**

Doug Burbank (Postdoctoral advisor – UCSB)  
Clark Burchfiel and Kelin Whipple (Ph.D. advisors – MIT)  
Karl Karlstrom (M.S. advisor – UNM)

## **STUDENTS AND POSTDOCTORAL ASSOCIATES**

*M.S.* – Charlie Angerman (2006), Brian Culp (current), Will Hoffman (2009), Nooreen Meghani (current), Andrea Mullen (2007), Tye Numelin (2005), Russell Rosenberg (current), Shi Xuhua (2011)

*Ph.D.* – Bill Craddock (2011), Nate Harkins (2008), Christine Regalla (current), Nicole West (current), Shi Xuhua (current)

*Postdoc* – Will Ouimet (2007)

Total students: 13

Total postdocs: 1

**Kenneth J. Davis**, Professor of Meteorology

Department of Meteorology  
The Pennsylvania State University  
University Park, PA 16802-5013

phone: 814-863-8601  
fax: 814-865-9429  
email: davis@meteo.psu.edu

**Education:**

Princeton University, Physics, A.B. with honors, and a certificate in theater and dance, 1987.  
University of Colorado, Astrophysical, Planetary and Atmospheric Sciences, Ph.D., 1992.  
National Center for Atmospheric Research, Postdoc, Trace gas micrometeorology, 1993-94.

**Employment:**

2008-present Professor, Department of Meteorology, The Pennsylvania State University  
2005-2008 John T. Ryan, Jr. Faculty Fellow, The Pennsylvania State University  
2000-2008 Associate Professor, Dept of Meteorology, The Pennsylvania State University  
Fall 2006 Visiting Scientist, Laboratoire des Sciences du Climat et de l'Environnement, Centre d'Energie Atomique, France  
1996-2000 Assistant Professor, Department of Soil, Water, and Climate, U. of Minnesota.  
Fall 1996 Guest Scientist, Institute for Atmospheric Physics, German Aerospace Research Establishment (DLR).  
1995-1996 Research Associate, University of Colorado, Cooperative Institute for Research in Environmental Sciences  
1995-1996 Visiting Scientist, Mesoscale and Microscale Meteorology Division, National Center for Atmospheric Research  
1993-1994 Postdoctoral Fellow, NCAR, Advanced Studies Program.

**5 relevant publications** (student and postdoctoral lead authors supervised by Davis in bold).

**Lauvaux, T.**, A. E. Schuh, M. Uliasz, S. Richardson, N. Miles, A. E. Andrews, C. Sweeney, L. I. Diaz, D. Martins, P. B. Shepson, and K. J. Davis, 2012. Constraining the CO<sub>2</sub> budget of the corn belt: exploring uncertainties from the assumptions in a mesoscale inverse system, *Atmos. Chem. Phys.* **12**, 337-354.

**Xiao, J.**, K. J. Davis, N. M. Urban, K. Keller, and N. Z. Saliendra, 2011. Upscaling carbon fluxes from towers to the regional scale: Influence of parameter variability and land cover representation on regional flux estimates, *J. Geophys. Res.*, **116**, G00J06, doi:10.1029/2010JG001568.

**Ricciuto, D. M.**, M. P. Butler, K. J. Davis, B. D. Cook, P. S. Bakwin, A. E. Andrews, and R. M. Teclaw, 2008. Causes of interannual variability in ecosystem-atmosphere CO<sub>2</sub> exchange in a northern Wisconsin forest using a Bayesian synthesis inversion. *Agricultural and Forest Meteorology*, **148**, 309-327, doi:10.1016/j.agrformet.2007.08.007

**Desai, A.R.**, A. Noormets, P. V. Bolstad, J. Chen, B. D. Cook, K. J. Davis, E. S. Euskirchen, C. Gough, J. M. Martin, D. M. Ricciuto, H. P. Schmid, J. Tang, and W. Wang, 2008. Influence of vegetation and seasonal forcing on carbon dioxide fluxes across the Upper Midwest, USA: Implications for regional scaling. *Agricultural and Forest Meteorology*, **148**, 288-308, doi:10.1016/j.agrformet.2007.08.001.

Davis, K.J., P.S. Bakwin, B.W. Berger, C. Yi, C. Zhao, R.M. Teclaw and J.G. Isebrands, 2003. The annual cycle of CO<sub>2</sub> and H<sub>2</sub>O exchange over a northern mixed forest as observed from a very tall tower. *Global Change Biology*, **9**, 1278-1293.

### **5 additional publications:**

- Miles, N. L., S. J. Richardson, K. J. Davis, T. Lauvaux, A. E. Andrews, T. O. West, V. Bandaru, and E. R. Crosson, 2012. Large amplitude spatial and temporal gradients in atmospheric boundary layer CO<sub>2</sub> mole fractions detected with a tower-based network in the U.S. upper Midwest, *J. Geophys. Res.*, **117**, G01019, doi:10.1029/2011JG001781.
- Kang S.-L.**, K.J. Davis, 2008. The effects of mesoscale surface heterogeneity on the fair-weather convective atmospheric boundary layer, *J. Atmos. Sci.*, **65**, 3197-3213, doi: 10.1175/2008JAS2390.1.
- Ricciuto, D. M.**, K. J. Davis, and K. Keller, 2008. A Bayesian calibration of a simple carbon cycle model: The role of observations in estimating and reducing uncertainty, *Global Biogeochem. Cycles*, **22**, GB2030, doi:10.1029/2006GB002908.
- Wang, W.**, K. J. Davis, B. D. Cook, M. P. Butler, D. M. Ricciuto, 2006. Decomposing CO<sub>2</sub> fluxes measured over a mixed ecosystem at a tall tower and extending to a region: A case study, *Journal of Geophysical Research Biogeosciences*, **111**(G2), G02005, doi:10.1029/2005JG000093.
- Yi, C.**, K.J. Davis, P.S. Bakwin, and B.W. Berger, 2001. Long-term observations of the evolution of the planetary boundary layer. *J. Atmospheric Sciences*, **58**, 1288-1299.

### **Synergistic activities:**

- Co-chair of the North American Carbon Program Science Steering Group and Member, Carbon Cycle Science Steering Group, February 2008 – present.
- Coordinating member, North American Carbon Program interim synthesis activities, spring 2008 – present.
- Contributing Author, A New U.S. Carbon Cycle Science Plan, published 2011.
- Director, Department of Energy's Northeastern Regional Center of the National Institute for Climatic Change Research, 2005 – 2011.
- Chair, American Meteorological Society's Committee on Boundary Layers and Turbulence, 2003 - 2005. Member, 1998 – 2002.

**Graduate Advisor:** William Blumen, U. Colorado (deceased)

**Postdoctoral Advisor:** Donald H. Lenschow, NCAR

**Graduate Advisees:** M.P. Butler, Ph.D., PSU; A.R. Desai, Ph.D., U. Wisc; T.W. Hilton, Ph.D., U. New Mexico; S.-L. Kang, Ph.D., Texas Tech U.; D.R. Ricciuto, Ph.D., ORNL; W. Wang, Ph.D., NOAA

**Postdoctoral and research associates:** B. Berger, Copper Mountain College; F. Gibert, CNRS, France; R. Kubesh, Mankato State; N. Miles, Penn State; E.G. Patton, NCAR; D. Roy, unknown; J. Xiao, UNH; C. Yi, Queen's College

**Collaborators:** B.Amiro, U. British Col.; I.Baker, CSU; R.Birdsey, USDA; P.Bolstad, UMinn.; E. Browell, NASA; R. Cook, ORNL; K.Corbin, CSU; E.Crosson, Picarro; P.Curtis, UMich.; A.S.Denning, CSU; G.Ehret, DLR; E. Euskirchen, UAlaska; C. Gough, UMich.; F.Heinsch, USDA; D. Hollinger, USDA; D.Huntzinger, NAU; S.R.Kawa, NASA; R. Kennedy, UOregon; G.Koch, NASA; J.Masek, NASA; S.Ogle, CSU; W.M.Post, ORNL; C.Rella, Picarro; A. Richardson, Harvard; M.Roman, NASA; K. Schaefer, UColo; C.Schwalm, NAU; P.Shepson, Purdue; B.Stephens, NCAR; C.Sweeney, NOAA; J.Tang, WHOI; N.Urban, LANL

**Total students:** 6 M.S. grads; 6 Ph.D. (current)      **Total postdocs:** 11 (3 current)

## **BIOGRAPHICAL SKETCH: JASON PHILIP KAYE**

---

Associate Professor, Department of Crop and Soil Sciences, The Pennsylvania State University  
116 ASI Building, State College PA 16802-3504; Phone: (814) 863-1614; Email:  
jason.kaye@asu.edu

### **PROFESSIONAL PREPARATION**

University of Virginia, Chemistry, B.A., 1993

Northern Arizona University, Forestry, M.S., 1997

Colorado State University, Ecology, Ph.D., 2000

Colorado State University, Biogeochemistry, Postdoctoral, Aug. 2000 to Jul. 2002

### **APPOINTMENTS**

January 2005-present, Assistant then Associate Professor, Department of Crop and Soil Sciences, The Pennsylvania State University; August 2002-January 2005, Assistant Professor, School of Life Sciences, Arizona State University; August 2000-July 2002, USDA Postdoctoral Research Fellow, Shortgrass Steppe LTER, Colorado State University; August 1997-July 2000, Graduate Research Assistant, Graduate Degree Program in Ecology, Colorado State University; January 1995-June 1997, Graduate Research Assistant, School of Forestry, Northern Arizona University; June 1993-June 1994, Research Assistant, Harvard Forest LTER; June 1992-August 1992, Research Assistant, Virginia Coastal Reserve LTER.

### **REFEREED PUBLICATIONS (5 RECENT AND MOST RELATED TO PROPOSAL)**

- Ross, C., J.P. Kaye, M.W. Kaye, V.J. Kurth, R. Brimmer, S.C. Hart, and P.Z. Fulé. In press. Labile carbon constrains soil respiration in ponderosa pine forests following crown fires and precipitation manipulations. *Ecosystems*
- Sponseller, R., S. Hall, D. Huber, N. Grimm, J. Kaye, C. Clark, and S. Collins. In press. Scott Variation in monsoon precipitation drives spatial and temporal patterns of *Larrea tridentata* growth in the Sonoran Desert. *Functional Ecology*
- Lewis, D. and J.P. Kaye. 2012. Inorganic nitrogen immobilization in live and sterile soil of old-growth conifer and hardwood forests: implications for ecosystem nitrogen retention. *Biogeochemistry*. DOI 10.1007/s10533-011-9627-6
- Castellano, M., J.P. Kaye, H. Lin, and J. Schmidt. 2011. Linking carbon saturation concepts to nitrogen saturation and retention. *Ecosystems*. DOI: doi:10.1890/100068
- Collins, S.L., S.R. Carpenter, S.M. Swinton, D. Orstein, D.L. Childers, T.L. Gragson, N.B. Grimm, J.M. Grove, S.L. Harlan, J.P. Kaye, A.K. Knapp, G.P. Kofinas, J.J. Magnuson, W.H. McDowell, J.M. Melack, L.A. Ogden, G.P. Robertson, M.D. Smith, A.C. Whitmer. 2011. An integrated conceptual framework for long-term social-ecological research. *Frontiers in Ecology and the Environment*. doi:10.1890/100068

### **REFEREED PUBLICATIONS (OTHER SELECTED)**

- Kaye, J.P., Romanya, J., and R. Vallejo. 2010. Plant and soil carbon accumulation following fire in Mediterranean woodlands. *Oecologia*. 164:533-543.
- Kaye, J.P., P. Groffman, N.B. Grimm, L. Baker, and R. Pouyat. 2006. A distinct urban biogeochemistry? *Trends in Ecology and Evolution* 21:192-199.

- Kaye, J.P., J.E. Barrett, and I.C. Burke. 2002. Stable carbon and nitrogen pools in grassland soils of variable texture and carbon content. *Ecosystems* 5: 461-471.
- Boone, R.D., K.J. Nadelhoffer, J.D. Canary, and J.P. Kaye. 1998. Roots determine the temperature sensitivity of soil respiration. *Nature (London)* 396:570-572.
- Kaye, J.P. and S.C. Hart 1997. Competition for nitrogen between plants and soil microorganisms. *Trends in Ecology and Evolution* 12:139-143.

### **SYNERGISTIC ACTIVITIES**

Advisory board for PSUs CarbonEARTH GK-12 program (2010-present). One of ~20 scientists on the Conference Committee, planning the next generation of synthesis research in ecology with NSF grant (DEB 0435546; Scott Collins, PI)“Preparing the LTER Network for Collaborative Science, Education and Synthesis” (2004 to 2008); Development of new courses in Ecosystem Nutrient Cycles (graduate), and Environmental Sustainability (undergraduate) at PSU. Mentoring undergraduate student research projects funded by NSF REU program and other grants (2000- present); Proposal review panels for USDA (Managed Ecosystems and Soil Processes) and NSF (Ecosystem Studies).

### **COLLABORATORS AND OTHER AFFILIATIONS**

*Graduate and Postdoctoral Advisors:* M.S., Steve Hart, Northern Arizona University; Ph.D., Dan Binkley, Colorado State University; Postdoctoral, Ingrid Burke, Colorado State University.

*Advisor and Postgraduate-Scholar Sponsor:* Arlene Adviento-Borbe, Postdoc, PSU; Rachel Brimmer, Ph.D., PSU; Mike Castellano, Ph.D., PSU; Denise Finney, Ph.D., PSU; Barbara Fricks, M.S., PSU; Alison Grantham, Ph.D., PSU; Michelle Gresalfi, M.S., PSU; Kari Horn, M.S., ASU; Tracy Johns, M.S., ASU; David Lewis, Postdoc, PSU; Matt McCoy, M.S., PSU; Marshall McDaniel, Ph.D., PSU; Chris Ross, M.S., PSU; Meagan Schipanski, Postdoc, PSU; Julie Weitzman, M.S., PSU; Charlie White, Ph.D., PSU.

Total students: 13

Total post-docs: 3

## HANGSHENG (HENRY) LIN

Associate Professor of Hydropedology/Soil Hydrology  
The Pennsylvania State University

Email: [henrylin@psu.edu](mailto:henrylin@psu.edu)

Phone: (814) 742-8622

Fax: (814) 863-7043

---

### *Professional Preparation*

- Fujian Agricultural University      Soil Sci. & Agrochemistry      **B.A.**, 1985
- The Chinese Academy of Sciences      Pedology & Soil Geography      **M.S.**, 1988
- Texas A&M University      Soil Physics & Pedology      **Ph.D.**, 1995
- University of Arkansas      Soil Physics & GIS      **Postdoc**, 1995-96

### *Professional Appointments*

- 7/2006 – Present: **Associate Professor** of Hydropedology/Soil Hydrology. Department of Crop and Soil Sciences, The Pennsylvania State University, University Park, PA.
- 7/2001 – 6/2006: **Assistant Professor** of Hydropedology/Soil Hydrology. Department of Crop and Soil Sciences, The Pennsylvania State University, University Park, PA.
- 8/1998 – 6/2001: **Assistant Professor** of Soils and GIS, and **Director** of Advanced Computing/GIS Lab. College of Natural Resources, Univ. of Wisconsin, Stevens Point.
- 10/1996 – 7/1998: **Research Assistant Professor** of Geoenvironmental Science & Engineering. Center for Environmental Engineering & Science Technologies, Dept. of Civil & Environmental Engineering, Univ. of Massachusetts, Lowell, MA.
- 1/1995 – 9/1996: **Research Associate** of Soil Physics & GIS. Dept. of Crop, Soil, and Environmental Sciences, Univ. of Arkansas, Fayetteville, AR.
- 12/1988 – 8/1990: **Research Associate** of Pedology/Soil Geography. Nanjing Institute of Soil Science, The Chinese Academy of Sciences, Nanjing.

### *Publications*

#### *5 relevant*

- Takagi, K. and H.S. Lin. 2012. Changing controls of soil moisture spatial organization in the Shale Hills Catchment. *Geoderma* 173-174:289-302
- Graham, C., and H.S. Lin. 2011. Controls and frequency of preferential flow occurrence: A 175-event analysis. *Vadose Zone Journal* 10:816–831.
- Takagi, K. and H.S. Lin. 2011. Temporal evolution of soil moisture spatial variability in the Shale Hills catchment. *Vadose Zone Journal* 10:832–842.
- Andrews, D.M., H.S. Lin, Q. Zhu, L. Jin, and S.L. Brantley. 2011. Dissolved organic carbon export and soil carbon storage in the Shale Hills Critical Zone Observatory. *Vadose Zone Journal* 10:943–954.
- Jin, L., D. M. Andrews, G. H. Holmes, H.S. Lin, and S. L. Brantley. 2011. Opening the “black box”: Water chemistry reveals hydrological controls on weathering in the Susquehanna Shale Hills Critical Zone Observatory. *Vadose Zone Journal* 10:928–942.

#### *5 others*

- Lin, H.S., J. Hopmans, and D. Richter. 2011. Interdisciplinary sciences in a global network of Critical Zone Observatories. *Vadose Zone Journal* 10:781–785.

- Lin, H.S. 2011. Three principles of soil change and pedogenesis in time and space. *Soil Science Society of America Journal* 75:1-22.
- Lin, H.S. 2011. Hydropedology: Towards new insights into interactive pedologic and hydrologic processes in the landscape. *Journal of Hydrology* 406:141–145.
- Lin, H.S. 2010. Linking principles of soil formation and flow regimes. *Journal of Hydrology*. 393:3-19.
- Lin, H.S. 2010. Earth's Critical Zone and hydropedology: Concepts, characteristics, and advances. *Hydrology and Earth System Science* 14:25-45.

### ***Synergistic Activities***

- Conference Chair of the *1<sup>st</sup> International Conference on Hydropedology*, July 28-31, 2008, Penn State Univ., University Park, PA.
- Founding Chair of the *Hydropedology Working Group* of the Soil Science Society of America (2003– 2008) and the International Union of Soil Sciences (2005–Present).
- Co-PI of the Shale Hills Critical Zone Observatory funded by the NSF EAR (PI: Chris Duffy), which involves a large team of interdisciplinary scientists within and outside Penn State for the integrated study of the Earth's Critical Zone.
- PI of a USDA National Needs Fellowship program that involves a number of faculty members from across the Penn State campus and adjunct scientists from the USDA-ARS Pasture Systems and Watershed Management Unit.
- PI of an international, interdisciplinary team for completing a vision paper on hydropedology for the Consortium of Universities for the Advancement of Hydrologic Science, Inc. (CUAHSI).

### ***Collaborators and Co-Editors in the Last Five Years***

Susan Brantley (Penn State), Toby Buda (USDA-ARS), Jin Chen (Beijing Normal Univ.), James Doolittle (USDA-NRCS), Patrick Drohan (Penn State), Christopher Duffy (Penn State), Dave Eissenstat (Penn State), Hannes Flüher (ETH, Zürich, Switzerland), Jan Hopmans (UC-Davis), Xiaoyan Li (Beijing Normal Univ.), M. M. Nobles (Alabama A&M), Wilfred Otten (SIMBIOS, UK), Dan Richter (Duke Univ.), Jan Seibert (Stockholm Univ.), Jialiang Tang (The Chinese Academy of Sciences), James Thompson (Univ. of West Virginia), Hans-Jörg Vogel (UFZ Center for Environmental Research, Germany), Larry Wilding (Texas A&M)

### ***Graduate Advisors and Postdoctoral Sponsors***

Qiguo Zhao (Nanjing Institute of Soil Science, The Chinese Academy of Sciences), Kevin McInnes (Texas A&M), Don Scott (Univ. of Arkansas), Larry Wilding (Texas A&M)

### ***Thesis Advisor and Postgraduate-Scholar Sponsor***

- *Graduated:* Tahir Ali Akbar (Univ. of Calgary), Danielle Andrews (Penn State), Doug Baldwin (Penn State), Michael Castellano (Iowa State Univ.), R. C. Cook (Wisconsin Dept. of Natural Resources), John DeGroote (Univ. of Wisconsin-Stevens Point), Jody Gibson (TGE-Houston), Shujiang Kang (Oak Ridge National Lab), Nitin Khandelwal (Virginia Tech), Lifang Luo (USDA Salinity Lab), Ken Takagi (Boston Univ.), Chuck Walker (USGS), Qing Zhu (The Chinese Academy of Sciences)
- *Current graduate students:* Will Burger, Li Guo
- *Postdocs sponsored:* Chris Graham (Boise State), Nan Hong (Monsanto), Chuck Walker (USGS, Baltimore), Xiaobo Zhou (Iowa State Univ.), Yanhong Zhu (Penn State)

*Total students:* 15

*Total postdocs:* 5

**Kamini Singha**  
**Department of Geosciences**  
**The Pennsylvania State University**  
**311 Deike Building, University Park, PA 16802**  
**Phone: (814) 863-6649 Fax: (814) 863-7823**  
**Email: ksingha@psu.edu**

### **Education and Training**

1999            B.Sc. with Honors, Geophysics, University of Connecticut  
2005            Ph.D., Hydrogeology, Stanford University

### **Research and Professional Experience**

2010-present   Associate Professor, Department of Geosciences, Penn State University  
2005-present   Associate, Earth and Environmental Systems Institute, Penn State University  
2005-2011      Assistant Professor, Department of Geosciences, Penn State University  
1997-2000      Student Trainee (Hydrology), U.S. Geological Survey, Water Resources Division

### **Awards**

2011            Penn State George W. Atherton Award for Excellence in Teaching  
2009            Environmental and Engineering Geophysical Society Early Career Award  
2008            National Science Foundation CAREER Award  
2003            Outstanding Student Paper, Fall AGU Meeting, Hydrology Section  
2000            Environmental Protection Agency STAR Fellow  
1999            Cecil Green Fellow, Stanford University Geophysics Department  
1999            Outstanding Woman in the College of Liberal Arts and Sciences, University of Connecticut  
1999            John B. Lucke Award for Outstanding Geology Student, University of Connecticut

### **Five Relevant Publications** (\*student authors)

Ward, A.S.\*, M.N. Gooseff, and **Singha, K.** (2012). How does subsurface characterization affect predictions of hyporheic exchange? *Ground Water*, doi: 10.1111/j.1745-6584.2012.00911.x, 15 p.

Kuntz, B.\*, Rubin, S.\*, Berkowitz, B., and **Singha, K.** (2011). Quantifying solute transport behavior at the Shale Hills Critical Zone Observatory. *Vadose Zone Journal*, 10, doi:10.2136/vzj2010.0130, 15 p.

Regberg, A.\*, **Singha K.**, Tien, M., Picardal, F., Zhang, Q., Schieber, J., Roden, E. and Brantley S. L. (2011). Electrical conductivity as an indicator of iron reduction rates in abiotic and biological systems. *Water Resources Research*, 47, W04509, doi:10.1029/2010WR009551, 14 p.

**Singha, K.**, Li, L., Day-Lewis, F.D., and Regberg, A. B.\* (2011). Quantifying Solute Transport Processes: Are Chemically “Conservative” Tracers Electrically Conservative? *Geophysics*, 76(1), doi: 10.1190/1.3511356, 11 p.

**Singha, K.**, F. D. Day-Lewis and J. W. Lane, Jr. (2007), Geoelectrical evidence for bicontinuum transport in groundwater, *Geophysical Research Letters*, L12401, doi:10.1029/2007GL030019.

## Five Other Publications

- Irving, J. and **Singha, K.** (2010). Stochastic inversion of tracer test and electrical geophysical data to estimate hydraulic conductivities. *Water Resources Research*, 46, W11514, doi:10.1029/2009WR008340, 16 p.
- Wheaton, D.D.\* and **Singha, K.** (2010). Investigating the impact of advective and diffusive controls in solute transport on geoelectrical data. *Journal of Applied Geophysics*, doi:10.1016/j.jappgeo.2010.06.006, 10 p.
- Ward, A.S.\*, Gooseff, M.N. and **Singha, K.** (2010). Imaging hyporheic zone solute transport using electrical resistivity. *Hydrological Processes*, 24, doi: 10.1002/hyp.7672, p. 948-953.
- Day-Lewis, F.D. and **Singha, K.** (2008). Geoelectrical inference of mass transfer parameters: theoretical basis and numerical experiments. *Water Resources Research*, 44, W05201, doi:10.1029/2007WR006750, 6 p.
- Singha, K.**, Pidlisecky, A., Day-Lewis, F.D., and Gooseff, M.N. (2008). Electrical characterization of non-Fickian transport in groundwater and hyporheic systems. *Water Resources Research*, 44, W00D07, doi:10.1029/2008WR007048, 14 p.

## Synergistic Activities

- Chair, AGU Hydrogeophysics Executive Committee (member since 2004, Deputy from 2005-2008): 2009-Present
- Associate Editor, Vadose Zone Journal: 2009-2011
- Associate Editor, Water Resources Research: 2012-present
- Member, CUAHSI Hydrologic Measurement Facility Geophysics Advisory Group: 2006-2008
- Peer reviewer for: Environmental Research Letters, Environmental Science & Technology, Geofluids, Geophysics, Geophysical Research Letters, Hydrological Processes, Hydrology and Earth System Science, Hydrogeology Journal, Inverse Problems in Science and Engineering, Journal of Environmental Quality, Journal of Geophysics and Engineering, Journal of Geophysical Research-Biogeosciences, Journal of Hydrology, Near Surface Geophysics, Vadose Zone Journal, Water Resources Research (~60 papers in last 6 years)

## Collaborators & Other Affiliations

Collaborators and Co-Editors: Brian Berkowitz (Weizmann Institute of Science), Andrew Binley (Lancaster University), Diogo Bolster (Notre Dame), Susan Brantley (Penn State), Fred Day-Lewis (USGS), Brian Ebel (USGS), Matt Fantle (Penn State), Michael Gooseff (Penn State), Roy Haggerty (Oregon State University), Klaus Holliger (University of Lausanne), David Hyndman (Michigan State), Tissa Illangasekare (Colorado School of Mines), James Irving (University of Lausanne), Rosemary Knight (Stanford University), Li Li (Penn State), Steven Loheide (University of Wisconsin), Jenn Macalady (Penn State), Stephen Moysey (Clemson University), John Nimmo (USGS), Patrick Reed (Penn State), Remke van Dam (Michigan State), Chunmiao Zheng (Univ. of Alabama)

Graduate Mentor: Gorelick, Steven M. (Stanford University)

Thesis Advisor and Post-graduate Scholar Sponsors: Pallavi Chattopadhyay (Postdoc, 2012-present), Sean Culkin (M.S., 2007), Michael Fitzgerald (Postdoc, 2010-2011), Katelyn Gerech (Ph.D., 2010-present), Julianne Hagarty (M.S., 2010-present), Brad Kuntz (M.S., 2010), Aaron Regberg (Ph.D., 2011), Ryan Swanson (Ph.D., 2009-present), Rachel Urban (M.S., 2010-present), Daniel Wheaton (M.S., 2009)

Total students: 8

Total post-docs: 2

**Jennifer Zan Williams**  
**Earth and Environmental Systems Institute**  
**2217 Earth and Engineering Building**  
**The Pennsylvania State University**  
**University Park, PA 16802**  
**Phone: (814)865-9910 Fax: (814) 865-3191**  
**Email: jzw126@psu.edu**

### **Education and Training**

2005            B. Sc. Geology, Crimson Scholar, New Mexico State University  
2008            M. Sc. Geosciences, Pennsylvania State University

### **Research and Professional Experience**

2010-present   Data/Communications Coordinator for Susquehanna Shale Hills Critical Zone  
                         Observatory  
2009-2010      Research Assistant, Earth and Environmental Systems Institute  
2005-2008      Graduate Research and Teaching Assistant  
Spring 2004    Undergraduate Teaching Assistant

### **Awards**

2008            11th Annual Environmental Chemistry Student Symposium  
                         • 1st Place Presentation  
2008            Department of Geosciences Graduate Colloquium  
                         • 2nd Place Presentation  
2007            10<sup>th</sup> Annual Environmental Chemistry Student Symposium  
                         • 1<sup>st</sup> Place Presentation  
2005-2006      Bunton-Waller Graduate Fellowship for Minorities  
2005-2006      Charles E. Knopf, Sr. Memorial Scholarship  
2003-2005      Russ Jentgen Endowment Scholarship  
2005            AWG Outstanding Geology Student Award  
2005            NMSU, Outstanding Geology Senior Award  
2004            NMGS Lucille Pipkin Undergraduate Research Award  
2004            NMGS Fall Field Conference Scholarship

### **Five Relevant Publications**

Mathur, R., Prush, V., Paul, J., Ebersole, C., Fornadel, A., Jin, L., **Williams, J.Z.**, Brantley, S.L.  
Insights into the weathering processes of black shale through Cu Isotopes and  
Concentrations of the Marcellus Formation shale, Pennsylvania. (*accepted for 2012*  
Chemical Geology)

- Hausrath, E.M., Navarre-Sitchler, A.K., Sak, P.B., **Williams, J.Z.**, Brantley, S.L. (2011) Soil profiles as indicators of mineral weathering rates on a basalt diabase. *Chemical Geology* 290:89-100, doi: 10.1016/j.chemgeo.2011.08.014
- Niu, X., Lehnert, K.A., **Williams, J.Z.**, Brantley, S.L. (2011), CZChemDB and EarthChem: Advancing Management and Access of Critical Zone Geochemical Data, *Applied Geochemistry* 26:S108-S111, doi:10.1016/j.apgeochem.2011.03.042
- Godd ris, Y., **Williams, J.Z.**, Schott, J., Pollard, D., Brantley, S.L. (2010) Time evolution of the mineralogical composition of Mississippi Valley loess over the last 10 kyr: Climate and geochemical modeling. *Geochimica et Cosmochimica Acta* 74 (22):6357-6374, doi:10.1016/j.gca.2010.08.023
- Williams, J.Z.**, Bandstra, J.Z., Pollard, D., Brantley, S.L. (2010) The temperature dependence of feldspar dissolution determined using a coupled weathering – climate model for Holocene-aged loess soils. *Geoderma* 156:11-19, doi:10.1016/j.geoderma.2009.12.029

### **Synergistic Activities**

Peer reviewer for: *Geoderma*

### **Collaborators & Other Affiliations**

Collaborators and Co-Editors: Joel Bandstra (St. Francis University), Susan Brantley (Penn State University), Yves Godd ris (CNRS, Universit  de Toulouse), Elisabeth Hausrath (University of Nevada, Las Vegas), Lixin Jin (University of Texas, El Paso), Kerstin Lehnert (LDEO, Columbia University), Nancy McMillan (New Mexico State University), Ryan Mathur (Juniata College), Alexis Navarre-Sitchler (Colorado School of Mines), Xianzeng Niu (Penn State University), David Pollard (Penn State University), Peter Sak (Dickinson College), Jacques Schott (CNRS, Universit  de Toulouse)

Graduate Mentor: Susan L. Brantley (Penn State)

Total students: n/a

Total postdocs: n/a

## BUDGET JUSTIFICATION

**Personnel** – The principal investigator is budgeted at the percentage of time shown using his/her actual salary in the calculation. The principal investigator's time includes both technical and project management functions. Any other individuals/positions shown are technical support with the percentage of time shown and actual salaries used. For project time occurring after June 30 of any given year, the salaries have been adjusted at the University approved rate of 3.0% per year each July 1.

- Principal Investigator – Sue Brantley, 9% effort, 12 months (approx 1 month)
- Co-PI – Chris Duffy, ~6% effort, 12 months (3 weeks)
- Co-PI – Dave Eissenstat, ~6% effort, 12 months (3 weeks)
- Co-PI – Eric Kirby, ~6% effort, 12 months (3 weeks)
- Co-I – Ken Davis, ~4% effort, 12 months (2 weeks)
- Co-I – Jason Kaye, ~4% effort, 12 months (2 weeks)
- Co-I – Henry Lin, ~4% effort, 12 months (2 weeks)
- Co-I – Kamini Singha, ~4% effort, 12 months (2 weeks)
- Research Assistant/ Program and Data Coordinator – Jennifer Williams, 100% effort, 12 mths
- Watershed Specialist, To be named – 100% effort, 12 months
- Cyberspecialist, To be named – 50% effort, 12 months
- Postdoctoral Scholars, To be named, 4 @ 100% effort, 12 months
- Graduate Assistants – 2 Grade 12 stipend, half-time for Fall & Spring semester, 9 months
- Graduate Researchers - 2 Wages, 50% effort, 3 months

As PI, Brantley will lead the project. She will be the ultimate supervisor of all postdocs and will coordinate their work and provide guidance in terms of how they allocate their workload and demands of co-Investigators. She will also work on aspects of geochemical interpretation. All Co-PIs and Co-Is will co-mentor the postdoctoral students and provide their expertise in solving SSHO problems. Williams will coordinate data compilation as well as other aspects of running the project – making sure investigators are not doing activities that jeopardize other researchers activities, producing maps of instrumentation, coordinating travel to conferences and other CZO functions, etc. The Watershed Specialist will manage all instrumentation at the site and will collect samples. The Cyberspecialist will aid Williams in aspects of data management requiring cyber-tools and will aid in interfacing with the San Diego supercomputer center and Mark Williams of Univ. of Boulder on all aspects of data cyberinfrastructure and CZO websites. Support is requested for 4 postdoctoral scholars mostly to synthesize data; some of the postdocs will also collect and analyze new data, as described for the hypotheses summarized in the proposal. Support is requested to support two graduate students (Zhang, Dere) for Fall, Spring and Summer to complete their research at SSHO.

Dr. Brantley is requesting one month's salary on this project, which with her current NSF awards, exceeds the NSF Salary Reimbursement Policy as per the NSF 11-1 Guide. During this time, this research requires supervision and administration of this project, advising post-docs and students (especially those who are finishing work on this project), and providing expertise in geochemistry and microbiology. This additional time will impact the progress of the project significantly; therefore, Dr. Brantley is requesting an exception to the 2-month rule for this proposal.

Dr. Eissenstat is requesting three-quarter month's salary on this project, which with his current NSF awards, exceeds the NSF Salary Reimbursement Policy as per the NSF 11-1 Guide. During this time, this research requires advising of post-docs and students (especially those who are finishing work on this project) and providing expertise in root distribution and sapflux. This additional time will impact the progress of the project significantly; therefore, Dr. Eissenstat is requesting an exception to the 2-month rule for this proposal.

Dr. Kirby is requesting three-quarter month's salary on this project, which with his current NSF awards, exceeds the NSF Salary Reimbursement Policy as per the NSF 11-1 Guide. During this time, this

research requires advising of post-docs and students (especially those who are finishing work on this project) and providing expertise in cosmogenic isotope and erosion regime. This additional time will impact the progress of the project significantly; therefore, Dr. Kirby is requesting an exception to the 2-month rule for this proposal. Note that Dr. Kirby will only exceed the 2-month rule for a small portion of this proposed project (first two months).

Dr. Singha is requesting one-half month's salary on this project, which with her current NSF awards, exceeds the NSF Salary Reimbursement Policy as per the NSF 11-1 Guide. During this time, this research requires advising of post-docs and students (especially those who are finishing work on this project) and providing expertise in drilling and geophysics. This additional time will impact the progress of the project significantly; therefore, Dr. Singha is requesting an exception to the 2-month rule for this proposal.

Jennifer Williams (along with the two fixed-term Research Assistants to be named) currently holds a non-tenured appointment at Penn State University. She is appointed on a 12-month basis and is considered to be a Research Assistant. Her current appointment does not include teaching responsibilities nor mentoring of students. This type of appointment allows her to spend 100% of time on sponsored-funded research and is considered her regular organizational salary. Therefore, she requests salary compensation which may exceed the NSF Salary Reimbursement Policy as per the NSF-11-1 Guide.

**Fringe Benefits** – Fringe benefits are computed using the rates of 31.8% applicable to Category I Salaries, 14.1% applicable to Category II Graduate Assistants, 7.9% applicable to Category III Salaries and Wages and 0.2% applicable to Category IV Student Wages for the current fiscal year July 1, 2011, through June 30, 2012. If this proposal is funded, the rates quoted above shall, at the time of funding, be subject to adjustment for any period subsequent to June 30, 2012, if superseding Government approved rates have been established. The fringe benefit rates are negotiated and approved by the Office of Naval Research, Penn State's cognizant federal agency.

**Supplies and Materials** – Supply and expense items categorized as project specific, are for expenses directly related to this project, and are reasonable and necessary for the performance of this work. **Drilling work:** Funds are requested in the amount of \$7,000 for costs related to drilling and pump tests. We request funding for Hobo pressure transducers (11 x \$500/each), new drill bits for the portable rig (\$1,000), and PVC for casing (\$500). Drilling work will largely be completed by K. Singha. **Hydrologic sensor work:** Funds in the amount of \$9,000 are requested for supplies and materials to (1) upgrade the weir at shale hills by installing a new metal weir plate, cleaning and sealing the rubber liner, installing a concrete approach section to catch sediments and debris, and installing a bubbling system to keep it ice-free in the winter (\$4,000); (2) install ADCP (Acoustic Doppler Current Profiler) at old USGS gauge site location on Shaver Creek including radio communication via cellphone (~\$2,000), and (3) upgrade or maintain sapflux measurement devices (\$3,000). **Soil moisture work:** Funds in the amount of \$15,079 are requested for maintenance and upgrade of soil moisture studies, including soil moisture sensors, multiplexers, and datalogger replacements or upgrades.

**Communication Services** – Funds are requested in the amount of \$1,275 for costs related to conference calling and video conferencing expenses, as well as for internet access at our Shale Hills site.

**Domestic Travel** – All travel will be in accordance with University travel regulations and mileage will be charged at the current rate on the date of travel. Travel estimates are based on costs that were incurred on previous projects of a similar nature for federal and state agencies. **All-Hands Meeting:** Travel funds are requested in the amount of \$15,000 for 10 Penn State scientists and students to travel to the annual All-Hands meeting for all six CZO sites. Travel expenses are estimated at \$1,500 per person to include, airfare, ground transportation, lodging, and meals. **Professional Conferences:** Travel funds in the amount of \$15,000 are requested for all six students (4 postdocs and 2 grads) and 4 CZO advisors (10 total travelers) to attend one professional meeting to present research findings or travel to a satellite CZO

site for field work. Depending on conference location, funds are estimated to be \$1,500 per person for airfare, ground transportation, lodging, and meals. **Travel to Vermont:** Funds in the amount of \$4,000 are requested for co-PI Kirby and student to complete cosmogenic analyses with Paul Bierman at the Univ. of Vermont. We estimate two trips of 5 days each back and forth to Vermont. Expenses will include transportation, lodging and meals.

**Analytical Analyses** – Funds in the amount of \$26,000 are requested for geochemical analyses in the Materials Characterization Laboratory, the Laboratory for Isotopes and Metals Analysis (LIME), as well as Agricultural Sciences Analysis Laboratory at Penn State. These analyses will include chemical characterization, X ray diffraction, scanning electron microscopy, transmission electron microscopy, organic carbon analysis, and ion chromatography as needed (see *Facilities*). Funds are also allocated for U series analysis, to be made in collaboration with Lin Ma, Univ. of Texas, El Paso. Funds in the amount of \$16,000 are requested for cosmogenic analyses, to be analyzed in collaboration with Paul Bierman, Univ. of Vermont. (Total funds requested for analytical analyses is \$42,000.)

**Purchased services** – Funds in the amount of \$13,500 are requested for drilling of one 100 foot well (at about \$100/ft), with geophysics, and for Geoprobe drilling. This will be completed by K. Singha. Funds in the amount of \$1000 are also requested for the annual cost of electrical service at the Shale Hills site.

**Maintenance Contracts** – Funds in the amount of \$2,500 are requested for our annual maintenance contracts to outside sources for the RTH\_NET, real-time soil moisture sites, real-time redox, rain gauges, snow survey, outside contract to climb tower to service data-loggers, camera, etc.

**Laptop Computers** – Funds in the amount of \$5,576 are requested for laptop computers for the new post-docs. They will be required to synthesize data, collect data, analyze data, and write up syntheses of data investigating the 5 hypotheses summarized in the proposal. This will require extensive field work and data portability is essential. All post-docs will be working 100% time on this CZO project and the laptops will not be used for any other purpose. In addition, funds in the amount of \$3000 are requested to replace the 4-year old backup field computer in the communication shed at Shale Hills to assure data flow under all environmental conditions. (Total funds requested for laptop computers is \$8,576.)

**Undergraduate Student Stipends** – Funds in the amount of \$8,000 are requested to support two undergraduate students for 8 weeks in the summer to participate in field work at the CZO. Stipend consists of \$500/wk for 8 weeks per each student. Students will come from the satellite site institutions.

**Seed Grants** – Funds in the amount of \$50,000 are requested to provide funding opportunities in the form of seed grants to non-PSU scientists interested in participating in research projects at our Shale Hills CZO. We will solicit beyond the current SSHO workers to find researchers to apply for these funds. The Steering Committee will make funding decisions.

**Graduate Assistant Tuition Remission** - Computed using the approved tuition charges for a one-half (1/2) time graduate assistant of \$7,315 for Fall semester 2011 and Spring semester 2012, and \$3,658 for summer session 2012. The charges quoted above are increased by six (6.0) percent for any project period occurring after summer session 2012, and each summer session thereafter.

**F&A – On Campus Research** – F&A rates are negotiated and approved by the Office of Naval Research, Penn State's cognizant federal agency. Penn State's current on-campus rates for research are 49% of Modified Total Direct Costs (MTDC) from July 1, 2011, to June 30, 2013. New awards and new competitive segments with an effective date of July 1, 2013, or later shall be subject to adjustment when superseding Government approved rates are established. Per OMB Circular A-21, the actual F&A rates used will be fixed at the time of the initial award for the duration of the competitive segment.

## Current and Pending Support

(See GPG Section II.C.2.h for guidance on information to include on this form.)

The following information should be provided for each investigator and other senior personnel. Failure to provide this information may delay consideration of this proposal.	
Investigator: Susan Brantley	Other agencies (including NSF) to which this proposal has been/will be submitted.
<p>Support:   <input checked="" type="checkbox"/> Current   <input type="checkbox"/> Pending   <input type="checkbox"/> Submission Planned in Near Future   <input type="checkbox"/> *Transfer of Support</p> <p>Project/Proposal Title:   Regolith and the Critical Zone in the Susquehanna River Basin: The Shale Experiment (Co-PI w/C. Duffy)</p> <p>Source of Support:       National Science Foundation</p> <p>Total Award Amount: \$   4,250,000 Total Award Period Covered:   11/01/07 - 10/31/12</p> <p>Location of Project:     The Pennsylvania State University</p> <p>Person-Months Per Year Committed to the Project.   Cal:0.00   Acad: 0.00   Sumr: 0.50</p>	
<p>Support:   <input checked="" type="checkbox"/> Current   <input type="checkbox"/> Pending   <input type="checkbox"/> Submission Planned in Near Future   <input type="checkbox"/> *Transfer of Support</p> <p>Project/Proposal Title:   Signatures of Life from Earth and Beyond (1 of 14 Co-PIs)</p> <p>Source of Support:       NASA</p> <p>Total Award Amount: \$   8,024,017 Total Award Period Covered:   02/01/09 - 01/31/14</p> <p>Location of Project:     The Pennsylvania State University</p> <p>Person-Months Per Year Committed to the Project.   Cal:0.00   Acad: 0.00   Sumr: 0.00</p>	
<p>Support:   <input checked="" type="checkbox"/> Current   <input type="checkbox"/> Pending   <input type="checkbox"/> Submission Planned in Near Future   <input type="checkbox"/> *Transfer of Support</p> <p>Project/Proposal Title:   CZO: Luquillo Critical Zone Observatory (Co-PI w/F. Scatena &amp; A. White)(Lead: Univ. Pennsylvania)</p> <p>Source of Support:       National Science Foundation</p> <p>Total Award Amount: \$   559,984 Total Award Period Covered:   10/01/09 - 09/30/13</p> <p>Location of Project:     The Pennsylvania State University</p> <p>Person-Months Per Year Committed to the Project.   Cal:0.00   Acad: 0.50   Sumr: 0.00</p>	
<p>Support:   <input checked="" type="checkbox"/> Current   <input type="checkbox"/> Pending   <input type="checkbox"/> Submission Planned in Near Future   <input type="checkbox"/> *Transfer of Support</p> <p>Project/Proposal Title:   ARRA: MRI-R2: Acquisition of a multiple collector inductively-coupled mass spectrometer (MC-ICP-MS) for multi-disciplinary biogeochemical research at Penn State</p> <p>Source of Support:       National Science Foundation</p> <p>Total Award Amount: \$   724,002 Total Award Period Covered:   03/15/10 - 02/28/13</p> <p>Location of Project:     The Pennsylvania State University</p> <p>Person-Months Per Year Committed to the Project.   Cal:0.00   Acad: 0.00   Sumr: 0.00</p>	
<p>Support:   <input checked="" type="checkbox"/> Current   <input type="checkbox"/> Pending   <input type="checkbox"/> Submission Planned in Near Future   <input type="checkbox"/> *Transfer of Support</p> <p>Project/Proposal Title:   Collaborative Research: Acquisition of nitrogenase metal cofactors in soils: Role of metallophores and limitation of N<sub>2</sub>-fixation (w/Princeton Univ)</p> <p>Source of Support:       National Science Foundation</p> <p>Total Award Amount: \$   39,682 Total Award Period Covered:   09/01/10 - 08/31/13</p> <p>Location of Project:     The Pennsylvania State University</p> <p>Person-Months Per Year Committed to the Project.   Cal:0.00   Acad: 0.00   Summ: 0.00</p>	
*If this project has previously been funded by another agency, please list and furnish information for immediately preceding funding period.	

## Current and Pending Support

(See GPG Section II.C.2.h for guidance on information to include on this form.)

The following information should be provided for each investigator and other senior personnel. Failure to provide this information may delay consideration of this proposal.	
Investigator: Susan Brantley	Other agencies (including NSF) to which this proposal has been/will be submitted.
<p>Support:   <input checked="" type="checkbox"/> Current   <input type="checkbox"/> Pending   <input type="checkbox"/> Submission Planned in Near Future   <input type="checkbox"/> *Transfer of Support</p> <p>Project/Proposal Title: Supplement Request: CZO: Susquehanna/Shale Hills Critical Zone Observatory (funds to support a national CZO program director @ PSU)</p> <p>Source of Support: National Science Foundation</p> <p>Total Award Amount: \$ 168,925 Total Award Period Covered: 07/01/10 - 10/31/12</p> <p>Location of Project: The Pennsylvania State University</p> <p>Person-Months Per Year Committed to the Project. Cal:0.00 Acad: 0.00 Sumr: 0.00</p>	
<p>Support:   <input checked="" type="checkbox"/> Current   <input type="checkbox"/> Pending   <input type="checkbox"/> Submission Planned in Near Future   <input type="checkbox"/> *Transfer of Support</p> <p>Project/Proposal Title: Soils and vegetation as a record of anthropogenic pollutants: Mn in the Shale Hills CZO (w/C. Martinez)</p> <p>Source of Support: National Science Foundation</p> <p>Total Award Amount: \$ 150,800 Total Award Period Covered: 08/15/11 - 07/31/13</p> <p>Location of Project: The Pennsylvania State University</p> <p>Person-Months Per Year Committed to the Project. Cal:0.00 Acad: 0.00 Sumr: 0.00</p>	
<p>Support:   <input checked="" type="checkbox"/> Current   <input type="checkbox"/> Pending   <input type="checkbox"/> Submission Planned in Near Future   <input type="checkbox"/> *Transfer of Support</p> <p>Project/Proposal Title: An investigation of roughness and weathering at the bedrock-regolith interface</p> <p>Source of Support: DOE</p> <p>Total Award Amount: \$ 690,000 Total Award Period Covered: 09/01/11 - 08/31/14</p> <p>Location of Project: The Pennsylvania State University</p> <p>Person-Months Per Year Committed to the Project. Cal:0.00 Acad: 0.75 Sumr: 0.25</p>	
<p>Support:   <input checked="" type="checkbox"/> Current   <input type="checkbox"/> Pending   <input type="checkbox"/> Submission Planned in Near Future   <input type="checkbox"/> *Transfer of Support</p> <p>Project/Proposal Title: Biochemical mechanisms and associated biomolecular signatures underlying energy strategies of Geobacter sulfurreducens (Co-PI w/M. Tien)</p> <p>Source of Support: DOE</p> <p>Total Award Amount: \$ 527,982 Total Award Period Covered: 09/15/11 - 09/14/14</p> <p>Location of Project: The Pennsylvania State University</p> <p>Person-Months Per Year Committed to the Project. Cal:0.00 Acad: 0.38 Sumr: 0.12</p>	
<p>Support:   <input checked="" type="checkbox"/> Current   <input type="checkbox"/> Pending   <input type="checkbox"/> Submission Planned in Near Future   <input type="checkbox"/> *Transfer of Support</p> <p>Project/Proposal Title: RCN-SEES: The Marcellus Shale Network</p> <p>Source of Support: National Science Foundation</p> <p>Total Award Amount: \$ 750,000 Total Award Period Covered: 10/01/11 - 09/30/15</p> <p>Location of Project: The Pennsylvania State University</p> <p>Person-Months Per Year Committed to the Project. Cal:0.00 Acad: 0.38 Summ: 0.12</p>	
*If this project has previously been funded by another agency, please list and furnish information for immediately preceding funding period.	

## Current and Pending Support

(See GPG Section II.C.2.h for guidance on information to include on this form.)

The following information should be provided for each investigator and other senior personnel. Failure to provide this information may delay consideration of this proposal.	
Investigator: Susan Brantley	Other agencies (including NSF) to which this proposal has been/will be submitted.
<p>Support:    <input type="checkbox"/> Current    <input checked="" type="checkbox"/> Pending    <input type="checkbox"/> Submission Planned in Near Future    <input type="checkbox"/> *Transfer of Support</p> <p>Project/Proposal Title: Collaborative Research: Using weathering rind information along environmental gradients to quantify weathering rates in tropical Guadeloupe (Co-PI w/Lin Ma)</p> <p>Source of Support: National Science Foundation</p> <p>Total Award Amount: \$ 64,460 Total Award Period Covered: 01/16/12 - 01/15/15</p> <p>Location of Project: The Pennsylvania State University</p> <p>Person-Months Per Year Committed to the Project. Cal:0.00 Acad: 0.19 Sumr: 0.06</p>	
<p>Support:    <input type="checkbox"/> Current    <input checked="" type="checkbox"/> Pending    <input type="checkbox"/> Submission Planned in Near Future    <input type="checkbox"/> *Transfer of Support</p> <p>Project/Proposal Title: From the Earth to the Stars: Young Children's Understanding of Earth Systems (Co-PI w/D. Smith &amp; J. Plummer)</p> <p>Source of Support: National Science Foundation</p> <p>Total Award Amount: \$ 1,976,512 Total Award Period Covered: 07/01/12 - 06/30/16</p> <p>Location of Project: The Pennsylvania State University</p> <p>Person-Months Per Year Committed to the Project. Cal:0.00 Acad: 0.38 Sumr: 0.12</p>	
<p>Support:    <input type="checkbox"/> Current    <input checked="" type="checkbox"/> Pending    <input type="checkbox"/> Submission Planned in Near Future    <input type="checkbox"/> *Transfer of Support</p> <p>Project/Proposal Title: Using climate simulations to drive models of hydrologic flow and soil chemical evolution</p> <p>Source of Support: US DOE, Terrestrial Ecosystem Science</p> <p>Total Award Amount: \$ 1,041,710 Total Award Period Covered: 01/01/12 - 12/31/14</p> <p>Location of Project: The Pennsylvania State University</p> <p>Person-Months Per Year Committed to the Project. Cal:0.00 Acad: 1.13 Sumr: 0.38</p>	
<p>Support:    <input type="checkbox"/> Current    <input checked="" type="checkbox"/> Pending    <input type="checkbox"/> Submission Planned in Near Future    <input type="checkbox"/> *Transfer of Support</p> <p>Project/Proposal Title: How micro-organisms contribute to fracturing and weathering of basaltic rocks (w/L. Liermann &amp; T. White)</p> <p>Source of Support: NASA</p> <p>Total Award Amount: \$ 321,441 Total Award Period Covered: 09/01/12 - 08/31/14</p> <p>Location of Project: The Pennsylvania State University</p> <p>Person-Months Per Year Committed to the Project. Cal:0.00 Acad: 0.38 Sumr: 0.13</p>	
<p>Support:    <input type="checkbox"/> Current    <input checked="" type="checkbox"/> Pending    <input type="checkbox"/> Submission Planned in Near Future    <input type="checkbox"/> *Transfer of Support</p> <p>Project/Proposal Title: An Accomplishment-Based Request for Renewal of the Susquehanna-Shale Hills Critical Zone Observatory (SSHO)(this proposal)</p> <p>Source of Support: National Science Foundation</p> <p>Total Award Amount: \$ 1,000,000 Total Award Period Covered: 11/01/12 - 10/31/13</p> <p>Location of Project: The Pennsylvania State University</p> <p>Person-Months Per Year Committed to the Project. Cal:0.00 Acad: 0.81 Summ: 0.27</p>	
*If this project has previously been funded by another agency, please list and furnish information for immediately preceding funding period.	

## Current and Pending Support

(See GPG Section II.C.2.h for guidance on information to include on this form.)

The following information should be provided for each investigator and other senior personnel. Failure to provide this information may delay consideration of this proposal.	
Investigator: Christopher Duffy	Other agencies (including NSF) to which this proposal has been/will be submitted.
Support: <input checked="" type="checkbox"/> Current <input type="checkbox"/> Pending <input type="checkbox"/> Submission Planned in Near Future <input type="checkbox"/> *Transfer of Support Project/Proposal Title: Chesapeake Bay Watershed Modeling Technical Support  Source of Support:    National Science Foundation Total Award Amount: \$    868,643 Total Award Period Covered:    01/01/11 - 12/31/17 Location of Project:    University of Arizona Person-Months Per Year Committed to the Project.    Cal:0.50    Acad: 0.00    Sumr: 0.00	
Support: <input checked="" type="checkbox"/> Current <input type="checkbox"/> Pending <input type="checkbox"/> Submission Planned in Near Future <input type="checkbox"/> *Transfer of Support Project/Proposal Title: Center for Green Infrastructure and Stormwater Management  Source of Support:    EPA Total Award Amount: \$    2,173,026 Total Award Period Covered:    01/01/12 - 12/31/17 Location of Project:    The Pennsylvania State University Person-Months Per Year Committed to the Project.    Cal:0.00    Acad: 0.00    Sumr: 0.50	
Support: <input checked="" type="checkbox"/> Current <input type="checkbox"/> Pending <input type="checkbox"/> Submission Planned in Near Future <input type="checkbox"/> *Transfer of Support Project/Proposal Title: CZP" Susquehanna/Shale Hills Critical Zone Observatory  Source of Support:    National Science Foundation Total Award Amount: \$    4,250,000 Total Award Period Covered:    11/01/07 - 10/31/12 Location of Project:    The Pennsylvania State University Person-Months Per Year Committed to the Project.    Cal:1.00    Acad: 0.00    Sumr: 0.00	
Support: <input checked="" type="checkbox"/> Current <input type="checkbox"/> Pending <input type="checkbox"/> Submission Planned in Near Future <input type="checkbox"/> *Transfer of Support Project/Proposal Title: Resolving the role of groundwater in multi-scale land-atmosphere dynamics using simulations, sensor networks and satellites  Source of Support:    NOAA Total Award Amount: \$    580,000 Total Award Period Covered:    01/01/10 - 12/31/13 Location of Project:    The Pennsylvania State University Person-Months Per Year Committed to the Project.    Cal:1.00    Acad: 0.00    Sumr: 0.00	
Support: <input checked="" type="checkbox"/> Current <input type="checkbox"/> Pending <input type="checkbox"/> Submission Planned in Near Future <input type="checkbox"/> *Transfer of Support Project/Proposal Title: European Commission SoilTrEC and Critical Zone Observatories  Source of Support:    National Science Foundation Total Award Amount: \$    250,000 Total Award Period Covered:    07/01/10 - 06/30/15 Location of Project:    The Pennsylvania State University Person-Months Per Year Committed to the Project.    Cal:0.50    Acad: 0.00    Summ: 0.00	
*If this project has previously been funded by another agency, please list and furnish information for immediately preceding funding period.	

## Current and Pending Support

(See GPG Section II.C.2.h for guidance on information to include on this form.)

The following information should be provided for each investigator and other senior personnel. Failure to provide this information may delay consideration of this proposal.	
Investigator: Christopher Duffy	Other agencies (including NSF) to which this proposal has been/will be submitted.
<p>Support:    <input type="checkbox"/> Current    <input checked="" type="checkbox"/> Pending    <input type="checkbox"/> Submission Planned in Near Future    <input type="checkbox"/> *Transfer of Support</p> <p>Project/Proposal Title:    An Accomplishment-Based Request for Renewal of the Susquehanna-Shale Hills Critical Zone Observatory (SSHO)(PI: S. Brantley)(this proposal)</p> <p>Source of Support:    National Science Foundation</p> <p>Total Award Amount: \$    1,000,000    Total Award Period Covered:    11/01/12 - 10/31/13</p> <p>Location of Project:    The Pennsylvania State University</p> <p>Person-Months Per Year Committed to the Project.    Cal:0.00    Acad: 0.57    Sumr: 0.19</p>	
<p>Support:    <input type="checkbox"/> Current    <input type="checkbox"/> Pending    <input type="checkbox"/> Submission Planned in Near Future    <input type="checkbox"/> *Transfer of Support</p> <p>Project/Proposal Title:</p> <p>Source of Support:</p> <p>Total Award Amount: \$                         Total Award Period Covered:</p> <p>Location of Project:</p> <p>Person-Months Per Year Committed to the Project.    Cal:                      Acad:                      Sumr:</p>	
<p>Support:    <input type="checkbox"/> Current    <input type="checkbox"/> Pending    <input type="checkbox"/> Submission Planned in Near Future    <input type="checkbox"/> *Transfer of Support</p> <p>Project/Proposal Title:</p> <p>Source of Support:</p> <p>Total Award Amount: \$                         Total Award Period Covered:</p> <p>Location of Project:</p> <p>Person-Months Per Year Committed to the Project.    Cal:                      Acad:                      Sumr:</p>	
<p>Support:    <input type="checkbox"/> Current    <input type="checkbox"/> Pending    <input type="checkbox"/> Submission Planned in Near Future    <input type="checkbox"/> *Transfer of Support</p> <p>Project/Proposal Title:</p> <p>Source of Support:</p> <p>Total Award Amount: \$                         Total Award Period Covered:</p> <p>Location of Project:</p> <p>Person-Months Per Year Committed to the Project.    Cal:                      Acad:                      Sumr:</p>	
<p>Support:    <input type="checkbox"/> Current    <input type="checkbox"/> Pending    <input type="checkbox"/> Submission Planned in Near Future    <input type="checkbox"/> *Transfer of Support</p> <p>Project/Proposal Title:</p> <p>Source of Support:</p> <p>Total Award Amount: \$                         Total Award Period Covered:</p> <p>Location of Project:</p> <p>Person-Months Per Year Committed to the Project.    Cal:                      Acad:                      Summ:</p>	

\*If this project has previously been funded by another agency, please list and furnish information for immediately preceding funding period.

## Current and Pending Support

(See GPG Section II.C.2.h for guidance on information to include on this form.)

The following information should be provided for each investigator and other senior personnel. Failure to provide this information may delay consideration of this proposal.	
Investigator: David Eissenstat	Other agencies (including NSF) to which this proposal has been/will be submitted.
<p>Support:    <input checked="" type="checkbox"/> Current    <input type="checkbox"/> Pending    <input type="checkbox"/> Submission Planned in Near Future    <input type="checkbox"/> *Transfer of Support</p> <p>Project/Proposal Title: CZO: The Susquehanna/Shale Hills Critical Zone Observatory (1 of 11 Co-PIs)</p> <p>Source of Support:        National Science Foundation</p> <p>Total Award Amount: \$ 4,250,000 Total Award Period Covered: 11/01/07 - 10/31/12</p> <p>Location of Project:     The Pennsylvania State University</p> <p>Person-Months Per Year Committed to the Project.    Cal:0.00    Acad:0.38    Sumr: 0.12</p>	
<p>Support:    <input checked="" type="checkbox"/> Current    <input type="checkbox"/> Pending    <input type="checkbox"/> Submission Planned in Near Future    <input type="checkbox"/> *Transfer of Support</p> <p>Project/Proposal Title: The influence of tree species on soil organic matter dynamics in temperate forests</p> <p>Source of Support:        NSF - DEB - Ecosystem Studies</p> <p>Total Award Amount: \$ 209,735 Total Award Period Covered: 08/01/08 - 07/31/12</p> <p>Location of Project:     The Pennsylvania State University, Poland, Germany</p> <p>Person-Months Per Year Committed to the Project.    Cal:0.00    Acad:0.75    Sumr: 0.25</p>	
<p>Support:    <input checked="" type="checkbox"/> Current    <input type="checkbox"/> Pending    <input type="checkbox"/> Submission Planned in Near Future    <input type="checkbox"/> *Transfer of Support</p> <p>Project/Proposal Title: Nutrient foraging by mycorrhizal roots of different morphology: Are roots and fungi complementary?</p> <p>Source of Support:        NSF - IOB - Physiological and structural systems</p> <p>Total Award Amount: \$ 520,000 Total Award Period Covered: 09/01/11 - 08/31/14</p> <p>Location of Project:     The Pennsylvania State University and China</p> <p>Person-Months Per Year Committed to the Project.    Cal:0.00    Acad:0.75    Sumr: 0.25</p>	
<p>Support:    <input checked="" type="checkbox"/> Current    <input type="checkbox"/> Pending    <input type="checkbox"/> Submission Planned in Near Future    <input type="checkbox"/> *Transfer of Support</p> <p>Project/Proposal Title: Linking below ground phenology and ecosystem function in a warming arctic</p> <p>Source of Support:        NSF - ARO</p> <p>Total Award Amount: \$ 873,871 Total Award Period Covered: 07/01/11 - 06/30/15</p> <p>Location of Project:     The Pennsylvania State University</p> <p>Person-Months Per Year Committed to the Project.    Cal:0.00    Acad:0.75    Sumr: 0.25</p>	
<p>Support:    <input checked="" type="checkbox"/> Current    <input type="checkbox"/> Pending    <input type="checkbox"/> Submission Planned in Near Future    <input type="checkbox"/> *Transfer of Support</p> <p>Project/Proposal Title: Scaling root processes: Global Impacts Workshop</p> <p>Source of Support:        NSF - DEB</p> <p>Total Award Amount: \$ 7,990 Total Award Period Covered: 02/15/12 - 07/31/12</p> <p>Location of Project:     The Pennsylvania State University</p> <p>Person-Months Per Year Committed to the Project.    Cal:0.00    Acad:0.09    Summ: 0.03</p>	
*If this project has previously been funded by another agency, please list and furnish information for immediately preceding funding period.	



## Current and Pending Support

(See GPG Section II.C.2.h for guidance on information to include on this form.)

The following information should be provided for each investigator and other senior personnel. Failure to provide this information may delay consideration of this proposal.	
Investigator: Eric Kirby	Other agencies (including NSF) to which this proposal has been/will be submitted.
<p>Support:    <input checked="" type="checkbox"/> Current    <input type="checkbox"/> Pending    <input type="checkbox"/> Submission Planned in Near Future    <input type="checkbox"/> *Transfer of Support</p> <p>Project/Proposal Title:    ARRA: Probing the Rheology of Tibetan Lithosphere: Surface Deformation in Response to Climatically-Induced Changes in Lake Loads</p> <p>Source of Support:    National Science Foundation</p> <p>Total Award Amount: \$    459,877 Total Award Period Covered:    01/01/10 - 12/31/12</p> <p>Location of Project:    The Pennsylvania State University</p> <p>Person-Months Per Year Committed to the Project.    Cal:0.00    Acad: 0.75    Sumr: 0.00</p>	
<p>Support:    <input checked="" type="checkbox"/> Current    <input type="checkbox"/> Pending    <input type="checkbox"/> Submission Planned in Near Future    <input type="checkbox"/> *Transfer of Support</p> <p>Project/Proposal Title:    Inner Forearc Deformation along an Erosive Convergent Margin, Northeastern Japan</p> <p>Source of Support:    National Science Foundation</p> <p>Total Award Amount: \$    355,033 Total Award Period Covered:    07/01/08 - 06/30/12</p> <p>Location of Project:    The Pennsylvania State University</p> <p>Person-Months Per Year Committed to the Project.    Cal:0.00    Acad: 0.00    Sumr: 0.00</p>	
<p>Support:    <input checked="" type="checkbox"/> Current    <input type="checkbox"/> Pending    <input type="checkbox"/> Submission Planned in Near Future    <input type="checkbox"/> *Transfer of Support</p> <p>Project/Proposal Title:    CZO: Susquehanna/Shale Hills Critical Zone Observatory (PI: C. Duffy)</p> <p>Source of Support:    National Science Foundation</p> <p>Total Award Amount: \$    4,250,000 Total Award Period Covered:    11/01/07 - 10/31/12</p> <p>Location of Project:    The Pennsylvania State University</p> <p>Person-Months Per Year Committed to the Project.    Cal:0.00    Acad: 0.00    Sumr: 0.25</p>	
<p>Support:    <input checked="" type="checkbox"/> Current    <input type="checkbox"/> Pending    <input type="checkbox"/> Submission Planned in Near Future    <input type="checkbox"/> *Transfer of Support</p> <p>Project/Proposal Title:    Targeted Math Science Partnership: Middle Grades Earth &amp; Space Science Education</p> <p>Source of Support:    National Science Foundation</p> <p>Total Award Amount: \$    9,205,578 Total Award Period Covered:    09/01/10 - 08/31/15</p> <p>Location of Project:    The Pennsylvania State University</p> <p>Person-Months Per Year Committed to the Project.    Cal:0.00    Acad: 0.75    Sumr: 0.25</p>	
<p>Support:    <input checked="" type="checkbox"/> Current    <input type="checkbox"/> Pending    <input type="checkbox"/> Submission Planned in Near Future    <input type="checkbox"/> *Transfer of Support</p> <p>Project/Proposal Title:    Collaborative Research: Upward and Outward: Tibetan Plateau Growth and Climate Consequences</p> <p>Source of Support:    National Science Foundation</p> <p>Total Award Amount: \$    358,742 Total Award Period Covered:    09/01/05 - 08/31/12</p> <p>Location of Project:    The Pennsylvania State University</p> <p>Person-Months Per Year Committed to the Project.    Cal:0.00    Acad: 0.00    Summ: 0.00</p>	
*If this project has previously been funded by another agency, please list and furnish information for immediately preceding funding period.	

## Current and Pending Support

(See GPG Section II.C.2.h for guidance on information to include on this form.)

The following information should be provided for each investigator and other senior personnel. Failure to provide this information may delay consideration of this proposal.	
Investigator: Eric Kirby	Other agencies (including NSF) to which this proposal has been/will be submitted.
Support: <input checked="" type="checkbox"/> Current <input type="checkbox"/> Pending <input type="checkbox"/> Submission Planned in Near Future <input type="checkbox"/> *Transfer of Support Project/Proposal Title: Collaborative Research: CREST: Colorado Rockies Seismic Experiment and Transect: Time-space patterns of Cenozoic uplift-magmatism and their correspondence to the Aspen  Source of Support: National Science Foundation Total Award Amount: \$ 210,000 Total Award Period Covered: 11/01/06 - 10/31/12 Location of Project: The Pennsylvania State University Person-Months Per Year Committed to the Project. Cal:0.00 Acad:0.00 Sumr: 0.00	
Support: <input checked="" type="checkbox"/> Current <input type="checkbox"/> Pending <input type="checkbox"/> Submission Planned in Near Future <input type="checkbox"/> *Transfer of Support Project/Proposal Title: EAGER: Upper-Plate Response to a Great Earthquake: Integrating Deformation from Seismic to Geologic Timescales  Source of Support: National Science Foundation Total Award Amount: \$ 102,167 Total Award Period Covered: 01/01/12 - 12/31/12 Location of Project: The Pennsylvania State University Person-Months Per Year Committed to the Project. Cal:0.00 Acad:0.19 Sumr: 0.06	
Support: <input type="checkbox"/> Current <input checked="" type="checkbox"/> Pending <input type="checkbox"/> Submission Planned in Near Future <input type="checkbox"/> *Transfer of Support Project/Proposal Title: An Accomplishment-Based Request for Renewal of the Susquehanna-Shale Hills Critical Zone Observatory (SSHO) (PI: S. Brantley)(this proposal)  Source of Support: National Science Foundation Total Award Amount: \$ 1,000,000 Total Award Period Covered: 11/01/12 - 10/31/13 Location of Project: The Pennsylvania State University Person-Months Per Year Committed to the Project. Cal:0.00 Acad:0.57 Sumr: 0.19	
Support: <input type="checkbox"/> Current <input type="checkbox"/> Pending <input type="checkbox"/> Submission Planned in Near Future <input type="checkbox"/> *Transfer of Support Project/Proposal Title:  Source of Support: Total Award Amount: \$                      Total Award Period Covered: Location of Project: Person-Months Per Year Committed to the Project. Cal:                      Acad:                      Sumr:	
Support: <input type="checkbox"/> Current <input type="checkbox"/> Pending <input type="checkbox"/> Submission Planned in Near Future <input type="checkbox"/> *Transfer of Support Project/Proposal Title:  Source of Support: Total Award Amount: \$                      Total Award Period Covered: Location of Project: Person-Months Per Year Committed to the Project. Cal:                      Acad:                      Summ:	

\*If this project has previously been funded by another agency, please list and furnish information for immediately preceding funding period.

## CURRENT AND PENDING SUPPORT

### Current Support – Kenneth Davis

NSF EAR 07-25019, 7/1/07 – 6/30/12, \$4,250,000, 0.19 Acad mths, 0.07 Sumr mths, “Regolith and the critical zone in the Susquehanna River Basin: the shale experiment.” (thru PSEII w/Duffy) (60TV)

NASA 4/1/08 – 3/31/12 (1 year no-cost extension), \$625,373, 0.63 Acad mths, 0.21 Sumr mths, “Probabilistic carbon flux upscaling across a northern forest ecoregion” (Keller 2% co-PI) (57T1)

Colorado State Univ. G-1968-2 (NASA Prime, NNX08AK08G) 6/1/08 – 3/31/12 (1 year no-cost extension), \$112,675, 0.18 Acad mths, 0.06 Sumr mths, “Resolving net CO<sub>2</sub> exchange in the mid-continent region of North America by comparing and reconciling results.” (2AA6)

NOAA, 7/1/10 – 6/30/13, \$511,636, 0.72 Acad mths, 0.24 Sumr mths, “Resolving the role of groundwater-surface dynamics in land-atmosphere interactions within a multiscale computation sensor network: Juniata River Basin.” (PI: Duffy, PSIEE).

NIST, 10/1/2010-9/30/2013, \$1,259,073 (first two years of funding), 1.35 Acad mths, 0.45 Sumr mths, “Estimation of urban greenhouse gas emissions using regional atmospheric inversions,” Davis, PI. Lauvaux, Miles, Richardson, Sweeney and Turnbull, co-Is.

NASA, 3/1/11 – 2/28/14, \$742,970, 1.13 Acad mths, 0.38 Sumr mths, “Regional atmospheric inversions to determine land-atmosphere carbon fluxes in the southeastern forests of the United States,” Davis, PI. Lauvaux, Miles and Richardson, co-Is.

NASA, 7/1/11 – 6/30/14, \$180,482, 0.54 Acad mths, 0.18 Sumr mths, “Influence of disturbance and seasonality on regional carbon flux upscaling.” Co-I with Smithwick, PI.

NOAA, 9/1/2011 – 8/31/2014, \$555,219, 0.45 Acad mths, 0.15 Sumr mths, “North American carbon cycle diagnoses using flux and mixing ratio observations, and high-resolution regional transport modeling,” Davis, PI. Keller, Miles, Richardson, Co-Is.

### Pending Support – Kenneth Davis

NASA, 11/1/2011 - 10/31/2014, \$328,724, 0.72 Acad mths, 0.24 Sumr mths, A proposal to serve on the science team for the Orbital Carbon Observatory – 2 mission.

National Science Foundation, 9/1/2011 - 8/31/2015, \$1,992,558, 0.75 Acad mths, 0.25 Sumr mths, "CPS: Medium: A Prototype for Multi-State Sensor Control for Adaptive Flood Simulation Using Coupled Watershed and Weather Prediction Models", Davis co-I with PI C. Duffy.

U.S. Department of Energy, 4/1/2012 - 3/31/2015, \$783,848, 0.90 Acad mths, 0.30 Sumr mths, "How well can flux towers and experimental data improve the hindcast and projection skill of terrestrial carbon cycle and Earth system models?", PI Davis with co-Is K Keller, M Dietze and D Ricciuto.

U.S. Department of Energy, 4/1/2012 - 3/31/2014, \$569,028, 0.75 Acad mths, 0.25 Sumr mths, "Reconstructing forest carbon dynamics over Centennial time scales using tree ring width and isotopic composition", Co-PI with PI A. Taylor.

Smithsonian Tropical Research Institute, 4/1/2012 - 3/31/2013, \$29,500, 0.00 Acad mths, 0.00 Sumr mths, "Reconstruction of long-term CO<sub>2</sub> assimilation and climate in the Amazon basin using tree-rings <sup>13</sup>C and <sup>18</sup>O", Co-PI with S. Belmecheri.

National Oceanic and Atmospheric Administration, 3/1/2012 - 2/28/2015, \$512,613, 0.45 Acad mths, 0.15 Sumr mths, "Improved representation of land-atmosphere interactions in metropolitan-scale greenhouse gas inversions", Co-I with PI N. Miles.

National Aeronautics and Space Administration, 6/1/2012 - 5/31/2015, \$820,665, 0.36 Acad Mths, 0.12 Sumr mths, "Terrestrial Carbon Upscaling Model Intercomparison Project (TCUP)", Institutional PI with Science PI K. Naithani.

Colorado State University, NASA prime, 5/1/2012 - 4/30/2014, \$186,752, 0.36 Acad mths, 0.12 Sumr mths, "Using Multiple Constraints to Investigate Inter-annual Variations in NEE in the Mid-Continent Intensive region of the U.S.", PSU PI with co-I T Lauvaux.

National Science Foundation, 9/1/2012 – 8/31/2014, \$9,974, 0.09 Acad mths, 0.03 Sumr mths (Year 1 only), "The coal-to-gas transition: Uncertainties in methane leakage, emissions timing and climate response".

Battelle – Pacific Northwest National Laboratory, 6/1/2012 – 5/31/2015, \$37,726, 0.38 Acad mths, 0.13 Sumr mths, "AmeriFlux Network Management".

National Science Foundation, 11/1/2012 – 10/31/2013, \$1,000,000, 0.38 Acad mths, 0.13 Sumr mths, "An Accomplishment-Based Request for Renewal of the Susquehanna-Shale Hills Critical Zone Observatory (SSHO)".

## Current and Pending Support

(See GPG Section II.C.2.h for guidance on information to include on this form.)

The following information should be provided for each investigator and other senior personnel. Failure to provide this information may delay consideration of this proposal.	
Investigator: Jason Kaye	Other agencies (including NSF) to which this proposal has been/will be submitted.
<p>Support:   <input checked="" type="checkbox"/> Current   <input type="checkbox"/> Pending   <input type="checkbox"/> Submission Planned in Near Future   <input type="checkbox"/> *Transfer of Support</p> <p>Project/Proposal Title: Finding the right mix: Multifunctional cover crop cocktails for organic</p> <p>Source of Support:       USDA-OREI</p> <p>Total Award Amount: \$ 2,296,803 Total Award Period Covered: 09/01/11 - 08/31/15</p> <p>Location of Project:     The Pennsylvania State University</p> <p>Person-Months Per Year Committed to the Project.   Cal:0.00   Acad: 0.00   Sumr: 1.00</p>	
<p>Support:   <input checked="" type="checkbox"/> Current   <input type="checkbox"/> Pending   <input type="checkbox"/> Submission Planned in Near Future   <input type="checkbox"/> *Transfer of Support</p> <p>Project/Proposal Title: Cover crop cocktails: Harnessing diversity to enhance nitrogen retention</p> <p>Source of Support:       USDA NE SARE Graduate Fellowship</p> <p>Total Award Amount: \$ 14,998 Total Award Period Covered: 09/01/11 - 08/31/13</p> <p>Location of Project:     The Pennsylvania State University</p> <p>Person-Months Per Year Committed to the Project.   Cal:0.00   Acad: 0.25   Sumr: 0.00</p>	
<p>Support:   <input checked="" type="checkbox"/> Current   <input type="checkbox"/> Pending   <input type="checkbox"/> Submission Planned in Near Future   <input type="checkbox"/> *Transfer of Support</p> <p>Project/Proposal Title: Transitions to Prosperity and Sustainability: Enhancing Small and Medium-sized Farms in the Rural Exurban-Urban Transitional Zone</p> <p>Source of Support:       USDA NRI</p> <p>Total Award Amount: \$ 491,018 Total Award Period Covered: 10/01/07 - 09/30/12</p> <p>Location of Project:     The Pennsylvania State University</p> <p>Person-Months Per Year Committed to the Project.   Cal:0.00   Acad: 0.25   Sumr: 0.00</p>	
<p>Support:   <input checked="" type="checkbox"/> Current   <input type="checkbox"/> Pending   <input type="checkbox"/> Submission Planned in Near Future   <input type="checkbox"/> *Transfer of Support</p> <p>Project/Proposal Title: Quantifying the N retention capacity of legacy sediments and hydric soils</p> <p>Source of Support:       PA WRRC</p> <p>Total Award Amount: \$ 16,700 Total Award Period Covered: 03/01/11 - 06/30/12</p> <p>Location of Project:     The Pennsylvania State University</p> <p>Person-Months Per Year Committed to the Project.   Cal:0.00   Acad: 0.25   Sumr: 0.00</p>	
<p>Support:   <input checked="" type="checkbox"/> Current   <input type="checkbox"/> Pending   <input type="checkbox"/> Submission Planned in Near Future   <input type="checkbox"/> *Transfer of Support</p> <p>Project/Proposal Title: A combined modeling and monitoring study to assess biofuel feedstock production systems greenhouse gas emissions and ecosystem services</p> <p>Source of Support:       DOT NE Sun Grant</p> <p>Total Award Amount: \$ 150,000 Total Award Period Covered: 01/01/11 - 12/31/14</p> <p>Location of Project:     The Pennsylvania State University</p> <p>Person-Months Per Year Committed to the Project.   Cal:0.00   Acad: 0.25   Summ: 0.00</p>	
*If this project has previously been funded by another agency, please list and furnish information for immediately preceding funding period.	

## Current and Pending Support

(See GPG Section II.C.2.h for guidance on information to include on this form.)

The following information should be provided for each investigator and other senior personnel. Failure to provide this information may delay consideration of this proposal.	
Investigator: Jason Kaye	Other agencies (including NSF) to which this proposal has been/will be submitted.
<p>Support:    <input checked="" type="checkbox"/> Current    <input type="checkbox"/> Pending    <input type="checkbox"/> Submission Planned in Near Future    <input type="checkbox"/> *Transfer of Support</p> <p>Project/Proposal Title:    Testing a model of the terrestrial nitrogen cycling including rapid stabilization of nitrogen in soil</p> <p>Source of Support:    NSF - DEB - Ecosystem Studies</p> <p>Total Award Amount: \$    532,371 Total Award Period Covered:    08/01/08 - 07/31/12</p> <p>Location of Project:    The Pennsylvania State University</p> <p>Person-Months Per Year Committed to the Project.    Cal:0.00    Acad: 0.00    Sumr: 1.00</p>	
<p>Support:    <input checked="" type="checkbox"/> Current    <input type="checkbox"/> Pending    <input type="checkbox"/> Submission Planned in Near Future    <input type="checkbox"/> *Transfer of Support</p> <p>Project/Proposal Title:    Weed management, environmental quality and profitability in organic feed and forage production systems</p> <p>Source of Support:    USDA RAMP</p> <p>Total Award Amount: \$    980,804 Total Award Period Covered:    10/01/07 - 09/30/12</p> <p>Location of Project:    The Pennsylvania State University</p> <p>Person-Months Per Year Committed to the Project.    Cal:0.00    Acad: 0.50    Sumr: 0.00</p>	
<p>Support:    <input checked="" type="checkbox"/> Current    <input type="checkbox"/> Pending    <input type="checkbox"/> Submission Planned in Near Future    <input type="checkbox"/> *Transfer of Support</p> <p>Project/Proposal Title:    International research experiences for students: Training global change ecologists through US-Spain collaboration</p> <p>Source of Support:    NSF OISE</p> <p>Total Award Amount: \$    150,000 Total Award Period Covered:    01/01/11 - 12/31/13</p> <p>Location of Project:    The Pennsylvania State University</p> <p>Person-Months Per Year Committed to the Project.    Cal:0.00    Acad: 0.00    Sumr: 0.50</p>	
<p>Support:    <input checked="" type="checkbox"/> Current    <input type="checkbox"/> Pending    <input type="checkbox"/> Submission Planned in Near Future    <input type="checkbox"/> *Transfer of Support</p> <p>Project/Proposal Title:    Regolith and the Critical Zone in the Susquehanna River: The Shale Experiment</p> <p>Source of Support:    National Science Foundation</p> <p>Total Award Amount: \$    4,250,000 Total Award Period Covered:    11/01/07 - 10/31/12</p> <p>Location of Project:    The Pennsylvania State University</p> <p>Person-Months Per Year Committed to the Project.    Cal:0.00    Acad: 0.00    Sumr: 0.25</p>	
<p>Support:    <input checked="" type="checkbox"/> Current    <input type="checkbox"/> Pending    <input type="checkbox"/> Submission Planned in Near Future    <input type="checkbox"/> *Transfer of Support</p> <p>Project/Proposal Title:    Integrated pasture-crop rotations</p> <p>Source of Support:    USDA ARS</p> <p>Total Award Amount: \$    168,970 Total Award Period Covered:    10/01/10 - 09/30/14</p> <p>Location of Project:    The Pennsylvania State University</p> <p>Person-Months Per Year Committed to the Project.    Cal:0.00    Acad: 0.25    Summ: 0.00</p>	
*If this project has previously been funded by another agency, please list and furnish information for immediately preceding funding period.	



## Current and Pending Support

(See GPG Section II.C.2.h for guidance on information to include on this form.)

The following information should be provided for each investigator and other senior personnel. Failure to provide this information may delay consideration of this proposal.	
Investigator: Henry Lin	Other agencies (including NSF) to which this proposal has been/will be submitted.
<p>Support:   <input checked="" type="checkbox"/> Current   <input type="checkbox"/> Pending   <input type="checkbox"/> Submission Planned in Near Future   <input type="checkbox"/> *Transfer of Support</p> <p>Project/Proposal Title: The Susquehanna/Shale Hills Critical Zone Observatory (PI: C. Duffy)</p> <p>Source of Support: National Science Foundation</p> <p>Total Award Amount: \$ 4,250,000 Total Award Period Covered: 11/01/07 - 10/31/12</p> <p>Location of Project: The Pennsylvania State University</p> <p>Person-Months Per Year Committed to the Project. Cal:0.00 Acad:0.00 Sumr: 1.00</p>	
<p>Support:   <input checked="" type="checkbox"/> Current   <input type="checkbox"/> Pending   <input type="checkbox"/> Submission Planned in Near Future   <input type="checkbox"/> *Transfer of Support</p> <p>Project/Proposal Title: Developing a Web-based forecasting tool for nutrient management (Co-PI w/T. Buda, P. Kleinman, &amp; B. Beegle)</p> <p>Source of Support: USDA-NIFA</p> <p>Total Award Amount: \$ 466,555 Total Award Period Covered: 01/01/12 - 12/31/16</p> <p>Location of Project: The Pennsylvania State University</p> <p>Person-Months Per Year Committed to the Project. Cal:0.00 Acad:0.40 Sumr: 0.00</p>	
<p>Support:   <input checked="" type="checkbox"/> Current   <input type="checkbox"/> Pending   <input type="checkbox"/> Submission Planned in Near Future   <input type="checkbox"/> *Transfer of Support</p> <p>Project/Proposal Title: The 2nd International Conference on Hydropedology</p> <p>Source of Support: USDA-NIFA</p> <p>Total Award Amount: \$ 15,000 Total Award Period Covered: 03/01/12 - 02/28/14</p> <p>Location of Project: Leipzig, Germany</p> <p>Person-Months Per Year Committed to the Project. Cal:0.00 Acad:0.10 Sumr: 0.00</p>	
<p>Support:   <input checked="" type="checkbox"/> Current   <input type="checkbox"/> Pending   <input type="checkbox"/> Submission Planned in Near Future   <input type="checkbox"/> *Transfer of Support</p> <p>Project/Proposal Title: Continuing real-time soil hydrologic monitoring at the Penn State living filter</p> <p>Source of Support: PSU OPP</p> <p>Total Award Amount: \$ 68,945 Total Award Period Covered: 07/01/11 - 06/30/12</p> <p>Location of Project: The Pennsylvania State University</p> <p>Person-Months Per Year Committed to the Project. Cal:0.00 Acad:0.50 Sumr: 0.00</p>	
<p>Support:   <input type="checkbox"/> Current   <input checked="" type="checkbox"/> Pending   <input type="checkbox"/> Submission Planned in Near Future   <input type="checkbox"/> *Transfer of Support</p> <p>Project/Proposal Title: WSC-Category 1: Collaborative Research: Unifying Geo-, Bio-, Eng-, and Social Sciences for Integrated Water Management: A Novel Application of Thermodynamics in a Rapidly-Urbanizin</p> <p>Source of Support: National Science Foundation</p> <p>Total Award Amount: \$ 75,000 Total Award Period Covered: 07/01/12 - 06/30/14</p> <p>Location of Project: The Pennsylvania State University</p> <p>Person-Months Per Year Committed to the Project. Cal:0.00 Acad:0.00 Summ:0.30</p>	
*If this project has previously been funded by another agency, please list and furnish information for immediately preceding funding period.	



## Kamini Singha – Current & Pending

### *In Progress*

Investigators	Role	Dates	Title	Source	Amount	Person Months
Singha	PI	8/1/08 - 7/31/13	CAREER: Mass Transport in Groundwater: an Integration of Research and Experiential Education	NSF-CAREER (EAR, Hydrologic Sciences)	\$411,274	1.25
Duffy, Brantley, Singha, Slingerland, Davis, Kirby, Toran, Eissenstat, Kaye, Lin, Reed, Salvage	Co-I	10/01/07 - 9/30/12	Regolith and the Critical Zone of the Susquehanna River Basin: The Shale Experiment	NSF EAR, Critical Zone Observatories	\$4.25M	0.72
Day-Lewis, Singha, Haggerty, Ward, Binley, Lane	Co-I	4/1/09 - 3/31/12	Geoelectrical Measurement of Multiscale Mass Transfer Parameters	DoE Environmental Remediation Sciences Program	\$255,288 (\$1.1M total)	1.0
Gooseff, Singha	Co-I	6/1/09 - 5/31/12	What are the seasonal controls on stream-riparian groundwater exchange during baseflow recession in headwater catchments?	NSF EAR, Hydrologic Sciences	\$455,887	1.0
Tschakert, Singha, Smithwick, Ward, Oppong	Co-I	8/1/09 - 7/31/14	Climatic Extremes, Mining, and <i>Mycobacterium Ulcerans</i> : A Coupled Systems Perspective	NSF Coupled Natural and Human Systems	\$1.42M	0.5

### *Proposed*

Investigators	Role	Dates	Title	Source	Amount	Person Months
Singha	PI	1/1/12 - 12/31/13	Early Career: Acquisition of Instrumentation to Measure Electrical Resistivity at the Field and Lab Scale	NSF Instrumentation & Facilities	\$92,711	0
Gooseff, Singha, Bowden	Co-I	8/15/12 - 8/14/16	Collaborative Research: How does the changing structure of the frost table affect the storage and movement of water and solutes in permafrost dominated hillslopes in arctic tundra?	NSF Office of Polar Programs	\$1.15M	1.0
Singha, Fantle, Bolster	PI	8/15/12 – 8/14/15	Collaborative Research: Quantifying Physical Parameters Controlling Non-local Transport: An Integration of Isotopic	NSF EAR, Hydrologic Sciences	\$309,575	0.5

			Tracers, Geophysical Data, and Numerical Modeling			
Investigators	<i>Role</i>	Dates	Title	<i>Source</i>	Amount	Person Months
Singha	<i>PI</i>	5/1/12 – 4/30/13	SEG-AGU Hydrogeophysics Workshop	<i>NSF</i>	\$16,500	0
Brantley, Davis, Duffy, Eissenstat, Kaye, Kirby, Lin, Singha	<i>Co-I</i>	11/1/12 – 10/31/13	An Accomplishment-Based Request for Renewal of the Susquehanna-Shale Hills Critical Zone Observatory (SSHOC) (this proposal)	<i>NSF</i>	\$1M	0.5



## Facilities

*The Observation Network at Shale Hills.* Shale Hills has a comprehensive instrument base for physical, chemical and biological characterization of water, energy, stable isotopes and geochemical conditions (see Figure 2). This includes a dense network of soil moisture observations at multiple depths (120), a shallow observation well network (25 wells), soil lysimeters at multiple depths (80+), a research weather station including eddy flux measurements for latent and sensible heat flux/ $\text{CO}_2$ /water vapor, radiation, barometric pressure, temperature, relative humidity, wind speed/direction, snow depth sensors, leaf wetness sensors, and a load cell precipitation gauge. A laser precipitation monitor (LPM: rain, sleet, hail, snow, etc.) was installed in 2008, as were automated water samplers (daily) for precipitation, groundwater, and stream water for chemistry and stable isotopes.

For approximately 3 years, porous cup tension lysimeters were sampled weekly during the non-winter months and samples are available. Arrays of sapflow measurements have been carried out each year as a function of tree species (25 species in the watershed). Geochemical measurements for solution chemistry, and water isotopes were carried out approximately every other week for more than two years on the soil lysimeter profiles, and continue currently for stream, groundwater and precipitation. Real time observations for soil moisture, groundwater level, streamflow, and weather are collected at 10 minute intervals. Partial pressure of oxygen has been measured *in situ* every ten minutes in the soil atmosphere at several depths at two locations near the valley floor for more than a year. Recently a multi-hop wireless sensor network has been deployed for groundwater level, ground temperature, and electrical conductance at 25 observation well locations.

In addition, Andrew Richardson ([Harvard Univ.](#)) has recently provided a high resolution video camera (StarDot NetCam SC Megapixel Hybrid IP Camera) that we have mounted at the eddy flux tower at the Shale Hills CZO. This camera monitors changes in phenology (leaf emergence and fall leaf senescence are basic examples) and snow cover with greater temporal resolution than is logistically feasible for individual observers. This camera also helps support a PSU student-initiated project to monitor phenology in central PA (*PennPhen*, [www.sites.google.com/site/psuphenology](http://www.sites.google.com/site/psuphenology)), contributes data to a larger network of camera based phenology observations (<http://phenocam.sr.unh.edu/>), and provides data that supports ongoing projects at the CZO.

PSU Geosciences grad students Beth Herndon and Ashlee Dere work with Princeton geochemist Anne Krapiel (Table 4) to sample and analyze the chemistry of vegetation samples that are being archived for later sharing. Krapiel's work, funded by NSF, targets analysis of Mo and V usage in enzymes in the watershed.

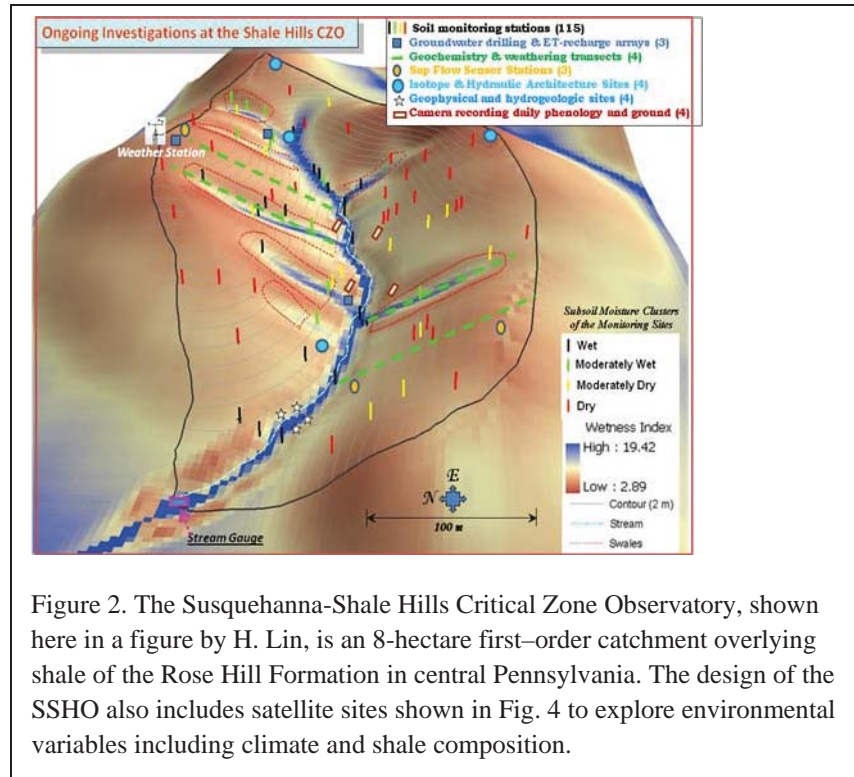
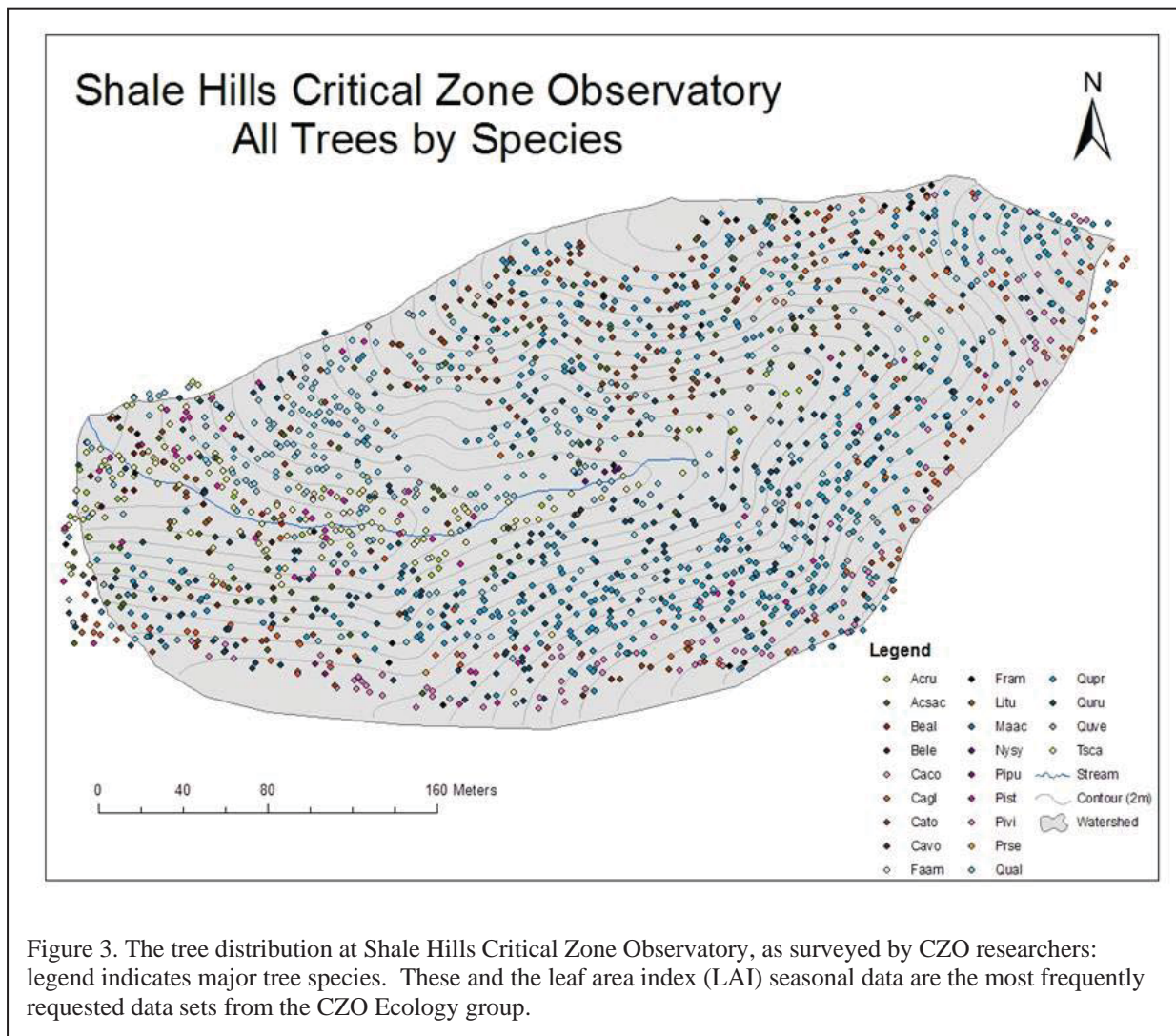


Table 4. Partial list of collaborators working at SSHO who are not listed as coInvestigators but who provide additional data or samples

Name	Institution	Focus of Project	Status of Project
Mezimir Wagaw	Alabama A&M	Soil on shale in AL	Satellite team
Rob Jacob	Bucknell Univ	gravity measurements	Unfunded, ongoing
Brian Reynolds	CEH, Wales	Soil on shale in Wales	Satellite team
Rich April	Colgate Univ	Soil development on shale till	Satellite team
Jed Sparks	Cornell Univ	Sr and Si cycling	NSF prop. Submitted
Lou Derry	Cornell Univ	Sr and Si cycling	NSF prop. Submitted
Andrew Richardson	Harvard Univ	PhenoCam	Unfunded, ongoing
Ryan Mathur	Juniata College	Soil on Marcellus shale	Satellite team
Taylor Perron	MIT	Fractures, fluid flow, topography	Unfunded, ongoing
Anne Krapiel	Princeton Univ	Mo cycling	NSF funded, ongoing
Karen Salvage	SUNY Binghamton	Hydrogeological modelling	NSF funded, 1st round
Laura Toran	Temple Univ	Hydrogeophysics	NSF funded, 1st round
Fangzhen Teng	Univ of Arkansas	Mg isotopes at Shale Hills	Unfunded, ongoing
Diana Karwan	Univ of DE	sediment transport, Cs, Pb isotopes	NSF funded, ongoing
Tom Johnson	Univ of Puerto R.	Soil development on shale	Satellite team
Chris Fedo	Univ of Tennessee	Soil on shale in TN	Satellite team
Paul Biermann	Univ of VT	Cosmogenic isotopes	Ongoing
Lin Ma	Univ TX, El Paso	REE in shale transect sites	USGS funded, ongoing
Lixin Jin	Univ TX, El Paso	C isotopes at Shale Hills	UTEP funded, ongoing
David Woodruff	USDA Forest Service	Sap flux and tree water relations	PSU & Forest Service
Frederick Meinzer	USDA Forest Service	Sap flux and tree water relations	PSU & Forest Service
Elisabeth Knapp	Wash and Lee	Soil on shale in VA	Satellite team
Beth Boyer	Penn State	DOC, precipitation monitoring	Unfunded, ongoing
Mary Ann Bruns	Penn State	Soil microbiology	Unfunded, ongoing
Rudy Slingerland	Penn State	Sediment transport, tree throw	NSF funded, 1st round
Maureen Feinmann	Penn State	Li isotopes at SSHO	Unfunded, ongoing
Matt Fantle	Penn State	Ca isotopes at SSHO	Unfunded, ongoing
Margot Kaye	Penn State	Assessment of litterfall	PSU funded, ongoing
David Pollard	Penn State	Climate modelling for transect	Unfunded, ongoing
Tim White	Penn State	Transect	NSF funded, 1st round

*Available datasets.* A large number of datasets have been collected that are either on line or will soon be on line for the CZO. The Shale Hills watershed and the larger Shaver Creek watershed has hosted 3 airborne LIDAR flights with the most recent flights at 0.5 m resolution to evaluate micro-topography and tree species identification. Bedrock elevation surveys have been carried out with ground-penetrating radar and verified with rotary air-drilling and hand augering. Ground-based LiDAR and total-station surveys have been carried out for all instrument elevations. A tree survey of all trees >20cm diameter at breast height (dbh) is available including GIS coordinates, species and crown height. The survey is illustrated in Figure 3. Leaf Area Index (LAI), greenness index, distribution and CO<sub>2</sub> flux are regularly measured. An analysis of microbial cell density, including analysis for Fe-related bacteria, has been

completed on a hillslope transect on the south side and a description has been submitted for publication [25].



A complete suite of borehole logging was done at 4 locations to 17m [7] and complete chemical and mineralogical data is available for the same sites [28]. Logs and geochemical characterization are also available for one deep borehole (25 m) on the north side of the catchment [19, 23, 27]. Some of the boreholes have logs available for (1) spectral gamma – a measure of the U, K, and Th decay within the subsurface materials; (2) caliper -- borehole-diameter log to locate broken and fractured zones; (3) fluid resistivity -- total dissolved solids in the water column; (4) fluid temperature; (5) heat-pulse flowmeter--rate and direction of vertical flow in a borehole; and (6) optical tele-viewer for a continuous, oriented, true-color 360° image of the borehole wall. Additionally hydraulic and tracer tests were done to estimate the effective hydraulic properties in all wells in the field. Other datasets are summarized online or in the *Data Management* section.

*Available samples.* The following samples from the CZO have also been collected and archived: soils, fractured rock, bedrock, leaf litter, green leaf samples, woody materials, soil porewaters, streamwaters and tree increment cores. These samples are being archived after analysis and labeled using notation developed as part of the geochemical sample data effort described in the *Data Management*

section. Samples have already been shared with several researchers outside of PSU (e.g. Ma, L.; Jin, L.; Krapiel, A; Derry, L.; see Table 4).

Regolith samples are also available for the satellite sites, as described in the next section, either through the satellite team institutions (Table 4) or in the PSU archive.

*Satellite sites.* We have established a set of satellite sites on Marcellus shale (PA), Rose Hill shale (in NY, VA, TN, AL), or its compositional or stratigraphic equivalent (Puerto Rico; Plynlimon, Wales). These sites are being monitored using a mini-meteorological station that PSU designed and built for each site. Meteorological stations have not been implemented for the Marcellus because it lies in the same climate zone as SSHO nor for Plynlimon, because it is the site of a very large and well studied hydrologic investigation by the Center for Ecology and Hydrology, Wales. Colleagues from local institutions (Table 4) utilize these sites, and the sites will comprise part of the foci of the PhD theses of PSU grad students A. Dere and N. West. Samples are available for the sites from regolith to bedrock.

*Other Facilities at Penn State. Materials Characterization Laboratory (MCL).* At Penn State, the MCL provides analytical services, specialized instruments, personnel and expertise in materials and minerals characterization in support of research and training. Researchers, including students, who are competent in the use of a particular instrument or technique, can use the facilities to obtain their own data. Other persons may complete work by hiring or collaborating with fulltime MCL personnel.

Equipment available include (underlined equipment will be used for the proposed work): AFM (Digital Instruments Digital Instruments AFM/LFM Scanning Probe Microscope and Digital Instrument Nanoscope IIIa Dimension 3100 microscope), EM (Cameca SX-50 electron microprobe), ICP-AES (Perkin-Elmer Optima 5300) inductively coupled plasma emission spectrophotometer, two ICP-MS (Thermo X-Series II quadrupole ICP-MS), IR (several models of infrared spectrometers are available for both solution and solid state analysis), SEM (ISI SX 40 secondary electron microscope, ISI SX 40A with energy dispersive xray analysis capability, JEOL JSM-6300F with EDS detector and analysis, SIMS (Cameca IMS-3F secondary ion mass spectrometer/ion microscope), DTA and TGA (DuPont 2100 and Netzsch STA 429 thermal analyzers for thermogravimetric analysis and differential thermal analysis), TEM (Hitachi HF 2000 and Philips EM420ST transmission electron microscopes), XPS/AES (Kratos Analytical XSAM800 pci for xray photoelectron spectroscopy and Auger electron spectroscopy, XRD (Scintag PAD V diffractometer).

MCL charges user fees to run all instruments according to approved federal guidelines and Penn State's approved federal auditing entities. MCL fees are posted online. Each instrument is maintained by MCL technical staff and supervised by a tenure line faculty. Brantley supervises the ICP-AES and ICP-MS facility. Recently, several of the MCL instruments have become a part of the new Laboratory for Isotope and Metals in the Environment (LIME) which is run identically as a multi-user facility.

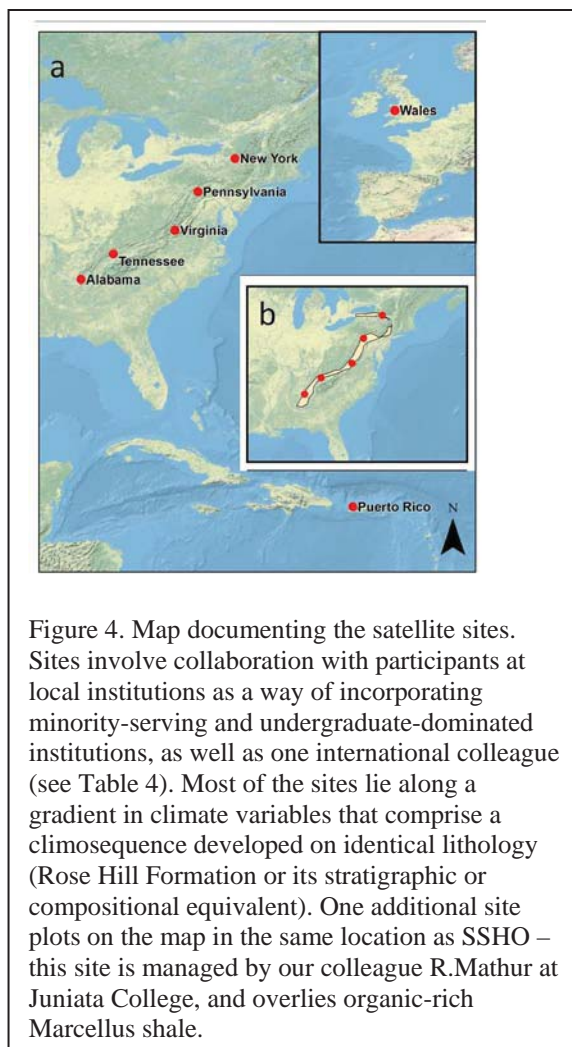


Figure 4. Map documenting the satellite sites. Sites involve collaboration with participants at local institutions as a way of incorporating minority-serving and undergraduate-dominated institutions, as well as one international colleague (see Table 4). Most of the sites lie along a gradient in climate variables that comprise a climosequence developed on identical lithology (Rose Hill Formation or its stratigraphic or compositional equivalent). One additional site plots on the map in the same location as SSHO – this site is managed by our colleague R.Mathur at Juniata College, and overlies organic-rich Marcellus shale.

*Department of Crop and Soil Sciences.* The *Soil Research Cluster Laboratory (SRCL)* in the Department of Crop and Soil Sciences (CSS) at The Pennsylvania State University is a multi-function, multi-user analytical laboratory that provides common and cutting edge analytical instrumentation in the areas of soil chemistry and biochemistry, soil fertility and nutrient cycling, soil physics, pedology, and hydrology. The SRCL was established to provide students, faculty and staff access to instrumentation and equipment that may not be available in individual laboratories and that find common use by several research groups. The SRCL analytical instruments and research methods and procedures are not limited to soil; they also have been employed in the analysis of plant and animal extracts and digests; water and waste water; biosolids; and geologic and synthetic materials. Equipment to be used in research outlined in this proposal includes a CE Instruments (Thermo Electron Corp) CHNS-O Elemental Analyzer EA 1110 with a thermal conductivity detector (TCD), and a LI-COR CO<sub>2</sub>/ H<sub>2</sub>O Analyzer (LI-7000).

*Computation and modeling, Institute for CyberScience at Penn State.* Senior Personnel Padma Raghavan (Director) directs the Institute which includes a peak Terascale networked computing & storage system with high resolution digital display wall for visualization and a high bandwidth parallel storage system. This facility was funded partially through an NSF MRI: Acquisition of a Scalable Instrument for Discovery through Computing (for additional information: <http://www.research.psu.edu/ics/index.html>.) Penn State has computing facilities all over campus available to students, faculty and visitors, including wireless access throughout much of the University. There is wide access to workstations, plotters, printers, digitizing tablets, and other hardware for spatial & temporal data analysis across the campus. The University holds site licenses to major GIS and image processing software such as Arc/Info and ERDAS, and to most major mathematical and statistical software such as MATLAB, S+, and SAS. We have developed the Penn State Integrated Hydrologic Model (<http://www.pihm.psu.edu/>). The Penn State Integrated Hydrologic Model (PIHM) is a multiprocess, multi-scale hydrologic model where the major hydrological processes are fully coupled using the semi-discrete finite volume method. The model itself is "tightly-coupled" with PIHMgis, an open-source Geographical Information System designed for PIHM. The PIHMgis provides the interface to PIHM, access to the digital data sets (terrain, forcing and parameters) and tools necessary to drive the model, as well as a collection of GIS-based pre- and post-processing tools. Collectively the system is referred to as the Penn State Integrated Hydrologic Modeling System. The modeling system has been written in C/C++, while the GIS interface is supported by Qt. The Penn State Hydrologic Modeling System is open source software, freely available for download at this site along with installation and user guides.

*Education.* Shaver's Creek Environmental Center is a Penn State-run facility (<http://www.outreach.psu.edu/shaverscreek/>) to teach about environmental science. The Center lies within 1 mile of the SSHO and is the host for many camps, scouting projects, summer visitors, and students. Shaver's Creek provides facilities that can facilitate in K-12 education efforts at SSHO. In addition, the SSHO benefits from interactions with the Center for Science and the Schools (CSATS), a unique Penn State facility whose purpose is to develop mutually beneficial and sustainable relationships between P-12 schools, faculty and researchers in Penn State's STEM colleges and College of Education. CSATS conducts external evaluations for projects unrelated to CSATS activities and works closely with Penn State Outreach, Penn State Public Broadcasting and other university entities across the state (<http://csats.psu.edu/>).

## Data Management in SSHO

The SSHO team has participated fully in all cross-CZO data management activities. Early on, the SSHO team articulated that the diversity of CZO data would require i) online publication of flat files of data; ii) development of specific databases for each sub-discipline within CZ science, and iii) eventual organization of data into databases specific to each sub-discipline. This is the current plan that is being pursued by the CZO national program. Some sub-disciplines are ahead in this three-prong approach (e.g. hydrological data which is being organized into the HIS in collaboration with CUAHSI efforts). SSHO is pursuing all of these activities for different datasets and we have lead the geochemical data efforts. These efforts are described more fully below.

During year one, the project website was developed off line to facilitate a common framework in style and structure across the original 3 CZO's. A common Data Agreement and a Metadata worksheet was developed to educate about data quality and accessibility. Publication of hydrological and meteorological time-series datasets to the CZO website has been facilitated since the installment of the wireless communications network. All SSHO data is accessed at <http://www.czo.psu.edu/data.html>. Hydrologic time series data is accessible in raw format (Level 0) or as processed data delivered at time steps of 10 minutes. In addition to the Level 0 data, we have Level 1 (Quality Controlled Data) and Level 4 (Knowledge Products) data available for public consumption. Metadata is published online (above) for all CZO data. These are further discussed below.

*Level 0.* The following data is available online. During the 2009 and 2011 growing seasons, sap flux was measured at 10 minute intervals from 26 individual trees representing 6 species and 24 individual trees representing 8 species. Over the same period, the flux tower collected temperature, wind direction, horizontal and vertical wind speed, CO<sub>2</sub> flux, sensible and latent heat flux, CO<sub>2</sub> concentration and water vapor concentration at 30 minute time steps. The laser precipitation monitor delivers raw unchecked data for precipitation at 10 minute intervals. RTH-NET provides a complete suite of real-time measurements for soil moisture, matric potential, stream stage, precipitation, groundwater levels at 10 minute intervals.

*Level 1.* Throughout the catchment, 14 data loggers are measuring eleven hydrologic properties at 10 minute intervals. This data is not real-time but is uploaded with a monthly update frequency. Other Level 1 data include: 10 flux tower parameters for 2009 and 2010; stream discharge for 2006 – 2010; soil moisture from 18 sensors (6 each at 0.10m, 0.20m, and 0.30m) for 2009 – 2010; groundwater depth from 3 wells for 2009 – 2010; and total precipitation from 2006 – 2010 at hourly intervals. More than 6000 stable isotope measurements for  $\delta^{18}O$  and  $\delta^2H$  precipitation, soil moisture, groundwater and streamflow are posted.

*Level 4.* Reanalysis data has been prepared using PIHM -- the Penn State Integrated Hydrologic Model. Three versions of the reanalysis data products are provided based on different model-data coupling strategies. Datasets describing landscape characteristics or physical and chemical properties of the catchment or the greater watershed have also been published under the categories, "Geospatial Data" and "Geochemical and Geophysical Data." The LiDAR dataset has been processed and is available through a viewer at: [http://pihm.ics.psu.edu/CZO\\_NOSL/Lidar.aspx](http://pihm.ics.psu.edu/CZO_NOSL/Lidar.aspx). The dataset includes a full Leaf Area Index Leaf-on flight in July and full Leaf-off flight in December. Terrestrial LiDAR captured in the catchment is available for download as a point-cloud. A ground survey was completed in summer 2011 to identify 3 permanent benchmarks at the site. Additional national geospatial data is available on the website for Shale Hills and for Shaver Creek: digital elevation model (DEM), geology, land cover, soils, watershed boundary (<http://www.czo.psu.edu/data.html>).

As stipulated by NSF, aging data -- those data which have matured past the embargo timeline -- are directly accessible in downloadable formats common to the particular discipline. Currently, 2010 hydrological time-series data are being processed for release. The geochemical data for regolith chemistry is available within a Microsoft Access database that has been largely developed by PI Brantley in collaboration with PSU's X. Niu, a database expert, and Kerstin Lehnert (Lamont Doherty Earth Observatory). Lehnert is largely in charge of EarthChem, an NSF-funded facility to house geochemical

data of all types. The data team is working to migrate the geochemical data from the Access database to EarthChem. Online at the SSHO website, the Access database provides a “How to Use” form. The database contains more than 25,000 data values which originate from the SSHO as well as from 46 field sites (255 regolith cores collected from the continental U.S.A., Puerto Rico and the United Kingdom). Relevant metadata describing the field locations, sample collection methods, sample preparation, treatment and analytical methods are included in addition to contact information and journal citations. The database is starting to house geochemical data from more than one CZO (currently SSHO, AZ, and Puerto Rico) but has also been under modification off and on during the last year in preparation for translocation to EarthChem. A manuscript written by the geochemical data team is in preparation for publication to describe the CZO data efforts with respect to sample-based data (Fig. 5).

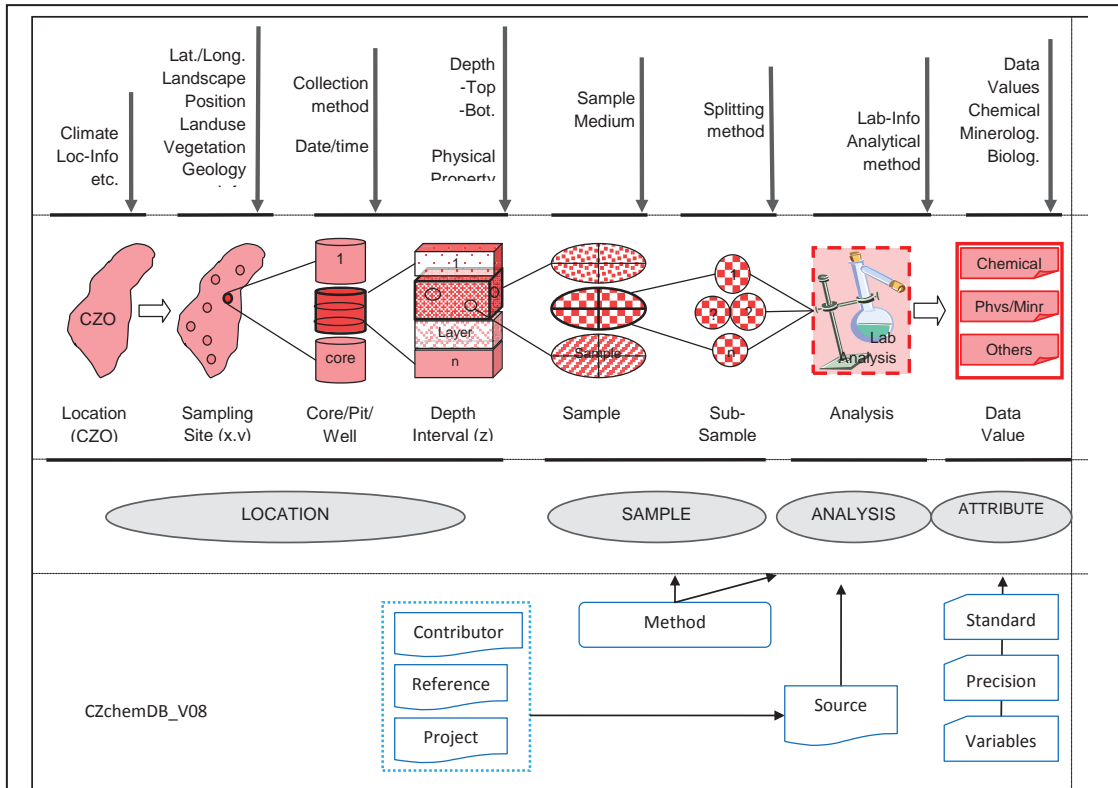


Figure 5. Schema developed for sample-based geochemical data for the CZOs. This schema is in use in the ACCESS database at the SSHO CZO website. The schema was developed by the SSHO team in collaboration with members from other CZOs. Brantley is currently working with the Director of CUAHSI, R. Hooper, to coordinate this sample-based schema with the more sensor-based schema developed for CUAHSI HIS. Figure from Niu, X., Williams J., Lehnert, K., Brantley, S.L. (manuscript in preparation for submission for publication).

## **Postdoctoral scholars and post-PhD professional development**

*Professional development of postdocs:* We will provide support for 1 year each for four postdoctoral researchers who will be fully integrated into our CZO team. CZO faculty will promote professional development activities for the postdocs (as well as all grad students). These activities will include campus-specific and cross-CZO programs and opportunities and will follow all recommendations for best practices in research and education. For example, the Penn State Graduate School organizes workshops on preparing grants and research and teaching statements for upper level graduate students or postdoctoral scholars. PSU also hosts the Penn State Postdoctoral Society which promotes a postdoctoral research exhibition on campus. All faculty will encourage the postdocs to take part in these activities. Furthermore, the Earth and Environmental Systems Institute (EESI) at Penn State (of which Brantley is director) provides a video conferencing center that can be used to promote virtual meetings among all the participants of the different CZOs. Video conferencing centers are also available in each college on campus. We will use these facilities to promote interactions among all the CZO postdocs at all sites.

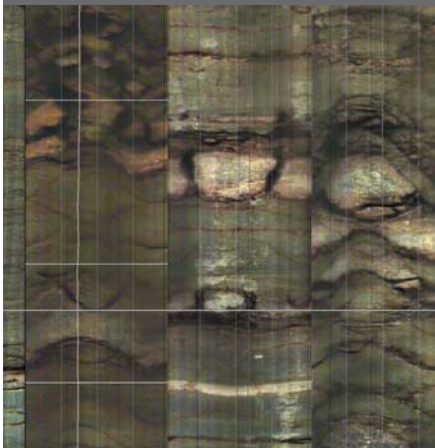
All postdocs will be encouraged to enroll in the National Postdoctoral Association, which provides resources for professional development, personal and financial coaching, job and funding announcements. We anticipate that at least one of the postdocs will organize sessions at professional meetings such as the American Geophysical Union, the Goldschmidt Conference, or the European Geophysical Union. Postdoc conference participation will be supported from grant travel funds.

*Academic career development:* CZO faculty members will mentor postdocs who seek an academic career by providing opportunities to guest lecture in courses, if desired, while receiving constructive feedback. Guidance in the preparation of curriculum materials and in the teaching process itself will be provided. At PSU, a semester-long course is available for PhD students within the Dept of Geosciences on preparing for the academic job market. Materials from this course can be shared with all postdocs. Postdoctoral scholars will be encouraged to learn about alternate career paths by meeting informally with visiting researchers from industry, government labs and stakeholder institutions as appropriate. Furthermore, postdoctoral scholars will be encouraged to engage in outreach activities as appropriate. For example, the postdocs will be encouraged to learn about shale gas in the PA region where Marcellus shale is under rapid and dense exploitation. This activity will be mentored by Brantley who is developing an NSF-funded water quality database for the Marcellus development area.

*Advising and mentoring:* Research mentoring will be accomplished by pairing each postdoc with several faculty mentors as indicated in the text of the proposal. As PI, Brantley will ultimately be the budgetary supervisor for each postdoc and she will make sure that the scholars are not spread too thin but are getting their work done appropriately. Brantley has significant experience in this type of mentoring because she has previously been PI of a very successful NSF-funded IGERT training grant, the Biogeochemical Research Initiative for Education (BRIE) and an Environmental Molecular Sciences Institute (the Penn State Center for Environmental Kinetics Analysis, CEKA). Both BRIE and CEKA provided NSF funds for postdocs who were mentored by more than one PSU faculty member. These postdocs are now pursuing successful careers as faculty members (e.g., Northwestern Univ., Univ. of FLA, Univ. TX El Paso), workers at government agencies (e.g., Bureau of Land Management, U.S. Geological Survey), or in industry (e.g., 3M).

*Timing:* We anticipate hiring the postdocs as soon as possible.

Brad W. Kuntz\*  
Shira Rubin  
Brian Berkowitz  
Kamini Singha



We quantify solute transport in geologic media with the mobile-immobile and continuous-time random walk models. Breakthrough curves from soil cores and a field-scale tracer experiment reveal anomalous early breakthrough and long tailing. Transport is controlled by preferential flow pathways, the abundance of rock fragments, and soil weathering.

B.W. Kuntz and K. Singha, Dep. of Geosciences, Pennsylvania State Univ., University Park, PA 16802; and S. Rubin and B. Berkowitz, Dep. of Environmental Sciences and Energy Research, Weizmann Institute of Science, Rehovot 76100, Israel. \*Corresponding author (bkuntz@psu.edu).

Vadose Zone J. 10:843–857  
doi:10.2136/vzj2010.0130  
Received 29 Oct. 2010.  
Posted online 29 July 2011.

© Soil Science Society of America  
5585 Guilford Rd., Madison, WI 53711 USA.  
All rights reserved. No part of this periodical may be reproduced or transmitted in any form or by any means, electronic or mechanical, including photocopying, recording, or any information storage and retrieval system, without permission in writing from the publisher.

## Quantifying Solute Transport at the Shale Hills Critical Zone Observatory

We collected and analyzed Br<sup>-</sup> breakthrough curve (BTC) data to identify the parameters controlling transport from a series of soil cores and a field-scale tracer test at the Shale Hills Critical Zone Observatory (SH-CZO) in central Pennsylvania. The soil cores were retrieved from a continuous hole that extended through the soil profile to quantify also how solute transport behavior changes with depth and weathering. Additionally, we performed a field-scale doublet tracer test to determine transport behavior in the weathered shale bedrock. Hydraulic conductivity and porosity were as low as 10<sup>-15</sup> m s<sup>-1</sup> and 0.035, respectively, in the shale bedrock and upward of 10<sup>-5</sup> m s<sup>-1</sup> and 0.45, respectively, in the shallow soils. Bromide BTCs demonstrated significant tailing in soil cores and field tracer experiments, which does not fit classical advection–dispersion processes. To quantify the behavior, numerical simulation of solute transport was performed with both a mobile–immobile (MIM) model and a continuous-time random walk (CTRW) approach. One-dimensional MIM modeling results yielded low mass transfer rates (<1 d<sup>-1</sup>) coupled with large immobile domains (immobile/mobile porosity ratio of 1.5–2). The MIM modeling results also suggested that immobile porosity was a combination of soil texture, fractures, and porosity development on shale fragments. One-dimensional CTRW results yielded a parameter set indicative of a transport regime that is consistently non-Fickian within the soil profile and bedrock. These modeling results confirm the important role of preferential flow paths, fractures, and mass transfer between more- and less-mobile fluid domains and advance the need to incorporate a continuum of mass transfer rates to more accurately quantify transport behavior within the SH-CZO.

Abbreviations: ADE, advection–dispersion equation; BTC, breakthrough curve; CTRW, continuous-time random walk; MIM, mobile–immobile; pdf, probability density function; PSD, particle size distribution; SH-CZO, Shale Hills Critical Zone Observatory; TPL, truncated power law.

**The SH-CZO** has been developed as a natural laboratory to predict the creation and function of regolith within a multidisciplinary context. The flow of water and transport of solutes within this catchment are key to dating groundwater, estimating soil weathering rates, predicting nutrient availability, classifying primary and secondary fluid pathways, and identifying controls on the residence time of solutes in the subsurface (Amundson et al., 2007; Brantley et al., 2007; Anderson et al., 2008; Dere et al., 2010). Identifying groundwater age is a useful means to investigate watershed-scale processes including discharge and recharge areas, preferential flow paths, and drought vulnerability or resource protection (Kazemi et al., 2006). Calculating groundwater ages has traditionally been accomplished by advection-only models (e.g., Reilly et al., 1994), although the importance of dispersion and diffusion processes is well recognized (e.g., Goode, 1996; Varni and Carrera, 1998; Bethke and Johnson, 2008). Recent models, such as those described in Duffy (2010), incorporate the diffusion of solutes between dead-end pore space and the advective fluid domain; however, data are required to (i) constrain the residence times of fluids within these more- and less-mobile domains, and (ii) evaluate the distribution of the pore space within the subsurface. This study provides data for these two requirements and explores the assumptions within conceptual transport models at the SH-CZO.

Classically, transport is described by the advection–dispersion equation (ADE). With the ADE, the shape of the breakthrough history is fitted by estimating the dispersivity (e.g., Koch and Flühler, 1993; Perfect et al., 2002; Javaux and Vanclooster, 2003; Vanderborght and Vereecken, 2007); however, the assumption of Fickian transport intrinsic in the ADE prevents its ability to effectively predict and characterize solute transport behavior in heterogeneous environments (e.g., Adams and Gelhar, 1992; Silliman and Simpson, 1987; Huang et al., 1995; Javaux and Vanclooster, 2004; Gorelick et al., 2005).

Of particular interest in this work was an evaluation of the physical processes trapping solutes in immobile pore space, the matrix, or less-mobile pathways. The SH-CZO's regolith and bedrock are dominated largely by silty-loam soils and fractured shale bedrock that are likely to contain significant immobile pore space (Lin, 2006). The presence of immobile pore space has been documented in many geologic materials and scales ranging from well-sorted sandstone (e.g., Coats and Smith, 1964) to saprolitic soils (e.g., Gwo et al., 2007) and fractured bedrock (e.g., Jardine et al., 1999). Fundamental to quantifying transport within these materials is a sufficient accounting of scale-dependent processes including dispersion, diffusion, and mass transfer. Incorporating the transfer of mass between less-mobile pore space and the mobile pore space has facilitated improved fitting of BTCs in many settings where long concentration tailing behavior is seen (e.g., van Genuchten and Wierenga, 1976; Cameron and Klute, 1977; Seyfried and Rao, 1987; Haggerty and Gorelick, 1994; Maraqa et al., 1997; Jardine et al., 1999; Gao et al., 2009). We followed the approach of Gao et al. (2009) to compare alternative conceptual and numerical models to constrain, predict, and interpret solute transport behavior. We inspected a well-characterized catchment by performing tracer experiments in the laboratory and field to interpret solute transport behavior given two different conceptual transport models of varying complexity.

## Conceptual Models of Solute Transport

Recognition that heterogeneous environments contain fast and slow paths (fracture and matrix, mobile and immobile zones, or preferential pathways and dead-end pore space) advocated the development of alternative transport models to the ADE. One simple model is the MIM model (van Genuchten and Wierenga, 1976), shown here in one dimension:

$$\theta_m \frac{\partial c_m}{\partial t} + \theta_{im} \frac{\partial c_{im}}{\partial t} = \theta_m D \frac{\partial^2 c_m}{\partial x^2} - v_m \theta_m \frac{\partial c_m}{\partial x} \quad [1]$$

where  $\theta$  is the porosity ( $\text{cm}^3 \text{cm}^{-3}$ ),  $c$  is the concentration of the solute [ $\text{M L}^{-3}$ ],  $v_m$  is the average fluid flow velocity [ $\text{L T}^{-1}$ ],  $D$  is the hydrodynamic dispersion coefficient [ $\text{L}^2 \text{T}^{-1}$ ],  $t$  is time [ $\text{T}$ ],  $x$  is distance [ $\text{L}$ ], and the subscripts  $m$  and  $im$  denote the mobile and immobile domains, respectively. The relative concentration difference between the domains drives the transfer of mass

$$\theta_{im} \frac{\partial c_{im}}{\partial t} = \alpha (c_m - c_{im}) \quad [2]$$

where  $\alpha$  controls the rate of exchange between the domains [ $\text{T}^{-1}$ ]. The mass transfer rate  $\alpha$  has been derived using Fick's first law and is used to represent diffusion across a length scale (e.g., Goltz and Roberts, 1986; Parker and Valocchi, 1986; Brusseau et al., 1991, 1994):

$$\alpha = \frac{D^*}{l^2} \quad [3]$$

where  $D^*$  is the effective diffusion coefficient [ $\text{L}^2 \text{T}^{-1}$ ] and  $l$  is representative of either sphere diameter or a length scale of mixing between the two domains (e.g., Haggerty and Gorelick, 1995; Griffioen et al., 1998).

The MIM model has been applied successfully to solute transport problems using both conservative tracers and reactive tracers in a variety of hydrogeologic settings by dividing the flow field into advective-flow and no-flow regions (e.g., van Genuchten and Wierenga, 1976; Cameron and Klute, 1977; Haggerty and Gorelick, 1994; Jardine et al., 1999; Gwo et al., 2007). One of the benefits of the MIM model is that the fitting parameters  $\theta_m$ ,  $\theta_{im}$ , and  $\alpha$  may be related to and therefore constrained by porosity, particle size, diffusion coefficients, or geophysical measurements (e.g., Brusseau et al., 1994; Vanderborght et al., 1997; Casey et al., 1999; Al-Jabri et al., 2002; Lee et al., 2000; Singha et al., 2007; Luo et al., 2008; Gong et al., 2010). The assumed velocity partitioning in the MIM model into flowing and not-flowing zones is not an accurate representation of the true velocity field, however, and a single mass transfer rate fails to match BTCs with particularly long tails (e.g., Haggerty and Gorelick, 1995; Gao et al., 2009). The MIM model is a highly restricted case of the CTRW formalism described below.

The CTRW is an approach based on the conceptual picture of tracer particles undergoing a series of transitions, characterized by a distribution of transition times. The physics and geochemical mechanisms involved in the transport process, as well as the structure of the heterogeneous porous medium or nature of the flow regime, determine the relevant transition time distribution and control the interpretation of its parameters. In the CTRW framework, a solute particle undergoes a series of transitions of length  $\mathbf{s}$  and time  $t$ . Together with a master equation conserving solute mass, the random walk is developed into a transport equation in partial differential form. For a concise derivation starting from a simple random walk and leading to the transport equation, and an extensive review of the CTRW, see Berkowitz et al. (2006). The transport equation in Laplace space  $\mathcal{L}$  (denoted by a tilde  $\sim$  and Laplace variable  $u$ ) is

$$u\tilde{c}(\mathbf{s}, u) - c_o(\mathbf{s}) = -\tilde{M}(u) [v_\psi \cdot \nabla \tilde{c}(\mathbf{s}, u) - \mathbf{D}_\psi : \nabla \nabla \tilde{c}(\mathbf{s}, u)] \quad [4]$$

where

$$v_\psi = \frac{1}{t_1} \int p(\mathbf{s}) \mathbf{s} d\mathbf{s}$$

is an average tracer transport velocity [i.e., based on the first moment of the probability density function (pdf) of the transition lengths,  $p(\mathbf{s})$ , divided by a characteristic time],

$$\mathbf{D}_\psi = \frac{1}{t_1} \int \frac{1}{2} p(\mathbf{s}) \mathbf{s} \mathbf{s} d\mathbf{s}$$

is a generalized dispersion tensor, the dyadic symbol (colon) denotes a tensor product,  $c_0(\mathbf{s})$  represents the initial condition,

$$\tilde{M}(u) = t_1 u \frac{\tilde{\psi}(u)}{1 - \tilde{\psi}(u)}$$

is a “memory” function, and  $t_1$  is the characteristic transition time (Berkowitz et al., 2006, and references therein). Note that  $v_\psi$  is distinct from and therefore need not equal the average fluid flow velocity  $v_m$ ;  $v_m$  is averaged across all water particles, whereas the tracer velocity,  $v_\psi$ , is averaged across the tracer particles. We solved the one-dimensional form of Eq. [4].

The pdf  $\psi(t) = \mathcal{L}^{-1}[\tilde{\psi}(u)]$  is defined as the probability rate for a transition time  $t$  between sites. Its determination lies at the heart of the CTRW because it controls the nature of the transport. The truncated power law (TPL) form of  $\psi(t)$  has been applied successfully to a wide range of physical scenarios (Berkowitz et al., 2006); the “cut off” of the power law allows a transition from anomalous behavior to Fickian behavior at longer times. The TPL form can be written as

$$\psi(t) = \frac{n}{t_1} \frac{\exp(-t/t_2)}{[1 + (t/t_1)]^{1+\beta}}; \quad 0 < \beta < 2$$

where

$$n = \left[ \left( \frac{t_1}{t_2} \right)^\beta \exp\left(\frac{t_1}{t_2}\right) \Gamma\left(-\beta, \frac{t_1}{t_2}\right) \right]^{-1}$$

is a normalization factor,  $\beta$  is a measure of the dispersion,  $t_2$  ( $\gg t_1$ ) is a “cutoff” time, and  $\Gamma(a, x)$  is the incomplete gamma function. Note that  $\psi(t) \sim (t/t_1)^{-1-\beta}$  for  $t_1 \ll t \ll t_2$ , and decreases exponentially  $\psi(t) \sim \exp(-t/t_2)$  for  $t \gg t_2$ . Fickian transport occurs for  $\beta > 2$ , while the smaller  $\beta$  is, the more dispersive the transport. A recent study shed more light on the choice of these parameters and their interpretation in the context of flow-velocity-dependent tailing (Berkowitz and Scher, 2009). Note also that specific forms of  $\psi(t)$  can be defined for the MIM and other related models (for a detailed discussion, see Berkowitz et al., 2006).

This general concept of transport can therefore quantify a wide range of non-Fickian transport patterns. The CTRW has been applied successfully in many different settings (e.g., Berkowitz and Scher, 1998; Deng et al., 2008). Significantly, it consistently captures BTC behavior in column experiments of even well-sorted materials, where conventionally predicted classic advective–dispersive behavior does not always occur (Cortis and Berkowitz, 2004). In most cases, the transport behavior can be quantified effectively with a single

transition time distribution (Berkowitz and Scher, 2009); however, if there is clear evidence for the nature of the underlying transport mechanisms, an explicit two-scale CTRW formulation (Bijeljic et al., 2011) or a fully coupled space–time distribution may also be considered (Dentz et al., 2008).

Our understanding of the physical environment is shaped by the assumptions within our models. For example, interpretations from a MIM model assume the existence of a dual-porosity network that may or may not exist, whereas modeling the same data set with a classic ADE model may only suggest that the subsurface is highly heterogeneous. In each case, we can only infer actual behavior given concentration histories. We explored two conceptual models—CTRW and a simplified version of CTRW, the MIM model—with the goal of developing consistent interpretations of the subsurface hydrogeology.

## Field Site and Experimental Methods

### Location and Site Details

The SH-CZO is an 8-ha V-shaped catchment containing one first-order stream located in central Pennsylvania within the Valley and Ridge physiographic province of the Appalachian Mountain Front (Fig. 1). The SH-CZO is underlain almost entirely by the Silurian Rose Hill shale. The Rose Hill shale extends across much of the Appalachian Basin; locally, the Rose Hill shale is a yellow-brown, olive to blue-gray fossiliferous shale marked by well-developed fracture cleavage (Flueckinger, 1969). The resultant residual and colluvial silt loam soils are well drained and contain many shale fragments (Lin et al., 2006). Five soil series have been identified within the catchment, the Berks, Weikert, Rushtown, Blairtown, and Ernest series (Lin, 2006). Experiments were performed on

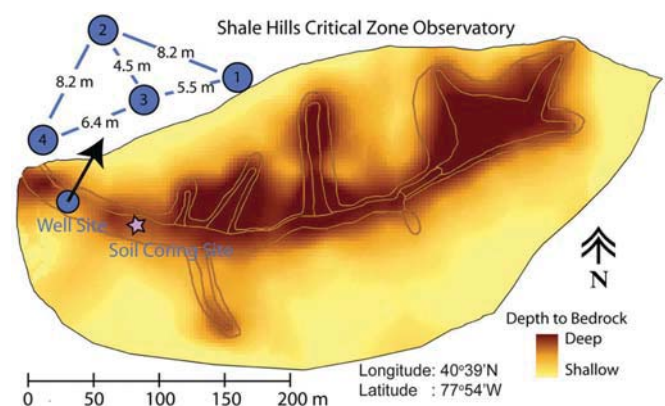


Fig. 1. The well field and soil core retrieval localities within the Shale Hills catchment (after Lin et al., 2006). Soil depth is  $>2$  m in the valley floor and  $<0.3$  m at the ridgetops. Critical Zone Monitoring Wells (CZMWs) 1, 2, and 3 are located north of the stream and CZMW 4 is located south of the stream. The field tracer test injected salt (NaBr) into CZMW 3 and extracted and sampled the tracer breakthrough at CZMW 2. Natural groundwater flow direction is approximately southwest to west.

soils retrieved from the valley bottom within the Ernest soil series, a fine-loamy, mixed, superactive, mesic Aquic Fragiudult consistent with U.S. Soil Taxonomy (Lin and Zhou, 2008). For additional details on soil distribution and descriptions, climate and hydrologic information, and geochemical composition across the catchment, see Lin (2006) and Jin et al. (2010).

We follow here the terminology introduced in Jin et al. (2011) to characterize the soil profile. The soil profile includes the regolith and saprock. Regolith is the near-surface, disaggregated, and highly altered material extending to a depth that can be reasonably sampled using a hand auger. Below this regolith lies the saprock, which is somewhat fractured and altered in place bedrock. Chemically unaltered, in place, and less-fractured shale we denote as bedrock. The soil samples for the experiments were collected in the regolith and saprock, while the field tracer experiment occurred in the transition zone between the saprock and bedrock. We found that regolith and saprock extended approximately 1 to 3 m below the land surface based on hand augering, well penetrations, and geoprobe sampling of the valley floor. Near the outlet of the catchment within the valley floor, a set of shallow boreholes ( $\sim 16$  m) was drilled and geophysical logs were collected in each (Fig. 2 and 3). Drilling and well log data revealed a Ca-rich slow drilling zone around 6 to 7 m below the land surface, above which was the transition between saprock and highly weathered bedrock with a comparatively high fracture density, and beneath which was a less-fractured and rather geochemically homogeneous blue-gray shale (Fig. 3). Additionally, a low natural  $\gamma$ -ray count in the upper  $\sim 7$  m of the boreholes indicated a removal of clay-rich materials and deletion of the parent bedrock material (Fig. 3).

Soil core samples were collected from across the  $\sim 3$ -m-deep soil profile with 7.6-cm-diameter Shelby tubes, a thin-walled aluminum tube with a cutting edge on one end. Shelby tubes were hydraulically pressed into the soil using a tracked Geoprobe (Geoprobe Model 6620DT, Geoprobe Systems, Salina, KS). Because of the many rock fragments in the soil, in addition to hydraulically pressing, deeper Shelby Tubes were lightly hammered by the Geoprobe to reach the targeted soil depths. Field-sampled core lengths varied from 0.15 to 0.75 m, reaching a total depth of approximately 2.75 m. Because of the difficulty in obtaining cores due to rock fragments, poor

cohesion, and mechanical failures, we collected one sample at each depth and note that our analyses are not representative of heterogeneity within the catchment. Within 8 h of removal, samples were capped and stored in a  $10^{\circ}\text{C}$  walk-in storage cooler. An additional set of 5.08-cm-diameter samples was collected in clear acetate liners to visually inspect the soil color, texture, and particle size and composition with depth. This visual inspection helped target four separate zones that showed marked compositional differences with increased depth. This sample set provided a starting point to quantify behavior with depth.

### Physical and Hydraulic Properties

Hydraulic conductivity was measured in the intact, fixed-volume Shelby tube samples from depths of 0 to 0.2, 0.6 to 0.8, 1.6 to 1.8, and 2.3 to 2.5 m by both constant-head and falling-head

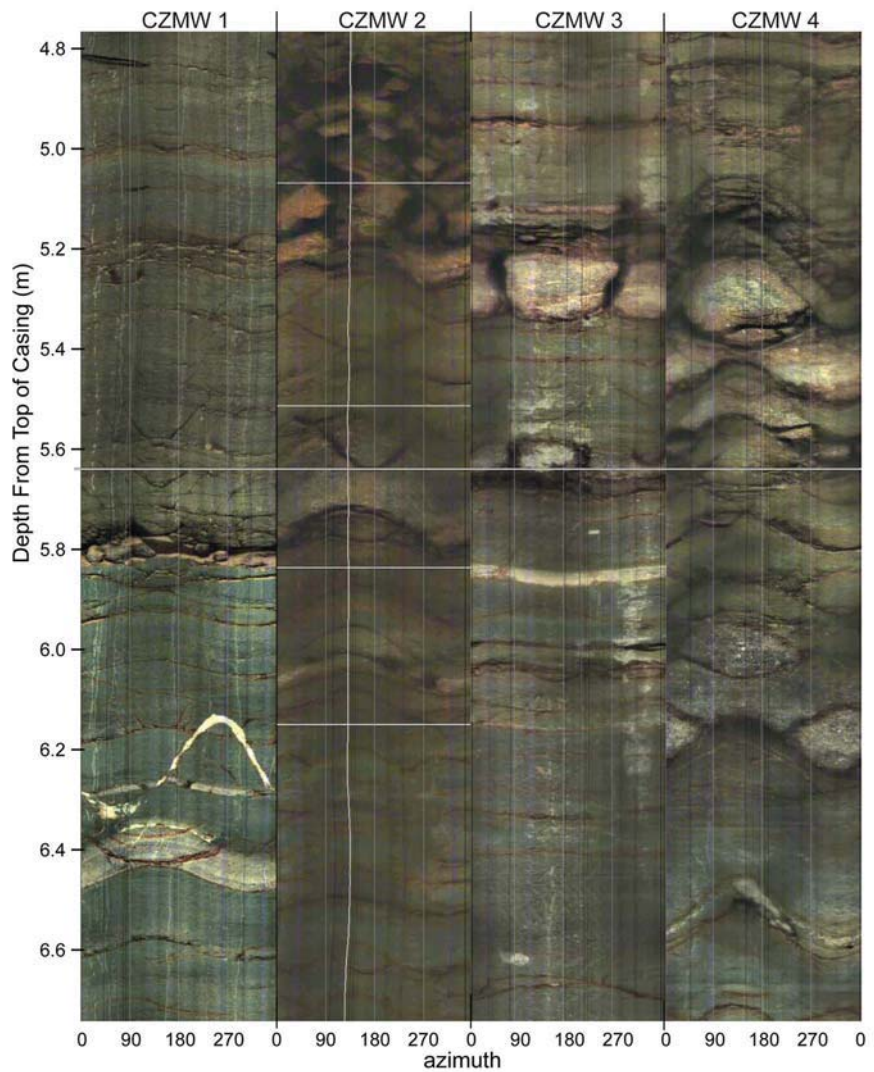


Fig. 2. Optical televiewer log of the four 16-m-deep critical zone monitoring wells (CZMWs; see Fig. 1 for location). Above approximately 6 m, the shale bedrock is olive-brown to yellow-brown, while below this depth the shale is fractured and blue-gray in color, as seen most clearly in CZMW 1. Fracturing is greatest above 6 m and decreases with depth (not seen here). The wells are cased to consolidated rock at the 2.8-m depth, so no images of the soil could be produced. These logs reveal that, on average, bedding strikes to the southwest  $\sim 230^{\circ}$  and dips to the northwest 25 to  $30^{\circ}$ .

methods (Reynolds et al., 2002). One end of the samples was prepared with porous sintered-metal frits (bubbling pressure <20 cm) to distribute pressure evenly across the base of the sample. Total porosity was measured on 4- to 7-cm-long Shelby tube samples immediately below and adjacent to the sections used for transport experiments. Samples were fully saturated with 5 mmol L<sup>-1</sup> CaCl<sub>2</sub> under vacuum, weighed, subsequently dried at 40°C to prevent mineralogic transformation, and weighed until no resolvable change in mass occurred between measurements. Note that this drying temperature could possibly result in a lower porosity value if samples are not fully dried at the standard 105°C.

To investigate the porosity and permeability of the shale bedrock matrix, we sampled the Rose Hill shale from a nearby outcrop (~15 km northeast). Porosity was estimated by Hg porosimetry (measured by Porous Materials Inc., Ithaca, NY). Permeability was measured on the consolidated Rose Hill shale via curve matching with the transient pulse-decay method (Brace et al., 1968; Hsieh et al., 1981) in a triaxial pressure apparatus. The pressure at one end of the sample was instantaneously pulsed with 300 kPa and then allowed to equilibrate across the sample. The pressure was monitored for the decay and the increase from the pulse at the upstream and downstream sides of the sample, respectively. Theoretical curves were then matched to the data until the error was minimized.

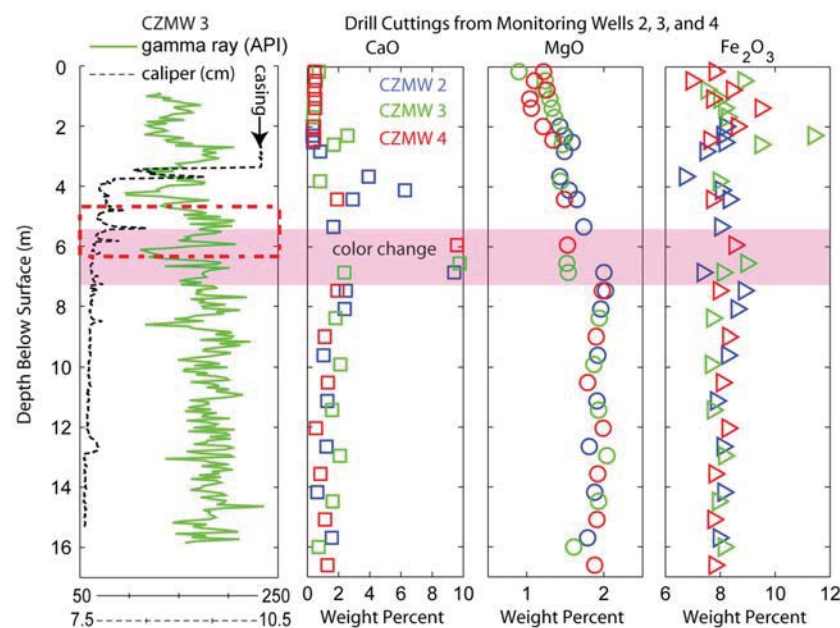


Fig. 3. Natural gamma-ray and three-arm caliper logs from Critical Zone Monitoring Well (CZMW) 3 and chemical analysis from drill cuttings from CZMWs 2, 3, and 4. Gamma curves for all four wells were collected and have a character distinctly similar to CZMW 3. A Ca-rich zone around 6 m correlates to a slow drilling zone and marks the transition between less-weathered and more-weathered shale as evidenced by (i) depletion of CaO and MgO, (ii) an increase in fracture density, and (iii) a decrease in the relative clay content as recorded by the natural gamma ray. The dashed rectangle on CZMW 3 denotes the region where the tracer was injected into the subsurface.

Particle size distribution data were analyzed on regolith and saprock from the Shelby tube samples at six depths within the soil profile. Analysis was performed by wet sieving large (>6.35 mm) and small (6.35–2.00 mm) rock fragments, sand-sized particles, and assuming that silt- and clay-sized particles comprised the remainder of the sampled material. Drill cuttings from each of the boreholes were ground and analyzed for major cation concentrations by inductively coupled plasma atomic emission spectroscopy (Penn State Materials Characterization Laboratory, University Park, PA).

## Column Tracer Experiments

Tracer experiments using SrBr<sub>2</sub> were performed on four Shelby tube core samples extracted from the soil and saprock at depths of 0 to 0.20, 0.60 to 0.80, 1.6 to 1.8, and 2.3 to 2.5 m. The Shelby tube samples were carefully cut with the aid of a low-speed band saw into 19.5 ± 0.5 cm sections from the larger field-recovered cores. Chlorinated polyvinyl chloride caps were prepared for each core by filling the convex top with an impermeable epoxy to eliminate dead volume between the sample and the cap. One brass tube fitting was fixed into the center of each cap, and the caps were secured to the sectioned Shelby tube core with adhesive; a porous sintered disk was placed at the inlet boundary between the sample and the cap to distribute the solute and pressure evenly across the sample. Fluid delivery was provided by a Masterflex L/S drive (Cole-Parmer, Vernon Hills, IL) with a six-channel pump head. To minimize solute diffusion

within the line before entering the geologic media, a three-way valve was placed at the base of the sample to switch between background influent and tracer solution.

Effluent fluid conductivity was monitored continuously by an inline conductivity meter (Model 542, Campbell Scientific, Logan, UT). The flow rate was measured regularly within a graduated cylinder as 5 mmol L<sup>-1</sup> CaCl<sub>2</sub> (fluid conductivity = 1.2 ± 0.2 mS cm<sup>-1</sup>) was pumped through the cores for several days (>30 pore volumes) until the flow rate and effluent conductivity stabilized; we chose this solution to minimize the impact of the small fraction of swelling clays (vermiculite) within the sample. The SrBr<sub>2</sub> was added to the prepared background CaCl<sub>2</sub> solution, creating a 5 mmol L<sup>-1</sup> SrBr<sub>2</sub> tracer solution (fluid conductivity = 2.3 ± 0.2 mS cm<sup>-1</sup>). Each core was saturated with three to five pore volumes of SrBr<sub>2</sub> tracer before reintroducing the background CaCl<sub>2</sub> solution. Intermittently, effluent was allowed to drip into 20-mL scintillation vials for Br<sup>-</sup> analysis. Water samples were diluted and Br<sup>-</sup> concentrations were measured on an ICS 2500 ion chromatography system (Dionex Corp., Sunnyvale, CA), using an IonPac AS18 column with an isocratic 39 mmol L<sup>-1</sup> KOH elution

program at a flow rate of 1 mL min<sup>-1</sup> and an oven temperature of 31°C. The Br<sup>-</sup> detection limit was 0.05 mg L<sup>-1</sup>.

In this study, we analyzed only the Br<sup>-</sup> data to examine the physical transport processes. In addition to the results presented here, tracer experiments were also attempted for soil cores from depths of 0.4 to 0.6, 1.10 to 1.31, and 2.5 to 2.75 m. These tracer experiments exhibited signs of edge effects or bypass around the sample, including nearly instantaneous first arrival of tracer and blocky or stepwise breakthrough character, and therefore these experiments were not utilized in our analysis. Replicate tracer experiments were conducted on each core that exhibited no signs of edge effects. While it is challenging to rule out the possibility of edge effects by BTC data alone, our soil extraction methods and tracer experiment setup parallel former successful studies using intact soil cores (e.g., Ward et al., 1995; Casey et al., 1999; Comegna et al., 2001; Mayes et al., 2000; Koestel et al., 2009).

### Field Tracer Test

A modified doublet tracer test was performed between Critical Zone Monitoring Well (CZMW) 3 and CZMW 2, which are 4.5 m apart (Fig. 1). The depth to water was 1 m below the land surface during the time of the tracer test. A NaBr tracer was injected at CZMW 3 below the soil into the transition between the saprock and fractured bedrock at a packed-off zone between 5 and 6 m below the land surface (Fig. 3). Extraction occurred in CZMW 2, which is cased wellbore from 0 to 2.8 m and an open wellbore from 2.8 to 10 m; the pump was placed at 9.5 m to capture tracer across the entire open borehole. The test was set up as a doublet for the first 700 min; after this period, only the extraction well was utilized. Injection of fresh water occurred for 40 min to establish steady state, followed by 150 min of saltwater injection (10 g L<sup>-1</sup> NaBr, fluid conductivity = 14.2 mS cm<sup>-1</sup>), which was followed again by freshwater injection for 550 min. Fresh water was retrieved from a local limestone and dolomite aquifer (Gatesburg formation), which has a slightly basic pH, fluid conductivity = 300 ± 20 μS cm<sup>-1</sup>, and the dominant species include Ca<sup>2+</sup>, Mg<sup>2+</sup>, HCO<sub>3</sub><sup>-</sup>, SO<sub>4</sub><sup>2-</sup>, and Cl<sup>-</sup> (for more details, see Fulton et al., 2005). The injection rate was constant at 1.7 L min<sup>-1</sup>. The extraction well ran continuously at 2 L min<sup>-1</sup> for the entirety of the test, plus an additional 1440 min after the injection well was turned off. The natural flow gradient of 0.04 is along a bedding strike, which is nearly perpendicular to the direction of the injection–extraction well orientation (Fig. 1).

### Mobile–Immobile Solute Transport Modeling

We created a one-dimensional finite-element transport model with the MIM framework using the Earth Sciences Solute Transport module of COMSOL Multiphysics (COMSOL Inc., Burlington, MA). Initial and boundary conditions of the forward simulations were dictated by experimental conditions. Solute concentration within the mobile domain is controlled by Eq. [1] and mass is exchanged between that domain and the immobile domain by Eq.

[3]. To create an immobile pore space using COMSOL, we implemented two solute transport modules, one with a fluid velocity (Eq. [1]) and one in which the velocity and the dispersion coefficient were set to zero (Eq. [3]).

Specific discharge measurements are defined by  $q = Q/A$ , where  $Q$  is the effluent discharge [L T<sup>-1</sup>] and  $A$  is the area of the column [L<sup>2</sup>], which dictates the flux input to the model domain (Table 1). A Dirichlet boundary condition is used at the inlet boundary, which sets the concentration to a step function of time  $c = c(t)$ , reflecting the switch between the background solution (CaCl<sub>2</sub>) and tracer solution (SrBr<sub>2</sub>) in the mobile domain. The outlet boundary is an advective-flux condition or free boundary, which neglects transport by diffusion perpendicular to the boundary, defined by

$$\mathbf{n} \left( \theta D \frac{\partial c}{\partial x} \right) = 0$$

where  $\mathbf{n}$  is the vector normal to the boundary.

Field tracer breakthrough was modeled similarly to the columns. Flux input was estimated by calculating the advective velocity from the mean arrival time of the tracer breakthrough at the extraction well and was estimated from temporal moments. In this fractured system, the matrix hydraulic conductivity of the shale is very low (10<sup>-15</sup> m s<sup>-1</sup>), making the fractured pathways the primary controls of transport. We expected highly channelized flow and therefore assumed a channel model where the two wells are hydraulically connected by a discrete conduit (e.g., Shapiro and Nicholas, 1989), rather than a typical doublet-test flow field in a porous medium. As such, while reality is certainly more complex, we used a simple one-dimensional conceptual model that considers tracer arrival through a cross-sectional average of the domain. Similar one-dimensional assumptions are common in the fractured rock literature (e.g., Hadermann and Heer, 1996; Himmelsbach et al., 1998; Kosakowski, 2004; Novakowski et al., 2004; Goldscheider, 2008). While doublet tests in porous media tend to produce path lines with different velocities and lengths, thus producing tailing behavior that could be mistaken for mobile–immobile transport, we note here that a three-dimensional model ADE of the field site

Table 1. Physical properties of laboratory- and field-scale experiments and experimental setup.

Depth	Total porosity	Saturated hydraulic conductivity	Injection period	Flux
m		m s <sup>-1</sup>	d	cm d <sup>-1</sup>
0–0.2	0.44	4.9–58 × 10 <sup>-7</sup>	0.54	66
0.6–0.8	0.34	1.8–2.7 × 10 <sup>-7</sup>	0.45	63
1.6–1.8	0.29	1.3–1.7 × 10 <sup>-8</sup>	0.81	29
2.3–2.5	0.29	1.3–2.3 × 10 <sup>-9</sup>	0.58	37
5–6	–	~10 <sup>-6</sup>	0.08	–
Shale	0.035	2.7 × 10 <sup>-15</sup>	–	–

(not shown here) could not produce appropriate tailing without the inclusion of a less-mobile domain. In the presence of fracture-controlled flow, the one-dimensional conceptual model applied here provides insight into the nature of the transport behavior within this domain, although it is not in general considered “proper calibration” (Małłoszewski and Zuber, 1992). Concentrations at the outlet well were normalized to account for mass loss.

Goodness of fit to each BTC, column or field, was determined by constraining the total porosity of the model by the measured total porosity  $\theta_T \sim \theta_m + \theta_{im}$ , calculating the log-transformed RMSE, the error (%) between the measured electrical conductivity (EC) data points and model output, and plotting the solutions in log-log space to examine the tailing. To explore the range of values for the MIM solutions, we utilized the parametric sweep options in Multiphysic and performed a sensitivity analysis on the MIM model fitting parameters  $\alpha$ ,  $\theta_{im}$ , and  $\theta_m$ . The simulations chosen for the sensitivity analysis were constrained by  $\theta_T = \theta_m + \theta_{im}$ , and  $\alpha$  ranged from 0.1 to 10 d<sup>-1</sup>.

## Continuous Time Random Walk Solute Transport Modeling

For the one-dimensional CTRW model, the initial condition is  $c_r(x, t = 0) = 0$ , where  $c_r$  is the resident concentration. The inlet boundary condition is a Robin type, i.e.,

$$\tilde{c}_r(x=0, u) - \frac{D_\psi}{v_\psi} \left( \frac{\partial \tilde{c}_r}{\partial x} \right)_{x=0} = 1$$

In flux-averaged concentration terms, this boundary is also Dirichlet, as in the ADE and MIM model cases. The outlet boundary condition is a Neumann type, i.e.,  $[\partial \tilde{c}_r / \partial x]_{x=L} = 0$ .

## Results

### Porosity and Hydraulic Conductivity

Soil porosity and hydraulic conductivity both decreased from top-soil to subsoil. The uppermost soil had a  $\theta_T$  of 0.44, while deeper soils had a  $\theta_T$  of only 0.34 to 0.29 (Table 1). Hydraulic conductivity also had a decreasing trend with increased soil depth, reducing by three orders of magnitude through the soil profile (Table 1) from  $5.8 \times 10^{-6}$  m s<sup>-1</sup> at the top to  $2.3 \times 10^{-9}$  m s<sup>-1</sup> at a depth of 2.5 m. Lin (2006) also measured hydraulic conductivity on the Ernest soils down to a depth of 1.37 m, yielding hydraulic conductivity measurements between  $10^{-4}$  and  $10^{-5}$  m s<sup>-1</sup>. Values reported for weathered shale saprolite, however, commonly have hydraulic conductivities in the  $10^{-6}$  to  $10^{-9}$  m s<sup>-1</sup> range (e.g., Mayes et al., 2000). The hydraulic conductivity reported here is lower than that of Lin (2006) and probably reflects the effect of averaging because samples used in this study were about four times longer and about six times larger by volume. Hydraulic conductivity and porosimetry measurements on the consolidated Rose Hill shale matrix yielded a very low hydraulic conductivity of  $2.7 \times 10^{-15}$  m

s<sup>-1</sup> and a porosity of 0.035 (Table 1). Neuzil (1994) identified a log-linear relationship between porosity and permeability for shales and clay-rich materials from numerous laboratory data sets, and the measured porosity and permeability of the Rose Hill shale falls within the lower limits of this permeability–porosity relationship. Porosimetry data showed that only about 15% of the shale matrix is composed of pore throats >0.1 μm, with the largest 1% of the pore throats reaching 2 or 3 μm (Fig. 4). In contrast to the shale matrix, the aquifer at the SH-CZO has a high hydraulic conductivity; several slug tests and pumping tests performed in the boreholes suggest that the effective hydraulic conductivity of the aquifer is approximately  $10^{-6}$  m s<sup>-1</sup>.

Profiles observed in caliper and optical televiewer logs (Fig. 2 and 3) suggest that the primary or short-term controls on groundwater flow are secondary structures such as bedding planes, fractures, and preferential pathways rather than the low-permeability matrix. Simulating groundwater flow and transport in fractured rock provides a substantial challenge given the wide range in hydraulic conductivity across a short interval. Fracture sets typically occur as groups of tens to thousands of individual fractures, although only a small proportion of those may be relevant for conducting fluids (e.g., Long et al., 1991; Renshaw, 1995; Hsieh and Shapiro, 1996). The lack of spatial and hydrologic resolution of the fracture network at the SH-CZO limits our ability to simulate flow using a discrete fracture network.

Complicating efforts to predict solute transport in fractured media is a fundamental uncertainty regarding the physical processes at work. For example, long tails on solute BTCs can be attributed to either rate-limited mass transfer between fractures and matrix (Grisak et al., 1980; Neretnieks, 1980; Rasmuson and Neretnieks, 1986) or the existence of multiple advective pathways

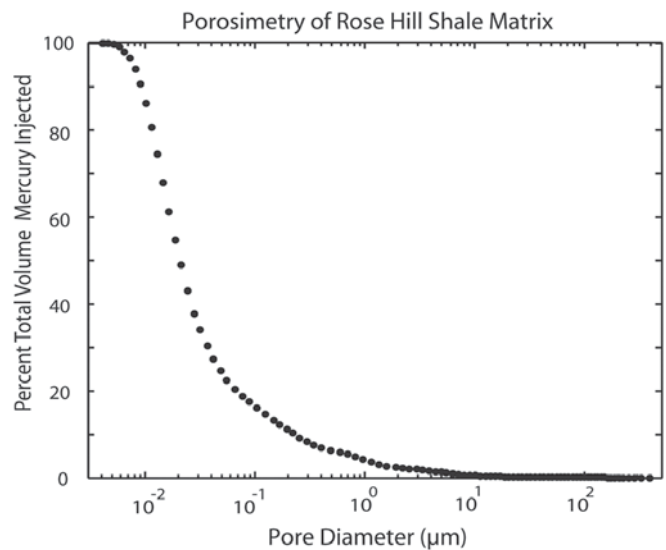


Fig. 4. Mercury porosimetry results performed on a consolidated, unfractured Rose Hill shale sample. Total calculated porosity for the sample, based on these porosimetry data, is 0.035.

of differing velocity (Becker and Shapiro, 2000, 2003). In this study, we observed that the majority of pores within the shale were  $<0.1 \mu\text{m}$  (Fig. 4), providing the capacity to store solutes but being less likely to permit advection. Assuming that diffusion controls the transfer of mass between these small pores and the adjacent advective pathways, we expect such processes could contribute to transport processes at long time scales. Macropores and preferential flow paths were also inferred from high spatially resolved soil-moisture data in the catchment (Lin, 2006). Given the large range in hydraulic conductivity, the presence of macropores, and the variability in porosity at the SH-CZO, we might expect BTCs from both the soil and aquifer to be asymmetric, having earlier than expected breakthrough times and exhibiting tailing behavior due to rate-limited mass transfer and variable or multiple advective pathways.

## Model Analysis

Figure 5 depicts the fluid EC together with  $\text{Br}^-$  concentrations in addition to ADE, MIM, and CTRW model solutions for the soil core tracer experiments. Each  $\text{Br}^-$  BTC is characterized by rapid breakthrough and tailing. The results are presented in a log-log plot, which allows detailed examination of the BTC tailing. Values for ADE, MIM, and CTRW model fitting parameters are listed in Tables 2 and 3. The MIM soil core parameters, in conjunction with soil properties, are plotted as a function of soil depth in Fig. 6. While the ADE could, in most cases, match the mean breakthrough time, it failed to match the observed tailing behavior. Additionally, the ADE consistently reached  $c/c_0 = 1$  during

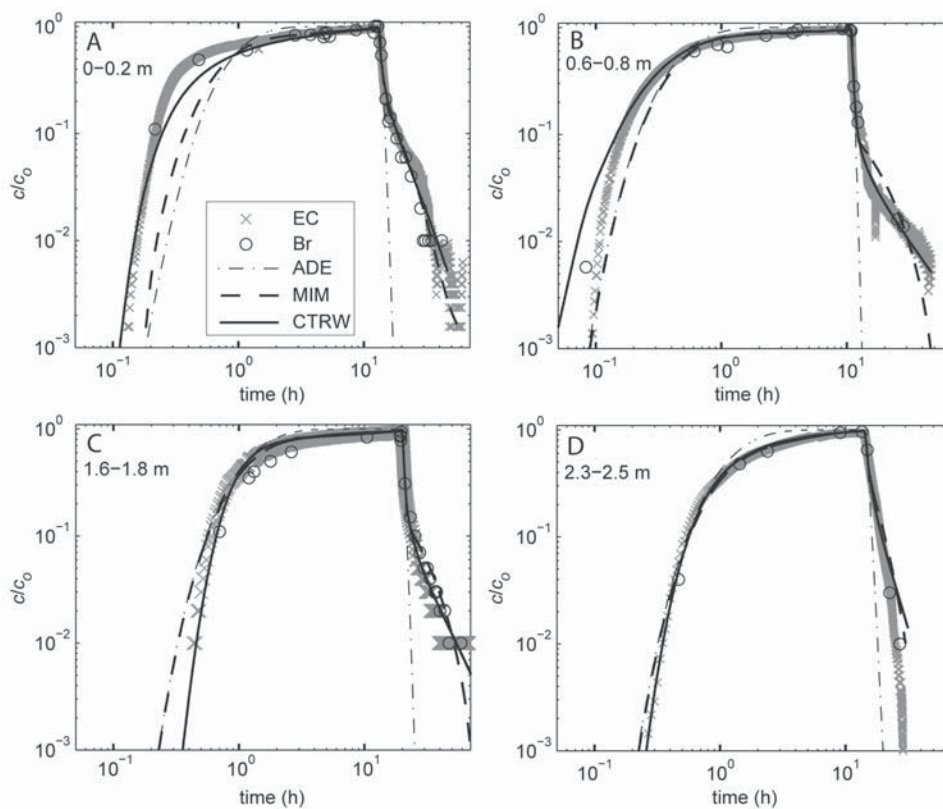


Fig. 5. Measured breakthrough curves with advection–dispersion equation (ADE), mobile–immobile (MIM) model, and continuous time random walk (CTRW) solutions for soil cores from (A) 0- to 0.2-, (B) 0.6- to 0.8-, (C) 1.6- to 1.8-, and (D) 2.3- to 2.5-m depths. EC = effluent electrical conductivity,  $\text{Br}^-$  =  $\text{Br}^-$  concentration.

breakthrough, while the observed maximum breakthrough was  $c/c_0 = 0.95 \pm 0.02$ . Therefore, the ADE was predicting an equilibrium state before we observed such a state in the measured data. Because the ADE failed to match much of the observed tracer transport behavior, we focus our analysis on the CTRW and MIM modeling results.

Figure 5A shows the results of the shallow core from a depth of 0 to 0.2 m. The breakthrough was fast and CTRW captured this behavior better than the ADE or MIM models. The tail was fit well by the

Table 2. Best-fit advection–dispersion equation (ADE) and mobile–immobile (MIM) model parameters (mobile-phase porosity,  $\theta_m$ ; immobile-phase porosity,  $\theta_{im}$ ; total porosity,  $\theta_T$ ; mass transfer rate,  $\alpha$ ) used for fitting laboratory- and field-scale data.

Depth	$\theta_m^\dagger$	$\theta_{im}$	$\theta_m/\theta_T$	$\alpha$	Dispersivity $^\dagger$
m				$\text{d}^{-1}$	m
0–0.2	0.18	0.26	0.41	1.17	0.035
0.6–0.8	0.10	0.23	0.30	0.67	0.05
1.6–1.8	0.11	0.18	0.38	0.41	0.05
2.3–2.5	0.14	0.15	0.48	1.13	0.052
Field tracer	0.045	0.08	0.36	0.30	0.50

$^\dagger$  ADE and MIM model parameters, first fit using ADE then fixed in MIM simulations and constrained to laboratory measurements.

Table 3. Best-fit continuous time random walk parameters (average tracer transport velocity,  $v_\psi$ ; generalized dispersion tensor  $\mathbf{D}_\psi$ ; dispersion measure,  $\beta$ ; characteristic transition time,  $t_1$ ; cutoff time,  $t_2$ ) used for fitting laboratory- and field-scale data.

Depth	$v_\psi$	$\mathbf{D}_\psi$	$\beta$	$t_1$	$t_2$
m	$\text{cm s}^{-1}$	$\text{cm}^2 \text{s}^{-1}$		s	d
0–0.2	$9.84 \times 10^{-2}$	$6.86 \times 10^{-3}$	0.91	3.31	1.11
0.6–0.8	$1.35 \times 10^{-1}$	$7.58 \times 10^{-1}$	1.05	$1.0 \times 10^{-3}$	9.19
1.6–1.8	$6.0 \times 10^{-2}$	$4.0 \times 10^{-2}$	1.01	$1.26 \times 10^{-2}$	3.66
2.3–2.5	$5.4 \times 10^{-2}$	$1.6 \times 10^{-2}$	0.91	2.19	0.73
Field tracer	3.35	2.87	0.83	$6.19 \times 10^{-1}$	$2.69 \times 10^3$

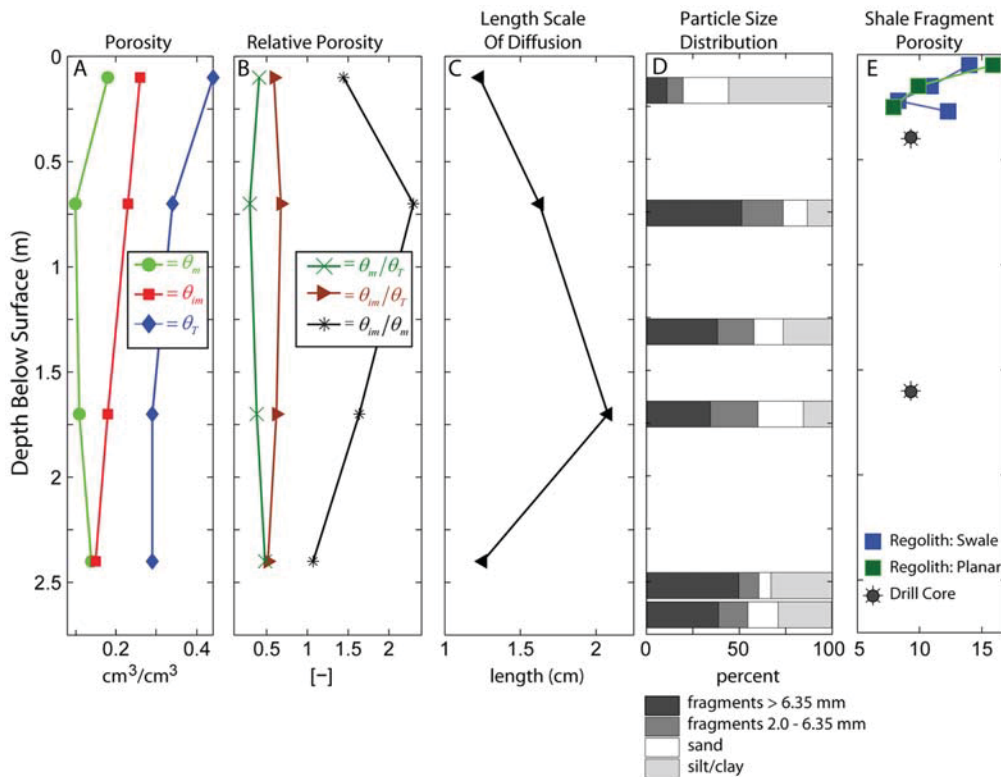


Fig. 6. Mobile-immobile modeling results plotted against soil depth, including (A) fit values for mobile and immobile porosity ( $\theta_m$ ,  $\theta_{im}$ , and  $\theta_T$  are mobile, immobile and total porosities, respectively), (B) relative porosities, (C) estimated length scale of diffusion using Eq. [3], (D) particle size distribution data from various sections in the soil profile, and (E) porosity measurements on Rose Hill shale fragments from various depths at different locations along the ridgetop of the Shale Hills Critical Zone Observatory (modified from Jin et al., 2011).

CTRW with the parameter  $\beta = 0.91$ , which indicates strong anomalous transport. The characteristic transition time  $t_1$  in this case was high, which allowed a good fit to the fast breakthrough observed. The average tracer velocity was  $\sim 50$  times faster than the measured fluid velocity. As noted below Eq. [4], the average tracer velocity may be larger or smaller than the average fluid (water) velocity. The difference between these two velocities arises because of the way that the velocities are averaged; in contrast to the definition of average fluid velocity  $v_m$ , the tracer velocity  $v_\psi$  is defined as the first moment of the transition length pdf,  $p(s)$ , divided by a characteristic time. The presence of fracturing, as in this study, can explain a tracer velocity higher than the average fluid velocity. In this case, most of the fluid flow was very slow, but a small fraction of the fluid advanced at high velocity through the fractured subsurface. Tracer injected in the vicinity of a fracture will allow most of the tracer to travel through the fracture at high velocity; these particles are excluded from low-permeability regions where water is present, yielding a much higher average velocity than that of the fluid. This difference in averaging can be considered in terms of tracer concentration, which varies throughout the domain. If the concentration is uniform throughout, then  $v_m = v_\psi$ . If the tracer concentration is higher in the high-velocity regions (e.g., tracer injection into a fracture), then  $v_\psi > v_m$ . If the tracer concentration is higher in the immobile regions (due to mass transfer), then  $v_\psi < v_m$ . Our findings are consistent with the fast breakthrough of solutes (arriving

before one pore volume) and may indicate fast channeling for solute migration in the strongly heterogeneous domain, corroborated by the relatively low  $\beta$  value.

According to the MIM model analysis, approximately 60% of the total pore space was immobile, and mass transfer between the mobile and immobile domain was fast relative to the rest of the soil cores. This shallow core deviated from the rest of the soil cores by having significant amounts of silt- and clay-sized particles containing far fewer rock fragments than deeper soil cores (Fig. 6D). The late-time tailing behavior was represented well by both MIM and CTRW models.

Data from a core from the 0.6- to 0.8-m depth are presented in Fig. 5B. The CTRW captures the early breakthrough of  $\text{Br}^-$ , which deviated slightly from the EC measurements in this case, perhaps due to dilution of the samples for the ion chromatograph during sample preparation. The CTRW best

describes the tailing shape observed in the EC record with a  $\beta$  value of 1.05. The CTRW parameters for this soil core are considerably different from the parameters for all other cores, with high solute velocity  $v_\psi$  and dispersion  $D_\psi$  values and a short transition time  $t_1$  (Table 3); these point to a transport regime controlled by fractured rock. These results are consistent with the particle size distribution (PSD) data, which indicate that  $\sim 75\%$  of the 0.6- to 0.8-m core was composed of rock fragments (Fig. 6D). The MIM model solution does not match the change in slope at  $\sim 15$  h or tailing during late time well, in contrast to the CTRW solution.

Figure 5C shows the results from the 1.6- to 1.8-m-depth core. In this case, only CTRW captures the anomalous early breakthrough as well as the long tailing, with a best-fit  $\beta$  of 1.01. The tracer velocity  $v_\psi$  is again  $\sim 50$  times greater than the flow velocity  $v_m$ , and the dispersion  $D_\psi$  falls roughly between the other dispersion values. Low mass transfer coupled with low mobile porosity is also apparent in this soil core (Fig. 6B and 6C). The significant late-time tailing behavior from this soil core was best represented by CTRW.

The BTC for the lowermost soil core does not exhibit the notable tailing observed for the intermediate soil cores but behaves more similarly to the uppermost soil core (Fig. 5D). The CTRW matches

the breakthrough portion of the curve exceptionally well, with  $v_{\psi}$ ,  $D_{\psi}$ , and  $\beta$  values similar to the 1.6- to 1.8-m soil core, while the transition time and cutoff times are quite similar to those of the uppermost soil core. The majority of the late-time tailing behavior was adequately captured by both CTRW and MIM models.

Results from the parametric sweep on the MIM model parameters  $\alpha$ ,  $\theta_{im}$ , and  $\theta_m$  for the soil cores are presented in Fig. 7. This sensitivity analysis suggests that (i) the uncertainty in the mobile and immobile porosities is larger than the uncertainty in the estimated mass transfer rates, (ii) the range of mobile–immobile porosities that result in a similar RMSE fit to the data is approximately  $\pm 0.025$  of the values reported in Table 2, and (iii) the mass transfer rates tend to reduce with depth in the 0- to 20-, 0.6- to 0.8-, and 1.6- to 1.8-m cores while increasing in the lowermost 2.3- to 2.5-m core. For the CTRW fits, the parameters (i.e., the values of  $\beta$ ,  $t_1$ , and  $t_2$  in  $\psi(t)$  and their interplay with  $v_{\psi}$  and  $D_{\psi}$ ) are all closely linked. This is because  $\psi(t)$  is based on the flow field, and thus the heterogeneity distribution, of the entire domain within the CTRW ensemble-averaged transport equation (for a detailed discussion, see Berkowitz et al., 2006). As such, while for this study the value of  $t_2$  was relatively insignificant because the transport was clearly non-Fickian, the other parameters values were indeed sensitive. Variations of as little as a few percentage points in the values reported in Table 3 led to notably poorer fits to the data.

With respect to the field-scale tracer test, the CTRW fit was notably better than the ADE and MIM model results (Fig. 8). The CTRW fitting parameters indicate a strongly anomalous transport behavior. Compared with the CTRW parameters of the core data analysis,  $\beta$  is slightly lower and  $t_2$  is significantly larger than the typical values obtained for the laboratory-scale core data, indicating the dominance of the non-Fickian nature of transport at the field scale. The inability of the MIM model to match the breakthrough portion and long tail of the field data also attests to highly non-Fickian transport.

## Implications and Discussion

The MIM modeling of the soil core tracer experiments indicated trends that mimicked those observed in the measured porosity and hydraulic conductivity in that MIM model parameters tended to decrease with increased depth. Our results suggest that (i) solutes appear to have been advecting in 30 to 50% of the total porosity across the soil profile, and (ii) the fraction of immobile pore space decreased linearly with depth (Fig. 6A). The low mobile porosity relative to the total pore space (<50%) signals the existence and control of preferential flow paths, consistent with similar MIM model analysis of undisturbed soil

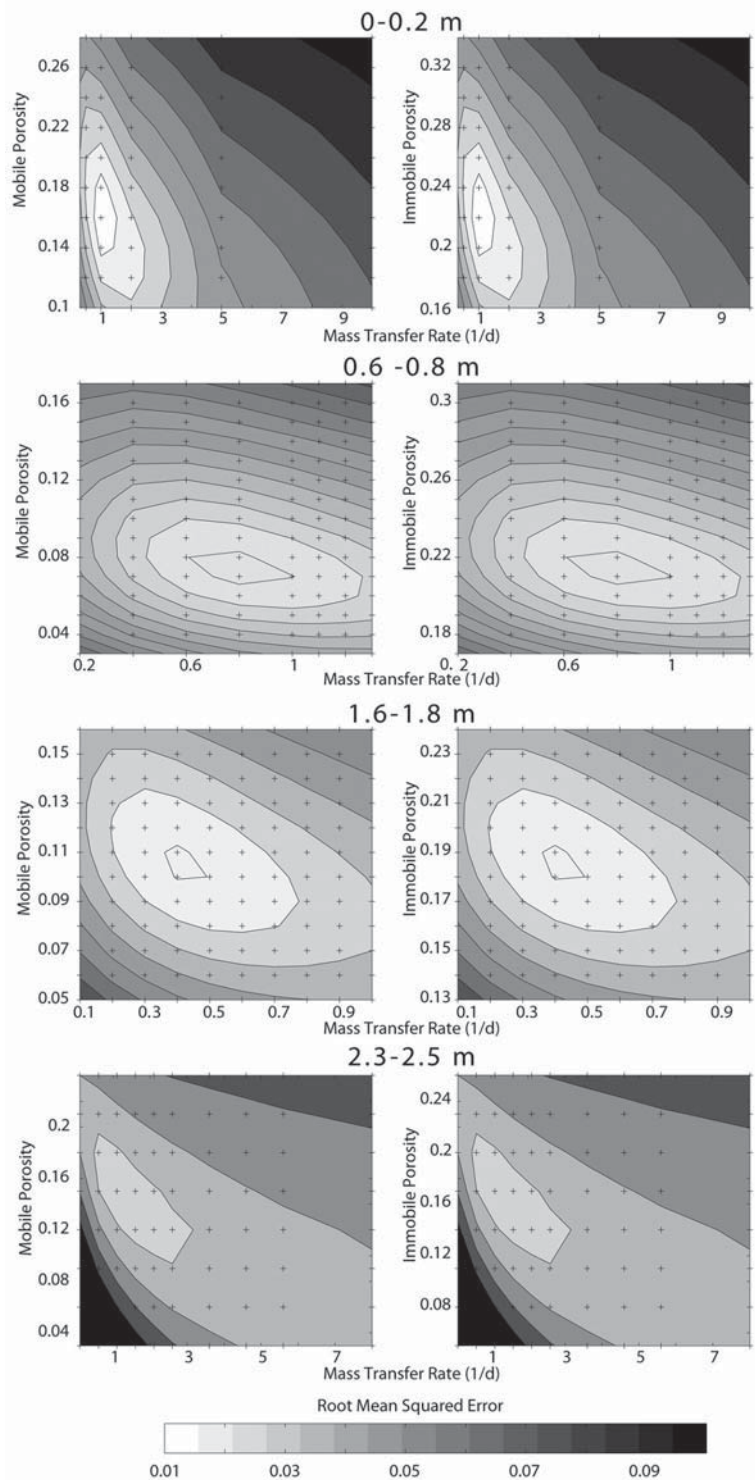


Fig. 7. Root mean square error (RMSE) results from a series of mobile–immobile model simulations for the four soil cores. Crosses represent simulated values.

cores (Seyfried and Rao, 1987). The effect of preferential flow may be especially important in the intermediate cores (0.6–0.8 and 1.6–1.8 m) where  $\theta_m/\theta_T < 0.4$ . In the regions of the soil profile dominated by rock fragments, we expected mass transfer to the less-mobile pore space to be controlled by diffusion (Griffioen et al., 1998).

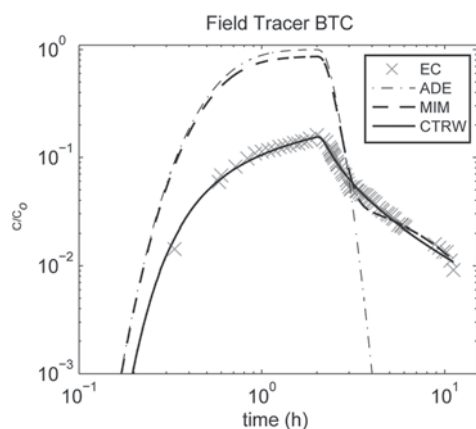


Fig. 8. Field tracer breakthrough curve (BTC) for measured effluent electrical conductivity (EC) at pumped Critical Zone Monitoring Well 2 and advection–dispersion equation (ADE), mobile–immobile (MIM) model, and continuous time random walk (CTRW) solutions.

The MIM model parameters for the soil cores may be indicative of physical properties related to weathering. The pattern of decreasing immobile porosity from shallow to deep soil cores (Fig. 6A) may be capturing the effect of increased weathering. This observation is supported by the neutron porosity work of Jin et al. (2011), which investigated the porosity of the shale fragments extending through the regolith and down into the bedrock. The porosity of the shale fragments was >15% in the uppermost soils, decreasing to ~8% at depth (Fig. 6E). Jin et al. (2011) suggested that three pore types exist within the shale bedrock: (i) interlayer pores (pores between 2:1 clay layers), (ii) intraparticle pores (pores between mineral assemblages), and (iii) interparticle pores (pores between particle boundaries), the smallest pores being the interlayer pores. The increase in shale porosity from weathering is thought to occur from the development of intraparticle pore space from the dissolution of clay minerals (Jin et al., 2011). Lower natural  $\gamma$ -ray values at the surface (1–6 m) measured in 16-m-deep boreholes near the catchment outlet attest to a reduction in clay content near the surface (Fig. 3). Above the  $\gamma$ -ray tool measurements (<1 m), we observed an increase in clay content in the 0- to 20-cm core, probably due to downslope transport and mass wasting (Fig. 6). Our modeling indicates that immobile pore space decreases with depth in the soil profile, which may be associated with the weathering of clay minerals in the shale fragments in the regolith and saprock. We cannot rule out, however, changes in the immobile pore space due to a reduction in total porosity and changes in the soil composition, texture, and PSD. We conceptualize the mobile pore space to be comprised of regions between and adjacent to the many rock fragments (preferential pathways), and some fraction of that immobile pore would be comprised of pores in the shale fragments themselves.

To examine the inferred relationship between weathering and immobile porosity, we examined the distribution of rock fragments

across the soil profile by analyzing the PSDs of the soil cores (Fig. 6D). The PSDs collected by wet sieving revealed that rock fragments comprised 20 to 50% of the total soil composition, and more than ~60% of those rock fragments were >6.35 mm. The weathering out of clay minerals results in higher porosity on the rock fragment and more connectivity within the shale fragments (Jin et al., 2011). This increase in porosity and connectivity on the shale fragments may be associated with the increased immobile porosity identified by the MIM modeling. Visual inspection revealed that rock fragments in the upper three soil cores were olive-gray to yellow and subangular to rounded, whereas fragments from a depth of 2.5 m and greater were bluish-gray and angular to subangular, with only slight visual indication of weathering. The rock fragment composition change is consistent with observations by the optical televiewer and geophysical logs, where shale bedrock changed from more weathered (saprock) to less weathered (bedrock) below the 6-m depth (Fig. 2 and 3). Soil cores from 0.6 to 0.8 and 1.6 to 1.8 m contained >60% weathered rock fragments and had relatively large immobile domains based on MIM modeling, suggesting a relationship between weathering of the shale fragments and the immobile domain porosity. Furthermore, mass balance results from the tracer experiments suggest that more mass remained in the deeper soil cores than the uppermost core. The lower mass recovery in the deeper cores with more shale fragments suggests retention of solutes in the shale-fragment-dominated media. Finally, we point out that rock fragments did not make up a large percentage of the shallow core, indicating that the structure of the immobile domain may be a combination of not only rock fragment porosity but also changes in soil texture and composition, a reduction in total porosity, and changes in the PSD with depth.

With the exception of the deepest soil core, the rate of mass transfer  $\alpha$  also decreased with depth into the soil profile and aquifer, being  $\sim 1 \text{ d}^{-1}$  in the uppermost core and  $< 1 \text{ d}^{-1}$  for soil cores from 0.6 to 0.8 and 1.6 to 1.8 m (Table 2). These mass transfer values are similar to those of Reedy et al. (1996), who also performed tracer experiments on an undisturbed shale saprolite core. A reduction in the mass transfer rate with depth might be expected if the mass transfer rate is reflecting the increased length of mixing (Eq. [3]) or the increased heterogeneity encountered by the mobile and immobile domains (Haggerty and Gorelick, 1995). The deepest soil core may break from the trend of decreasing mass transfer rate because the immobile pore space on the shale fragments is only poorly developed and therefore the mass transfer to this region is only minimal relative to the time scale of the experiment. Koch and Flüßler (1993) pointed out that simultaneously optimizing  $\theta_m$ ,  $\theta_{im}$ , and  $\alpha$  could result in highly correlated parameters that have little physical meaning. For example, it is not clear how to interpret the characteristic length scale of diffusion, as defined in Eq. [3]. The diffusion length scales estimated for the soil cores are on the order of centimeters, while >60% of the soil is composed of small rock fragments (2–6.35 mm) and sand- and silt-sized particles. The diffusion length scale may reflect the relationship

between the dead-end pore space and fracture spacing, the presence of large rock fragments, or a combination of these physical properties. We note that while it is difficult to measure many of these fitted parameters in the field directly, there is certainly correlation between physical properties and our estimated parameters. Failing to directly tie parameters such as mass transfer rates and diffusion scales directly to physical properties limits our ability to interpret solute transport behavior; however, we (i) have highlighted a potential relationship between immobile pore space and rock fragments, and (ii) validated the prevalence of preferential flow paths at four depths within the soil profile using this modeling analysis.

The CTRW provides additional interpretation of transport processes compared with the MIM model analysis above. The CTRW model fits provide a means to examine the degree of non-Fickian transport. The extent of non-Fickian transport is inferred from the parameters of  $\psi(t)$  (mainly  $\beta$ ) so that the shape of the transition rate probability, obtained by the fitting process, explains the dynamical aspects of the transport rather than offering a concrete suggestion as to the structure of the porous domain. As noted above, the heterogeneous structure of the porous medium is not the only cause of non-Fickian transport. In both soil cores and the field scale, we found anomalous early breakthrough and long tailing. The early breakthrough is consistent with the exceptionally high average solute velocity  $v_{\psi}$ , compared with the average fluid velocity  $v_m$ , which may result from the presence of strong preferential pathways. The highly anomalous nature of the transport observed by the long tailing was further confirmed by the low  $\beta$  values. Unlike the MIM model results, however, we did not find a distinct trend in the CTRW parameters with soil core depth. In all cases presented here, the parameter  $t_2$  indicated that the tracer injection experiment lay in the non-Fickian times, the power-law region of the TPL pdf, because  $t_2$  was larger than the experiment duration. When the cutoff time  $t_2$  is large, the mass transfer rate required to capture the tailing behavior is low and the goodness of the MIM model fit to the BTC diminishes (Fig. 5B, 5C, and 7). Despite contrasting properties between the soil cores at 0 to 0.2 and 2.3 to 2.5 m (Table 1), these cores showed similar CTRW-fitted parameters. This result is an interesting feature of the CTRW, which demonstrates that while media can appear to be quite different structurally, the transport behavior within them can be quite similar in terms of the extent of non-Fickian behavior, dictated by the transition rate probability  $[\psi(t)]$  parameters (for details, see, e.g., Berkowitz and Scher, 2009, 2010). This is because transport must be considered in terms of residence time and tracer interactions between “fast” and “slow” zones so that the controlling parameters are often dynamical rather than structural.

The CTRW fit the experimental data somewhat better than the MIM model and much better than the ADE in this system, but this is not simply a matter of parameterization. The CTRW has a well-defined number of parameters, whereas, e.g., the ADE

assumes an inherent Fickian transport so that the parameters needed to describe non-Fickian transport are discarded a priori. It is important to recognize that the non-Fickian nature of the tracer transport does not arise solely from mass transfer to immobile regions but also from the inherent heterogeneity of the medium and tracer residence time effects on concentration tailing that are not explicitly modeled by the MIM model. Insights regarding the overall non-Fickian behavior that arises from a combination of these mechanisms can be gained with CTRW modeling. In reality, all of these parameters vary in space, so all of these models are underparameterized. The question of “which model to choose” is often philosophical. That said, in combining the CTRW and MIM model analyses of the field tracer experiment, we conclude that solute transport in the aquifer is not well represented by classic advection and dispersion because there is prevalent non-Fickian transport. Solute transport in certain sections of the soil profile and within the aquifer indicate more complicated behavior than simple linear mass transfer between two domains, including early breakthrough and significant long tailing. In such cases, CTRW more accurately matches the BTCs than the MIM model.

Gao et al. (2009) also recognized the inadequacy of MIM modeling and the ability of CTRW to match long tails in a large column of highly heterogeneous materials. In those cases where the MIM model results were less adequate (0.6–0.8- and 1.6–1.8-m soil cores and the field tracer), we observed immobile domains that were more than 1.5 times the size of the mobile domain and mass transfer rates that were  $<1 \text{ d}^{-1}$ . This combination of low mass transfer rates, large immobile domains, and long cutoff times indicates the mass storage potential of the soil or aquifer matrix and suggests the need to incorporate more complex mass transfer processes such as a continuum of mass transfer rates. The MIM model has the capacity to fit either the early breakthrough or the tailing measured in the field but cannot fit the entire BTC with one set of parameters. The CTRW allows solutes to move separately from the fluid velocity and permits a slow release from storage via a distribution of mass transfer rates, providing a more complete representation of the solute transport behavior at the SH-CZO. Performing CTRW analysis without incorporating a MIM model analysis, however, cannot estimate the size of that storage zone (the immobile domain) or identify the time scale of mass transfer into and out of these storage zones.

The parameters considered here can, in principle, be used for transport prediction, although applying a transport model with parameters calibrated under specific conditions to the same domain with different conditions is clearly not trivial. While one usually aims for “robust” models that can be applied in many different circumstances, this is rarely attained in practice. Calibrated parameters can sometimes describe transport in a domain with different flow rates; this was demonstrated for two different domains, each with three different flow rates using a CTRW model (e.g., Berkowitz and Scher, 2009). In the data presented here, however,

there is no definitive pattern in the various model parameters with the depths of the cores, probably due to the overall heterogeneity of the domain. Application of these analyses across multiple scales is also difficult; the core experiments represent a smaller scale of heterogeneity than can be captured by the field test. The residence time of solutes is a key factor determining the degree of interaction between fast and slow zones; in this context, diffusive transfer may be more or less important at different scales, depending on the residence time. As the residence time increases, there is increased homogenization of the tracer plume between the fast and slow zones so that overall transport becomes more Fickian. Note that the relative influence of diffusion vs. advection could be further elucidated by conducting experiments at different flow rates.

Despite the complications associated with modeling these heterogeneous field systems, the CTRW and MIM modeling confirmed the heterogeneous nature of the regolith and shale-bedrock aquifer, offered insight into the nature of the flow field, and helped distinguish the operation of physical transport processes important to the SH-CZO. Failing to incorporate the variability of parameters into groundwater age or soil weathering models would lead to an underestimated residence time of solutes in the catchment because the rate-limiting step of mass transfer into and out of stagnant water regions retains solutes within the system longer than models that contain only advection and dispersion.

## Conclusions

Quantification of the operative solute transport processes at the column scale at four locations within the soil profile and at the field scale at the SH-CZO identified controls on the residence time of solutes, clarified the important role of preferential pathways in conducting fluid, and outlined how the composition of the regolith and aquifer contribute to the movement of solutes between more- and less-mobile domains. Additionally, we hypothesize that the MIM modeling results for the soil cores are indicative of soil properties and may reflect the effects of weathering on the soil profile. While the ADE can capture the mean arrival time of the BTCs, it consistently overestimated it at peak concentration. Consistent discrepancies between the ADE and all measured BTCs imply that transport at the SH-CZO cannot be solely characterized by advection and Fickian dispersion processes. Best-fit ADE models were found to require (i) a low effective porosity, and (ii) a large dispersivity value relative to the scale of the experiment.

Solute transport throughout the system cannot be ascribed solely to a simple MIM conceptualization. Solute transport in the soil and aquifer at the SH-CZO is characterized by highly non-Fickian behavior that in some cases is better described by a CTRW model than by a simple MIM model. In the presence of low mass transfer rates, large immobile domains, and long cutoff times, a continuum of mass transfer rates as described by the CTRW was needed to match the measured BTCs. With relation to geology, when the

subsurface is composed largely of shale fragments and fractured rock, the times required until Fickian behavior occurs tend to increase; applying a single mass transfer rate may be an oversimplification of the physical transport phenomenon. Moreover, allowing an average tracer velocity that is distinct from the fluid velocity permitted a match to the very early breakthrough and late-time tailing.

Conceptualizing solutes undergoing a series of transitions in space and time independent of the flow regime may prove useful to evaluate the function of the regolith at the SH-CZO. In this study, combining CTRW and MIM model results has helped investigation of the operative transport processes across a soil profile and within the fractured shale bedrock as a composite system. For example, the high tracer transport velocity  $v_{\psi}$  coupled with the low effective or mobile porosity  $\theta_m$  point to preferential flow. Similarly, long “cutoff” times  $t_2$  and low mass transfer rates  $\alpha$  point to significant tailing and extended residence times of solutes in the soil and aquifer. Analysis of the CTRW and MIM modeling results yielded alternative perspectives and subsequent interpretations of the subsurface transport regime, increasing our ability to define how solutes interact with, are transported through, and become retained within the geologic media. Without incorporating controlling features such as preferential flow, mass transfer, and distinctly high tracer transport velocities into solute transport models, we will inaccurately predict solute transport and, consequently, important processes like estimating the age of water at the SH-CZO.

## Acknowledgments

We wish to thank Laura Toran and Nate Wysocki for assistance in design and execution of the field tracer experiment. We thank Terryl Daniels for the collection and use of the well log data. We thank Andy Rathbun, Steve Swavely, Brett Carpenter, and Demian Saffer from the Penn State Rock Mechanics lab for assistance with the shale permeability experiments and Lixin Jin, Laura Liermann, and Lin Ma for assistance with geochemical data and particle size analysis. We thank Ryan Swanson for assistance with sensitivity analysis. Useful discussions with Susan Brantley, Michael Gooseff, and Richard Parizek are acknowledged. Funding for this research was provided from NSF Grants EAR-0725019 and EAR-0747629.

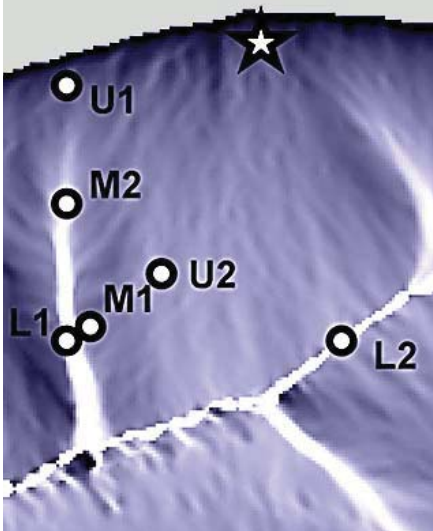
## References

- Adams, E.E., and L.W. Gelhar. 1992. Field study of dispersion in a heterogeneous aquifer: 2. Spatial moments analysis. *Water Resour. Res.* 28:3293–3307. doi:10.1029/92WR01757
- Al-Jabri, S., R. Horton, D.B. Jaynes, and A. Gaur. 2002. Field determination of soil hydraulic and chemical transport properties 1. *Soil Sci.* 167:353–368. doi:10.1097/00010694-200206000-00001
- Amundson, R., D.D. Richter, G.S. Humphreys, E.G. Jobbagy, and J. Gaillardet. 2007. Coupling between biota and earth materials in the critical zone. *Elements* 3:327–332. doi:10.2113/gselements.3.5.327
- Anderson, S.P., R.C. Bales, and C.J. Duffy. 2008. Critical Zone Observatories: Building a network to advance interdisciplinary study of earth surface processes. *Mineral. Mag.* 72:7–10. doi:10.1180/minmag.2008.072.1.7
- Becker, M.W., and A.M. Shapiro. 2000. Tracer transport in fractured crystalline rock: Evidence of nondiffusive breakthrough tailing. *Water Resour. Res.* 36:1677–1686. doi:10.1029/2000WR900080
- Becker, M.W., and A.M. Shapiro. 2003. Interpreting tracer breakthrough tailing from different forced-gradient tracer experiment configurations in fractured bedrock. *Water Resour. Res.* 39(1):1024. doi:10.1029/2001WR001190
- Berkowitz, B., A. Cortis, M. Dentz, and H. Scher. 2006. Modeling non-Fickian transport in geological formations as a continuous time random walk. *Rev. Geophys.* 44:RG2003. doi:10.1029/2005RG000178

- Berkowitz, B., and H. Scher. 1998. Theory of anomalous chemical transport in random fracture networks. *Phys. Rev. E* 57:5858–5869. doi:10.1103/PhysRevE.57.5858
- Berkowitz, B., and H. Scher. 2009. Exploring the nature of non-Fickian transport in laboratory experiments. *Adv. Water Resour.* 32:750–755. doi:10.1016/j.advwatres.2008.05.004
- Berkowitz, B., and H. Scher. 2010. Anomalous transport in correlated velocity fields. *Phys. Rev. E* 81:011128. doi:10.1103/PhysRevE.81.011128
- Bethke, C.M., and T.M. Johnson. 2008. Groundwater age and groundwater age dating. *Annu. Rev. Earth Planet. Sci.* 36:121–152. doi:10.1146/annurev.earth.36.031207.124210
- Bijeljic, B., S. Rubin, H. Scher, and B. Berkowitz. 2011. Non-Fickian transport in porous media with bimodal structural heterogeneity. *J. Contam. Hydrol.* 120–121:213–221. doi:10.1016/j.jconhyd.2010.05.007
- Brace, W.F., J.B. Walsh, and W.T. Frangos. 1968. Permeability of granite under high pressure. *J. Geophys. Res.* 73:2225–2236. doi:10.1029/JB073i006p02225
- Brantley, S.L., M.B. Goldhaber, and V. Ragnarsdottir. 2007. Crossing disciplines and scales to understand the critical zone. *Elements* 3:307–314. doi:10.2113/gselements.3.5.307
- Brusseau, M.L., Z. Gerstl, D. Augustijn, and P.S.C. Rao. 1994. Simulating solute transport in an aggregated soil with the dual-porosity model: Measured and optimized parameter values. *J. Hydrol.* 163:187–193. doi:10.1016/0022-1694(94)90028-0
- Brusseau, M.L., R.E. Jessup, and P.S.C. Rao. 1991. Nonequilibrium sorption of organic chemicals: Elucidation of rate-limiting processes. *Environ. Sci. Technol.* 25:134–142. doi:10.1021/es00013a015
- Cameron, D.R., and A. Klute. 1977. Convective–dispersive solute transport with a combined equilibrium and kinetic adsorption model. *Water Resour. Res.* 13:183–188. doi:10.1029/WR013i001p00183
- Casey, F.X.M., D.B. Jaynes, R. Horton, and S.D. Logsdon. 1999. Comparing field methods that estimate mobile–immobile model parameters. *Soil Sci. Soc. Am. J.* 63:800–806. doi:10.2136/sssaj1999.634800x
- Coats, K.H., and B.D. Smith. 1964. Dead-end pore volume and dispersion in porous media. *SPE J.* 4:73–84. doi:10.2118/647-PA
- Comegna, V., A. Coppola, and A. Sommella. 2001. Effectiveness of equilibrium and physical non-equilibrium approaches for interpreting solute transport through undisturbed soil columns. *J. Contam. Hydrol.* 50:121–138. doi:10.1016/S0169-7722(01)00100-0
- Cortis, A., and B. Berkowitz. 2004. Anomalous transport in “classical” soil and sand columns. *Soil Sci. Soc. Am. J.* 68:1539–1548. doi:10.2136/sssaj2004.1539
- Dane, J.H., and G.C. Topp (ed.). 2002. *Methods of soil analysis. Part 4. Physical methods.* SSSA Book Ser. 5. SSSA, Madison, WI.
- Deng, J., X. Jiang, X. Zhang, W. Hu, and J.W. Crawford. 2008. Continuous time random walk model better describes the tailing of atrazine transport in soil. *Chemosphere* 71:2150–2157. doi:10.1016/j.chemosphere.2008.01.001
- Dentz, M., H. Scher, D. Holder, and B. Berkowitz. 2008. Transport behavior of coupled continuous-time random walks. *Phys. Rev. E* 78:041110. doi:10.1103/PhysRevE.78.041110
- Dere, A., T. White, L. Jin, D. Harbor, M. Townsend, and S.L. Brantley. 2010. Shale weathering rates across a continental-scale climosequence. p. 27–30. *In* R.J. Gilkes and N. Prakongkap (ed.) *Soil solutions for a changing world: World Congr. Soil Sci., 19th, Brisbane, QLD, Australia.* 1–6 Aug. 2010. Int. Union Soil Sci., Sydney, Australia.
- Duffy, C.J. 2010. Dynamical modelling of concentration–age–discharge in watersheds. *Hydrol. Processes* 24:1711–1718. doi:10.1002/hyp.7691
- Flueckinger, L.A. 1969. *Geology of a portion of the Allensville quadrangle, Centre and Huntingdon Counties, Pennsylvania.* Rep. 176. Topogr. and Geol. Surv., Middletown, PA.
- Fulton, J.W., E.H. Koerkle, S.D. McAuley, S.A. Hoffman, and L.F. Zarr. 2005. Hydrogeologic setting and conceptual hydrologic model of the Spring Creek basin, Centre County, Pennsylvania, June 2005. *Sci. Invest. Rep.* 2005-5091. USGS, Reston, VA.
- Gao, G., H. Zhan, S. Feng, G. Huang, and X. Mao. 2009. Comparison of alternative models for simulating anomalous solute transport in a large heterogeneous soil column. *J. Hydrol.* 377:391–404. doi:10.1016/j.jhydrol.2009.08.036
- Goldscheider, N. 2008. A new quantitative interpretation of the long-tail and plateau-like breakthrough curves from tracer tests in the artesian karst aquifer of Stuttgart, Germany. *Hydrol. J.* 16:1311–1317.
- Goltz, M.N., and P.V. Roberts. 1986. Interpreting organic solute transport data from a field experiment using physical nonequilibrium models. *J. Contam. Hydrol.* 1:77–93. doi:10.1016/0169-7722(86)90008-2
- Gong, R., C. Lu, W.-M. Wu, H. Cheng, B. Gu, D.B. Watson, C.S. Criddle, P.K. Kitanidis, S.C. Brooks, P.M. Jardine, and J. Luo. 2010. Estimating kinetic mass transfer by resting-period measurements in flow-interruption tracer tests. *J. Contam. Hydrol.* 117:37–45. doi:10.1016/j.jconhyd.2010.06.003
- Goode, D.J. 1996. Direct simulation of groundwater age. *Water Resour. Res.* 32:289–296. doi:10.1029/95WR03401
- Gorelick, S.M., G. Liu, and C. Zheng. 2005. Quantifying mass transfer in permeable media containing conductive dendritic networks. *Geophys. Res. Lett.* 32:L18402. doi:10.1029/2005GL023512
- Griffioen, J.W., D.A. Barry, and J.Y. Parlange. 1998. Interpretation of two-region model parameters. *Water Resour. Res.* 34:373–384. doi:10.1029/97WR02027.
- Grisak, G.E., J.A. Pickens, and J.A. Cherry. 1980. Solute transport through fractured media: 2. Column study of fractured till. *Water Resour. Res.* 16:731–739. doi:10.1029/WR016i004p00731
- Gwo, J., M.A. Mayes, and P.M. Jardine. 2007. Quantifying the physical and chemical mass transfer processes for the fate and transport of Co(II)EDTA in a partially-weathered limestone–shale saprolite. *J. Contam. Hydrol.* 90:184–202. doi:10.1016/j.jconhyd.2006.09.013
- Hadermann, J., and W. Heer. 1996. The Grimsel (Switzerland) migration experiment: Integrating field experiments, laboratory investigations and modeling. *J. Contam. Hydrol.* 21:87–100. doi:10.1016/0169-7722(95)00035-6
- Haggerty, R., and S.M. Gorelick. 1994. Design of multiple contaminant remediation: Sensitivity to rate-limited mass transfer. *Water Resour. Res.* 30:435–446. doi:10.1029/93WR02984
- Haggerty, R., and S.M. Gorelick. 1995. Multiple-rate mass transfer for modeling diffusion and surface reactions in media with pore-scale heterogeneity. *Water Resour. Res.* 31:2383–2400.
- Himmelsbach, T., H. Hoetzel, and P. Malozewski. 1998. Solute transport in a highly permeable fault zone of Lindau Fractured Rock Test Site (Germany). *J. Ground Water* 36:792–800. doi:10.1111/j.1745-6584.1998.tb02197.x
- Hsieh, P.A., and A.M. Shapiro. 1996. Hydraulic characteristics of fractured bedrock underlying the FSE well field at the Mirror Lake site, Grafton County, New Hampshire. *In* U.S. Geol. Surv. Toxic Substances Hydrol. Progr., Proc. Tech. Mtg., Colorado Springs, CO. 20–24 Sept. 1993. *Water-Resour. Invest. Rep.* 94-4015. USGS, Reston, VA.
- Hsieh, P.A., J.V. Tracy, C.E. Neuzil, J.D. Bredehoeft, and S.E. Silliman. 1981. A transient laboratory method for determining the hydraulic properties of ‘tight’ rocks: I. Theory. *Int. J. Rock Mech. Min. Sci. Geomech. Abstr.* 18:245–252. doi:10.1016/0148-9062(81)90979-7
- Huang, K., N. Toride, and M.Th. van Genuchten. 1995. Experimental investigation of solute transport in large, homogenous and heterogeneous, saturated soil columns. *Transp. Porous Media* 18:283–302. doi:10.1007/BF00616936
- Jardine, P.M., W.E. Sanford, J.P. Gwo, O.C. Reedy, D.S. Hicks, J.S. Riggs, and W.B. Bailey. 1999. Quantifying diffusive mass transfer in fractured shale bedrock. *Water Resour. Res.* 35:2015–2030. doi:10.1029/1999WR900043
- Javaux, M., and M. Vanclooster. 2003. Scale- and rate-dependent solute transport within an unsaturated sandy monolith. *Soil Sci. Soc. Am. J.* 67:1334–1343.
- Javaux, M., and M. Vanclooster. 2004. In situ long-term chloride transport through a layered, nonsaturated subsoil. 2. Effect of layering on solute transport processes. *Vadose Zone J.* 3:1331–1339.
- Jin, L., R. Ravella, B. Ketchum, P.R. Bierman, P. Heaney, T. White, and S.L. Brantley. 2010. Mineral weathering and elemental transport during hillslope evolution at the Susquehanna/Shale Hills Critical Zone Observatory. *Geochim. Cosmochim. Acta* 74:3669–3691. doi:10.1016/j.gca.2010.03.036
- Jin, L., G. Rother, D.R. Cole, D.F.R. Mildner, C.J. Duffy, and S.L. Brantley. 2011. Characterization of deep weathering and nanoporosity development in shale—A neutron study. *Am. Mineral.* 96:498–512. doi:10.2138/am.2011.3598.
- Kazemi, G.A., J.H. Lehr, and P. Perrochet. 2006. *Groundwater age.* John Wiley & Sons, Hoboken, NJ.
- Koch, S., and H. Flüßler. 1993. Solute transport in aggregated porous media: Comparing model independent and dependent parameter estimation. *Water Air Soil Pollut.* 68:275–289. doi:10.1007/BF00479408
- Koestel, J., J. Vanderborght, M. Javaux, A. Kemna, A. Binley, and H. Vereecken. 2009. Noninvasive 3-D transport characterization in a sandy soil using ERT: 1. Investigating the validity of ERT-derived transport parameters. *Vadose Zone J.* 8:711–722.
- Kosakowski, G. 2004. Anomalous transport of colloids and solutes in a shear zone. *J. Contam. Hydrol.* 72:23–46. doi:10.1016/j.jconhyd.2003.10.005
- Lee, J., R. Horton, and D.B. Jaynes. 2000. A time domain reflectometry method to measure immobile water content and mass exchange coefficient. *Soil Sci. Soc. Am. J.* 64:1911–1917. doi:10.2136/sssaj2000.6461911x
- Lin, H.S. 2006. Temporal stability of soil moisture spatial pattern and subsurface preferential flow pathways in the Shale Hills catchment. *Vadose Zone J.* 5:317–340. doi:10.2136/vzj2005.0058
- Lin, H.S., W. Kogelmann, C. Walker, and M.A. Bruns. 2006. Soil moisture patterns in a forested catchment: A hydrogeological perspective. *Geoderma* 131:345–368. doi:10.1016/j.geoderma.2005.03.013
- Lin, H.S., and X. Zhou. 2008. Evidence of subsurface preferential flow using soil hydrologic monitoring in the Shale Hills catchment. *Eur. J. Soil Sci.* 59:34–49. doi:10.1111/j.1365-2389.2007.00988.x

- Long, J.C.S., K. Karasaki, A. Davey, J. Peterson, M. Landsfeld, J. Kemeny, and S. Martel. 1991. An inverse approach to the construction of fracture hydrology models conditioned by geophysical data: An example from the validation exercises at the Stripa Mine. *Int. J. Rock Mech. Min. Sci. Geomech. Abstr.* 28:121–142. doi:10.1016/0148-9062(91)92162-R
- Luo, J., W. Wu, J. Carley, M.N. Fienen, H. Cheng, D. Watson, C.S. Criddle, P.M. Jardine, and P.K. Kitanidis. 2008. Estimating first-order reaction rate coefficient for transport with nonequilibrium linear mass transfer in heterogeneous media. *J. Contam. Hydrol.* 98:50–60. doi:10.1016/j.jconhyd.2008.03.002
- Małozewski, P., and A. Zuber. 1992. On the calibration and validation of mathematical models for the interpretation of tracer experiments in groundwater. *Adv. Water Resour.* 15:47–62. doi:10.1016/0309-1708(92)90031-V
- Maraqqa, M.A., R.B. Wallace, and T.C. Voice. 1997. Effects of degree of water saturation on dispersivity and immobile water in sandy soil columns. *J. Contam. Hydrol.* 25:199–218. doi:10.1016/S0169-7722(96)00032-0
- Mayes, M.A., P.M. Jardine, I.L. Larsen, S.C. Brooks, and S.E. Fendorf. 2000. Multispecies transport of metal-EDTA complexes and chromate through undisturbed columns of weathered fractured saprolite. *J. Contam. Hydrol.* 45:243–265. doi:10.1016/S0169-7722(00)00108-X
- Neretnieks, I. 1980. Diffusion in the rock matrix: An important factor in radionuclide migration? *J. Geophys. Res.* 85:4379–4397. doi:10.1029/JB085iB08p04379
- Neuzil, C.E. 1994. How permeable are clays and shales? *Water Resour. Res.* 30:145–150. doi:10.1029/93WR02930
- Novakowski, K.S., G. Bickerton, and P. Lapcevic. 2004. Interpretation of injection-withdrawal tracer experiments conducted between two wells in a large single fracture. *J. Contam. Hydrol.* 73:227–247. doi:10.1016/j.jconhyd.2004.02.001
- Parker, J.C., and A.J. Valocchi. 1986. Constraints on the validity of equilibrium and first-order kinetic transport models in structured soils. *Water Resour. Res.* 22:399–407. doi:10.1029/WR022i003p00399
- Perfect, E., M.C. Sukop, and G.R. Hasler. 2002. Prediction of dispersivity for undisturbed soil columns from water retention parameters. *Soil Sci. Soc. Am. J.* 66:696–701. doi:10.2136/sssaj2002.0696
- Rasmuson, A., and I. Neretnieks. 1986. Radionuclide transport in fast channels in crystalline rock. *Water Resour. Res.* 22:1247–1256. doi:10.1029/WR022i008p01247
- Reedy, O.C., P.M. Jardine, G.V. Wilson, and H.M. Selim. 1996. Quantifying the diffusive mass transfer of nonreactive solutes in columns of fractured saprolite using flow interruption. *Soil Sci. Soc. Am. J.* 60:1376–1384. doi:10.2136/sssaj1996.03615995006000050012x
- Reilly, T.E., L.N. Plummer, P.J. Phillips, and E. Busenberg. 1994. The use of simulation and multiple environmental tracers to quantify groundwater flow in a shallow aquifer. *Water Resour. Res.* 30:421–433. doi:10.1029/93WR02655
- Renshaw, C.E. 1995. On the relationship between mechanical and hydraulic apertures in rough-walled fractures. *J. Geophys. Res.* 100:24629–24636. doi:10.1029/95JB02159
- Reynolds, W.D., D.E. Elrick, E.G. Youngs, A. Amoozegar, H.W.G. Boutilink, and J. Bouma. 2002. Saturated and field-saturated water flow parameters. p. 797–877. *In* J.H. Dane and G.C. Topp (ed.) *Methods of soil analysis. Part 4. Physical methods.* SSSA Book Ser. 5. SSSA, Madison, WI.
- Seyfried, M.S., and P.S.C. Rao. 1987. Solute transport in undisturbed columns of an aggregated tropical soil: Preferential flow effects. *Soil Sci. Soc. Am. J.* 51:1434–1444. doi:10.2136/sssaj1987.03615995005100060008x
- Shapiro, A.M., and J.R. Nicholas. 1989. Assessing the validity of the channel model of fracture aperture under field conditions. *Water Resour. Res.* 25:817–828.
- Silliman, S.E., and E.S. Simpson. 1987. Laboratory evidence of the scale effect in dispersion of solutes in porous media. *Water Resour. Res.* 23:1667–1673. doi:10.1029/WR023i008p01667
- Singha, K., F. Day-Lewis, and J.W. Lane, Jr. 2007. Geoelectrical evidence of bicontinuum transport in groundwater. *Geophys. Res. Lett.* 34:L12401. doi:10.1029/2007GL030019
- Vanderborght, J., D. Mallants, M. Vanclooster, and J. Feyen. 1997. Parameter uncertainty in the mobile-immobile solute transport model. *J. Hydrol.* 190:75–101. doi:10.1016/S0022-1694(96)03064-8
- Vanderborght, J., and H. Vereecken. 2007. Review of dispersivities for transport modeling in soils. *Vadose Zone J.* 6:29–52. doi:10.2136/vzj2006.0096
- van Genuchten, M.Th., and P.J. Wierenga. 1976. Mass transfer studies in sorbing porous media: I. Analytical solutions. *Soil Sci. Soc. Am. J.* 40:473–480. doi:10.2136/sssaj1976.03615995004000040011x
- Varni, M., and J. Carrera. 1998. Simulation of groundwater age distributions. *Water Resour. Res.* 34:3271–3281. doi:10.1029/98WR02536
- Ward, A.L., R.G. Kachanoski, A.P. von Bertoldi, and D.E. Elrick. 1995. Field and undisturbed-column measurements for predicting transport in unsaturated layered soil. *Soil Sci. Soc. Am. J.* 59:52–59. doi:10.2136/sssaj1995.03615995005900010008x

Chris B. Graham\*  
Henry S. Lin\*



A unique long-term soil moisture data set was analyzed to identify controls and frequency of vertical and lateral preferential flow. Preferential flow was shown to occur during most precipitation events as a topographically dependent function of antecedent soil moisture conditions, precipitation characteristics, and storm timing factors.

C.B. Graham and H.S. Lin, Dep. of Crop and Soil Sciences, Pennsylvania State Univ., University Park, PA, 16802. \*Corresponding author (chris.b.graham@gmail.com, henrylin@psu.edu).

Vadose Zone J. 10:816–831  
doi:10.2136/vzj2010.0119  
Received 27 Sept. 2010.  
Posted online 29 July 2011.

© Soil Science Society of America  
5585 Guilford Rd., Madison, WI 53711 USA.  
All rights reserved. No part of this periodical may be reproduced or transmitted in any form or by any means, electronic or mechanical, including photocopying, recording, or any information storage and retrieval system, without permission in writing from the publisher.

# Controls and Frequency of Preferential Flow Occurrence: A 175-Event Analysis

Despite the widespread acceptance of hydrologic importance, controls on the initiation of preferential flow in natural soil profiles and the frequency of its occurrence at different times of year remain elusive. This study determined the controls and frequency of preferential flow occurrence in the Shale Hills Critical Zone Observatory. Soil moisture profiles and precipitation were monitored at 10 sites along a topographic gradient for >3 yr, encompassing 175 precipitation events. For each event and each site, the flow regime was classified as either preferential flow, sequential flow, or nondetectable flow based on the sequence of soil moisture response at various depths within the same site. Preferential flow here specifically refers to out-of-sequence soil moisture response, with a deeper horizon responding to precipitation earlier than a shallower horizon. Indices describing antecedent precipitation, precipitation characteristics, precipitation timing, and initial soil moisture were examined to determine the characteristics of events that resulted in preferential flow vs. those that resulted in sequential flow. Analyses showed that preferential flow was common throughout the catchment, occurring during 17 to 54% of the 175 events at each of the 10 monitored sites. Preferential flow occurred in at least one site during 90% of the 175 events. While the frequency of preferential flow appeared insensitive to topographic position, the controls on preferential flow initiation varied with landscape position. Analysis of subsets of the time series data showed that while the frequency of preferential flow can be determined from 1 yr of real-time monitoring, the controls on preferential flow require much longer ( $\geq 3$  yr) monitoring to be reliably identified.

Abbreviations: API, antecedent precipitation index; CPI, current precipitation index.

**Preferential flow of water** is ubiquitous from the soil core to the catchment scale, yet the controls on preferential flow initiation and the frequency of its occurrence under natural conditions remain poorly understood. We define *preferential flow* here as the flux of water via flow paths that bypass portions of the soil matrix. Whether due to macropores such as root channels (McDonnell, 1990; Noguchi et al., 2001), fractures (Kneale and White, 1984), or animal burrows (Shipitalo and Gibbs, 2000; Wang et al., 1996), or due to hydraulic conductivity discontinuities (Germann, 1990; Mosley, 1982), hydrophobicity (Bauters et al., 1998; Dekker and Ritsema, 1996), or other reasons, preferential flow can dramatically affect hydrologic processes. Preferential flow, at the pedon to the hillslope scales, has been shown to induce rapid vertical transport of nutrients and contaminants (Jarvis, 2007), increase peak storm-flow generation (Beven and Germann, 1982), and encourage landslide generation through increased pore pressure (Uchida et al., 2001), among many other impacts.

Despite the importance of preferential flow in hydrologic processes at all spatial and temporal scales (Lin, 2010), and an increased understanding of the pore-scale physics controlling preferential flow initiation (Jarvis, 2007), the dominant controls on the initiation and location of preferential flow remain unclear at the pedon to the hillslope scales. Critical questions remain to be answered regarding the effects of topographic position, storm timing, and storm dynamics on preferential flow initiation, including such basic questions as: What precipitation events result in preferential flow at the pedon scale? Where in the landscape does preferential flow occur? What are the dominant controls on preferential flow initiation in the forested hillslope?

Traditional methods of estimating the in situ spatial extent of preferential flow include dye tracer studies (Anderson et al., 2009; Weiler and Flühler, 2004), and soil trenching and excavations (Graham et al., 2010; Mosley, 1982). More recently, geophysical methods such as electrical resistivity tomography and ground penetrating radar have been used to quantify preferential flow without disturbance (Garre et al., 2010; Oberdorster et al., 2010). While

## Shale Hills Critical Zone Observatory

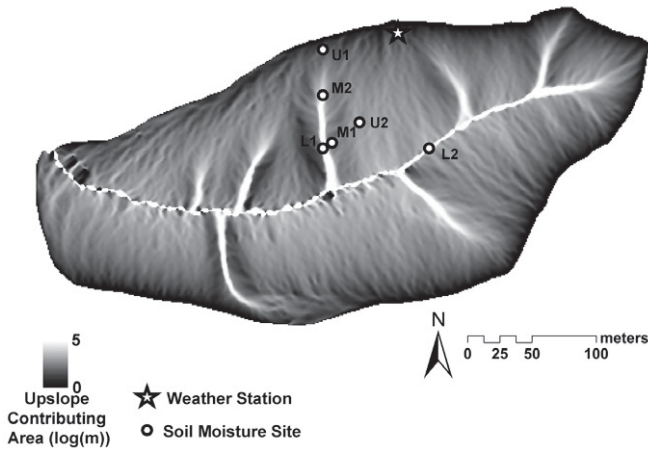


Fig. 1. Map of the Shale Hills Critical Zone Observatory and the location of soil moisture monitoring sites used in this study. The gray scale is the logarithm of the upslope contributing area based on LiDAR data.

these methods can be effective in demonstrating the spatial extent of preferential flow, they are much less effective in determining the temporal dynamics of preferential flow. Despite the recent increase in the deployment of soil moisture sensor networks (such as time domain reflectometry [TDR] or frequency domain reflectometry), limited work has been done to use in situ measurements of soil water content to identify the occurrence and controls on preferential flow. Ritsema and Dekker (1996) demonstrated preferential flow with a dense TDR network at a site where water repellency was known to encourage fingering but did not examine the temporal controls on preferential flow initiation. Kienzler and Naef (2008) used water velocity measurements made with TDR in conjunction with high-intensity irrigation, excavation, and tracer experiments to demonstrate preferential flow at a number of hillslopes in Switzerland. Taumer et al. (2006), using TDR measurements, were able to show that preferential flow due to water repellency peaked in late summer and autumn. This body of research, while clearly demonstrating the widespread prevalence of preferential flow, has done little to identify the controls on preferential flow initiation and its occurrence frequency in natural hillslopes, either temporally or spatially. To our knowledge, no one has attempted to simultaneously determine the temporal and spatial pattern of preferential flow and its underlying controls across the landscape in a forested catchment.

This study built on previous research in the Shale Hills Critical Zone Observatory by Lin and Zhou (2008), who analyzed the real-time soil moisture response to 15 precipitation events in seven distinct topographic positions. Operationally, they defined preferential flow as an increase in soil water content out of sequence with respect to soil depth. While sequential but rapid response to precipitation could be another characteristic of preferential flow, such behavior can also be due to differences in particle and pressure responses (Rasmussen et al., 2000; Torres and Alexander, 2002) or

simply high soil matrix permeability. Due to uncertainties in this kind of preferential flow, rapid, sequential soil moisture response to precipitation was not classified as preferential flow in this study.

From previous work at the Shale Hills, two types of preferential flow that affect different parts of the landscape have been identified. From the analysis of 15 precipitation events from September 2006 to January 2007, Lin and Zhou (2008) determined that preferential flow at the Shale Hills consisted of vertical flow via macropores, cracks, or other preferential flow paths under dry conditions, and lateral subsurface flow during larger precipitation events with wet soils in the valley and lower portion of swales. Our study extended the analysis of Lin and Zhou (2008) to >3 yr of real-time soil moisture response to a total of 175 distinct precipitation events. With this larger data set, we hoped to better reveal the dominant controls on preferential flow in this catchment and address the following three questions:

1. What is the frequency of preferential flow across this landscape?
2. How do the controls on preferential flow initiation vary with topographic position?
3. What are the characteristics of precipitation events that result in widespread preferential flow across the catchment?

## Site Description Shale Hills Catchment

This study was conducted in the Shale Hills Critical Zone Observatory in central Pennsylvania. The Shale Hills is a 7.9-ha, V-shaped catchment characteristic of the low-lying, shale-underlain hills of the Ridge and Valley physiographic province in the eastern United States. The catchment is drained by a first-order stream that runs mostly from September through June and after large rainstorms. The sideslopes of the stream are asymmetrical, with steeper slopes on the north-facing hillslope. The south-facing hillslope, where the soil moisture monitoring in this study was concentrated (Fig. 1), is bisected by three large swales, which seem to serve as the conduits of lateral subsurface flow from the hillslopes to the stream channel. Slopes on the south-facing hillslope are moderate, ranging from 4 to 42% (average 23%).

The vegetation cover on the south-facing slope is deciduous forest, with limited understory. The dominant species are oaks (*Quercus alba* L., *Q. rubra* L., *Q. montana* Willd., and *Q. velutina* Lam.), hickory [*Carya tomentosa* (Lam.) Nutt. and *C. glabra* (Mill.) Sweet], hemlock [*Tsuga canadensis* (L.) Carrière], and pine (*Pinus virginiana* Mill. and *P. strobes* L.).

## Soils

The soils were formed from shale residuum and colluvium. Five soil series were identified, characterized, and mapped from our previous studies (Lin, 2006; Lin and Zhou, 2008). The soils are generally silt loams and silty clay loams in texture, with some clay

Table 1. Site characteristics and soil moisture probe installation depth for each of the 10 monitoring sites. The specific locations and their relative topographic relationships are shown in Fig. 1 and 2.

Site label	Soil series	Landform	Depth to bedrock cm	Upslope contributing area m <sup>2</sup>	Distance from stream m	Local slope %	Depth of soil moisture probes and their horizon (in parentheses) cm
U1	Weikert	ridgetop	22	14	107	23.1	5 (Oe), 8 (A), 10 (A), 17 (C), 37 (R)
U2a	Weikert	planar hillslope	37	66	30	28.3	5 (Oe), 8 (A), 21 (Bw), 31 (CR), 39 (R)
U2b	Weikert	planar hillslope	37	66	30	28.3	5 (Oe), 8 (A), 15 (Bw), 28 (CR), 38 (R)
M1	Berks	sideslope of swale	>150	38	35	31.3	14 (Bw1), 41 (Bw2), 86 (Bw3), 90 (Bw3), 111 (C)
M2a	Berks	sideslope of swale	110	676	93	35.5	5 (Oe), 10 (A), 40 (Bw2), 88 (Bw3), 103 (C)
M2b	Rushtown	upper swale	150	676	93	35.5	5 (Oe), 10 (A), 40 (Bw2), 97 (BC), 112 (C)
M2c	Rushtown	upper swale	150	676	93	35.5	10 (A), 22 (Bw1), 44 (Bw2), 73 (Bw3), 123 (C)
L1a	Rushtown	lower swale	>300	1,122	34	10.7	8 (A), 18 (Bw), 39 (Bw3), 115 (C1), 156 (C2)
L1b	Rushtown	lower swale	>300	1,122	34	10.7	5 (Oe), 8 (A), 12 (Bw1), 15 (Bw1), 22 (Bw2), 40 (Bw3), 68 (BC), 92 (BC), 122 (C1), 162 (C2)
L2	Blairton	valley	>250	19,054	0	4.2	13 (A), 20 (BA), 35 (Bt1), 66 (Bt2), 86 (Bt2), 95 (CB1), 123 (CB2)

loams and sandy clay loams. Soil thickness, landscape position, and depth to redoximorphic features were the main criteria used to differentiate these soil series. The four soil series selected for this monitoring study are described in the following, with a general schematic of topographic position and soil horizonation shown in Table 1 and Fig. 2:

1. The Weikert series (loamy-skeletal, mixed, active, mesic Lithic Dystrudepts): This is the predominant soil type in the catchment, comprising 78% of the area, and is characterized as a thin soil on hilltops or on planar or convex hillslopes, with depth to fractured shale bedrock <0.5 m (mostly <0.3 m). The soil at the monitoring sites U1, U2a, and U2b investigated in this study were identified as the Weikert soil series.
2. The Rushtown series (loamy-skeletal over fragmental, mixed, active, mesic Typic Dystrachrepts): This soil series is mostly located in the center of the four dominant swales in the downstream two-thirds of the catchment and the majority of the upper 100 m of the south-facing portion of the catchment. These soils are generally >1-m depth to bedrock (often >2–3 m). The soils at our monitoring sites L1a, L1b, M2b, and M2c were identified as the Rushtown soil series.
3. The Berks series (loamy-skeletal, mixed, active, mesic Typic Dystrudepts): This soil series is largely distributed along the slope transitional zones between the shallow Weikert and the deep Rushtown soils, with 0.5- to 1-m depth to bedrock. The soils at the monitoring sites M1 and M2a were identified as the Berks soil series.
4. The Blairton series (fine-loamy, mixed, active, mesic Aquic Hapludults): This soil series is located in the valley bottom and is deep (>2–3-m depth to bedrock), with an argillic horizon at the 0.2- to 0.8-m depth and few (2–5%) redox features starting at the 0.8- to 1.1-m depth. Monitoring site L2 included in this study was identified as the Blairton soil.

Because the entire catchment is overlain by forest cover, nearly all soils have an approximately 0.05-m-thick organic layer (Oe horizon) comprised of decaying leaf litter and other organic materials. The entire catchment is underlain by >200-m-thick Rose Hill shale, a Silurian formation frequently associated with the Fe-rich Clinton ore. Many channery shale fragments (2–150 mm) were found throughout the

soil profiles, and the near-surface shale was characterized by fractured bedrock. Additional information about the soils and the Shale Hills catchment can be found in Lin (2006) and Lin and Zhou (2008).

## Climate

The climate of the study area is typical of the inland northeastern United States, with cold, wet winters and hot, humid summers. Temperatures range from >30°C in the summer to less than –10°C during the winter, with a mean annual temperature of 10°C. Precipitation is distributed relatively uniformly throughout the year, characterized by short, high-intensity rainfall except during the winter months, when snow predominates. Measured annual precipitation based on locally installed rain gauges at various moni-

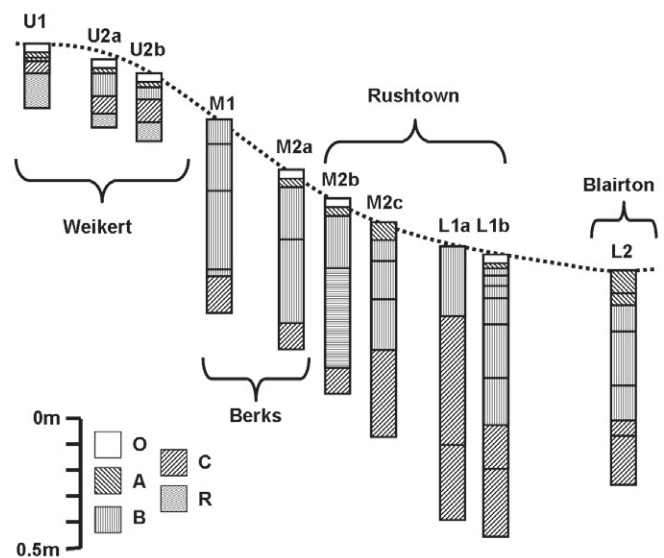


Fig. 2. Schematic of soil moisture sensor installation depths and their relative topographic positions in the Shale Hills landscape. Horizontal lines indicate soil moisture sensor positions, while box fill patterns indicate different soil horizons within the same soil profile. Soil series names are indicated for each site.

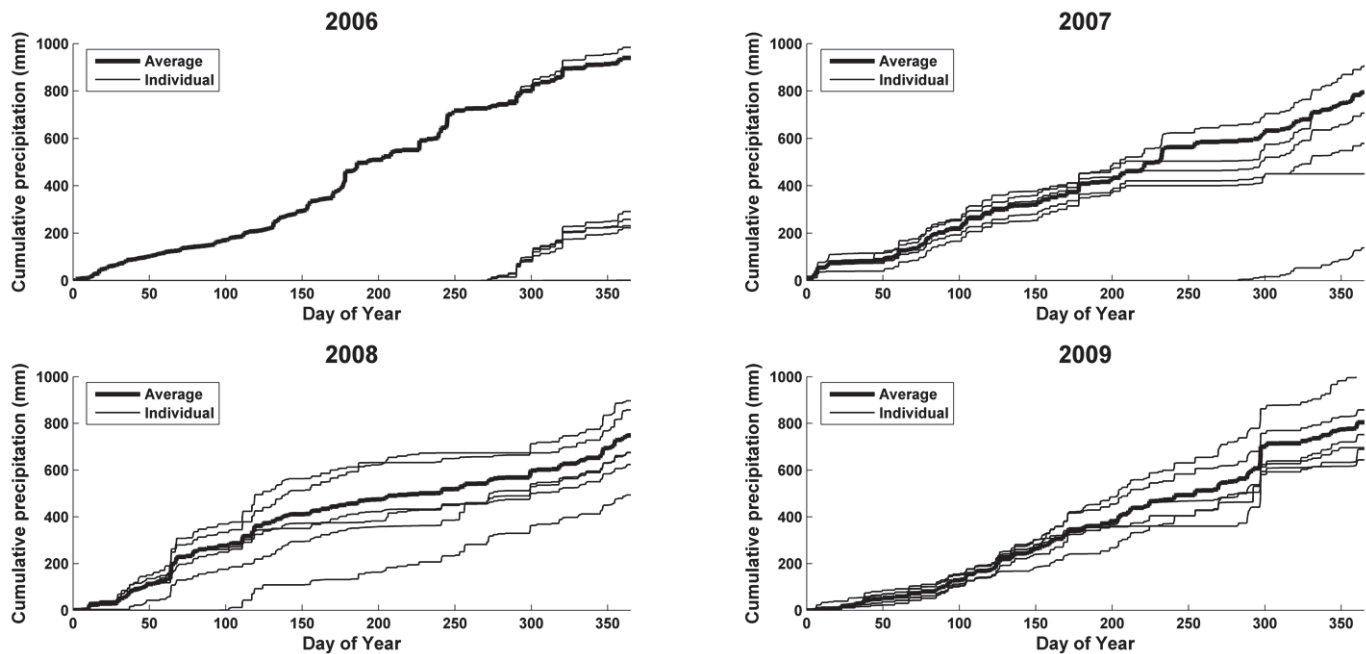


Fig. 3. Cumulative precipitation for six precipitation gauges (fine curves) and their overall averages (bold curves). Individual gauges did not consistently over- or underpredict the average value.

toring sites averaged 823 mm from 2006 through 2009, with a range of 749 to 940 mm (Fig. 3).

## Materials and Methods

### Soil Moisture and Precipitation Monitoring

Soil moisture has been monitored in real time since September 2006 at six sites, with four to 10 depths at each site (depending on soil thickness and horizonation). These sites were located from the ridgetop to the valley bottom, sampling both planar or convex hillslopes and concave swales (Fig. 1). At each site, a pit was excavated from the soil surface to either the soil–bedrock interface or as deep as was safe. In the excavated pit, soil moisture probes were installed on the upslope face, plus additional side faces in selected sites. Probes were installed based on soil horizons and their interfaces, so were irregularly located vertically, with the vertical distance between probes ranging from 3 to 40 cm. The shallowest probe at each site ranged from 5 to 15 cm, while the deepest ranged from 37 to 162 cm, depending on the soil type (Table 2; Fig. 2). At three of these sites, two or three vertical sets of probes were installed 0.5 to 1 m apart, leading to a total of 10 vertical soil profiles monitored. At Site M2, a vertical profile was instrumented on the left, right, and center of the excavated pit (labeled as M2a, M2b, and M2c, respectively). At Site L1, vertical profiles were installed on the left and right (labeled as L1a and L1b), while at Site U2, probes were installed at an upslope and a nearby downslope site (labeled as U2a and U2b). At Sites U1, M1, and L2, only one vertical profile was instrumented. Further details on the soil moisture probe installations can be found in Lin and Zhou (2008).

Soil moisture was monitored with two models of capacitance-type probes (Decagon Devices, Pullman WA). At Site L2, which was instrumented the earliest, soil moisture was monitored with EC10 probes available at the time of installation (accuracy  $\pm 4\%$ , precision  $\pm 0.2\%$ ), while at the remaining sites soil moisture was measured with EC5 probes (accuracy  $\pm 3\%$ , precision  $\pm 0.1\%$ ). The EC5 probes were chosen for the second phase rather than the EC10 due to their enhanced accuracy and precision, although with a smaller measurement volume ( $62 \text{ cm}^3$  for EC5 vs.  $125 \text{ cm}^3$  for EC10). The soil moisture data reported here were all collected at 10-min intervals.

Precipitation was measured at six rain gauges in the catchment, installed during three periods between 2005 and 2008. Five of these rain gauges were collocated with the soil moisture monitoring sites, while the sixth was located in a clearing on the north ridge of the catchment. The gauge at the north ridge is a Pluvio load cell rain gauge (OTT Hydrometry, Kempton, Germany; precision 0.01 mm), while the five collocated gauges are TE525-WS tipping bucket rain gauges (Texas Electronics, Dallas, TX; precision 0.025 mm). Annual precipitation for the six gauges ranged from 571 to 908 (2007), 624 to 897 mm (2008), and 669 to 1026 mm (2009) (Fig. 3). Differences in annual precipitation are attributed to differences in vegetation interception and topographic effects, as well as occasional clogging of the rain gauges by fallen leaf litter, as noted in routine site visits.

Because rain gauges were not collocated with all of the soil moisture monitoring sites, and due to occasional clogging, we did not attempt to use site-specific precipitation data in this study. Our analysis of the hyetographs did not show evidence of topographic or site-specific patterns in the precipitation data. No sites were consistently

Table 2. Number of events leading to each of the three flow categories (preferential flow, sequential flow, and nondetectable response) at each site during the >3-yr monitoring period (upper part) and for different numbers of sites in the catchment that displayed preferential flow (lower part). Results are shown for each of the 10 monitoring sites that are arranged from ridgetop to valley floor (from left to right).

Flow type	Number of events resulting in each flow scenario									
	U1	U2a	U2b	M1	M2a	M2b	M2c	L1a	L1b	L2
Preferential flow	93	53	74	31	91	63	36	41	95	60
Sequential flow	38	107	71	57	35	61	93	81	32	75
Nondetectable	29	15	30	87	48	50	45	48	43	40
	≥1 site	≥2 sites	≥3 sites	≥4 sites	≥5 sites	≥6 sites	≥7 sites	≥8 sites		
Preferential flow	157	144	121	87	66	39	18	7		
Sequential flow	171	146	117	83	65	36	23	4		
Nondetectable	119	92	66	50	38	27	20	14		

greater or less than the average, with the exception of the Pluvio gauge located in the clearing, which showed greater precipitation than the average throughout the monitoring. To account for the differences in measured precipitation rates, as well as the staggered installation of the gauges, the rainfall amounts from the functioning and installed gauges at each time step were averaged to provide the catchment-wide rainfall rate used for the analysis in this study.

### Precipitation Event Delineation and Soil Moisture Response to Precipitation

Rather than using a hydrometric response to determine precipitation event duration and timing (Tromp-van Meerveld and McDonnell, 2006), events were delineated in this study solely using the precipitation record itself (Bonta, 2003). Individual events were defined as beginning when >1 mm of precipitation fell after >24 h of no precipitation. Once an event began, it was considered to continue until the total precipitation in any given 24 h was <1 mm. The precipitation threshold (1 mm) and minimum inter-event period (24 h), while somewhat arbitrary, were chosen to maximize the information that could be extracted from the soil moisture response to diverse events. Very small precipitation events (<1 mm) were unlikely to result in subsurface flow in this forested catchment, so events of lesser precipitation were not delineated in this study. The other goal of the precipitation event delineation in this study was to create the maximum number of significant events without artificially separating longer events. Due to the nature of precipitation at the site (shorter, high-intensity storms separated by longer periods without rain), the traditional inter-event interval of 6 h (Huff, 1967) was determined to be too short, and a minimum inter-event duration of 24 h was therefore chosen. In our preliminary analyses, using an inter-event duration >24 h led to some very long events (>20 d), running counter to the observed patterns of precipitation at the site. Because we included many small precipitation events, down to 1-mm events spread across 24 h, we use the term *event*, rather than *storm*, that has a connotation of large amounts of high-intensity rainfall.

During the >3-yr (1400-d or 3.8-yr) monitoring period, 207 distinct events were delineated from the precipitation record, of which 197 occurred during the soil moisture monitoring period. The events

that occurred before soil moisture monitoring were used to better characterize the precipitation but were not used to identify instances of preferential flow. Due to uncertainties in the timing of snowmelt and errors in soil moisture measurements under frozen soil conditions, 18 events were removed from the analysis because the average air temperature for the events was <1°C. There was probably some augmentation of precipitation with snowmelt during rain-on-snow events occurring just above the 1°C threshold. Anecdotally, however, rain-on-snow events are uncommon at the Shale Hills and thus make up a small fraction of the overall precipitation events analyzed in this study.

In late October 2009, a large, early snowstorm resulted in extensive litterfall and subsequent widespread clogging of rain gauges. After the snowstorm, the gauges were unclogged and the stored precipitation was allowed to flow through the tipping buckets. This resulted in an apparent large, very high intensity precipitation event. While this water volume was retained to complete the annual water balance of the catchment, this special event and the three events afterward were removed from our analysis to avoid impacting analyses dependent on antecedent precipitation indices. This resulted in a total of 175 events used for the final analysis reported here.

Once the events were delineated, the soil moisture response to precipitation was examined. A significant response to precipitation was defined as an increase in soil moisture content >1% (v/v). The precision of the two models of soil moisture probes used was 0.1 to 0.2%; however, diel fluctuations in soil moisture due to hydraulic redistribution from vegetation and capillary action of up to 0.6% (v/v) water content were observed in our soil moisture time series data analysis. A minimum soil moisture response of 1% (v/v) was therefore chosen for this study because this value maximized the number of identified soil moisture responses to precipitation while removing false positive soil moisture responses (i.e., the observed diel signals).

Both event delineation and soil moisture response were determined with an automated program written in MATLAB software (The MathWorks, Natick, MA). Before further analysis, isolated events were delineated by hand, and event characteristics and soil

moisture responses were computed independently to confirm the function of the automated program.

## Identifying Preferential Flow Response

Preferential flow has been traditionally characterized in two ways: (i) rapid fluxes through the soil profile, characterized by a sequential response with depth at a velocity greater than saturated soil hydraulic conductivity (Beven and Germann, 1982; Flühler et al., 1996), and (ii) an out-of-sequence response to precipitation, where deeper horizons respond before shallower horizons (Lin and Zhou, 2008). In this study, we focused on the second expression of preferential flow.

An automated program was written in MATLAB to analyze the 10-min-interval time series of soil moisture data at each site and each horizon and to determine the sequence of horizon response during each delineated precipitation event. For each event, the time series of volumetric soil moisture ( $\theta$ ) at each probe location was examined, and if soil moisture increased above the threshold of 1%  $\theta$ , the time of the initial rise was recorded. Once the soil moisture response (or lack thereof) to precipitation was identified, the soil moisture response throughout the profile was then classified into the following three flow categories:

1. The first category included events where probes in soil horizons responded in sequence, with the surface probe responding first, then the next deeper probe, and so on through all of the responding probes. This category includes events where between one and all probes in a soil profile responded, as long as the surface horizon responded first and the subsequent probes then responded in sequence. This category is classified as sequential flow and is thought to consist mainly of matrix flux (as that would be expected in a uniform vertical flow). Note that a rapid, sequential soil moisture response to precipitation may suggest another type of preferential flow due to wave propagation or high permeability, but this scenario was not separated out in this study (hence, the frequency of preferential flow has probably been underestimated in this study). Because we acknowledge that some preferential flow events may fall into this category, we refer to these events as causing “sequential” flow, rather than “matrix” flow, or “uniform” flow.
2. The second category included events where the probes did not respond to precipitation sequentially. This could include events where at least one deeper probe responded to precipitation before a shallower probe, or where shallow and deep probes responded sequentially but a probe intermediate between the two did not respond. This category is classified as preferential flow because the flow response is not characterized by a sequential response with soil depth. This response could be due to either flow bypassing a certain portion of the soil profile or subsurface lateral flow from the surrounding area.
3. The final category included events where no horizons responded to precipitation. This was classified as nondetectable flow and is thought to have occurred when either the precipitation amount was insufficient to infiltrate to the uppermost horizon or was removed by evaporation before percolation could reach the upper sensor location. Another scenario could be a flow that bypassed all of the soil moisture sensors. This could be another possibility in which the frequency of preferential flow reported in this study has probably been underestimated.

Our operational definition of preferential flow (nonsequential soil moisture response to precipitation with soil depth) allows for two types of preferential flow: vertical bypass and lateral subsurface flow. In the case of vertical bypass flow, water bypasses surface horizons via cracks and other types of macropores, causing subsurface horizons to respond out of sequence. In this case, water moves through a relatively small volume of soil (e.g., macropores) that is not monitored by a soil moisture sensor and then fills the storage in a lower horizon where the increase in soil moisture is captured by a sensor. In the case of lateral subsurface flow, water is transmitted rapidly from upslope areas after a precipitation event via macropores, horizon boundaries, or the soil–bedrock interface such that water moves more quickly downslope than vertically. As these two preferential flow types cannot be distinguished based on the operational definition of preferential flow used in this study, further analyses are required to assess the relative frequencies of each.

As noted above, these analyses may miss some forms of preferential flow, therefore the reported absolute frequency of preferential flow should be thought of as lower bounds. Similarly, the controls on preferential flow determined in this study should be thought of as controls on the observed preferential flow reported here.

To demonstrate the method used for classifying unsaturated flow regimes, the soil moisture response to an event starting on 11 Sept. 2007 is presented in Fig. 4. After 19.85 d of no precipitation, this event consisted of 16.9 mm of rain falling in two bursts. In the first burst, 12.9 mm fell within 3 h, followed by another 4 mm after a dry spell of 3 h. At Site U1, the initial response occurred at 37 cm (C horizon), with a rapid increase in soil moisture 10 min after the first rainfall was observed at the rain gauge. Shortly afterward, the 5-cm probe responded with a spike in soil moisture, followed by soil moisture increases at the 8-, 10-, and 17-cm depths (Fig. 4). This out-of-sequence response (i.e., the probe at 37 cm responded 40 min before any of the other probes) indicates that this was a preferential flow scenario. This particular precipitation event also resulted in preferential flow at five other sites (L1b, L2, M2a, M2c, and U2b), nondetectable flow at one site (M2b), and sequential flow at the other three sites (U2a, M1, and L1b) (Fig. 4). There was no topographic separation of the preferential vs. sequential flow sites for this particular event, with preferential flow occurring at all topographic positions (i.e., ridgetop, midslope, swale, and valley). Sequential flow also occurred at all topographic positions.

## Precipitation Indices and Soil Moisture Indices

For each precipitation event, a number of precipitation indices and soil moisture characteristics were derived from the soil and precipitation time series data (see below) to determine the controls on preferential flow initiation. These indices were then sorted according to flow categories (preferential, sequential, or nondetectable) and the means were statistically compared. When the mean of an index was significantly different for the

set of events that resulted in preferential flow vs. the events that resulted in sequential flow, it was considered to be a significant control on preferential flow.

## Precipitation Indices

For this study, 33 indices were derived from the precipitation time series. These indices can be classified into three groups, with some overlap between these groups: (i) antecedent precipitation, (ii) precipitation event characteristics, and (iii) timing of precipitation.

Indices describing the precipitation record before the precipitation event include the antecedent precipitation index (API) and the current precipitation index (CPI). The API used in this study is simply the sum of precipitation in a given number of days before the initiation of the event (using a recession constant of 1 for the formula of Linsley et al., 1949). For these analyses, we calculated the 1-, 2-, 3-, 4-, 5-, 6-, 7-, and 14-d APIs (referred to as API1, API2, API3, API4, API5, API6, API7, and API14, respectively).

The CPI (Smakhtin and Masse, 2000) is calculated as

$$CPI(t) = aCPI(t-1) + P(t) \quad [1]$$

where  $a$  is a recession coefficient controlling the memory of the CPI function,  $t$  is the time step (precipitation data were collected in 10-min intervals), and  $P(t)$  is the precipitation at time step  $t$ . The initial value,  $CPI(0)$ , is defined as the mean precipitation intensity for the duration of the time series, and all subsequent values [ $CPI(1) - CPI(N)$ ] are built off of this value. For these analyses, values of  $a$  were 0.9 (CPI9), 0.99 (CPI99), and 0.999 (CPI999). These values of  $a$  are higher than those usually used in the hydrologic literature, where the CPI function is traditionally applied to daily precipitation. In this study, it was applied to 10-min precipitation data, warranting higher recession coefficients to maintain a similar memory effect.

Event characteristics included total event precipitation, event duration, maximum precipitation intensity, average precipitation intensity, and average precipitation intensity from the start of the event until the time of maximum intensity. Statistical analyses of the event included the variance, skew, and kurtosis of the precipitation intensity distribution for each event. Indices that characterize the internal temporal distribution of rainfall within the event included the time and total precipitation until maximum precipitation intensity, the length of time from the start of the event to 5, 10, and 20 mm of total rainfall, and internal event CPI. Internal event CPIs (EventCPI) were determined using Eq. [1], except that the initial EventCPI value was reset for each event [EventCPI(1) = 0 at the start of each individual event]. Thus, the EventCPI is a measure of the cumulative precipitation during the event and served to index the buildup and recession of precipitation inside the event. The maximum EventCPI and the time from the start of the event to the maximum EventCPI were

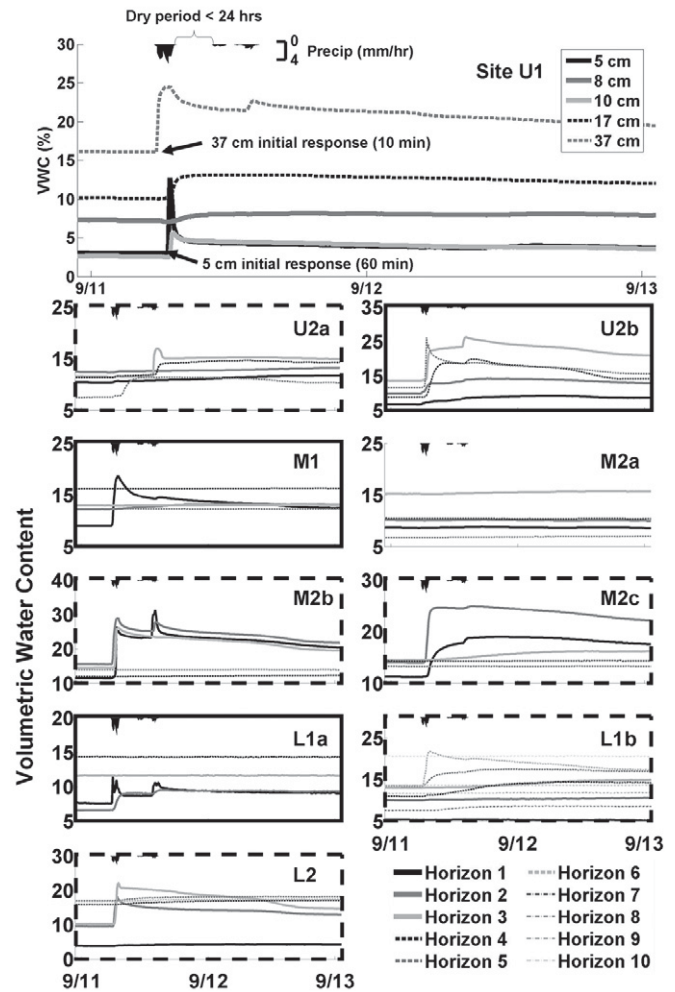


Fig. 4. Examples of soil moisture response to precipitation events that occurred during 11 to 13 Sept. 2007 at various depths in each of the 10 monitoring sites. Sites are organized from top to bottom with the ridgetop and hillslope sites (U1, U2a, and U2b) above the midslope sites (M1, M2a, M2b, and M2c) and above the lower swale and valley sites (L1a, L1b, and L2). Sites with identified preferential flow are indicated by a dashed box around the data plots, sequential flow is indicated by a solid box, and nondetectable flow is identified by no box. The response at Site U1 is highlighted at the top to demonstrate the details of preferential flow that showed out-of-sequence soil moisture response to precipitation events, where the 37-cm probe responded before the remaining probes. Horizons 1 to 10 are numbered sequentially from the soil surface downward to the deepest depth where a soil probe was installed.

determined for each event. Again,  $a$  values of 0.9 (EventCPI9), 0.99 (EventCPI99), and 0.999 (EventCPI999) were used.

Precipitation timing indices include the day of the year of event initiation and the average air temperature for the event duration, which was used as a proxy for potential evapotranspiration. The time between events (which could also be considered as an antecedent condition index) was also considered.

## Initial Soil Moisture Indices

An additional eight to 14 indices describing the initial soil moisture conditions were derived for each site. For each probe, the average volumetric soil water content for 3 h before the start of a precipitation event was determined. Soil moisture was monitored at four to 10 depths at each site (depending on soil depth and horizons), leading to four to 10 initial values for each event. In addition, the profile average and depth-weighted average initial soil moisture contents were also determined for each event at each site. The profile average is the average of the soil moisture readings at the start of precipitation (from the same 3-h window) for all horizons within each site. The depth-weighted average used the same values but weighted for the depth range that each soil moisture sensor represented. For the analysis of controls on widespread preferential flow, the catchment-wide average initial surface and deep soil moisture contents were also recorded for each site. These values were determined by simply averaging the surface and the deepest soil moisture measurements at each of the monitoring sites from the start of the precipitation events. Analyses were repeated using relative saturation (water content divided by the maximum observed at the site and depth) for the profile averages and depth-weighted averages; however, identical patterns of soil moisture control on preferential flow were observed, so they are not presented here.

## Determining the Impacts of Precipitation and Soil Moisture Indices on Flow Type

To determine whether the above-mentioned indices of antecedent precipitation, event characteristics, timing of event initiation, and initial soil moisture controlled the flow type (preferential vs. sequential flow), *t*-tests were performed on the indices for events that led to preferential flow vs. those that led to sequential flow. These analyses were performed to determine the influence of soil moisture and precipitation characteristics on the flow response at individual sites as well as across the catchment.

To identify the controls on preferential flow at each site, the precipitation and soil moisture indices for events that either did or did not result in preferential flow were grouped into two sets, and a *t*-test was performed to determine if the mean values of each index were significantly different. If the mean values were significantly different, that index was determined to be a control on preferential flow. Similarly, precipitation events that resulted in preferential flow at a given number of sites (from one to seven) were grouped, and the indices for preferential flow vs. sequential flow were compared. This grouping allowed the determination of precipitation event and soil moisture characteristics that led to widespread or localized preferential flow occurrence throughout the catchment. All *t*-tests were performed in MATLAB using a 95% confidence level.

To further determine the impact of the length of time series data on the results of our analyses, the analyses were repeated for various subsets of the total 175 events. For time series with <24 events,

there were not enough instances of preferential vs. sequential flow at the monitoring sites for adequate analysis (more than two events of each flow type at each site were needed for the statistical analysis). For time series with 24 or more events, the number of preferential and sequential events was tabulated, and the controls on preferential flow initiation were determined using the methods described above but using only the precipitation events in the chosen time series window. The event subsets were chosen as starting from the beginning of our monitoring through a chosen number of events (which represented different time periods).

## Results and Discussion What is the Frequency and Extent of Preferential Flow?

At each of the 10 monitored sites, the frequency of each flow type (preferential flow, sequential flow, or nondetectable flow) varied from event to event and from site to site. Of the 175 analyzed events, between 88 and 160 events at each site were identified as either preferential or sequential flow (Fig. 5A; Table 2). During the remaining 15 to 87 events, no soil moisture increase >1% from the initial conditions was observed. The overall frequency of preferential flow produced from the 88 to 160 events ranged from 18% (Site M1, at the sideslope of a swale) to 54% (Site L1b, at the right side of a lower swale). At three sites (U1, L1b, and M2a) preferential flow occurred in >50% of the 175 events. There was little evidence for topographic control on the absolute or relative frequency of preferential flow occurrence (Fig. 5). The correlation was low between preferential flow frequency and upslope contributing area ( $R^2 < 0.01$ ), soil depth ( $R^2 = 0.11$ ), and distance from the stream ( $R^2 = 0.01$ ). While the frequency of preferential flow at each site varied from year to year (Fig. 5), when looking at a continuous frequency distribution, the frequency of preferential flow was consistent throughout the 3-yr monitoring period (Fig. 6).

Preferential flow occurred at one or more sites during 157 events (90% of all 175 events analyzed). Widespread preferential flow across the catchment was less common, with 87, 66, and 39 events (50, 38, and 22% of all analyzed events) causing preferential flow at four, five, and six or more sites, respectively (Table 2). Sequential flow was observed at approximately the same frequency, occurring at one or more sites during 171 events (98% of the total events), and 83, 65, and 36 events (47, 37, and 21%) at four, five, and six or more sites, respectively. Widespread nondetectable flow was observed less frequently, occurring at more than one site during 119 events and observed during 50, 38, and 27 events (29, 15, and 11%) at four, five, and six or more sites, respectively. In short, preferential flow at the Shale Hills was often widespread and occurred frequently at least somewhere in the catchment. While preferential flow has been speculated as being nearly ubiquitous (Uhlenbrook, 2006; Jarvis, 2007; Lin, 2010), this study provides the actual quantification of preferential flow occurrence frequency across the catchment. As noted above, there are other types of preferential flow that were not considered in this study, and only 10 sites out of the 7.9-ha catchment were monitored. Therefore we suspect that

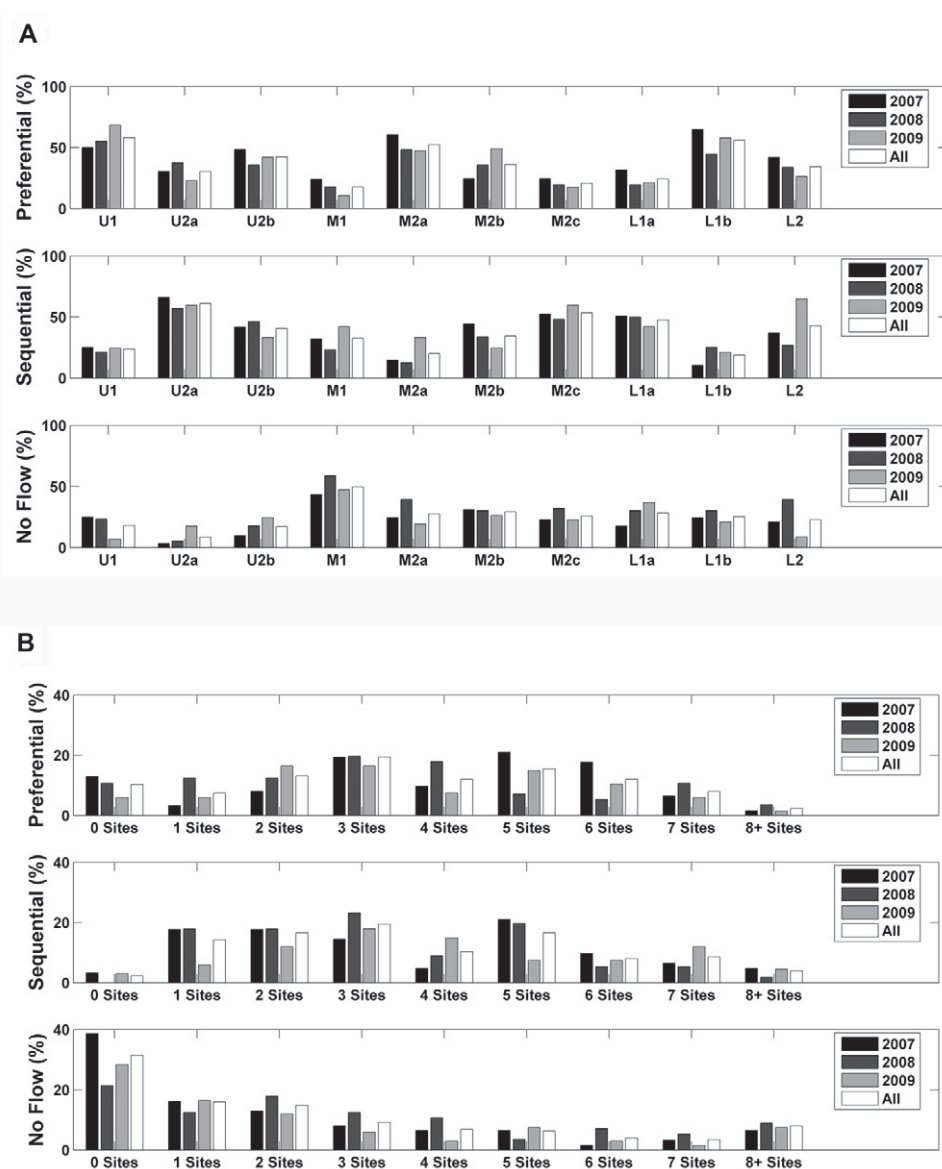


Fig. 5. Frequency of occurrence of three flow regimes (preferential flow, sequential flow, and nondetectable response) as a percentage of the total 175 events in each of the 3 yr and their overall average throughout the 3-yr monitoring period (A) at each site and (B) for different numbers of sites that displayed preferential flow.

the frequency and extent of all kinds of preferential flow occurrence throughout the entire catchment is higher.

### What Are the Characteristics of Events That Result in Preferential Flow at a Given Site?

On a site-by-site basis, indices for events that produced preferential vs. sequential flows were placed in two separate bins. When a *t*-test indicated a >95% chance that the mean values of these two data sets were different, the index was considered to be a significant factor influencing the initiation of preferential flow at a site (Table 3). Due to possible false positives at the 5% confidence interval, only general patterns were considered significant rather than each individual index.

While the indices that controlled preferential and sequential flows were different for each site, some general trends emerged. Some

indices appeared to control the preferential flow response across topographic positions. Initial soil moisture in the upper four horizons was a significant control on preferential flow occurrence at five to seven sites (Table 3), with the initial soil moisture being greater for preferential flow events at Sites L2, L1a, and L1b (sites in the valley or lower swale) but lower for Sites M2b, M2a, U2a, U2b, and U1 (sites higher in the hillslope or with shallow soils). The timing of the events was also significant: the day of the year was significantly later for preferential flow occurrence at three sites (L1a, U2a, and U2b), while the air temperature was significant at six sites, with preferential flow occurring at Sites L2, M2b, M2a, and M2c when the temperature was lower and at Sites U2a and U1 when the temperature was higher. Four of the event characteristic indices were deemed significant at four or more sites: skew (lower at the valley and midslope sites but higher at the ridge and

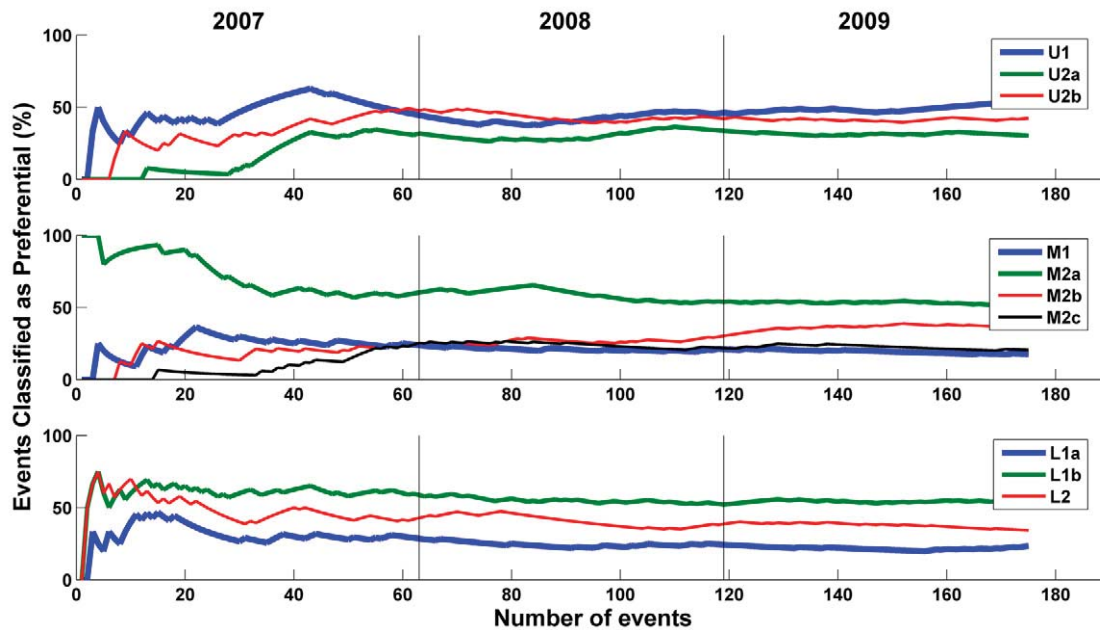


Fig. 6. Percentage of events identified as causing preferential flow vs. the total number of events considered in each of the 10 monitoring sites. Sites are organized from top to bottom with the ridgetop and hillslope sites (U1, U2a, and U2b) above the midslope sites (M1, M2a, M2b, and M2c) and above the lower swale and valley sites (L1a, L1b, and L2). Vertical lines separate the events occurring in 2007, 2008, and 2009.

hillslope sites), kurtosis (lower at the valley and midslope sites but higher at the ridge and hillslope sites), precipitation amount and average intensity from the start of the event until the time of maximum intensity (a greater value favors preferential flow occurrence). Interestingly, while the precipitation amount and average intensity from the start of the event until the time of maximum intensity was significant at four sites, neither the timing nor the magnitude of maximum precipitation intensity were significant at more than two sites. Of the antecedent precipitation indices (API or CPI), only API1 and CPI99 were significant controls at more than three sites (Table 3). Three of the antecedent precipitation indices were not significant at any site (API5, API6, and API14).

Topographic patterns in the significant indices appeared when the monitoring sites were grouped into three types (Fig. 2): ridgetop and planar hillslopes (Sites U1, U2a, and U2b), midslope (Sites M1 and M2b, M2a, and M2c), and valley or lower swale (Sites L2, L1a, and L1b).

The ridgetop and planar hillslope sites were especially sensitive to the initial soil moisture condition (dry soils), air temperature (hot temperatures), and the day of the year (late in the year). With the exception of skew, where preferential flow was more likely with highly skewed precipitation distributions (indicating time steps with high-intensity precipitation), the ridgetop and planar hillslope sites were insensitive to most of the indices describing internal precipitation dynamics (maximum precipitation intensity, EventCPI, total precipitation, and others) (Table 3). Similar to the observed influence of dry soils and hot temperatures on preferential initiation at the Shale Hills, many researchers have found correlations between dry soils and preferential flow due to either soil cracking

in desiccated soils or hydrophobicity (Taumer et al., 2006); both phenomena were observed in the catchment monitored.

At the valley and lower swale sites, when preferential flow occurred, the precipitation amount and average intensity from the start of the event to the maximum intensity were greater, the times from the start of an event until 10-mm of precipitation were significantly higher, and the total precipitation was higher. The maximum event CPI was significantly greater at two of the three valley and lower swale sites. Preferential flow was more likely to occur when soils were initially wet at the valley and lower swale sites, which is the opposite to that at the ridgetop and planar hillslope sites (where preferential flow was more likely to occur when the soils were dry). Preferential flow at the valley and lower swale sites is thought to consist, to a greater extent, of lateral subsurface flow coming from adjacent hillslopes (Lin, 2006). This type of preferential flow would require sufficient precipitation to initiate lateral flow, as expressed in the significance of total precipitation. This coincides with the in-depth storm analyses of Lin and Zhou (2008), who came to similar conclusions while analyzing the shape and timing of the soil moisture response at these sites for a smaller subset of storms.

At the midslope sites (M1, M2a, M2b, and M2c), the dominant controls on preferential flow occurrence were the initial soil moisture and the internal dynamics of the precipitation events. As with the valley and lower swale sites, the soil moisture was significantly higher for preferential flow events at two of the midslope sites (M2b and M2a). Events that led to preferential flow at the midslope sites had lower skew and kurtosis and a greater time to peak EventCPI. This describes an event with relatively even precipitation that continues a long time before the peak precipitation

Table 3. Comparison of 45 indices of precipitation and initial soil moisture for events that produced preferential flow vs. those that produced sequential flow. Presented are *P* values from *t*-tests. Bold type indicates the indices with a significant difference between preferential flow and sequential flow events (95% confidence interval). Results are shown for each of the 10 monitoring sites that are arranged from ridgetop to valley floor (from left to right).

Index†	Index <i>P</i> value for preferential vs. sequential events at each site									
	U1	U2a	U2b	M1	M2a	M2b	M2c	L1a	L1b	L2
Total ppt.	0.81	0.19	0.31	0.77	<b>0.00</b>	0.16	0.91	<b>0.02</b>	0.06	<b>0.01</b>
Ppt. duration	0.29	<b>0.03</b>	0.92	0.21	<b>0.01</b>	<b>0.01</b>	0.21	0.26	0.37	0.65
Avg. ppt. intensity	0.63	0.80	0.37	0.56	<b>0.04</b>	0.42	0.53	<b>0.03</b>	0.22	0.21
Max. ppt. intensity	0.09	0.17	0.52	0.22	0.96	<b>0.04</b>	<b>0.01</b>	0.70	0.44	0.74
Time to max. ppt. density	0.25	0.19	0.99	<b>0.02</b>	0.06	<b>0.03</b>	0.17	0.34	<b>0.05</b>	0.34
Ppt. amount to max. intensity	0.59	0.46	0.40	0.39	<b>0.01</b>	0.36	0.54	<b>0.01</b>	<b>0.01</b>	<b>0.01</b>
Avg. intensity to max. intensity	0.57	0.45	0.40	0.38	<b>0.01</b>	0.37	0.54	<b>0.01</b>	<b>0.01</b>	<b>0.01</b>
Variance	0.17	0.53	0.42	0.16	0.25	0.46	0.07	0.62	0.53	0.08
Skew	<b>0.02</b>	<b>0.00</b>	0.78	0.38	<b>0.00</b>	<b>0.00</b>	<b>0.01</b>	0.35	0.82	<b>0.02</b>
Kurtosis	0.06	<b>0.01</b>	0.55	0.38	<b>0.01</b>	<b>0.00</b>	<b>0.01</b>	0.38	0.96	<b>0.02</b>
Time to 5 mm of ppt.	0.48	0.50	<b>0.00</b>	0.39	<b>0.03</b>	0.46	<b>0.05</b>	0.09	0.50	0.40
Time to 10 mm of ppt.	0.61	0.22	0.73	0.17	<b>0.04</b>	0.19	0.11	<b>0.00</b>	<b>0.02</b>	<b>0.05</b>
Time to 20 mm of ppt.	0.06	0.10	0.93	0.06	0.31	<b>0.00</b>	0.13	0.39	0.93	0.50
Max. EventCPI9	0.14	0.32	0.13	0.30	0.08	0.41	<b>0.02</b>	0.15	0.12	<b>0.05</b>
Max. EventCPI99	0.67	0.61	0.16	0.60	<b>0.00</b>	0.34	0.48	<b>0.03</b>	0.09	<b>0.00</b>
Max. EventCPI999	0.93	0.26	0.27	0.83	<b>0.00</b>	0.18	0.86	<b>0.02</b>	0.06	<b>0.01</b>
Time to max. EventCPI9	0.77	0.20	0.59	<b>0.01</b>	0.07	<b>0.01</b>	0.10	0.55	0.08	0.18
Time to max. EventCPI99	0.41	0.15	0.64	<b>0.01</b>	<b>0.04</b>	<b>0.01</b>	0.08	0.57	0.10	0.30
Time to max. EventCPI999	0.26	<b>0.02</b>	0.68	0.10	<b>0.02</b>	<b>0.01</b>	0.11	0.43	0.34	0.94
API1	<b>0.02</b>	0.61	0.38	<b>0.01</b>	0.91	0.43	<b>0.00</b>	0.22	0.78	0.11
API2	<b>0.01</b>	0.38	0.55	<b>0.05</b>	0.60	0.44	0.10	0.54	0.23	0.29
API3	<b>0.05</b>	0.35	0.42	<b>0.05</b>	0.41	0.52	0.21	0.24	0.09	0.24
API4	0.11	0.48	0.64	<b>0.03</b>	0.39	0.15	0.06	0.50	0.14	0.17
API5	0.10	0.56	0.96	0.10	0.11	0.15	0.09	0.75	0.28	0.17
API6	0.09	0.50	0.47	0.09	0.13	0.32	0.17	0.75	0.29	0.11
API7	0.16	0.83	0.35	0.15	0.33	0.22	0.37	0.59	<b>0.03</b>	0.25
API14	0.76	0.10	0.95	0.17	0.66	0.08	0.30	0.27	0.19	0.80
CPI9	0.15	0.73	0.44	<b>0.02</b>	0.51	0.22	<b>0.03</b>	0.26	0.82	0.15
CPI99	<b>0.02</b>	0.88	0.54	<b>0.00</b>	0.76	0.17	<b>0.00</b>	0.35	0.59	0.07
CPI999	0.30	0.20	0.90	0.06	0.55	<b>0.02</b>	0.10	0.66	<b>0.03</b>	0.37
Time since last event	0.37	<b>0.02</b>	0.36	0.42	0.56	0.52	0.99	0.18	0.17	0.25
Air temperature	<b>0.00</b>	<b>0.00</b>	0.98	0.09	<b>0.00</b>	<b>0.00</b>	<b>0.00</b>	0.83	0.36	<b>0.00</b>
Day of year	<b>0.05</b>	<b>0.00</b>	<b>0.00</b>	0.09	0.87	0.75	0.06	<b>0.01</b>	0.25	0.19
Initial avg. $\theta$	<b>0.00</b>	<b>0.00</b>	<b>0.01</b>	0.67	0.29	0.10	0.81	<b>0.00</b>	<b>0.02</b>	0.41
Initial depth-weighted avg. $\theta$	<b>0.00</b>	<b>0.00</b>	<b>0.00</b>	0.73	0.28	<b>0.03</b>	0.82	<b>0.01</b>	<b>0.02</b>	0.48
Horizon 1 initial $\theta$	<b>0.01</b>	<b>0.00</b>	<b>0.00</b>	0.30	0.92	0.61	0.09	<b>0.00</b>	<b>0.00</b>	<b>0.05</b>
Horizon 2 initial $\theta$	<b>0.00</b>	<b>0.00</b>	<b>0.00</b>	0.78	0.92	<b>0.03</b>	0.65	<b>0.03</b>	<b>0.04</b>	0.24
Horizon 3 initial $\theta$	<b>0.00</b>	<b>0.00</b>	<b>0.01</b>	0.49	<b>0.05</b>	<b>0.00</b>	0.58	<b>0.01</b>	0.13	<b>0.01</b>
Horizon 4 initial $\theta$	<b>0.00</b>	<b>0.00</b>	<b>0.01</b>	0.41	<b>0.01</b>	<b>0.03</b>	0.88	<b>0.01</b>	0.13	0.07
Horizon 5 initial $\theta$	0.85	<b>0.00</b>	<b>0.00</b>	0.70	<b>0.01</b>	0.09	0.52		<b>0.05</b>	0.15
Horizon 6 initial $\theta$									0.07	<b>0.05</b>
Horizon 7 initial $\theta$									0.12	
Horizon 8 initial $\theta$									<b>0.05</b>	
Horizon 9 initial $\theta$									0.06	
Horizon 10 initial $\theta$									<b>0.05</b>	

† Ppt., precipitation; EventCPI9 to 999, internal event current ppt. index (EventCPI) with recession coefficients of 0.9 (EventCPI9), 0.99 (EventCPI99), and 0.999 (EventCPI999); API1 to 14, antecedent ppt. index (API) for 1, 2, 3, 4, 5, 6, 7, and 14 d, respectively;  $\theta$ , volumetric soil moisture content; horizons 1 to 10 are numbered sequentially from the soil surface downward to the deepest soil depth where a probe was installed.

intensity. While CPI99 and CPI999 were significant for two of the midslope sites (M1 and M2c), the antecedent precipitation did not appear to be a significant control in general. These midslope sites appeared to act as an intermediary between the ridgetop and planar hillslope sites and the lower swale and valley bottom sites. Prewetting from long, even intensity events and high initial soil moisture promote lateral subsurface flow from upslope areas.

Rather than being organized by topographic position, the 10 monitoring sites could also be organized by soil series, soil depth, upslope contributing area, distance from the stream, or local slope (among others). If the sites were categorized by soil type, for instance, the order of sites in Table 3 and Fig. 5 would be the same but the sites would be split into four groups: Weikert (U1, U2a, and U2b), Berks (M1 and M2a), Rushtown (M2b, M2c, L1a, and L1b), and Blairton (L2). When comparing the significant indices for the different grouping criteria, the sites had a higher average number of common indices controlling preferential flow when grouped by topographic position (66% of indices in agreement) than soil series (61%), soil depth (61%), upslope contributing area (65%), distance from the stream (62%), or local slope (61%). Because none of these additional criteria performed significantly better than topographic position and because all are well correlated with (and thought to be controlled by) topographic position, we suggest that topographic position is a dominant criterion for site separation at the Shale Hills.

### What Are the Characteristics of Events that Result in Widespread Preferential Flow?

To determine the antecedent precipitation, event characteristics, timing of event initiation, and initial soil moisture status leading to widespread preferential flow across the catchment, events where a large number of sites responded with either preferential flow or sequential flow were identified and the event characteristics of the two data sets were statistically compared. A total of 39 events resulted in sequential flow at six or more sites (22% of total events), while 36 events resulted in preferential flow at six or more sites (21% of total events). There were fewer events (18) that resulted in seven or more sites having preferential flow, so the comparison of indices was limited to six or more sites. The analyses were repeated for events resulting in five or more sites, then four or more sites within each of the two flow categories (Table 4).

There was some overlap between the indices that were found to control preferential flow at the individual sites and those that led to widespread preferential flow. For events that produced widespread preferential flow, the soil moisture was higher, the day of the year was later, and the EventCPI99 was greater. Additional indices that were significant for events that produced widespread preferential flow included the time to maximum intensity, API1, API4, API5, the precipitation amount and average intensity from the start of the event until the time of maximum intensity, and the time to maximum EventCPI.

Air temperature, an index that was significant at six sites, was not significant with regard to widespread preferential flow initiation, probably due to the fact that preferential flow was more likely to occur in colder weather for the sites with high upslope contributing area (Sites L1a, L1b, and L2) and in hotter weather for the sites with low upslope contributing area (Sites U2a and U1). Similarly, the skew and kurtosis, indices that were deemed significant for a number of sites, were not significant for widespread preferential flow due to preferential flow occurring at the ridgetop and planar hillslope sites when events had higher skew and kurtosis and at the other sites when the skew and kurtosis were lower.

From these analyses, it is apparent that events that led to widespread preferential flow at the Shale Hills occurred in the fall, when temperatures were moderate (not particularly high or low, as indicated by the lack of temperature control seen in widespread preferential flow). While the antecedent soil moisture was lower for events that lead to widespread preferential flow, the API1, API4, API5, and CPI99 were all greater, indicating that these events occurred during the fall wetting period, when soils were initially dry, but rainfall had recently begun prewetting the soil. The events leading to widespread preferential flow had an extended period of higher intensity rainfall before a moderate spike in precipitation intensity. This event sequence allows for two of the major types of preferential flow to occur at the Shale Hills. The date and initial soil moisture ensure that the soil is dry in the upper hillslope sites, promoting soil cracking and hydrophobicity and thus preferential flow. The high API and CPI and high-intensity buildup before the peak precipitation intensity allows the eventual saturation of the deeper soils, hence promoting lateral subsurface flow at horizon interfaces and the soil–bedrock interface downslope toward the valley and swale sites, or both. A spike in precipitation intensity late in the event is then quickly transferred from the upper sites downslope in the form of lateral subsurface flow, manifesting as preferential flow at the swale and valley sites. Events characterized like this would be expected to result in greater water fluxes to the stream and reduced transit times of water to depth and to the stream channel.

### On the Value of Long-Term, In Situ Soil Moisture Monitoring

All analyses of the frequency and controls on preferential flow initiation were repeated with subsets of the total time series data consisting of various numbers of precipitation events (Fig. 6). Despite the observed annual variation in preferential flow frequency, most sites reached a relatively steady percentage of events causing preferential flow after around 40 events and the variance dropped afterward. The exceptions included (i) Site U1, which did not reach a steady value until the 80th event, and (ii) Site M2b, where the incidence of preferential flow appeared to increase throughout the monitoring period (Fig. 6).

In terms of the controls on preferential flow initiation, subsets of time series were compared with the controls found for the entire monitoring data set (Fig. 7). In this comparison, a value of 100%

Table 4. Comparison of various indices of precipitation and initial soil moisture for events that produced preferential flow vs. those that produced sequential flow. Presented are *P* values from *t*-tests. Bold type indicates the indices with a significant difference between preferential flow and sequential flow events (95% confidence interval). Tests were performed for events that resulted in preferential flow occurring at one or more through six or more sites.

Index†	Index <i>P</i> value for preferential vs. sequential events at one or more sites					
	≥1 site	≥2 sites	≥3 sites	≥4 sites	≥5 sites	≥6 sites
Total ppt.	0.67	0.37	0.23	0.27	0.11	0.09
Ppt. duration	0.80	0.57	0.47	0.38	0.14	0.15
Avg. ppt. intensity	0.42	0.18	0.18	0.30	0.90	0.54
Max. ppt. intensity	0.99	0.74	0.74	0.57	0.22	0.33
Time to max. intensity	0.77	0.43	0.28	0.17	0.07	<b>0.01</b>
Ppt. amount to max. intensity	0.70	0.42	0.24	0.20	0.07	<b>0.04</b>
Avg. intensity to max. intensity	0.70	0.42	0.24	0.21	0.07	<b>0.04</b>
Variance	0.94	0.97	0.84	0.96	0.89	0.70
Skew	0.64	0.27	0.19	0.17	0.10	0.13
Kurtosis	0.68	0.28	0.18	0.16	0.10	0.10
Time to 5 mm of ppt.	0.99	0.92	0.67	0.18	<b>0.03</b>	0.28
Time to 10 mm of ppt.	0.79	0.40	0.22	0.27	0.98	0.54
Time to 20 mm of ppt.	0.82	0.78	0.84	0.83	0.82	0.66
Max. EventCPI9	0.83	0.77	0.62	0.99	0.84	0.88
Max. EventCPI99	0.68	0.43	0.30	0.47	0.24	0.15
Max. EventCPI999	0.67	0.35	0.22	0.27	0.11	0.09
Time to max. EventCPI9	0.78	0.41	0.15	0.06	<b>0.01</b>	<b>0.00</b>
Time to max. EventCPI99	0.62	0.38	0.19	0.12	0.08	<b>0.03</b>
Time to max. EventCPI999	0.71	0.52	0.48	0.42	0.15	0.36
API1	0.13	0.16	<b>0.04</b>	<b>0.05</b>	0.06	<b>0.01</b>
API2	0.17	0.37	0.50	0.37	0.36	0.12
API3	0.29	0.64	0.37	0.26	0.20	0.05
API4	0.18	0.46	0.24	0.17	0.21	<b>0.03</b>
API5	0.26	0.61	0.19	0.13	0.19	<b>0.04</b>
API6	0.27	0.71	0.25	0.35	0.45	0.09
API7	0.48	0.81	0.50	0.76	0.87	0.18
API14	0.70	0.72	0.86	0.83	0.62	0.82
CPI9	0.55	0.52	0.09	0.17	0.25	0.18
CPI99	0.19	0.15	<b>0.04</b>	<b>0.03</b>	<b>0.05</b>	<b>0.02</b>
CPI999	0.36	0.65	0.44	0.63	0.74	0.25
Time since last event	0.65	0.77	0.49	0.36	0.62	0.61
Air temperature	0.89	0.35	0.48	0.22	0.11	0.52
Day of year	0.48	0.21	<b>0.01</b>	<b>0.00</b>	<b>0.00</b>	<b>0.00</b>
Surface avg. $\theta$	0.90	0.56	<b>0.01</b>	<b>0.00</b>	<b>0.00</b>	<b>0.00</b>
Subsurface avg. $\theta$	0.90	0.62	<b>0.01</b>	<b>0.00</b>	<b>0.00</b>	<b>0.00</b>

† Ppt., precipitation; EventCPI9 to 999, internal event current ppt. index (EventCPI) with recession coefficients of 0.9 (EventCPI9), 0.99 (EventCPI99), and 0.999 (EventCPI999); API1 to 14, antecedent ppt. index (API) for 1, 2, 3, 4, 5, 6, 7, and 14 d, respectively;  $\theta$ , volumetric soil moisture content.

indicates that the indices that were determined to control preferential flow for the chosen subset coincided perfectly with those determined from the entire monitoring data set (i.e., 175 events). If 0% agreement, that means that all of the significant controls determined from the entire time series data set were found insignificant for the chosen subset and vice versa. A possible null hypothesis is that none of the precipitation, timing, and initial soil moisture indices were significant controls (that is, preferential flow is completely random and not dependent on any of the analyzed indices). For ease of interpretation, Fig. 7 also shows the agreement (largely 60–80%) of this null hypothesis with the final set of significant

indices (horizontal lines). The null hypothesis agreement varied with each site because each site had a different number of indices that were determined to be significant.

The ridgetop and planar hillslope sites (U1, U2a, and U2b) showed a rapid convergence toward agreement with the final set of significant indices, with 90% agreement at all sites within 118 events and a greater agreement than the null hypothesis (that none of the indices were significant) within 38 events. The midslope sites (M1, M2a, M2b, and M2c), with moderate upslope contributing area and deeper soils, were all in greater agreement than the null

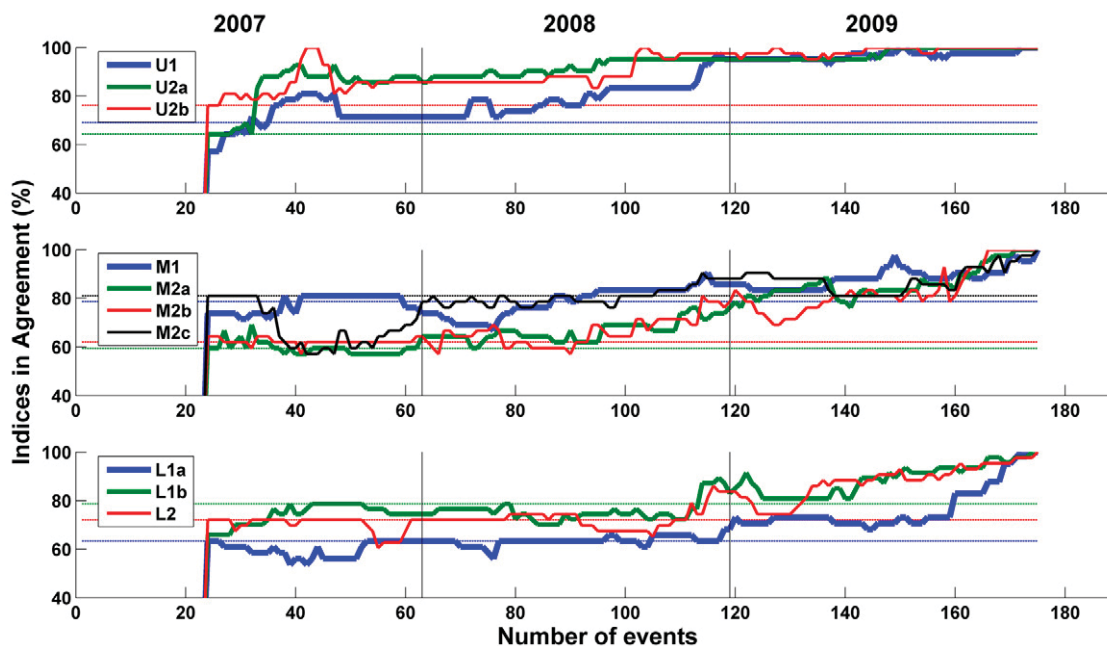


Fig. 7. Agreement on the controls of preferential flow initiation that were identified from 24 to 175 events in each of the 10 monitoring sites during the >3-yr monitoring period. Analyses were not performed with <24 events due to an insufficient number of events that resulted in different flow regimes. Complete agreement with the identified controls on preferential flow initiation using all 175 events is indicated as 100%. Horizontal lines of the same color indicate the agreement percentage if no indices are determined as significant (null hypothesis, which depends on the number of significant indices for each site). Sites are organized from top to bottom with the ridgetop and hillslope sites (U1, U2a, and U2b) above the midslope sites (M1, M2a, M2b, and M2c) and above the lower swale and valley sites (L1a, L1b, and L2). Vertical lines separate the events occurring in 2007, 2008, and 2009.

hypothesis within 100 events, although it did not reach 90% agreement until 162 events. The valley and lower swale sites (L1a, L1b, and L2), with the deepest soils and greatest upslope contributing area, all showed greater agreement than the null hypothesis within 120 events but did not reach >90% agreement until 170 events.

A marked difference is noted in the time period needed to determine the frequency of preferential flow at a given site and the time period needed to determine the controls on preferential flow. The frequency of preferential flow occurrence was determined after 40 precipitation events, or about 1 yr of monitoring (Fig. 6). The controls on preferential flow, however, required 1 to 3 yr of monitoring (Fig. 7). Unlike the frequency of preferential flow occurrence, there appeared to be topographic effects on the convergence toward the ultimate controls on preferential flow in this catchment (Fig. 7). All of the ridgetop and planar hillslope sites converged rather quickly on the significant indices, rising above the null hypothesis (that preferential flow occurred randomly) within 40 precipitation events and above 90% convergence within 120 events. The valley and swale sites, on the other hand, took a much longer time: up to 120 events to rise above the null hypothesis and 170 events to rise above 90% agreement, with the final sets of indices identified with the whole >3-yr data set.

One possible explanation for the difference in convergence between topographic positions lies in the number of events needed to fully explore the parameter space of the different indices. For instance, it took 67 events before one occurred with a total precipitation

>50% of the maximum observed. Many of the other indices took similar time periods to be fully explored. Day of the year, air temperature, and soil moisture, however, fully explored their respective parameter spaces within 1 yr. Until the parameter space of the index is fully explored, a clear understanding of the significance of that variable cannot be assessed. The ridgetop and planar hillslope sites were controlled by indices such as air temperature and soil moisture that explored their respective parameter spaces quickly within a year, possibly leading to the relatively rapid convergence of the controls at the ridgetop and hillslope sites. The valley and lower swale sites, on the other hand, were controlled by indices such as total precipitation that were slower to completely explore their parameter space until nearly all monitoring data sets were assessed.

Another possible explanation for the difference is the correlation between significant indices at the different sites. Preferential flow generally occurred at the ridgetop and hillslope sites when there was low soil moisture, high air temperatures, and it was late in the year. These three sets of indices all occurred for a subset of events occurring in late summer, when the air temperature was high, soil moisture was low, and the day of the year was late. Events meeting these criteria occur every summer due to the seasonal nature of soil moisture and air temperature. Thus, once one or two summers are sampled, the controls on preferential flow at the ridgetop and planar hillslope sites are easily determined. At the valley and lower swale sites, however, many of the controlling indices are not correlated with each other. Preferential flow occurred at these sites

when the soil moisture, total event precipitation, and the time and average precipitation intensity from the start of the event to the peak intensity were all high. These four indices were poorly correlated with each other (with the exception of total precipitation and time to peak intensity,  $R^2 = 0.74$ ). Thus, many more events were needed to adequately sample the entire range of each index independently, hence requiring a longer term data set.

The high number of events needed to adequately determine the controls on preferential flow, especially at the valley and lower swale sites, indicates that the time series analyzed is possibly not of sufficient duration to conclusively determine the controls. Further analysis of the individual controls showed that the false positive rate (i.e., indices found to be significant in the subset analysis but were not found to be significant for the entire monitoring data set) was much higher than the false negative rate (i.e., indices found to be not significant in the subset analysis but were found to be significant for the entire monitoring data set). This suggests a continual winnowing of the number of indices that are deemed to be significant controls on preferential flow with increasing monitoring duration. Analysis of longer time periods could possibly further winnow the number of significant controls on preferential flow, especially at the valley and lower swale sites (Fig. 7).

### Implications for Modeling and Prediction

From the analyses presented above and a review of the relevant literature, it is clear that preferential flow initiation is a complex process, resistant to simple characterization (Beven and Germann, 1982; Jarvis, 2007). One-dimensional Darcy and Richards' equation based models cannot replicate the observed, out-of-sequence soil moisture responses to precipitation. While the preferential flow observed at the valley and lower swale sites may be captured by a distributed model capable of routing water laterally along permeability contrasts (such as soil horizon interfaces and the soil–bedrock interface), the preferential flow observed at the ridge and hillslope sites would violate the assumptions of most of these models.

One interesting result of the above analyses was that the significance of initial soil moisture did not coincide with any of the antecedent precipitation indices. The API and CPI are traditionally used in hydrology as an indirect measure of the antecedent moisture state of the catchment, be it soil moisture or stream flow (Heggen, 2001). Because the initial soil moisture was clearly a control on preferential flow initiation, the antecedent precipitation indices would also be expected to be a control. Yet, while API and CPI were not consistent controls on preferential flow initiation at any topographic position in the Shale Hills, the initial soil moisture was a control at all topographic positions. Additional analyses comparing the different API and CPI with the initial soil moisture found a very poor correlation, with  $R^2 < 0.11$  for all combinations of precipitation indices and initial soil moisture. This is in sharp contrast to the often high correlation between these indices and stream discharge. Traditional antecedent precipitation-based moisture indices appear to be a poor tool for predicting the actual soil moisture status.

The discrepancy between the antecedent precipitation indices and the initial soil moisture, combined with the initial soil moisture condition control on preferential flow initiation, demonstrates the value of real-time soil moisture monitoring or modeling in the prediction of preferential flow initiation. While the majority of the indices used to predict preferential flow can easily be derived from the precipitation record (e.g., total precipitation, precipitation skew and kurtosis, and EventCPI), the initial soil moisture cannot. Soil moisture dynamics are controlled by a complex interplay among soil properties, topographic features, precipitation dynamics, vegetation water use, and water table proximity. The site-specific modeling of soil moisture needed to predict preferential flow initiation will need to encompass all of these factors.

## Conclusions

Through the analysis of real-time soil moisture response to 175 precipitation events in the Shale Hills Critical Zone Observatory from 2006 to 2009, the frequency of and controls on preferential flow initiation were determined. Preferential flow was common across the catchment, occurring at one or more sites during at least 90% of the monitored events. At the ridgetop and planar hillslope sites, the dominant controls on preferential flow initiation were the initial soil moisture (drier soils), air temperature (hotter), and the time of the year (late summer), factors that were correlated with soil hydrophobicity and soil cracking. At the valley and lower swale sites, initial soil moisture was significantly higher for preferential flow inducing events, and internal precipitation event dynamics (such as the value and timing of the maximum internal event and the CPI) as well as the average intensity also appeared to control preferential flow initiation. The valley and lower swale sites were also sensitive to the average precipitation rate and total precipitation from the start of an event until the time of maximum precipitation intensity. At the midslope sites, preferential flow occurrence was generally associated with longer events where the precipitation intensity distribution was more uniform as well as when the soil was wet. Widespread preferential flow was common in this catchment, especially in late summer to fall. Precipitation events that resulted in widespread preferential flow had greater duration, amount, and average intensity from the start of the event to the time of maximum intensity. Analyses of shorter time series data showed that while the frequency of preferential flow occurrence could be determined from 1 yr of continuous monitoring, the controls on preferential flow required  $\geq 3$  yr of real-time soil moisture monitoring.

Analysis of the long-term soil moisture data provided valuable information on the controls and the spatial-temporal pattern of preferential flow occurrence in the Shale Hills Critical Zone Observatory. Further work is desirable to apply the methodology developed in this study at additional sites for cross-site comparisons (such as other Critical Zone Observatories) to shed more light on the nature of preferential flow under various environmental conditions. Sites with different land cover, precipitation regimes,

soil types, and topographic features are expected to have different controls on preferential flow initiation and thus the frequency and timing of its occurrence. Such information will provide a valuable foundation for improving hydrologic models and their predictions as well as the determination of biogeochemical hot spots and hot moments, which are often associated with preferential flow in soils.

## Acknowledgments

This research was partially supported by the U.S. National Science Foundation through the Shale Hills Critical Zone Observatory grant (EAR-0725019). Probes were installed and data collected by the Penn State Hydrogeology team members, including Bob Zhou, Qing Zhu, Lifang Luo, Jun Zhang, Chuck Walker, Danielle Andrews, and others.

## References

- Anderson, A.E., M. Weiler, Y. Alila, and R.O. Hudson. 2009. Dye staining and excavation of a lateral preferential flow network. *Hydrol. Earth Syst. Sci.* 13:935–944. doi:10.5194/hess-13-935-2009
- Bauters, T.W.J., D.A. DiCarlo, T.S. Steenhuis, and J.-Y. Parlange. 1998. Preferential flow in water-repellent sands. *Soil Sci. Soc. Am. J.* 62:1185–1190. doi:10.2136/sssaj1998.03615995006200050005x
- Beven, K., and P. Germann. 1982. Macropores and water flow in soils. *Water Resour. Res.* 18:1311–1325. doi:10.1029/WR018i005p01311
- Bonta, J.V. 2003. Estimation of parameters characterizing frequency distributions of times between storms. *Trans. ASAE* 46:331–343.
- Dekker, L.W., and C.J. Ritsema. 1996. Preferential flow path in a water repellent clay soil with grass cover. *Water Resour. Res.* 32:1239–1249. doi:10.1029/96WR00267
- Flühler, H., W. Durner, and M. Flury. 1996. Lateral solute mixing processes: A key for understanding field-scale transport of water and solutes. *Geoderma* 70:165–183. doi:10.1016/0016-7061(95)00079-8
- Garre, S., J. Koestel, T. Gunther, M. Javaux, J. Vanderborght, and H. Vereecken. 2010. Comparison of heterogeneous transport processes observed with electrical resistivity tomography in two soils. *Vadose Zone J.* 9:336–349. doi:10.2136/vzj2009.0086
- Germann, P.F. 1990. Preferential flow and the generation of runoff: 1. Boundary layer flow theory. *Water Resour. Res.* 26:3055–3063.
- Graham, C.B., R.A. Woods, and J.J. McDonnell. 2010. Hillslope threshold response to rainfall: 1. A field based forensic approach. *J. Hydrol.* 393:65–76. doi:10.1016/j.jhydrol.2009.12.015
- Heggen, R.J. 2001. Normalized antecedent precipitation index. *J. Hydrol. Eng.* 6:377–381. doi:10.1061/(ASCE)1084-0699(2001)6:5(377)
- Huff, F.A. 1967. Time distribution of rainfall in heavy storms. *Water Resour. Res.* 3:1007–1019. doi:10.1029/WR003i004p01007
- Jarvis, N.J. 2007. A review of non-equilibrium water flow and solute transport in soil macropores: Principles, controlling factors and consequences for water quality. *Eur. J. Soil Sci.* 58:523–546. doi:10.1111/j.1365-2389.2007.00915.x
- Kienzler, P.M., and F. Naef. 2008. Subsurface storm flow formation at different hillslopes and implications for the 'old water paradox'. *Hydrol. Processes* 22:104–116. doi:10.1002/hyp.6687
- Kneale, W.R., and R.E. White. 1984. The movement of water through cores of a dry (cracked) clay-loam grassland topsoil. *J. Hydrol.* 67:361–365. doi:10.1016/0022-1694(84)90251-8
- Lin, H. 2006. Temporal stability of soil moisture spatial pattern and subsurface preferential flow pathways in the Shale Hills catchment. *Vadose Zone J.* 5:317–340. doi:10.2136/vzj2005.0058
- Lin, H. 2010. Linking principles of soil formation and flow regimes. *J. Hydrol.* 393:3–19.
- Lin, H., and X. Zhou. 2008. Evidence of subsurface preferential flow using soil hydrologic monitoring in the Shale Hills catchment. *Eur. J. Soil Sci.* 59:34–49. doi:10.1111/j.1365-2389.2007.00988.x
- Linsley, R.K., Jr., M.A. Kohler, and J.L. Paulhus. 1949. *Applied hydrology*. McGraw-Hill, New York.
- McDonnell, J.J. 1990. A rationale for old water discharge through macropores in a steep, humid catchment. *Water Resour. Res.* 26:2821–2832. doi:10.1029/WR026i011p02821
- Mosley, M.P. 1982. Subsurface flow velocities through selected forest soils, South Island, New Zealand. *J. Hydrol.* 55:65–92. doi:10.1016/0022-1694(82)90121-4
- Noguchi, S., Y. Tsuboyama, R.C. Sidle, and I. Hosoda. 2001. Subsurface runoff characteristics from a forest hillslope soil profile including macropores, Hitachi Ohta, Japan. *Hydrol. Processes* 15:2131–2149. doi:10.1002/hyp.278
- Oberdorster, C., J. Vanderborght, A. Kemna, and H. Vereecken. 2010. Investigating preferential flow processes in a forest soil using time domain reflectometry and electrical resistivity tomography. *Vadose Zone J.* 9:350–361. doi:10.2136/vzj2009.0073
- Rasmussen, T.C., R.H. Baldwin, J.F. Dowd, and A.G. Williams. 2000. Tracer vs. pressure wave velocities through unsaturated saprolite. *Soil Sci. Soc. Am. J.* 64:75–85. doi:10.2136/sssaj2000.64175x
- Ritsema, C.J., and L.W. Dekker. 1996. Influence of sampling strategy on detecting preferential flow paths in water-repellent sand. *J. Hydrol.* 177:33–45. doi:10.1016/0022-1694(95)02795-5
- Shipitalo, M.J., and F. Gibbs. 2000. Potential of earthworm burrows to transmit injected animal wastes to tile drains. *Soil Sci. Soc. Am. J.* 64:2103–2109. doi:10.2136/sssaj2000.6462103x
- Smakhtin, V.Y., and B. Masse. 2000. Continuous daily hydrograph simulation using duration curves of a precipitation index. *Hydrol. Processes* 14:1083–1100. doi:10.1002/(SICI)1099-1085(20000430)14:63.O.CO;2-2
- Taumer, K., H. Stoffregen, and G. Wessolek. 2006. Seasonal dynamics of preferential flow in a water repellent soil. *Vadose Zone J.* 5:405–411. doi:10.2136/vzj2005.0031
- Torres, R., and L.J. Alexander. 2002. Intensity–duration effects on drainage: Column experiments at near-zero pressure head. *Water Resour. Res.* 38:1240. doi:10.1029/2001WR001048
- Tromp-van Meerveld, H.J., and J.J. McDonnell. 2006. Threshold relations in subsurface stormflow: 1. A 147-storm analysis of the Panola hillslope. *Water Resour. Res.* 42:W02410. doi:10.1029/2004WR003778
- Uchida, T., K. Kosugi, and T. Mizuyama. 2001. Effects of pipeflow on hydrological process and its relation to landslide: A review of pipeflow studies in forested headwater catchments. *Hydrol. Processes* 15:2151–2174. doi:10.1002/hyp.281
- Uhlenbrook, S. 2006. Catchment hydrology: A science in which all processes are preferential. *Hydrol. Processes* 20:3581–3585. doi:10.1002/hyp.6564
- Wang, D.K., B. Lowery, J.M. Norman, and K. McSweeney. 1996. Ant burrow effects on water flow and soil hydraulic properties of Sparta sand. *Soil Tillage Res.* 37:83–93. doi:10.1016/0167-1987(96)01006-9
- Weiler, M., and H. Flühler. 2004. Inferring flow types from dye patterns in macroporous soils. *Geoderma* 120:137–153. doi:10.1016/j.geoderma.2003.08.014



This article appeared in a journal published by Elsevier. The attached copy is furnished to the author for internal non-commercial research and education use, including for instruction at the authors institution and sharing with colleagues.

Other uses, including reproduction and distribution, or selling or licensing copies, or posting to personal, institutional or third party websites are prohibited.

In most cases authors are permitted to post their version of the article (e.g. in Word or Tex form) to their personal website or institutional repository. Authors requiring further information regarding Elsevier's archiving and manuscript policies are encouraged to visit:

<http://www.elsevier.com/copyright>



## Regolith production rates calculated with uranium-series isotopes at Susquehanna/Shale Hills Critical Zone Observatory

Lin Ma<sup>a,\*</sup>, Francois Chabaux<sup>b</sup>, Eric Pelt<sup>b</sup>, Estelle Blaes<sup>b</sup>, Lixin Jin<sup>a</sup>, Susan Brantley<sup>a</sup>

<sup>a</sup> Earth and Environmental Systems Institute, Pennsylvania State University, University Park, PA 16802, USA

<sup>b</sup> Laboratoire d'Hydrologie et de Géochimie de Strasbourg, EOST, University of Strasbourg and CNRS, Strasbourg, France

### ARTICLE INFO

#### Article history:

Received 20 December 2009

Received in revised form 3 June 2010

Accepted 12 June 2010

Available online 7 July 2010

Editor: M.L. Delaney

#### Keywords:

U-series isotopes  
regolith formation  
chemical weathering  
erosion  
critical zone

### ABSTRACT

In the Critical Zone where rocks and life interact, bedrock equilibrates to Earth surface conditions, transforming to regolith. The factors that control the rates and mechanisms of formation of regolith, defined here as material that can be augered, are still not fully understood. To quantify regolith formation rates on shale lithology, we measured uranium-series (U-series) isotopes ( $^{238}\text{U}$ ,  $^{234}\text{U}$ , and  $^{230}\text{Th}$ ) in three weathering profiles along a planar hillslope at the Susquehanna/Shale Hills Observatory (SSHO) in central Pennsylvania. All regolith samples show significant U-series disequilibrium: ( $^{234}\text{U}/^{238}\text{U}$ ) and ( $^{230}\text{Th}/^{238}\text{U}$ ) activity ratios range from 0.934 to 1.072 and from 0.903 to 1.096, respectively. These values display depth trends that are consistent with fractionation of U-series isotopes during chemical weathering and element transport, i.e., the relative mobility decreases in the order  $^{234}\text{U} > ^{238}\text{U} > ^{230}\text{Th}$ . The activity ratios observed in the regolith samples are explained by i) loss of U-series isotopes during water–rock interactions and ii) re-deposition of U-series isotopes downslope. Loss of U and Th initiates in the meter-thick zone of “bedrock” that cannot be augered but that nonetheless consists of up to 40% clay/silt/sand inferred to have lost K, Mg, Al, and Fe. Apparent equivalent regolith production rates calculated with these isotopes for these profiles decrease exponentially from 45 m/Myr to 17 m/Myr, with increasing regolith thickness from the ridge top to the valley floor. With increasing distance from the ridge top toward the valley, apparent equivalent regolith residence times increase from 7 kyr to 40 kyr. Given that the SSHO experienced peri-glacial climate ~15 kyr ago and has a catchment-wide averaged erosion rate of ~15 m/Myr as inferred from cosmogenic  $^{10}\text{Be}$ , we conclude that the hillslope retains regolith formed before the peri-glacial period and is not at geomorphologic steady state. Both chemical weathering reactions of clay minerals and translocation of fine particles/colloids are shown to contribute to mass loss of U and Th from the regolith, consistent with major element data at SSHO. This research documents a case study where U-series isotopes are used to constrain the time scales of chemical weathering and regolith production rates. Regolith production rates at the SSHO should be useful as a reference value for future work at other weathering localities.

© 2010 Elsevier B.V. All rights reserved.

### 1. Introduction

Bedrock is converted to erodible regolith through physical, chemical, biological and hydrological processes operating together within the thin layer at Earth's surface – the Critical Zone – where rocks, vegetation, atmospheric gases and water interact (e.g., White et al., 1996; Heimsath et al., 1997; Anderson et al., 2002; Amundson, 2004; Brantley et al., 2007a; Brantley and White, 2009). Over time, the bedrock–regolith interface (the weathering front) propagates downward into the bedrock. The balance between rates of erosion and regolith production contribute to both the regolith thickness and the overall landscape morphology (Carson and Kirkby, 1972; Stallard, 1992; Heimsath et al., 1997; Minasny and McBratney, 1999). Furthermore, the products of

weathering, regolith, are vital for the sustainability of ecosystems and human society (Montgomery, 2007; Porder et al., 2007; Brantley, 2008). Human activities have resulted in a sharp increase in rates of continental erosion and sedimentation (Wilkinson and McElroy, 2007). It is currently of great importance to predict how regolith will respond to anthropogenic and climate perturbations. However, the factors that control the rates and mechanisms of regolith formation are still not fully understood.

Chemical weathering of bedrock mobilizes elements from the lithosphere, providing nutrients to the biosphere, controlling river and ocean chemistry in the hydrosphere, as well as regulating  $\text{CO}_2$  and global climate for the atmosphere (e.g., Kump et al., 2000; Drever, 2004; Godderis et al., 2009). Detailed chemical analyses and models of chemical mass balance have been routinely used to study chemical and physical changes during regolith formation (Brimhall and Dietrich, 1987; Taylor and Blum, 1995; White and Blum, 1995; Murphy et al., 1998; White et al., 1998; Amundson, 2004; Lebedeva et al., 2007; Yoo et al., 2007; Steefel,

\* Corresponding author. Tel.: +1 814 863 8055.  
E-mail address: [lxm59@psu.edu](mailto:lxm59@psu.edu) (L. Ma).

2008; Brantley and White, 2009). Such approaches generally require independent estimates of the regolith production rates. Cosmogenic isotopes (e.g.,  $^{10}\text{Be}$  and  $^{26}\text{Al}$ ) have been used to provide estimates of total denudation rates (e.g., Lal, 1991; Bierman and Nichols, 2004; von Blanckenburg, 2005). From these denudation rates, soil production rates can be inferred if soil thickness is constant over time (e.g., Heimsath et al., 1997; Small et al., 1999; Riebe et al., 2003). However, such an assumption is generally difficult to evaluate and has only been tested in a few instances (e.g., Heimsath et al., 1997, 2000; Dosseto et al., 2008b).

Uranium-series (U-series) isotopes (e.g.,  $^{238}\text{U}$ ,  $^{234}\text{U}$  and  $^{230}\text{Th}$ ) offer a powerful tool to investigate regolith production rates or residence times in a weathering system.  $^{238}\text{U}$  decays with a half-life ( $T_{1/2}$ ) of  $\sim 4.5$  Gyr to produce  $^{234}\text{U}$  ( $T_{1/2} = 244$  kyr), which in turn decays to  $^{230}\text{Th}$  ( $T_{1/2} = 75$  kyr). For a system closed to inputs or outputs of U-series isotopes for longer than  $\sim 1.3$  Myr, these isotopes will be in secular equilibrium (i.e., daughter/parent activity ratios equal unity). However, U is soluble in water while Th is “particle-reactive”, i.e., it generally associates with solid surfaces (Langmuir, 1978; Langmuir and Herman, 1980). Importantly, compared with  $^{238}\text{U}$ ,  $^{234}\text{U}$  is released to solution to great extent because  $^{234}\text{U}$  is produced by alpha particle emission from  $^{238}\text{U}$  and this heavy particle often damages the crystal lattice enabling preferential loss of the lighter isotope during water–rock interaction (Fleischer, 1980). In other words, congruent dissolution of U-containing materials releases both isotopes equivalently to solution but  $^{234}\text{U}$  can also be released preferentially to solution because of the alpha particle effect. Because of these reasons, the relative mobility of U-series isotopes during weathering is believed to be  $^{234}\text{U} > ^{238}\text{U} > ^{230}\text{Th}$  (e.g., Rosholt et al., 1966; Latham and Schwarcz, 1987a,b; Vigier et al., 2001; Chabaux et al., 2003a, 2008; Dosseto et al., 2008a). Therefore, fluid phases are generally characterized by  $(^{234}\text{U}/^{238}\text{U}) > 1$  and  $(^{230}\text{Th}/^{238}\text{U}) < 1$  (parenthesis means activity ratio hereafter), while materials that have weathered recently generally show  $(^{234}\text{U}/^{238}\text{U}) < 1$  and  $(^{230}\text{Th}/^{238}\text{U}) > 1$ . The amount of disequilibrium in the weathering residual depends on both the extent and duration of weathering processes. In particular, the disequilibrium tracks the development of mineral–water interfacial area for the major U-bearing phases. Hence, U-series isotopes have been used to place time constraints on the initiation and duration of chemical weathering over a wide range of spatial scales, including ocean sediment cores, weathering profiles and rinds, shallow aquifers, small river catchments, and large drainage basins (e.g., Gascoyne, 1992; Plater et al., 1994; Mathieu et al., 1995; Vigier et al., 2001; Dequincey et al., 2002; Chabaux et al., 2003a,b; Maher et al., 2004; Vigier et al., 2005; Chabaux et al., 2006; Depaolo et al., 2006; Dosseto et al., 2006a,b,c; Vigier et al., 2006; Granet et al., 2007; Chabaux et al., 2008; Dosseto et al., 2008a,b; Gaillardet, 2008; Pelt et al., 2008; Bourdon et al., 2009).

Here, we present a study of U-series isotopes in regolith profiles developed on shale bedrock at the Shale Hills catchment, an observatory established in central Pennsylvania as a part of a network of observatories to investigate Earth surface processes related to hydrology, geochemistry, ecology, and geomorphology within the Critical Zone (Brantley et al., 2007b). We show here that the regolith samples display significant U-series disequilibrium resulted from shale weathering processes. By using U-series isotopes, we determine the time scales of shale weathering and regolith production rates for this experimental watershed. The mobility behavior of U-series isotopes during weathering is also systematically investigated in this Critical Zone observatory. The success of this method in estimating rates of regolith formation also enhances our ability to use this technique in other environments to understand the response of regolith productions to climate perturbations.

## 2. Methods

### 2.1. Site description

Shale has been the focus of some pioneering weathering studies (Littke et al., 1991; Kolowith and Berner, 2002; Pierson-Wickmann et

al., 2002; Copard et al., 2007; Tuttle and Breit, 2009; Tuttle et al., 2009), as it covers about 25% of the land surface area (Amiotte-Suchet et al., 2003). Weathering of shale controls global geochemical fluxes of C, P, and Pt-group elements (Petsch et al., 2001; Kolowith and Berner, 2002; Amiotte-Suchet et al., 2003). To better understand shale weathering processes, the Susquehanna/Shale Hills Observatory (SSHO) is established in central Pennsylvania (Fig. 1a). This 8-hectare watershed is managed as a Pennsylvania State University experimental forest. Extensive field studies have been conducted at SSHO from forestry field experiments, global information system (GIS) and digital elevation models, soil moisture synoptic sampling, soil mapping, stream flow monitoring, and ongoing geophysics and geochemical observations (Lynch, 1976; Lynch and Corbett, 1985; Duffy and Cusumano, 1998; Lin et al., 2006; Qu and Duffy, 2007; Jin et al., 2010). As such, SSHO is an ideal site to study the fractionation of U-series isotopes during water–rock interactions.

At SSHO, the mean annual temperature is  $10^\circ\text{C}$  and the mean annual precipitation is 107 cm (NOAA, 2007). A 1st-order stream flows within the catchment and eventually joins the Susquehanna River (Fig. 1a). The V-shaped catchment is characterized by an average E–W channel and average local relief of 30 m (Lynch, 1976; Lin, 2006). The hillslopes are covered with deciduous trees (maple, oak, and beech) and the valley is covered by hemlocks and pines (Lin, 2006).

The SSHO has developed almost entirely upon Rose Hill Formation (Folk, 1960; Lynch, 1976; Lynch and Corbett, 1985). The 700-foot-thick Silurian-age formation consists of olive-pink, grayish-buff shales with a few interbedded limestones (Lynch, 1976). The shale bedrock is composed predominantly of illite (58 wt.%), quartz (30 wt.%), “vermiculized” chlorite (11 wt.%), and trace feldspar (plagioclase and K-feldspar), anatase ( $\text{TiO}_2$ ), Fe-oxides (magnetite and hematite) and zircon (Jin et al., 2010). Chemical weathering reactions in the regolith at SSHO are dominated by clay transformations wherein illite, “chlorite”, and plagioclase weather to a vermiculite phase and kaolinite. The regolith is defined here to be the zone that can be augered by hand. Beneath the regolith–bedrock interface, evidence is consistent with dissolution of carbonates and feldspar in the underlying rock (Jin et al., 2010). Regolith thickness averages 1.4 m over the catchment, ranging from shallow at the ridge top to much deeper in the valley floor and in topographic depressions (Fig. 1a).

Erosion rates of the Appalachian mountain region are estimated to range from 8 to 29 m/Myr (Roden and Miller, 1989; Blackmer et al., 1994; Reuter et al., 2004). One measurement of cosmogenic  $^{10}\text{Be}$  in a stream sediment sample from SSHO shows a catchment-averaged erosion rate of 15 m/Myr (Jin et al., 2010), a value that is consistent with other shale localities in the Appalachians. However, the SSHO has experienced at least two significant perturbations in the geologically recent past: a perturbation from peri-glacial to modern conditions ( $\sim 15$  kyr; Gardner et al., 1991), and clearing of forests during colonial occupation. The catchment lies  $\sim 80$  km south of the greatest advance of glacial ice in central Pennsylvania during the last glacial maximum (Braun, 2005).

### 2.2. Sample collection and U–Th isotope analyses

We focus here on the U-series isotopic compositions for previously collected samples of augered core from three sites along one planar hillslope on the southern slope of the catchment (southern planar ridge top: SPRT; southern planar middle slope: SPMS; and southern planar valley floor: SPVF). Here, fluid flow in the regolith is considered to be largely two-dimensional downslope, i.e., nonconvergent flow, and the hillslope is thus referred to as a 2-D weathering profile (Fig. 1). These compositions are compared to relatively unaltered “parent materials” obtained by drilling into the underlying bedrock (see further discussion below). The drilled core was obtained as powdered sample using a rotary air drill in the northern ridge of the catchment (Fig. 1a).

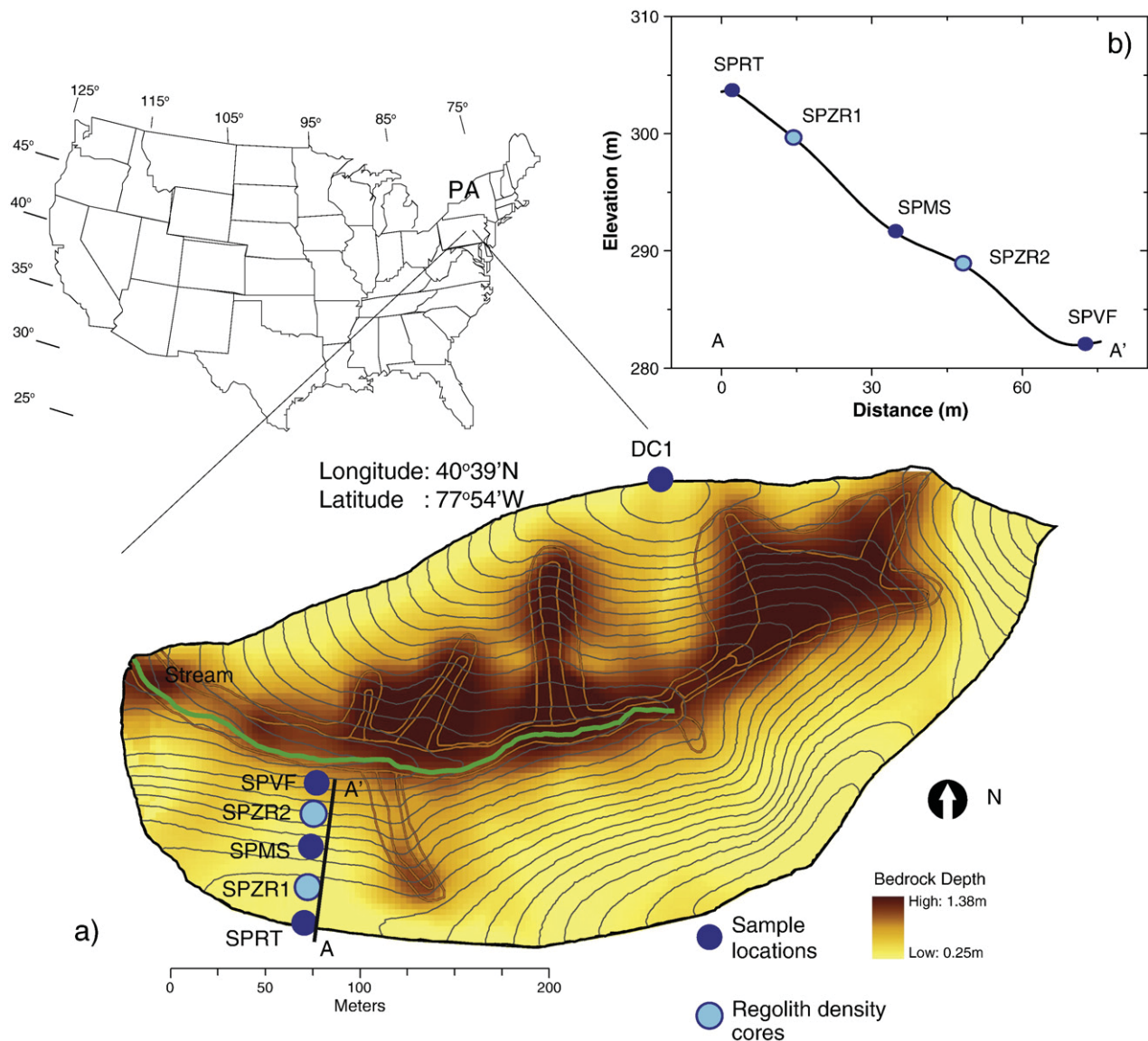


**Fig. 1.** a) Regolith sample locations in the Shale Hills catchment (modified after Lin et al., 2006). Background color indicates regolith thickness; yellow lines indicate the outlines of the five previously identified soil series (Lin et al., 2006); grey lines indicate topographic contours. DC1 is the drill core site where 24 m of parent shale was sampled for chips (Jin et al., 2010). Regolith cores SPRT, SPMS, and SPVF comprise a 2D planar transect (black line: A–A'). Two regolith cores (SPZR1 and SPZR2) sampled along the hillslope for bulk density analyses are also indicated; b) Cross section of the 2D planar transect (A–A'): notice that the surface varies from flat at SPRT, to linear at SPMS, to concave at SPVF.

Regolith samples were collected using a 2-inch diameter hand auger at about 10 cm intervals until refusal. Importantly, “regolith” defined here includes both the mobile layer near the surface (the “soils” or “mobile layer”, e.g., Dietrich et al., 2003) and the underlying “immobile layer”. “Bedrock” is here defined as fragmented or unfragmented rock that was inaccessible to the auger. The deepest regolith samples generally contained a high fraction of rock fragments. Importantly, the samples were not size-separated but rather, the entire sample of rock fragments + granular material was ground and analyzed. Zero depth was defined as the bottom of the 3-cm thick organic layer or, equivalently, the top of the mineral soil. The samples used in this study were derived as splits of the samples from the cores described previously (Jin et al., 2010).

Analyses of U and Th isotopes and concentrations were performed at the Laboratoire d’Hydrologie et de Géochimie de Strasbourg, University of Strasbourg (France), following the procedures as described in Granet et al. (2007) and Pelt et al. (2008) (see Appendix A for analytical details).

### 3. Results

The activity ratios and concentrations of U and Th in the regolith and bedrock samples are presented in Table 1. For splits of the same samples, regolith density, mineralogy, and mobility of major elements during chemical weathering are discussed by Jin et al. (2010).

#### 3.1. U-series activity ratios

The Silurian-aged bedrock samples (DC1–8 and DC1–26) show values of  $(^{234}\text{U}/^{238}\text{U})$  and  $(^{230}\text{Th}/^{238}\text{U})$  equal to 1 within error (Table 1, Fig. 2), as expected for secular equilibrium in a rock older than 1 Ma in age, i.e., a rock that has not lost significant  $^{234}\text{U}$  due to water–rock interaction. In contrast, regolith samples are not in secular equilibrium.  $(^{234}\text{U}/^{238}\text{U})$  values measured in regolith samples from the ridge top (SPRT), middle slope (SPMS), and valley floor (SPVF) profiles range from 0.936 to 0.951, from 0.934 to 0.972, and from 0.966 to 1.072, respectively (Table 1, Fig. 2). Furthermore, all three profiles show

**Table 1**  
U–Th concentrations and activity ratios of regolith and bedrock samples at the Shale Hills catchment.

Samples	Depth (cm)	U (ppm)	±2σ	Th (ppm)	±2σ	( <sup>234</sup> U/ <sup>238</sup> U) <sub>a</sub>	±2σ	( <sup>230</sup> Th/ <sup>238</sup> U) <sub>a</sub>	±2σ	( <sup>238</sup> U/ <sup>232</sup> Th) <sub>a</sub>	±2σ	( <sup>230</sup> Th/ <sup>232</sup> Th) <sub>a</sub>	±2σ	Zr (ppm)
SPRT0010	5	2.728	0.019	12.58	0.13	0.936	0.005	1.052	0.015	0.658	0.007	0.692	0.007	273
SPRT1020	15	2.780	0.019	12.60	0.13	0.943	0.005	1.040	0.015	0.669	0.007	0.696	0.007	275
SPRT2030	25	2.777	0.019	12.44	0.12	0.951	0.005	1.036	0.015	0.677	0.007	0.701	0.007	246
SPMS0010	5	2.733	0.019	12.56	0.13	0.934	0.005	1.096	0.015	0.660	0.007	0.723	0.007	351
SPMS1020	15	2.768	0.019	12.25	0.12	0.942	0.005	1.039	0.015	0.686	0.007	0.712	0.007	329
SPMS2030	25	2.800	0.020	12.20	0.12	0.958	0.005	1.032	0.014	0.696	0.007	0.719	0.007	295
SPMS3040	35	2.844	0.020	12.11	0.12	0.972	0.005	1.060	0.015	0.713	0.007	0.755	0.008	288
SPMS4050	45	3.046	0.021	13.29	0.13	0.957	0.005	1.019	0.014	0.695	0.007	0.708	0.007	277
SPMS5059	54.5	2.958	0.021	13.12	0.13	0.968	0.005	0.980	0.014	0.684	0.007	0.670	0.007	266
SPVF0010	5	2.644	0.019	10.22	0.10	0.973	0.005	1.070	0.015	0.784	0.008	0.839	0.008	349
SPVF1020	15	2.799	0.020	12.29	0.12	0.966	0.005	1.009	0.014	0.691	0.007	0.698	0.007	318
SPVF2030	25	2.746	0.019	12.23	0.12	0.996	0.005	0.992	0.014	0.681	0.007	0.675	0.007	258
SPVF3040	35	3.022	0.021	12.66	0.13	1.019	0.005	0.951	0.013	0.724	0.007	0.689	0.007	219
SPVF4050	45	3.106	0.022	12.71	0.13	1.061	0.005	0.928	0.013	0.742	0.007	0.688	0.007	208
SPVF5060	55	3.209	0.022	13.34	0.13	1.072	0.005	0.903	0.013	0.730	0.007	0.659	0.007	182
SPVF6067	63.5	3.152	0.022	13.30	0.13	1.058	0.005	0.920	0.013	0.719	0.007	0.661	0.007	191
DC1-8	115	3.134	0.022	15.23	0.15	0.995	0.005	1.003	0.014	0.624	0.006	0.626	0.006	179
DC1-26	620	3.026	0.021	14.71	0.15	0.997	0.005	1.004	0.014	0.624	0.006	0.627	0.006	172

(<sup>234</sup>U/<sup>238</sup>U) activity ratios calculated from measured <sup>234</sup>U/<sup>235</sup>U isotopic ratios assuming that <sup>238</sup>U/<sup>235</sup>U = 137.88 and using the following decay constant:  $\lambda_{238} = 1.551 \times 10^{-10} \text{ yr}^{-1}$  and  $\lambda_{234} = 2.826 \times 10^{-6} \text{ yr}^{-1}$  (Akovali, 1994; Cheng et al., 2000). Analytical uncertainties are 0.5%. (<sup>230</sup>Th/<sup>232</sup>Th) activity ratios calculated from measured <sup>232</sup>Th/<sup>230</sup>Th isotopic ratios using  $\lambda_{232} = 4.948 \times 10^{-11} \text{ yr}^{-1}$  and  $\lambda_{230} = 9.158 \times 10^{-6} \text{ yr}^{-1}$  (Cheng et al., 2000). Analytical precisions are 1% for the (<sup>230</sup>Th/<sup>232</sup>Th) activity ratios, 1% for the (<sup>238</sup>U/<sup>232</sup>Th) activity ratios and result in 1.4% for the (<sup>230</sup>Th/<sup>238</sup>U) activity ratios. Zr concentrations are from Jin et al. (2010). 'a' indicates activity ratio.

generally upward-decreasing values of (<sup>234</sup>U/<sup>238</sup>U) (Fig. 3a, b, c). (<sup>230</sup>Th/<sup>238</sup>U) ratios in the SPRT, SPMS, and SPVF profiles range from 1.036 to 1.052, from 0.980 to 1.096, and from 0.920 to 1.070, respectively (Table 1, Fig. 2). These values increase gradually towards the surface, displaying an opposite trend compared to the (<sup>234</sup>U/<sup>238</sup>U) activity ratios (Fig. 3d, e, f). Indeed, (<sup>234</sup>U/<sup>238</sup>U) and (<sup>230</sup>Th/<sup>238</sup>U) ratios for SSHO samples show a strong anti-correlation (Fig. 2). (<sup>230</sup>Th/<sup>232</sup>Th) ratios in the SPRT, SPMS, and SPVF profiles range from 0.692 to 0.701, from 0.670 to 0.755, and from 0.659 to 0.839, respectively (Table 1).

### 3.2. U and Th concentrations

Measured U and Th concentrations in all regolith samples range from 2.64 to 3.21 ppm and 12.11 to 13.34 ppm, respectively, values that are generally lower than the range in bedrock concentrations (3.03 to 3.13 ppm and 14.71 to 15.23 ppm, Table 1).

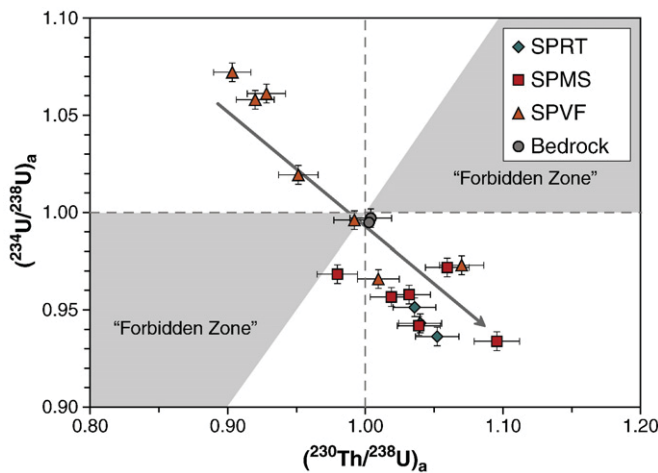


**Fig. 2.** Measured (<sup>234</sup>U/<sup>238</sup>U) and (<sup>230</sup>Th/<sup>238</sup>U) activity ratios for regolith samples from the south planar ridge top (SPRT), the south planar middle slope (SPMS), the south planar valley floor (SPVF), and two bedrock samples from DC-1. Grey area indicates the so-called “Forbidden Zone” (e.g., Dequincey et al., 2002). SSHO samples generally plot outside of the “forbidden zone”. The arrow indicates the general evolution of regolith samples with depths moving towards the surface, consistent with a dual process of both gain and loss of U-series isotopes and mobility of <sup>234</sup>U > <sup>238</sup>U > <sup>230</sup>Th (see text).

To evaluate the loss or gain of elements in a weathering profile (especially to correct for the effects of regolith expansion/compaction and for relative concentration changes due to changes of other elements in the regolith), concentration (C) of an immobile (i.e. conservative) element *i* is commonly used to compare with the relative loss or gain of a more mobile element (*j*) by calculating the mass transfer coefficient  $\tau_{ij}$  (e.g., Brimhall and Dietrich, 1987):

$$\tau_{ij} = \frac{C_{j,w}}{C_{j,p}} \cdot \frac{C_{i,p}}{C_{i,w}} - 1 \quad (1)$$

Positive  $\tau_{ij}$  values indicate the extent of enrichment of element *j* and negative values define the fractional depletion. A value of zero means that element *j* is as immobile in the weathered regolith (*w*) as the assumed immobile element *i* with respect to parent material (*p*). Elements that are commonly immobile in soils include Zr, Ti and Nb (Brimhall and Dietrich, 1987; Chadwick et al., 1990; Taylor and Blum, 1995; White et al., 1996; Price et al., 2005).

To calculate  $\tau$  values for the SSHO regolith, we used the same parent composition as we assumed previously (Jin et al., 2010), i.e., the average of concentrations of core material (DC1) drilled in northern ridge top sampled between 0.3 m and 20 m. Previous study at SSHO has identified Zr, which has been observed to occur in the relatively insoluble and stable mineral zircon in the Rose Hill shale, to be the most immobile element in the analyzed regolith samples (Jin et al., 2010).

The calculated  $\tau_{Zr,j}$  values for <sup>238</sup>U and <sup>232</sup>Th are shown in Figs. 4 and 5. For all regolith samples,  $\tau_{Zr,U}$  values vary from 0.00 to −0.57 and decrease generally towards the surface (Fig. 4). All  $\tau_{Zr,Th}$  values range from −0.14 to −0.66, also decreasing gradually towards the surface (Fig. 5).

## 4. Discussion

### 4.1. Mobility of <sup>238</sup>U and <sup>232</sup>Th during regolith formation

$\tau_{Zr,U}$  values show depletion profiles (Brantley and White, 2009) for all three cores along the planar transect at SSHO (Fig. 4). Thus, as bedrock dissolves and disaggregates to form regolith, U is readily released and lost, consistent with the notion that U is mobile under near-surface environments. Surprisingly,  $\tau_{Zr,Th}$  values also show depletion

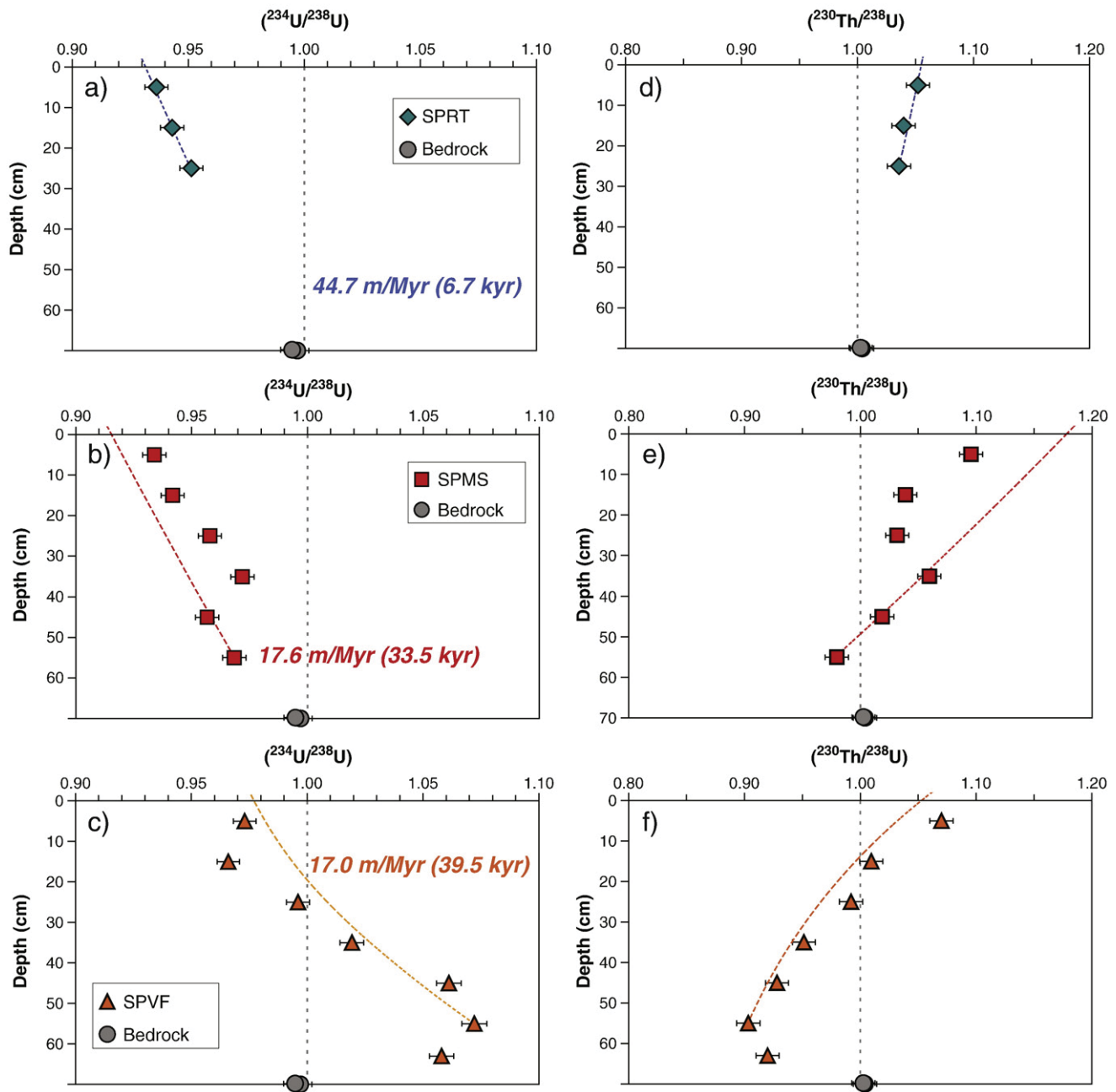


**Fig. 3.** Measured  $^{234}\text{U}/^{238}\text{U}$  and  $^{230}\text{Th}/^{238}\text{U}$  activity ratios for regolith samples from the ridge top profile (SPRT), the middle slope profile (SPMS), and the valley floor profile (SPVF) plotted against regolith depth.  $^{234}\text{U}/^{238}\text{U}$  and  $^{230}\text{Th}/^{238}\text{U}$  activity ratios of the two DC-1 bedrock samples are also shown. Dashed lines indicate  $^{234}\text{U}/^{238}\text{U}$  and  $^{230}\text{Th}/^{238}\text{U}$  activity ratios as a function of regolith depth calculated with parameters from Table 2 for each regolith profile using the model described in the text. Regolith production rates and residence times (in parentheses) for each profile are indicated. For each profile, the regolith depth is approximately 5 cm deeper than the deepest symbol.

profiles (Fig. 5). Normally, Th is immobile and particle-reactive during water–rock interaction due to the extremely low solubility of Th-containing phases (e.g., Rosholt et al., 1966; Latham and Schwarcz, 1987a,b; Gascoyne, 1992; Chabaux et al., 2003a). However, the negative  $\tau_{\text{Zr,Th}}$  values at SSHO indicate significant loss of Th during regolith formation. The extent of Th loss is similar to and sometimes greater than U (Figs. 4 and 5).

Enhancement of Th mobility during weathering could be partly explained by the presence of dissolved organic acids in the shallow soil profiles and formation of soluble Th-organic complexes or colloids (Langmuir and Herman, 1980; Chabaux et al., 2008). Such an increased Th mobility due to organic matter has been previously documented in studies of organic-rich river waters (e.g., Viers et al., 1997). Indeed, at SSHO, dissolved organic carbon in soil water col-

lected from lysimeters along the southern transect has been shown to vary from about 0.9 to 28 ppm (unpub. data), within the range that could significantly increase Th solubility in water (Langmuir and Herman, 1980).

Furthermore, similar depletion profiles are observed for the major elements Mg, K, Al, Fe, and Si in these regolith samples (Jin et al., 2010). Based on these regolith data and on stream chemistry data at SSHO, Jin et al. (2010) suggested that the transformation of illite and “chlorite” to vermiculite and kaolinite is accompanied by loss of micron-sized particles. They concluded that Mg, K, and some of the Si are released to the stream as solutes, but the less soluble elements Al and Fe are lost predominantly through sub-surface transport of particles larger than  $1.3\ \mu\text{m}$ , i.e. particles that were filtered out by suction lysimeters (Jin et al., 2010). The observations are consistent

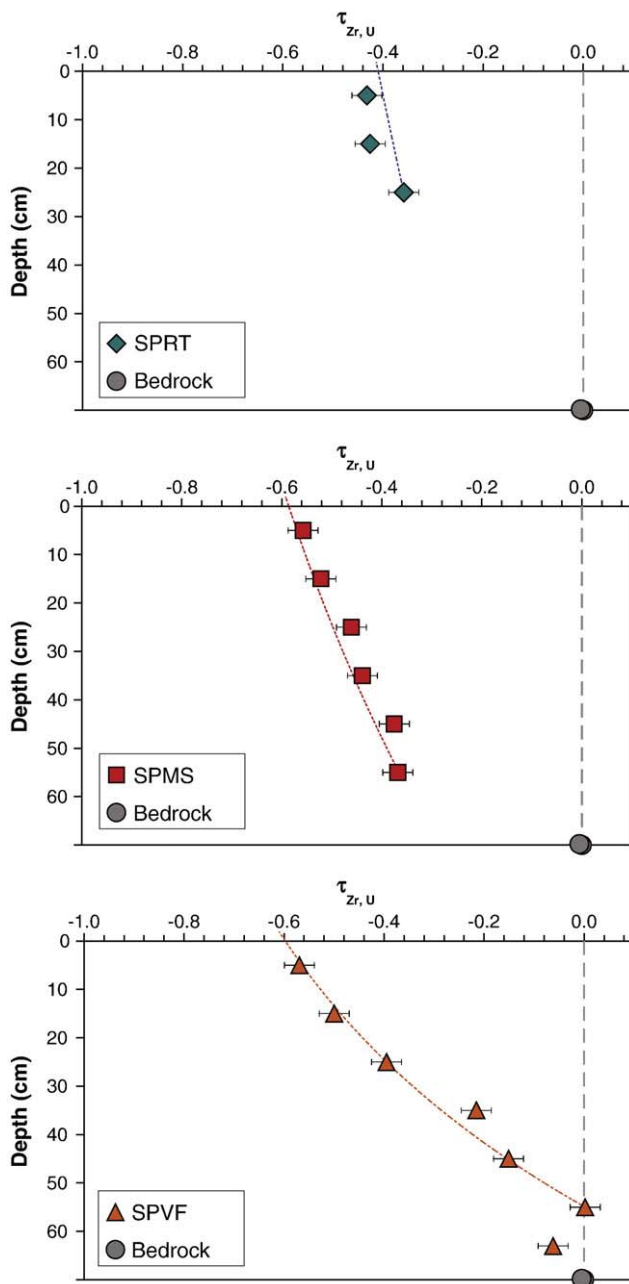


**Fig. 4.** Calculated  $\tau$  values of  $^{238}\text{U}$  with Zr as reference immobile element for regolith samples from SPRT, SPMS and SPVF. To complete the  $\tau$  calculations, a composition of unaltered parent material was determined from the average of samples drilled at DC-1 as described previously (Jin et al., 2010). Errors in  $\tau$  include the uncertainties of measured U and Zr concentrations as well as the error incurred due to heterogeneity of parent material (Jin et al., 2010). Dashed lines indicate  $\tau_{\text{Zr,U}}$  values calculated using the model with parameters from Table 2 for each profile (see text for details).

with loss of particles of secondary kaolinite or Fe + Al + Si-oxyhydroxides, presumably also containing organic material. This mechanism could explain the observed Th depletion profiles if Th were released during weathering of clay minerals but re-adsorbed onto particles. Given that relatively limited overland flow has been observed in the catchment (Qu and Duffy, 2007), the fine particles are thought to be translocated by flowing soil waters. Indeed, sub-surface particle transport is presumed to be promoted at SSHO because the field conditions are characterized by high infiltration rates, high soil moisture contents, and flow through macropores (Jin et al., 2010).

Furthermore, in these regolith samples, the mass loss of Th is strongly positively-correlated with the mass loss of Fe and Al ( $R^2 = 0.98$ ), again

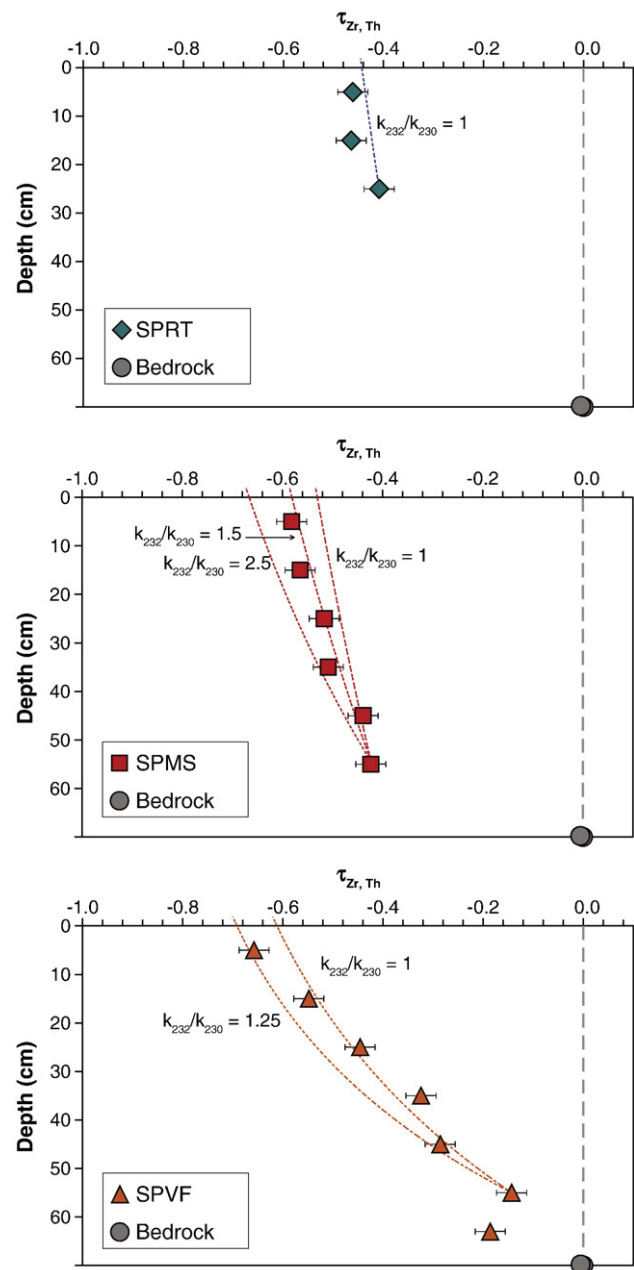


**Fig. 5.** Calculated  $\tau$  values of  $^{232}\text{Th}$  with Zr as reference immobile element for regolith samples from SPRT, SPMS, and SPVF. Dashed lines indicate  $\tau_{\text{Zr,Th}}$  values as a function of depth calculated with parameters from Table 2 for each profile, and lines calculated with different  $k_{232}/k_{230}$  ratios are indicated (see text for details).

consistent with fine particles or/colloids playing an important role for the observed Th loss. The loss of fine particles/colloids could also enhance U mobility above the mass loss of U as solute.

Values of  $\tau_{\text{Zr,U}}$  and  $\tau_{\text{Zr,Th}}$  in the deepest regolith samples of the SPRT and SPMS profiles do not reach zero at the regolith–bedrock interface (Figs. 4 and 5). Therefore, these samples have been significantly altered with respect to the parent bedrock. Such alteration at this depth was also observed as losses in major elements (Jin et al., 2010). Given that *rock fragments* sampled throughout the catchment from the bottom of profiles are compositionally similar to the average composition of parent bedrock, Jin et al. (2010) argued that the 10–20 cm thick layer lying directly below the regolith–bedrock interface is comprised of physically fractured but chemically unaltered shale together with chemically altered but difficult-to-sample sand/silt/clay. Thus, the bedrock–regolith interface defined

here by hand augering is a physical boundary to augering but not the chemical boundary defined by the lower limit of chemical weathering. Hypothetically, for example, the 10-cm layer just below augering at SPRT and SPMS sites could consist of ~60–80% rock fragments (observed in augered samples) identical to bedrock composition with 40–20% sand/silt/clay that is depleted 100% in Mg and K, ~60–90% in Fe, and ~80–100% in Al. When extrapolated versus depth, the depletion data are consistent with a depth to “bedrock” of ~1 m, where bedrock is now defined as lack of alteration in these elements. Of course, even at that depth the “bedrock” is not pristine: Jin et al. (2010) proposed that carbonate minerals may have dissolved to completion in the northern ridge top at 22 m depth and feldspar may begin dissolving at 6 m depth. Importantly, we note that the ( $^{234}\text{U}/^{238}\text{U}$ ) ratio at 1 and 6 m as sampled in bedrock is at secular equilibrium as discussed in next section: we conclude that depth to bedrock that is chemically unaltered with respect to U coincides with the depth of bedrock chemically unaltered with respect to Mg, K, Fe, and Al.

#### 4.2. Fractionation of $^{238}\text{U}$ , $^{234}\text{U}$ and $^{230}\text{Th}$ during regolith formation

In addition to the observed mass loss of U and Th, U-series activity ratios in regolith show significant fractionation from the two bedrock measurements (Figs. 2 and 3). Generally upward-decreasing values of ( $^{234}\text{U}/^{238}\text{U}$ ) are exhibited in every profile (Fig. 3a, b, c). This pattern is consistent with the typical behavior of U-series isotopes observed during chemical weathering of profiles where duration of weathering increases upward and regolith mixing is minimal (e.g., Chabaux et al., 2003a, 2008). More loss of the lighter isotope of U from regolith is consistent with enhanced mobility due to the phenomenon of alpha decay. Although not measured here, fluids from early stages of chemical weathering have been observed to have ( $^{234}\text{U}/^{238}\text{U}$ ) > 1 in other natural systems as well as in leaching experiments (e.g., Chabaux et al., 2003a; Andersen et al., 2009). The observed trend of ( $^{234}\text{U}/^{238}\text{U}$ ) ratios in these profiles is thus consistent with an increase in weathering intensity and duration towards the surface and rates of regolith mixing that are slow enough to not obscure weathering trends. Indeed, bioturbation is relatively ineffective in mixing the soils in New England where snow cover is significant (Kaste et al., 2007). Given the relatively similar climate, mixing processes may be slower than weathering for the SPRT, SPMS, and SPVF profiles at SSHO as argued previously for the major elements (Jin et al., 2010).

Unlike the bedrock sampled at 1 and 6 m depth, even the deepest regolith samples are characterized by ( $^{234}\text{U}/^{238}\text{U}$ ) ratios that are at disequilibrium (Fig. 3a, b). This is consistent with the inference made based on the concentrations of U, Th, and major elements that the upper 1-meter interval or so of non-augerable bedrock underlying regolith is nonetheless chemically altered: values of  $\tau$  for depleted elements returns to zero in SPRT and SPMS only at depths below the regolith–bedrock interface (Figs. 4 and 5). Furthermore, given that we have not observed significant depletion in Mg, K, Fe, and Al in the rock fraction in the deepest regolith samples or rock chips from the bedrock core (Jin et al., 2010), loss of  $^{234}\text{U}$  is inferred to occur as rock fragments transform to sand/silt/clay. Jin et al. (2010) reported the bulk regolith samples exhibit BET surface area of about 25 m<sup>2</sup>/g, whereas the surface area of the bedrock was presumably significantly lower. Therefore, based on the calculations above, the Rose Hill shale had to weather to produce at least 20% sand/silt/clay with this higher surface area to lose measurably significant amounts of  $^{234}\text{U}$  than  $^{238}\text{U}$  by direct ejection during alpha decay or due to incongruent dissolution.

In contrast to SPRT and SPMS, the deep regolith samples of the SPVF profile show ( $^{234}\text{U}/^{238}\text{U}$ ) ratios greater than 1 (Fig. 3c). These high ratios are consistent with input of U with ( $^{234}\text{U}/^{238}\text{U}$ ) > 1 in the profile. Such gains of U in regolith have been documented in previous U-series studies such as in soil profiles from Africa and Australia (DeQuincey et al., 2002; Chabaux et al., 2003b; Dosseto et al., 2008b), and in river

sediments from Asia, South America, and Europe (Andersson et al., 1998; Dosseto et al., 2006a; Granet et al., 2007, 2010). U inputs are also broadly consistent with the relatively soluble nature of U in the weathering environment (e.g., Chabaux et al., 2003a). For the sites described in previous studies, the U inputs are interpreted to reflect U that was precipitated or adsorbed from soil pore waters or from river waters that contain U characterized by ( $^{234}\text{U}/^{238}\text{U}$ ) > 1. Generally, the input of U has been attributed to co-precipitation or sorption of U in secondary Fe-hydroxides or clay minerals (Ames et al., 1983; Shirvington, 1983; Andersson et al., 1998; Duff et al., 2002; Chabaux et al., 2003a, 2008 and references therein). Similar processes could occur at SSHO as secondary Fe-hydroxides or clay minerals were observed to be common, especially in mid-slope and valley floor profiles (Jin et al., 2010).

( $^{230}\text{Th}/^{238}\text{U}$ ) ratios in the SPRT, SPMS, and SPVF profiles increase gradually towards the surface, displaying an opposite trend compared to the ( $^{234}\text{U}/^{238}\text{U}$ ) activity ratios (Fig. 3d, e, f). Such trends can be attributed to the differing behaviors of  $^{230}\text{Th}$  and  $^{238}\text{U}$  isotopes (Gascoyne, 1992): Th is less mobile, generally resulting in higher ( $^{230}\text{Th}/^{238}\text{U}$ ) ratios (> 1) in the residual weathering products and lower ( $^{230}\text{Th}/^{238}\text{U}$ ) ratios (< 1) in the weathering fluids (e.g., Vigier et al., 2001; Chabaux et al., 2003a; Dosseto et al., 2006a; Chabaux et al., 2008). While most of the regolith samples have ( $^{230}\text{Th}/^{238}\text{U}$ ) ratios > 1 as expected, a few deep regolith samples from the SPMS and SPVF profiles have ( $^{230}\text{Th}/^{238}\text{U}$ ) activity ratios < 1 (Fig. 3e, f). This observation is consistent with addition of U to the profiles as evidenced by the ( $^{234}\text{U}/^{238}\text{U}$ ) activity ratios.

$^{230}\text{Th}$  is less mobile compared to  $^{238}\text{U}$  in these regolith samples (Fig. 3), which may appear contradictory to the overall mobile behavior of Th (and by inference,  $^{232}\text{Th}$ ) as documented by the trend of decreasing  $\tau_{\text{Zr,Th}}$  values towards the surface. This latter trend indicates that the mobility of  $^{232}\text{Th}$  is similar to that of  $^{238}\text{U}$  during weathering in this system (Figs. 4 and 5). The different behaviors of  $^{230}\text{Th}$  and  $^{232}\text{Th}$  isotopes during regolith formation and the characteristic depletion profiles exhibited by U and Th will be further discussed in the following sections.

### 5. Model-derived regolith production rates and residence times

Determination of chemical weathering rates or residence times in a weathering profile from U-series disequilibrium relies on the use of a realistic model for U and Th mobility (e.g. Ghaleb et al., 1990; Scott et al., 1992; Vigier et al., 2001; DeQuincey et al., 2002; Chabaux et al., 2003a; Maher et al., 2004; DePaolo et al., 2006; Chabaux et al., 2008; Dosseto et al., 2008b; Bourdon et al., 2009). At SSHO, ( $^{234}\text{U}/^{238}\text{U}$ ) and ( $^{230}\text{Th}/^{238}\text{U}$ ) ratios are consistent with increasing extent of weathering and increasing residence times upward in the profile. The mobility of isotopes decreases in the order  $^{234}\text{U} > ^{238}\text{U} > ^{230}\text{Th}$ . In addition to the loss of U-series isotopes due to chemical weathering and translocation of fine particles/colloids, some of the regolith profiles appear also to have gained U. Such a scenario is consistent with both gain and loss of U-series isotopes as observed in other systems (e.g., DeQuincey et al., 2002).

#### 5.1. Model description

We develop a model to interpret the data that is similar to the model of Dosseto et al. (2008b) developed for a weathering regolith profile in Australia. Similar approaches have been used to solve for residence times of river sediments in catchments around the world (e.g., Vigier et al., 2001, 2005, 2005, 2006; Dosseto et al., 2006a,b,c; Granet et al., 2007). The system of equations summarized below describes the three positions SPRT, SPMS, and SPVF as one-dimensional systems of upward moving regolith material. It is assumed that each site is experiencing an input of U-series isotopes that is constant at every depth. Only at the ridge top (SPRT) is the input rate of U-series isotopes equal to zero.

U in the Rose Hill shale is presumed to reside in the primary clay and Fe oxide minerals. The depth interval within which these U-

containing minerals react to measurable extent with chemically non-equilibrated meteoric water is defined as the U weathering reaction front. Assuming the arguments of Jin et al. (2010) are correct, the lower depths of the weathering fronts for feldspar and carbonate lie at ~6 and ~22 m respectively in the bedrock. Nonetheless, secular equilibrium still is apparently maintained across these reaction fronts. The implication is that only minimal interfacial area between water and U-containing clay/Fe-oxides develops at the carbonate and feldspar fronts. Thus, the measurable U weathering front is located approximately at about a meter depth where the sand/silt/clay fraction reaches approximately 20%: at that depth, Mg, K, Al, and Fe begin to show significant depletion as clay minerals start to chemically weather.

From the perspective of the land surface, our model is based upon the conceptualization of the U weathering front as a zone maintained at some depth through which regolith particles move “upward”. During “ascent” of particles, the U-series isotopes are lost from the particle due to weathering and added due to sorption or co-precipitation reactions involving Fe-oxides, clay minerals, and fine particles/colloids. The mass conservation equations for  $^{238}\text{U}$ ,  $^{234}\text{U}$  and  $^{230}\text{Th}$  for each profile are then expressed as follows:

$$\frac{d^{238}\text{U}}{dt} = \frac{F_{238}}{\lambda_{238}} - k_{238}^{238}\text{U} - \lambda_{238}^{238}\text{U} \quad (2)$$

$$\frac{d^{234}\text{U}}{dt} = \frac{F_{234}}{\lambda_{234}} + \lambda_{238}^{238}\text{U} - k_{234}^{234}\text{U} - \lambda_{234}^{234}\text{U} \quad (3)$$

$$\frac{d^{230}\text{Th}}{dt} = \frac{F_{230}}{\lambda_{230}} + \lambda_{234}^{234}\text{U} - k_{230}^{230}\text{Th} - \lambda_{230}^{230}\text{Th} \quad (4)$$

Here,  $F_{238}$ ,  $F_{234}$ , and  $F_{230}$ , the input rates of  $^{238}\text{U}$ ,  $^{234}\text{U}$ , and  $^{230}\text{Th}$ , represent the processes that add U-series isotopes into profiles. These source terms, reported in activity per unit time ( $\text{yr}^{-2}$ ), are considered to be constant with time (Ghaleb et al., 1990; Dequincey et al., 2002).  $F_{234}/F_{238}$  and  $F_{230}/F_{238}$  represent the ( $^{234}\text{U}/^{238}\text{U}$ ) and ( $^{230}\text{Th}/^{238}\text{U}$ ) activity ratios of the input sources, respectively.

The parameters  $k_{238}$ ,  $k_{234}$ , and  $k_{230}$  are first-order rate constants ( $\text{yr}^{-1}$ ) for release of  $^{238}\text{U}$ ,  $^{234}\text{U}$ , and  $^{230}\text{Th}$  from U- and Th-containing minerals (Latham and Schwarcz, 1987a,b; Plater et al., 1992; Vigier et al., 2001), i.e. it is assumed that U- and Th-containing phases dissolve at rates equal to  $k_{238}^{238}\text{U}$ ,  $k_{234}^{234}\text{U}$  and  $k_{230}^{230}\text{Th}$ .  $\lambda_{238}$ ,  $\lambda_{234}$ , and  $\lambda_{230}$  are the decay constants for  $^{238}\text{U}$ ,  $^{234}\text{U}$ , and  $^{230}\text{Th}$  ( $\text{yr}^{-1}$ );  $t$  is the residence time (yr) of particles in the zone where these elements weather.  $k_{234}/k_{238}$  and  $k_{230}/k_{238}$  describe the relative rates of loss of  $^{234}\text{U}$  and  $^{230}\text{Th}$  respectively to  $^{238}\text{U}$  during leaching. Importantly, the ratio  $k_{234}/k_{238}$  documents the ratio of the release rate of  $^{234}\text{U}$  due to phenomena related to alpha particle damage to the crystal lattice ( $k_{234}$ ) compared to the release rate due to congruent dissolution of the mineral ( $k_{238}$ ).

In a weathering profile, the average integrated regolith production rate  $P$  (m/Myr) can be expressed as the following equation:

$$P = \frac{h}{t} \quad (5)$$

where  $t$  corresponds to the duration for a particle moving from a reference position to its sample position and  $h$  is the vertical distance between these two positions (Appendix B).

For each regolith profile at SSHO, with the measured ( $^{234}\text{U}/^{238}\text{U}$ ) and ( $^{230}\text{Th}/^{238}\text{U}$ ) ratios as input values (the mass loss of U and Th are not used as input values), the unknown parameters ( $F_{238}$ ,  $F_{234}$ ,  $F_{230}$ ,  $k_{238}$ ,  $k_{234}$ ,  $k_{230}$ , and  $P$ ) can be fully solved by using the Matlab™ *lsqnonlin* function (Table 2, Appendix B). To eliminate the number of unknown parameters for simplicity and tractability of the model, we assume the unknown parameters ( $F_{238}$ ,  $F_{234}$ ,  $F_{230}$ ,  $k_{238}$ ,  $k_{234}$ ,  $k_{230}$ ) are constant over time for each weathering profile. Instead of solving for multiple  $t$  for

individual samples within the profile, we also assume a constant production rate ( $P$ ) for each profile. Thus, the derived production rate  $P$  represents an average rate over the duration of weathering for each profile. With the derived rate  $P$ , the total duration of weathering (residence time in regolith) for each profile is then calculated with Eq. (5) as discussed in Appendix B.

It is important to note that in the original model of Dequincey et al. (2002), both the U-series input and output terms were conceptualized as U carried as solutes. In fact, transport of fine particles along a hillslope might also play a role in transporting U-series isotopes as discussed here. In our model, we implicitly lump transport of solutes and particles together into the rate terms ( $F$ ) and also into the leaching coefficients ( $k$ ), because these chemical weathering mechanisms cannot be distinguished.

## 5.2. Model results

When the model is solved, the activity ratios ( $^{234}\text{U}/^{238}\text{U}$ ) and ( $^{230}\text{Th}/^{238}\text{U}$ ) are calculated as a function of regolith depth as shown in Fig. 3. The curves agree well with the measured ratios. The regolith production rates derived from the model decrease systematically with increasing distance from the ridge: ~45 m/Myr at SPRT, the highest point along the hillslope, ~18 m/Myr at SPMS, and ~17 m/Myr at SPVF (Table 2, Fig. 6). The duration of chemical weathering within the vertical regolith profile starting from the regolith–bedrock interface, termed here the apparent regolith residence time, increases significantly with distance away from the ridge, from ~7 kyr for the SPRT, to 34 kyr at the SPMS site, and to 40 kyr at the SPVF site (Table 2, Fig. 6). Notice that our model, based on vertical movement only, is only strictly applicable to SPRT. The residence time and regolith production rates at SPRT are thus easily interpreted. In contrast, the times calculated for SPMS and SPVF are the *apparent equivalent residence times* needed for a hypothetical particle to move vertically from the base to the top of regolith at those locations while establishing an equivalent U-series isotopic ratios as the real particle achieved while actually moving both vertically and downslope along the transect.

Model-derived  $k_{238}$  values vary from  $1.4 \times 10^{-5}$  to  $3.0 \times 10^{-5} \text{ yr}^{-1}$  (Table 2), within the range of  $^{238}\text{U}$  leaching coefficients derived from weathering profiles or river sediments with similar weathering time scales (Dosseto et al., 2008a). Model-derived  $k_{234}/k_{238}$  ratios from the three profiles are all greater than one, varying from 1.12 to 1.26 (Table 2), consistent with the fact that  $^{234}\text{U}$  isotope is preferentially lost to the weathering fluids compared to  $^{238}\text{U}$  (e.g., Fleischer, 1980). Such a range of values agrees well with many field and experimental studies of U isotopic fractionation during water–rock interaction (e.g., Vigier et al., 2001; Dequincey et al., 2002; Dosseto et al., 2008b; Andersen et al., 2009).

$k_{230}/k_{238}$  ratios from the model range from 0.53 to 1.16 at SSHO (Table 2), indicating that  $^{230}\text{Th}$  during weathering is generally less mobile than  $^{238}\text{U}$ , but not completely immobile.

## 5.3. $^{238}\text{U}$ mass balance along the planar transect

Based on the model parameters (Table 2), the total  $^{238}\text{U}$  input and output are calculated for each profile and increase down slope (Fig. 6). Here we calculate the  $^{238}\text{U}$  mass balance for the 2D transect to test whether these  $^{238}\text{U}$  fluxes could be U carried downslope by subsurface fluid flow and fine particles from SPRT to SPMS to SPVF (Fig. 6). This mass balance was not assumed in setting up the model.

To complete this check, we note that U input from wet precipitation is normally negligible (e.g., Chabaux et al., 2005). We also assume no significant U input from dust. Thus, U-series isotopes are lost through weathering and radioactive decay at the SPRT profile but no U is added. In contrast, the U input to the SPMS profile is calculated to be non-negligible by the model and we can check if it can be provided by the output calculated from SPRT. Similarly, the U output

**Table 2**

Regolith production rates, residence times, leaching coefficients, and U-series inputs derived from the model.

Sample profile	Regolith thickness (cm)	Regolith production rate (m/Myr)	Residence time (kyr)	$k_{238}$ ( $10^{-5} \text{ yr}^{-1}$ )	$k_{234}/k_{238}$	$k_{230}/k_{238}$	$F_{238}/(\lambda_{238}^{238}\text{U}_0)$ ( $10^{-6} \text{ yr}^{-1}$ )	$F_{234}/F_{238}$	$F_{230}/F_{238}$
SPRT	30	$44.7 \pm 11.6$	6.7	$1.49 \pm 0.35$	$1.26 \pm 0.04$	$0.72 \pm 0.08$			
SPMS	59	$17.6 \pm 12.7$	33.5	$1.41 \pm 1.55$	$1.12 \pm 0.11$	$0.53 \pm 0.34$	$0.31 \pm 0.19$	$0.29 \pm 0.39$	$2.59 \pm 0.97$
SPVF	67	$17.0 \pm 13.9$	39.5	$3.00 \pm 1.65$	$1.16 \pm 0.08$	$1.16 \pm 0.05$	$1.15 \pm 0.39$	$2.07 \pm 1.04$	$5.64 \pm 2.85$

The model is solved multiple times to obtain 1000 sets of solutions for each profile as described in Appendix B. The model parameters are taken as the average of the sets of solution values and the uncertainties are calculated as the standard deviation on the sets of values.  $^{238}\text{U}_0$  is initial number of  $^{238}\text{U}$  atoms/g in the starting material of the system (Appendix B).

from SPMS is calculated to be non-negligible and it can be checked as an input to SPVF. Importantly, U inputs calculated by the model are accounted for with the U outputs from the site above (Fig. 6). This calculation demonstrates that no additional U input fluxes from deep groundwater or along-channel flow in the riparian zone at the valley floor.

#### 5.4. Mobility of $^{238}\text{U}$ and $^{232}\text{Th}$ during regolith formation

By using model parameters (Table 2), the cumulative amount of  $^{238}\text{U}$  that is lost through chemical weathering over time can be calculated (Eq. 2) (Fig. 4). The loss of  $^{232}\text{Th}$  due to chemical weathering can be similarly calculated with the following equation:

$$\frac{d^{232}\text{Th}}{dt} = \frac{F_{232}}{\lambda_{232}} - k_{232}^{232}\text{Th} - \lambda_{232}^{232}\text{Th} \quad (6)$$

where  $\lambda_{232}$  is the decay constant of  $^{232}\text{Th}$ . Because no parameters of  $^{232}\text{Th}$  are directly derived in the previous model, we assume here that the  $^{232}\text{Th}$  leaching coefficient ( $k_{232}$ ) is similar to that of  $^{230}\text{Th}$  ( $k_{230}$ ) just for modeling purposes. This latter value reflects the enhanced solubility due to the presence of organic complexes as well as loss of Th due to transport of fine particles. We calculate the value of  $F_{232}$  from model-derived  $F_{230}$  and average regolith  $^{230}\text{Th}/^{232}\text{Th}$  for each profile, assuming that the transported Th is mainly in particle form.

Calculated  $\tau$  values for  $^{238}\text{U}$  from the model decrease gradually towards the surface and agree well with the observed loss of  $^{238}\text{U}$  for the SPRT, SPMS and SPVF profiles (Fig. 4), consistent with our conceptual model that as regolith particles move “upward” in the

profile, dissolution of clay minerals in shale gradually releases U into weathering fluids.

The  $\tau$  values for  $^{232}\text{Th}$  calculated from the model agree well with the observed loss of  $^{232}\text{Th}$  for the SPRT, and for most of the SPVF profiles (Fig. 5), suggesting that similar to U, Th is also lost from the profile, probably by transport of both weathering fluids and fine particles. However, the SPMS and the uppermost SPVF profiles show more  $^{232}\text{Th}$  depletion than the model predictions (Fig. 5). Such  $^{232}\text{Th}$  depletion can be explained by using  $k_{232}/k_{230}$  ratios greater than 1, e.g., ranging from 1.25 to 2.5 (Fig. 5). These higher ratios are consistent with the presence of enhanced mobility of  $^{232}\text{Th}$  relative to  $^{230}\text{Th}$  for these uppermost samples.

Similarly, while the measured ( $^{230}\text{Th}/^{232}\text{Th}$ ) ratios in SPRT and parts of the SPVF profiles agree well with the previous model calculations while assuming  $k_{232}/k_{230} = 1$ , the measured ( $^{230}\text{Th}/^{232}\text{Th}$ ) ratios in SPMS and uppermost SPVF profiles show higher values that can only be explained by using  $k_{232}/k_{230}$  ratios greater than 1 (Fig. 7). Because  $^{230}\text{Th}$  is produced from  $^{238}\text{U}$  and not necessarily associated with  $^{232}\text{Th}$ -rich particles, such a change of  $^{230}\text{Th}/^{232}\text{Th}$  ratios in the residual phases is consistent with a loss of  $^{232}\text{Th}$ -rich particles (presumably with no  $^{230}\text{Th}$ ). Similar enhanced mobility due to preferential removal of  $^{232}\text{Th}$  in different carrier phases has been previously reported in U-series studies: selective dissolution of minerals with high  $^{232}\text{Th}$  concentrations has been suggested to explain the higher ( $^{230}\text{Th}/^{232}\text{Th}$ ) ratios in the soils as compared to saprolite and bedrock in Australia (Dosseto et al., 2008b). Similarly, removal of detrital particles, i.e. the major carrier phase of  $^{232}\text{Th}$  in Baltic seawater columns, has been proposed to account for a large increase of ( $^{230}\text{Th}/^{232}\text{Th}$ ) in the Baltic seawater as compared to riverine inputs (Andersson et al., 1995; Porcelli et al., 2001).

#### 5.5. Regolith production and duration of chemical weathering at SSHO

Previous studies report regolith formation rates on the order of 5 to  $\sim 100$  m/Myr for a number of parent rock types, e.g., granodiorite and granite (Heimsath et al., 2000; Riebe et al., 2001, 2003, 2004a,b; Heimsath et al., 2005; Dosseto et al., 2008b), turbidite, sandstone and siltstone (Heimsath et al., 1997, 2001), and sedimentary and metamorphic rocks (Von Blanckenburg et al., 2004). Sedimentary rocks such as quartz-rich sandstones are generally less susceptible to alteration than igneous or metamorphic rocks, as they are already significantly weathered. This study shows however that the rate of formation of regolith and development of mineral–water interfacial area in the shale at SSHO occurs at a rather fast rate (17–45 m/Myr).

What controls these relatively fast regolith production rates? As observed by Jin et al. (2010), the deepest weathering reaction at SSHO is dissolution of ankerite, hypothesized to occur at 22 m below the surface. Above this at  $\sim 6$  m below the surface lies the onset of the weathering front for feldspar dissolution. Based on arguments presented here, the onset of the weathering front of clay minerals (major U carrier phases) occurs within the upper meter below the bedrock–regolith interface. Porosity changes accompany chemical changes over these depths. Rock density data is consistent with an increase in porosity by 5% over the interval from 20 to 5 m depth. These changes are attributed partly to chemical weathering of carbonate minerals and feldspar and partly to ice-wedging from

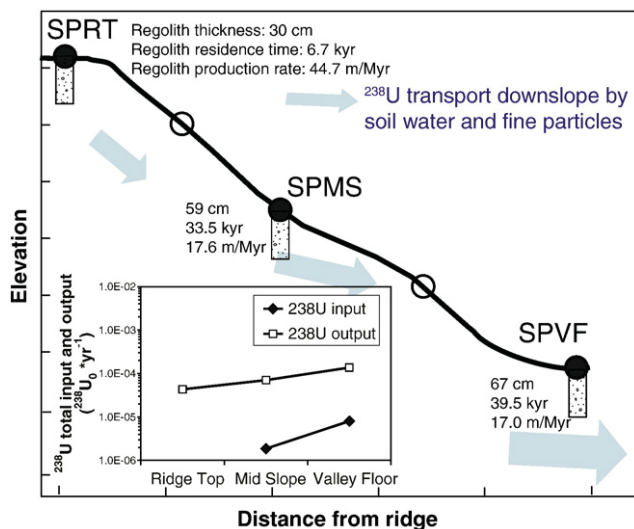


**Fig. 6.** a) Regolith thickness, residence time, and production rate calculated for the 2D planar transect at SSHO; b) Total input and output of  $^{238}\text{U}$  for each profile along the 2D transect, calculated with the model-derived U input rates and leaching coefficients (Table 2). Total input and output are described in units of  $^{238}\text{U}_0 \text{ yr}^{-1}$  where  $^{238}\text{U}_0$  in this figure is the initial number of  $^{238}\text{U}$  atoms in a 10 cm regolith column interval with a unit area.

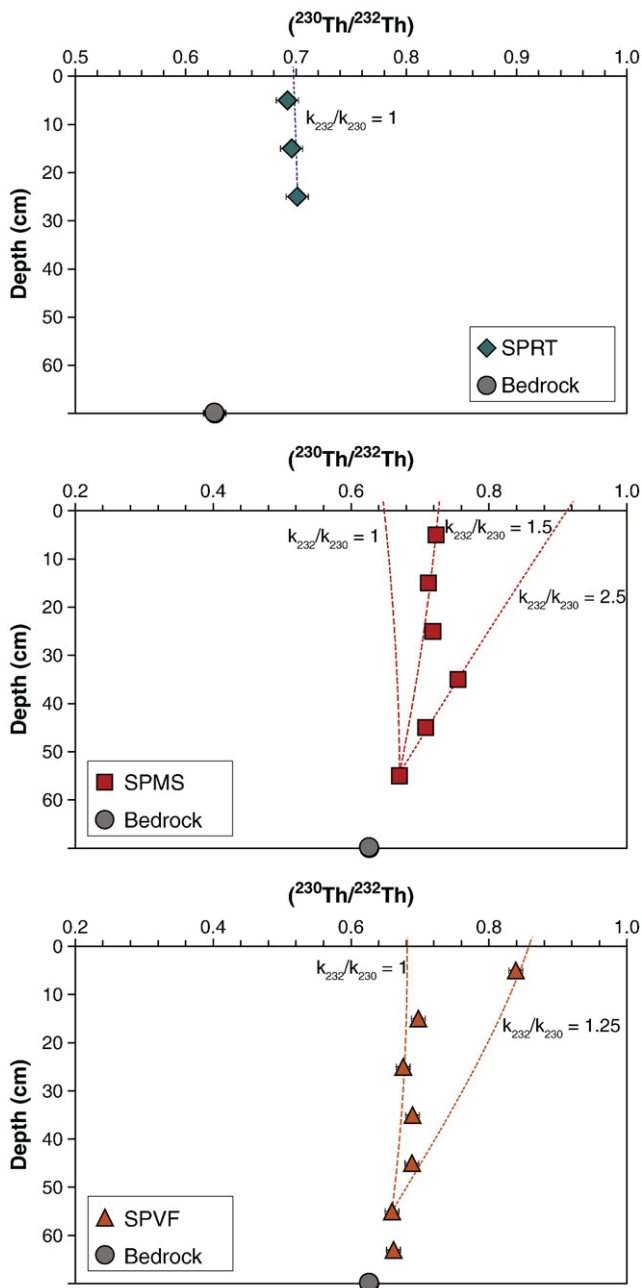


Fig. 7. Measured  $(^{230}\text{Th}/^{232}\text{Th})$  activity ratios for regolith samples from a) SPRT, b) SPMS, and c) SPVF.  $(^{230}\text{Th}/^{232}\text{Th})$  activity ratios of two DC-1 bedrock samples are also shown. Dashed lines indicate  $(^{230}\text{Th}/^{232}\text{Th})$  activity ratios as a function of regolith depth calculated with parameters from Table 2; lines calculated with different  $k_{232}/k_{230}$  ratios are indicated (see text for details).

peri-glacial activities (Jin et al., 2010). Fracture-inducing reactions have been documented or hypothesized to accelerate the rates of weathering compared to non-fractured rocks for other systems (Fletcher et al., 2006; Buss et al., 2008; Brantley and White, 2009). We infer that increases in porosity due to fracturing, induced by chemical and physical factors, explain the relatively high regolith production rates at SSHO.

The surprisingly fast production rates of bedrock–regolith interface at SSHO are consistent with shale playing an important role in global elemental cycles and  $\text{CO}_2$  consumption fluxes (Amiotte-Suchet et al., 2003). Thus, the wide distribution of shale worldwide and the ease of fracturing and high rate of particle loss of this rock type may accentuate the importance of shale in global weathering.

Regolith production rate at SPRT ( $\sim 45$  m/Myr) is significantly different from the production rates at SPMS and SPVF ( $\sim 17$  m/Myr). The regolith production rate at SPRT is also greater than the catchment-averaged erosion rate at SSHO ( $\sim 15$  m/Myr; Jin et al., 2010), perhaps suggesting that the regolith thickness is changing over time. These comparisons are consistent with the conclusion that the SSHO hillslope has not achieved steady state with respect to either regolith thickness or topography.

At SSHO, the regolith residence time increases with distance away from the ridge, from  $\sim 7$  kyr for the SPRT, to 34 kyr at the SPMS site, and to 40 kyr at the SPVF site (Table 2). Despite the uncertainties in the regolith production rates, the SPMS and SPVF profiles each have duration of chemical weathering that is significantly longer than the SPRT profile. The last peri-glacial conditions at SSHO resulted from the advance of the late Wisconsinan Ice-sheet into Pennsylvania about  $\sim 27$  kyr ago, changing to modern conditions  $\sim 15$  kyr ago (Braun, 2005). Thus, the SPRT profile is characterized by regolith that formed more recently than the last peri-glacial period. By contrast, the model suggests that SPMS and SPVF profiles have some regolith that formed before the last peri-glacial period. The model is thus consistent with the presence of pre-glacial regolith that has not yet been completely removed, again consistent with lack of geomorphic steady state for this SSHO hillslope.

In contrast to these results, in the Mackenzie Basin of Northern Canada, duration of chemical weathering estimated from U-series disequilibrium in river sediments was relatively short compared to the time since the last glaciation (Vigier et al., 2001). In that case, it was inferred that glaciation completely removed the pre-existing weathering profile. However, such a “reset” effect was not observed at SSHO, presumably because of the difference in geographic locations: indeed, during the last glacial period, the Mackenzie Basin was completely covered by an ice-sheet in northern Canada and was characterized by high glacial erosion rates, whereas SSHO was in a peri-glacial environment with relatively lower erosion rates (Braun, 1989).

With increasing distance away from the ridge (Fig. 1a), the regolith production rates at SSHO decrease systematically with increasing regolith thickness (Table 2). Several time-dependent factors that control temporal variations in chemical weathering rates have been proposed, including reactive surface area, nature and saturation state of weathering fluids, and formation of secondary minerals (e.g., White and Brantley, 2003; Maher et al., 2004; Fletcher et al., 2006; Anderson et al., 2007; Maher, 2010). The change of these factors over time could potentially explain the inverse correlation between regolith production rate and residence time observed at SSHO. For example, a high dissolution rate is favored for a thin regolith cover with short residence time, such as at the ridge top of SSHO, because of the availability of fresh materials, large reactive surfaces, and water chemistry far away from solubility equilibrium with respect to the silicate minerals. In contrast, a low mineral dissolution rate is expected under a thick regolith cover with long residence time, e.g., for the valley floor site. Regolith chemistry and mineralogy studies at SSHO are consistent with slower mineral dissolution in the valley floor as compared to ridgetop (Jin et al., 2010).

### 5.6. Regolith production function at SSHO

The variation in regolith production rate as a function of regolith thickness at SSHO (Fig. 8) is consistent with an exponential function:

$$P = P_0 e^{-\alpha h} \quad (7)$$

Here  $P$  is the regolith production rate (m/Myr),  $h$  is the regolith thickness (cm),  $P_0$  is the regolith production rate (m/Myr) with zero regolith thickness, and  $\alpha$  is the depth scaling factor ( $\text{cm}^{-1}$ ) (Fig. 8). Similar functions have been used in previous studies to describe the production rate of mobile soil from underlying saprolite (e.g., Cox, 1980;

Heimsath et al., 1997; Dietrich et al., 2003). The parameters in this function calculated from SSHO ( $R^2 = 0.97$ ,  $P_0 = 100.8$ ,  $\alpha = 0.0279$ ) are compatible with those inferred for mobile soil production rates in California, Oregon, and Australia based on the measurements of cosmogenic isotopes (Heimsath et al., 1997, 2000, 2001; Dietrich et al., 2003). For instance, it has been shown that  $P_0$  ranges from 50 to 2000 m/Myr, varying as a function of local lithology, climate, and tectonic uplift rates, whereas the depth scaling factors ( $\alpha$ ) lie within a narrow range from 0.02 to 0.04  $\text{cm}^{-1}$  (Dietrich et al., 2003). Such a narrow range of depth scaling factors and the exponential mobile soil production function have been previously explained by the inference that the conversion of non-mobile to mobile soil is mainly controlled by the variation with depth of the effects of physical weathering and biogenic disturbances such as animal burrowing, tree throw, and rooting (Heimsath et al., 1997; Roering et al., 2002; Dietrich et al., 2003).

At SSHO, both the U-series and major element depth profiles (Jin et al., 2010) are consistent with a minimum of regolith mixing within the studied SSHO profiles, especially for the lower depths, as expected in regolith where bioturbation is relatively ineffective due to significant snow cover (Kaste et al., 2007). Rather, it is inferred for SSHO that chemical weathering processes and physical peri-glacial processes have significantly weakened and broken up the bedrock such that physical–chemical processes may dominate over biological processes in regolith production (e.g., Cox, 1980; Minasny and McBratney, 1999). Nonetheless, downslope movement of soil is known to occur due to tree throw throughout the catchment and at this point, the precise location of the lowermost limit of the “mobile soil layer” is not well defined in the context of the present study.

To derive the soil production rates with the cosmogenic approach requires an assumption that the thickness of the mobile soil layer in regolith is constant and the derived soil production rates correspond to the conversion rates of soils from the underlying immobile layer (Heimsath et al., 1997). In contrast, the regolith production function presented here is derived from the U-series isotopes where no such assumption is required (e.g., Dosseto et al., 2008b). This case study illustrates that U disequilibrium analysis provides a new and independent tool to quantify the regolith production function in weathering profiles. The regolith production rates can be envisioned here as the result of the downward advance of the U weathering front over time, and thus it provides time information for production of the lower part of the regolith. In fact, the derived production rates here are complementary to the soil production rates derived from the previous cosmogenic studies (e.g., Heimsath et al., 1997) and the combination of these two approaches will provide valuable information to elucidate the factors that control the rates and mechanisms of regolith formation.

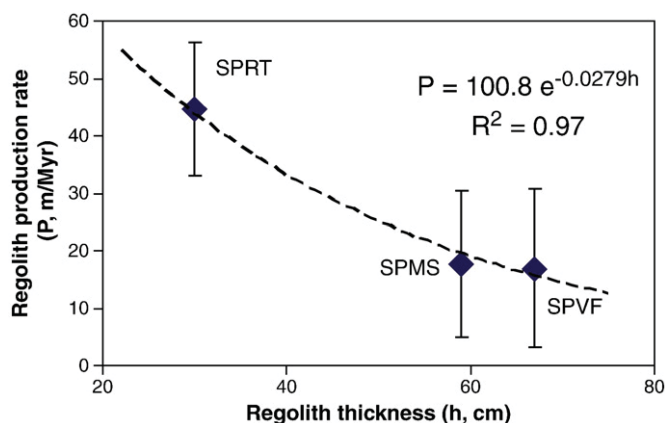


Fig. 8. Regolith production rates derived from the model plotted versus regolith thickness for three regolith profiles (SPRT, SPMS, and SPVF). Dashed line indicates the exponential fitted regolith production function.

## 6. Conclusions

To quantify regolith formation rates, we measured U-series isotopes ( $^{238}\text{U}$ ,  $^{234}\text{U}$ , and  $^{230}\text{Th}$ ) in three regolith profiles along a planar hillslope transect developed on shale bedrock in central Pennsylvania. Different from the bedrock, regolith samples show significant U-series disequilibrium and these activity ratios display depth trends consistent with the relative mobility of U and Th isotopes decreasing in the order  $^{234}\text{U} > ^{238}\text{U} > ^{230}\text{Th}$ . Depth profiles are explained by two processes: i) loss of U-series isotopes during water–rock interaction and ii) gain of U-series isotopes from upslope sites, e.g., U precipitated from circulating soil water and U and Th transported by particles.

Apparent equivalent regolith production rates calculated with U-series isotopes for these profiles decrease systematically from 45 m/Myr to 17 m/Myr, with increasing distance and regolith thickness from the ridge, suggesting that chemical weathering of shale at SSHO occurs actively at a rather fast rate. Regolith production rates at SSHO vary as an exponential function of regolith thickness. Apparent equivalent regolith residence times within these profiles range from 7 kyr to 40 kyr, increasing from the ridge to the valley floor. The presence of residence times longer than the last peri-glacial period ( $\sim 15$  kyr) may be consistent with lack of removal of pre-glacial regolith. Importantly, both chemical weathering reactions and sub-surface particle/colloid transport has been shown to contribute to mass losses of U and Th from the regolith at SSHO, as previously demonstrated for major elements (Jin et al., 2010).

For well-constrained field systems such as the hillslope studied here, the success of this method in estimating rates of regolith formation and duration of chemical weathering enhances our ability to use this technique in other environments to understand the response of regolith production to climate perturbations. The regolith production rates at SSHO also provide an important reference value for comparison to other critical zone observatories along both the lithology and climate gradients.

## Acknowledgements

This work benefitted from reviews by A. Dosseto, G. Hillel, and an anonymous reviewer, and editorial handling by P. Delaney. Discussions with P. Stille, P. Bierman, H. Lin, A. Dere, T. White, K. Singha, E. Kirby and R. Slingerland are also acknowledged. We thank Z. Ruge and B. Ketchum for help with regolith sampling. Logistical support and/or data were provided by the NSF-supported Susquehanna/Shale Hills Critical Zone Observatory. Financial support was provided by National Science Foundation Grant CHE-0431328 to SLB for Center for Environmental Kinetics Analysis and Grant EAR-0725019 to C. Duffy (Penn State) for Susquehanna Shale Hills Critical Zone Observatory. SLB and LM were partially funded by Department of Energy Grant DE-FG02-05ER15675 to SLB. Funding from the Region Alsace, France and the Laboratory network “REALISE” for LHyGeS (EOST), University of Strasbourg and CNRS to FC is also acknowledged.

## Appendix A. Analytical methods for U and Th isotopes

Samples consisted of all rock fragments, sand, silt, and clay recovered during augering. Bulk samples were air-dried and ground to pass through a 100- $\mu\text{m}$  sieve. About 100 mg powdered samples were weighed and spiked with a mixed artificial  $^{233}\text{U}$ – $^{229}\text{Th}$  tracer for measurements of both U–Th isotopic compositions and concentrations. The samples were completely dissolved using a three-step procedure with  $\text{HNO}_3$ – $\text{HF}$ ,  $\text{HClO}_4$ , and  $\text{HCl}$ – $\text{H}_3\text{BO}_3$  acids.

U and Th separation and purification were performed by conventional ion exchange chromatography following procedures developed at the Laboratoire d’Hydrologie et de Géochimie de

Strasbourg (LHyGeS), University of Strasbourg (France) (e.g., Granet et al., 2007; Pelt et al., 2008). U concentrations and activity ratios, ( $^{234}\text{U}/^{238}\text{U}$ ), were analyzed using  $\sim 70$  ng U. The measurements were performed on a Thermal Ionization Mass Spectrometer (TIMS) Thermo-Scientific Triton. U concentrations were calculated using the measured  $^{235}\text{U}/^{238}\text{U}$  isotopic ratios. ( $^{234}\text{U}/^{238}\text{U}$ ) activity ratios were calculated using the analyzed  $^{234}\text{U}/^{235}\text{U}$  ratios and assuming a constant  $^{235}\text{U}/^{238}\text{U}$  ratio of 137.88, with the following decay constant:  $\lambda_{238} = 1.551 \times 10^{-10} \text{ yr}^{-1}$  and  $\lambda_{234} = 2.826 \times 10^{-6} \text{ yr}^{-1}$  (Akovali, 1994; Cheng et al., 2000). The precision and accuracy of the U activity ratios were determined from analyses of the HU1 standard solution and the BEN rock standards. Over the data acquisition period, the mean of the HU1-standard analyses of ( $^{234}\text{U}/^{238}\text{U}$ ) is  $1.001 \pm 0.005$  ( $n=3$ ), was in good agreement with the laboratory 2008–2009 mean for ( $^{234}\text{U}/^{238}\text{U}$ ) of  $0.999 \pm 0.005$  ( $n=32$ ;  $2\sigma$ ) and consistent with secular equilibrium. In addition, two analyses of the BEN rock standard, spiked with  $^{233}\text{U}$ – $^{229}\text{Th}$  tracer, yielded a mean ( $^{234}\text{U}/^{238}\text{U}$ ) of  $1.002 \pm 0.002$  and a mean U concentration of  $2.465 \pm 0.008$  ppm, which are both consistent with the laboratory long-term mean values: ( $^{234}\text{U}/^{238}\text{U}$ ) =  $0.999 \pm 0.005$  ( $n=5$ ;  $2\sigma$ ) and  $\text{U} = 2.457 \pm 0.013$  ( $n=5$ ;  $2\sigma$ ), 2006–2009, and the reference values ( $\text{U} = 2.46$  ppm; Govindaraju, 1994). The reproducibility of U concentrations and

activity ratios by ID-TIMS was checked by duplicate analyses of 5 samples and is better than 0.5% and 0.4%, respectively.

$^{232}\text{Th}/^{230}\text{Th}$  isotopic ratios and Th concentrations were analyzed on  $\sim 600$  ng Th with the TIMS Thermo-Scientific Triton.  $^{230}\text{Th}$  and  $^{229}\text{Th}$  were measured on the central SEM detector and  $^{232}\text{Th}$  on a Faraday cup using the static collection mode. Th concentrations were determined using the measured  $^{232}\text{Th}/^{229}\text{Th}$  isotopic ratios.

During the course of this study, the reproducibility of Th isotopic ratio measurements, checked by the in-house standard solution Th-105, is  $\sim 1\%$  ( $n=3$ ). In addition, the two analyses of the BEN rock standard, spiked with the  $^{233}\text{U}$ – $^{229}\text{Th}$  tracer, yielded a mean ( $^{230}\text{Th}/^{238}\text{U}$ ) activity ratio of  $1.004 \pm 0.009$  ( $n=2$ ) and a mean Th concentration of  $10.723 \pm 0.079$  ppm ( $n=2$ ), which are consistent with secular equilibrium and the reference values (Th = 10.7 ppm; Govindaraju, 1994). The reproducibility of Th concentrations and activity ratios by ID-TIMS was checked by duplicate analyses of 4 samples and is better than 0.8% and 1.1%, respectively.

The total procedure blanks for U–Th isotopic and elemental analysis are about  $\sim 30$ – $70$  pg for U and  $\sim 180$ – $420$  pg for Th. They were negligible ( $<0.5\%$ ) compared to the amount of U and Th analyzed in the studies samples. The  $^{233}\text{U}$ – $^{229}\text{Th}$  tracer was regularly calibrated by TIMS with the in-house ATHo rock standard.

## Appendix B. Solving the system of Eqs. (2)–(5)

We present here how we solved the system of Eqs. (2)–(5) for regolith production rate ( $P$ ) or timescales of chemical weathering ( $t$ ), input rates of  $^{238}\text{U}$ ,  $^{234}\text{U}$ ,  $^{230}\text{Th}$  ( $F_{238}$ ,  $F_{234}$ ,  $F_{230}$ ), and leaching rate constants ( $k_{238}$ ,  $k_{234}$ ,  $k_{230}$ ). These values were derived to best reproduce the measured ( $^{234}\text{U}/^{238}\text{U}$ ) and ( $^{230}\text{Th}/^{238}\text{U}$ ) ratios as a function of depth.

Eqs. (2)–(4) were first solved analytically and the solutions were rearranged to describe ( $^{234}\text{U}/^{238}\text{U}$ ) or ( $^{230}\text{Th}/^{238}\text{U}$ ) for a weathering regolith sample as a function of  $F_{238}$ ,  $F_{234}$ ,  $F_{230}$ ,  $k_{238}$ ,  $k_{234}$ ,  $k_{230}$ , and  $t$  (Eqs. (A1) and (A2)):

$$\left(\frac{^{234}\text{U}}{^{238}\text{U}}\right)_{\text{activity}} = \frac{\left(\frac{\lambda_{234}}{a_4 - a_8} - \frac{\lambda_{234}F_{238}}{\lambda_{238}^{238}\text{U}_0 a_8 (a_4 - a_8)}\right)e^{-a_8 t} + \left(\left(\frac{^{234}\text{U}}{^{238}\text{U}}\right)_0 - \frac{\lambda_{234}}{a_4 - a_8} - \frac{\lambda_{234}F_{238}}{\lambda_{238}^{238}\text{U}_0 a_4 (a_4 - a_8)} - \frac{F_{234}}{\lambda_{238}^{238}\text{U}_0 a_4}\right)e^{-a_4 t} + \frac{F_{234}}{\lambda_{238}^{238}\text{U}_0 a_4} + \frac{\lambda_{234}F_{238}}{\lambda_{238}^{238}\text{U}_0 a_4 a_8}}{\left(1 - \frac{F_{238}}{\lambda_{238}^{238}\text{U}_0 a_8}\right)e^{-a_8 t} + \frac{F_{238}}{\lambda_{238}^{238}\text{U}_0 a_8}} \quad (\text{A1})$$

$$\left(\frac{^{230}\text{Th}}{^{238}\text{U}}\right)_{\text{activity}} = \frac{Ae^{-a_8 t} + Be^{-a_4 t} + Ce^{-a_0 t} + \frac{\lambda_{230}\lambda_{234}F_{238}}{\lambda_{238}^{238}\text{U}_0 a_0 a_4 a_8} + \frac{\lambda_{230}F_{234}}{\lambda_{238}^{238}\text{U}_0 a_0 a_4} + \frac{F_{230}}{\lambda_{238}^{238}\text{U}_0 a_0}}{\left(1 - \frac{F_{238}}{\lambda_{238}^{238}\text{U}_0 a_8}\right)e^{-a_8 t} + \frac{F_{238}}{\lambda_{238}^{238}\text{U}_0 a_8}} \quad (\text{A2})$$

where

$$A = \frac{\lambda_{230}\lambda_{234}}{(a_0 - a_8)(a_4 - a_8)} - \frac{\lambda_{230}\lambda_{234}F_{238}}{\lambda_{238}^{238}\text{U}_0 a_8 (a_4 - a_8)(a_0 - a_8)}$$

$$B = \frac{\lambda_{230}}{(a_0 - a_4)} \left(\frac{^{234}\text{U}}{^{238}\text{U}}\right)_0 - \frac{\lambda_{230}\lambda_{234}}{(a_0 - a_4)(a_4 - a_8)} - \frac{\lambda_{230}F_{234}}{\lambda_{238}^{238}\text{U}_0 a_4 (a_0 - a_4)} - \frac{\lambda_{230}\lambda_{234}F_{238}}{\lambda_{238}^{238}\text{U}_0 a_4 (a_0 - a_4)(a_4 - a_8)}$$

$$C = \left(\frac{^{230}\text{Th}}{^{238}\text{U}}\right)_0 - \frac{\lambda_{230}}{(a_0 - a_4)} \left(\frac{^{234}\text{U}}{^{238}\text{U}}\right)_0 + \frac{\lambda_{230}\lambda_{234}}{(a_0 - a_4)(a_4 - a_8)} - \frac{\lambda_{230}\lambda_{234}}{(a_0 - a_8)(a_4 - a_8)} - \frac{F_{230}}{\lambda_{238}^{238}\text{U}_0 a_0} - \frac{\lambda_{230}F_{234}}{\lambda_{238}^{238}\text{U}_0 a_0 a_4} + \frac{\lambda_{230}F_{234}}{\lambda_{238}^{238}\text{U}_0 a_4 (a_0 - a_4)} - \frac{\lambda_{230}\lambda_{234}F_{238}}{\lambda_{238}^{238}\text{U}_0 a_0 a_4 a_8} + \frac{\lambda_{230}\lambda_{234}F_{238}}{\lambda_{238}^{238}\text{U}_0 a_4 a_8 (a_0 - a_4)} - \frac{\lambda_{230}\lambda_{234}F_{238}}{\lambda_{238}^{238}\text{U}_0 a_8 (a_0 - a_4)(a_4 - a_8)} + \frac{\lambda_{230}\lambda_{234}F_{238}}{\lambda_{238}^{238}\text{U}_0 a_8 (a_0 - a_8)(a_4 - a_8)}$$

Here, we define

$a_8$  as  $\lambda_{238} + k_{238}$ ;

$a_4$  as  $\lambda_{234} + k_{234}$ ;

$a_0$  as  $\lambda_{230} + k_{230}$ ;

( $^{234}\text{U}/^{238}\text{U}$ )<sub>0</sub> and ( $^{230}\text{Th}/^{238}\text{U}$ )<sub>0</sub> are initial activity ratios for the regolith sample;  $^{238}\text{U}_0$  is the initial number of  $^{238}\text{U}$  atoms in the starting material.

The derivation of Eq. (5) is based on the implicit assumption of isovolumetric weathering. At SSHO, volume strain has been calculated for some samples from regolith bulk density along the 2D transect (Jin et al., 2010). It has been shown that, although the regolith has expanded, the variation in strain is less than  $\sim 18\%$  within the profile regolith volume from 17 to 54 cm. Only in the upper 3 cm layer has volume expanded significantly due to addition of organic matter (Jin et al., 2010). Future modeling efforts will explore the effect of this relatively modest non-isovolumetric weathering.

For each regolith profile, measured ( $^{234}\text{U}/^{238}\text{U}$ ) and ( $^{230}\text{Th}/^{238}\text{U}$ ) ratios in each sample are used to constrain the model. Instead of the measured bedrock samples (DC-1), the deepest sample from each profile was used to represent the starting material. To solve the model equations, we assume the unknown terms ( $F_{238}$ ,  $F_{234}$ ,  $F_{230}$ ,  $k_{238}$ ,  $k_{234}$ , and  $k_{230}$ ) and the regolith production rate  $P$  are constant for each profile. Thus, the calculated value of  $P$  represents an average rate over the duration of weathering for each profile and the total duration of weathering is calculated with Eq. (5).

The model is constrained by 4 observations for SPRT ( $^{234}\text{U}/^{238}\text{U}$  and  $^{230}\text{Th}/^{238}\text{U}$  activity ratios for samples SPRT 0010 and 1020 as data points). Sample SPRT 2030 is used as the initial activity value of the starting material. The model fits 4 parameters ( $k_{238}$ ,  $k_{234}$ ,  $k_{230}$ , and  $P$ ) to data describing the SPRT profile (we assume no U-series input sources for the ridge top site). The model for SPMS is constrained by 8 observations in the model (activity ratios for samples SPMS 0010, 1020, 2030, and 4050); and the activity ratios for SPMS5059 are used as the initial value of the starting material. The data from a depth of 35 cm, SPMS 3040, was not included in the model fit as it lies off the general trend of this profile (e.g., Fig. 2). The model calculated 7 parameters ( $F_{238}$ ,  $F_{234}$ ,  $F_{230}$ ,  $k_{238}$ ,  $k_{234}$ ,  $k_{230}$ , and  $P$ ) for the SPMS profile. The model is constrained by 10 observations for SPVF (activity ratios for SPVF 0010, SPVF1020, 2030, 3040, and 4050). The ratios for SPVF5060 were used as the initial value. SPVF6067 was not included in the calculation as it lies off the general trend of this profile (e.g., Fig. 2). Seven output parameters ( $F_{238}$ ,  $F_{234}$ ,  $F_{230}$ ,  $k_{238}$ ,  $k_{234}$ ,  $k_{230}$ , and  $P$ ) were derived for the SPVF profile. The number of model equations is equal to or greater than the number of unknowns, and thus the model is over-determined. The unknown parameters were solved in a similar manner to that of Dosseto et al. (2008b) as described below.

Best-fit parameters were calculated with the Matlab™ *lsqnonlin* function (version 7.1), which uses a large-scale algorithm to solve nonlinear least-squares problems. This function searches for the vector  $x$  that minimizes the sum of the square of the difference between observed and modeled values with a function  $f(x)$  which has  $m$  components of constraining equations. The calculation is initiated with an initial value  $x_0$ , provided by the user. In this case,  $x$  is the vector of output parameters ( $F_{238}$ ,  $F_{234}$ ,  $F_{230}$ ,  $k_{238}$ ,  $k_{234}$ ,  $k_{230}$ , and  $P$ ) and the components of  $f$  are the measured ( $^{234}\text{U}/^{238}\text{U}$ ) and ( $^{230}\text{Th}/^{238}\text{U}$ ) activity ratios. The model calculates output parameters such that they fit the observed activity ratios within approximately 1%. The model calculation was performed 1000 times to obtain solutions for different random values for  $x_0$ . The average of these solutions and their standard deviations are presented in Table 2.

## References

- Akovi, Y.A., 1994. Nuclear data sheets for  $A=234$ . Nucl. Data Sheets 71, 18.
- Ames, L.L., McGarrath, J.E., Walker, B.A., 1983. Sorption of trace constituents from aqueous solutions onto secondary minerals. I Uranium. Clays Clay Miner. 31, 321–334.
- Amiotte-Suchet, P., Probst, J., Ludwig, W., 2003. Worldwide distribution of continental rock lithology: implications for the atmospheric/soil  $\text{CO}_2$  uptake by continental weathering and alkalinity river transport to the oceans. Glob. Biogeochem. Cycles 17, 1038. doi:10.1029/2002GB001891.
- Amundson, R. (2004). Soil formation. In: Treatise on Geochemistry, H.D. Holland and K.K. Turekian (Eds in Chief). Elsevier Press, Amsterdam, pp. 1–35.
- Andersen, M.B., Erel, Y., Bourdon, B., 2009. Experimental evidence for  $^{234}\text{U}$ – $^{238}\text{U}$  fractionation during granite weathering with implications for  $^{234}\text{U}/^{238}\text{U}$  in natural waters. Geochim. Cosmochim. Acta 73, 4124–4141.
- Anderson, S.P., Dietrich, W.E., Brimhall, G.H., 2002. Weathering profiles, mass-balance analysis, and rates of solute loss: linkage between weathering and erosion in a small, steep catchment. Geol. Soc. Am. Bull. 114, 1143–1158.
- Anderson, S.P., von Blanckenburg, F., White, A.F., 2007. Physical and chemical controls on the Critical Zone. Elements 3, 315–319.
- Andersson, P.S., Wasserburg, G.J., Chen, J.H., Papanastassiou, D.A., Ingri, J., 1995.  $^{238}\text{U}$ – $^{234}\text{U}$  and  $^{232}\text{Th}$ – $^{230}\text{Th}$  in the Baltic Sea and in river water. Earth Planet. Sci. Lett. 130, 217–234.
- Andersson, P.S., Porcelli, D., Wasserburg, G.J., Ingri, J., 1998. Particle transport of  $^{234}\text{U}$ – $^{238}\text{U}$  in the Kalix River and in the Baltic Sea. Geochim. Cosmochim. Acta 62, 385–392.
- Bierman, P.R., Nichols, K.K., 2004. Rock to sediment, slope to sea with  $^{10}\text{Be}$ , rates of landscape change. Annu. Rev. Earth Planet. Sci. 32, 215–255.
- Blackmer, G.C., Omar, G.I., Gold, D.P., 1994. Post-Alleghanian unroofing history of the Appalachian Basin, Pennsylvania, from apatite fission trace analysis and thermal models. Tectonics 13, 1259–1276.
- Bourdon, B., Bureau, S., Andersen, M.B., Pili, E., Hubert, A., 2009. Weathering rates from top to bottom in a carbonate environment. Chem. Geol. 258, 275–287.
- Brantley, S.L., 2008. Understanding soil time. Science 321, 1454–1455.
- Brantley, S.L., White, T.S., Ragnarsdottir, K.V., 2007a. The Critical Zone: where rock meets life. Elements 3, 368.
- Brantley, S.L., Godhaber, M.B., Ragnarsdottir, K.V., 2007b. Crossing disciplines and scales to understand the Critical Zone. Elements 3, 307–314.
- Brantley, S.L., White, A.F., 2009. Approaches to modeling weathered regolith. Rev. Mineral. Geochem. 70, 435–484.
- Braun, D.D., 1989. Glacial and periglacial erosion of the Appalachians. Geomorphology 2, 233–256.
- Braun, D.D., 2005. Deglaciation of the Appalachian Plateau, northeastern Pennsylvania – till shadows, till knobs forming “beaded valleys”: revisiting systematic stagnation-zone retreat. Geomorphology 75, 248–265.
- Brimhall, G.H., Dietrich, W.E., 1987. Constitutive mass balance relations between chemical composition, volume, density, porosity, and strain in metasomatic hydrochemical systems: results on weathering and pedogenesis. Geochim. Cosmochim. Acta 51, 567–587.
- Buss, H.L., Sak, P.B., Webb, S.M., Brantley, S.L., 2008. Weathering of the Rio Blanco quartz diorite, Luquillo Mountains, Puerto Rico: coupling oxidation, dissolution, and fracturing. Geochim. Cosmochim. Acta 72, 4488–4507.
- Carson, M.A., Kirkby, M.J., 1972. Hillslope Form and Process. Cambridge Univ. Press, Cambridge.
- Chabaux, F., Riotte, J., Dequincey, O., 2003a. U–Th–Ra fractionation during weathering and river transport. Rev. Mineral. Geochem. 52, 533–576.
- Chabaux, F., Dequincey, O., Levesque, J.-J., Leprun, J.-C., Clauer, N., Riotte, J., Paquet, H., 2003b. Tracing and dating recent chemical transfers in weathering profiles by trace element geochemistry and  $^{238}\text{U}$ – $^{234}\text{U}$ – $^{230}\text{Th}$  disequilibria: the example of the Kaya lateritic toposequence (Burkina-Faso). C. R. Geosci. 335, 1219–1231.
- Chabaux, F., Riotte, J., Schmitt, A.-D., Carignan, J., Herckès, P., Pierret, M.-C., Wortham, H., 2005. Variations of U and Sr ratios in Alsace and Luxembourg rain waters: origin and hydrogeochemical implications. C. R. Geosci. 337, 1447–1456.
- Chabaux, F., Granet, M., Pelt, E., France-Lanord, C., Galy, V., 2006.  $^{238}\text{U}$ – $^{234}\text{U}$ – $^{230}\text{Th}$  disequilibria and timescale of sedimentary transfers in rivers: clues from the Gangetic plain rivers. J. Geochim. Explor. 88, 373–375.
- Chabaux, F., Bourdon, B., Riotte, J., 2008. U-series geochemistry in weathering profiles, river waters and lakes. Radioact. Environ. 13, 49–104.
- Chadwick, O.A., Brimhall, G.H., Hendricks, D.M., 1990. From a black to a grey box – a mass balance interpretation of pedogenesis. Geomorphology 3, 369–390.
- Cheng, H., Edwards, R.L., Hoff, J., Gallup, C.D., Richards, D.A., Asmerom, Y., 2000. The half-lives of uranium-234 and thorium-230. Chem. Geol. 169, 17–33.
- Copard, Y., Amiotte-Suchet, P., Di-Giovanni, C., 2007. Storage and release of fossil organic carbon related to weathering of sedimentary rocks. Earth Planet. Sci. Lett. 258, 345–357.
- Cox, N.J., 1980. On the relationship between bedrock lowering and regolith thickness. Earth Surf. Processes 5, 271–274.
- Drever, J.L., 2004. Surface and ground water, weathering, and soils. In: Holland, H.D., Turekian (Eds.), Treatise on Geochemistry, Volume 5. Elsevier, 626 pp.
- DePaolo, D.J., Maher, K., Christensen, J.N., McManus, J., 2006. Sediment transport time measured with U-series isotopes: results from ODP North Atlantic drift site 984. Earth Planet. Sci. Lett. 248, 394–410.
- Dequincey, O., Chabaux, F., Clauer, N., Sigmarsson, O., Liewig, N., Leprun, J.-C., 2002. Chemical mobilizations in laterites: evidence from trace elements and  $^{238}\text{U}$ – $^{234}\text{U}$ – $^{230}\text{Th}$  disequilibria. Geochim. Cosmochim. Acta 66, 1197–1210.
- Dietrich, W.E., Bellugi, D.G., Sklar, L.S., Stock, J.D., Heimsath, A.M., Roering, J.J., 2003. Geomorphic transport laws for predicting landscape form and dynamics. Prediction in Geomorphology. Geophysical Monograph 135. American Geophysical Union, pp. 1–30.
- Dosseto, A., Bourdon, B., Gaillardet, J., Allegre, C.J., Filizola, N., 2006a. Timescale and conditions of chemical weathering under tropic climate: study of the Amazon basin with U-series. Geochim. Cosmochim. Acta 70, 71–89.
- Dosseto, A., Turner, S.P., Douglas, G.B., 2006b. Uranium-series isotopes in colloids and suspended sediments: timescale for sediment production and transport in the Murray–Darling River system. Earth Planet. Sci. Lett. 246, 418–431.
- Dosseto, A., Bourdon, B., Gaillardet, J., Allegre, C.J., Maurice-Bourgoin, L., 2006c. Weathering and transport of sediments in the Bolivian Andes: time constraints from uranium-series isotopes. Earth Planet. Sci. Lett. 248, 759–771.
- Dosseto, A.D., Bourdon, B., Turner, S.P., 2008a. Uranium-series isotopes in river materials: insights into the timescales of erosion and sediment transport. Earth Planet. Sci. Lett. 265, 1–17.
- Dosseto, A., Turner, S.P., Chappell, J., 2008b. The evolution of weathering profiles through time: new insights from uranium-series isotopes. Earth Planet. Sci. Lett. 274, 359–371.
- Duff, M.C., Coughlin, J.U., Hunter, D.B., 2002. Uranium coprecipitation with iron oxide minerals. Geochim. Cosmochim. Acta 66, 3533–3547.
- Duffy, C.J., Cusumano, J.M., 1998. A low-dimensional model for concentration-discharge in ground-water–stream systems. Water Resour. Res. 34, 2235–2247.
- Fleischer, R.L., 1980. Isotopic disequilibrium of uranium: alpha-recoil damage and preferential solution effects. Science 207, 979–981.
- Fletcher, R.C., Buss, H.L., Brantley, S.L., 2006. A spheroidal weathering model coupling porewater chemistry to soil thickness during steady-state denudation. Earth Planet. Sci. Lett. 244, 444–457.
- Folk, R.L., 1960. Petrography and origin of the Tuscarora, Rose Hill, and Keefer Formations, Lower and Middle Silurian of eastern west Virginia. J. Sed. Petrol. 30, 1–58.
- Gaillardet, J., 2008. Isotope geochemistry as a tool for deciphering kinetics of water–rock interaction. In: Brantley, S.L., Kubicki, J.D., White, A.F. (Eds.), Kinetics of Water–Rock Interaction. Springer, New York, pp. 591–653.
- Gardner, T.W., Ritter, J.B., Shuman, C.A., Bell, J.C., Sasowsky, K.C., Pinter, N., 1991. A periglacial stratified slope deposit in the valley and ridge province of central

- Pennsylvania, USA: sedimentology, stratigraphy, and geomorphic evolution. *Permafrost Periglac. Process.* 2, 141–162.
- Gascoyne, M., 1992. Geochemistry of the actinides and their daughters. In: Ivanovich, M., Harmon, R.S. (Eds.), *Uranium-Series Disequilibrium: Application to Earth, Marine, and Environmental Sciences*. Oxford Sciences Publications, Oxford, pp. 34–61.
- Ghaleb, B., Hillaire-Marcel, C., Causse, C., Garipey, C., Vallieres, S., 1990. Fractionation and recycling of U and Th isotopes in a semiarid endoreic depression of central Syria. *Geochim. Cosmochim. Acta* 54, 1025–1035.
- Godderis, Y., Roelandt, C., Schott, J., Pierret, M.-C., Francois, L.M., 2009. Towards an integrated model of weathering, climate, and biospheric processes. *Rev. Mineral. Geochem.* 70, 411–434.
- Govindaraju, K., 1994. Compilation of working values and sample description for 383 geostandards. *Geostandards Newsletter* 18 (S1), 1–158.
- Granet, M., Chabaux, F., Stille, P., France-Lanord, C., Pelt, E., 2007. Time-scales of sedimentary transfer and weathering processes from U-series nuclides: clues from the Himalayan rivers. *Earth Planet. Sci. Lett.* 261, 389–406.
- Granet, M., Chabaux, F., Stille, P., Dosseto, A., France-Lanord, C., Blaes, E., 2010. U-series disequilibria in suspended river sediments and implication for sediment transfer time in alluvial plains: the case of the Himalayan rivers. *Geochim. Cosmochim. Acta* 74, 2851–2865.
- Heimsath, A.M., Dietrich, W.E., Nishiizumi, K., Finkel, R.C., 1997. The soil production function and landscape equilibrium. *Nature* 388, 358–361.
- Heimsath, A.M., Chappell, J., Dietrich, W.E., Nishiizumi, K., Finkel, R.C., 2000. Soil production on a retreating escarpment in southeastern Australia. *Geology* 28, 787–790.
- Heimsath, A.M., Dietrich, W.E., Nishiizumi, K., Finkel, R.C., 2001. Stochastic processes of soil production and transport: erosion rates, topographic variation and cosmogenic nuclides in the Oregon coast range. *Earth Surf. Process. Land.* 26, 531–552.
- Heimsath, A.M., Furbish, D.J., Dietrich, W.E., 2005. The illusion of diffusion: field evidence for depth-dependent sediment transport. *Geology* 33, 949–952.
- Jin, L., Ravello, R., Ketchum, B., Bierman, P.R., Heaney, P., White, T., Brantley, S.L., 2010. Mineral weathering and elemental transport during hillslope evolution at the Susquehanna/Shale Hills Critical Zone Observatory. *Geochim. Cosmochim. Acta* 74, 3669–3691.
- Kaste, J.M., Heimsath, A.M., Bostick, B.C., 2007. Short-term mixing quantified with fallout radionuclides. *Geology* 35, 234–246.
- Kolowith, L.C., Berner, R.A., 2002. Weathering of phosphorus in black shales. *Glob. Biogeochem. Cycles* 16, 1140. doi:10.1029/2001GB001887.
- Kump, L.R., Brantley, S.B., Arthur, M.A., 2000. Chemical weathering, atmospheric CO<sub>2</sub>, and climate. *Annu. Rev. Earth Planet. Sci.* 28, 611–667.
- Lal, D., 1991. Cosmic ray labeling of erosion surfaces: in situ nuclide production rates and erosion models. *Earth Planet. Sci. Lett.* 104, 424–439.
- Langmuir, D., 1978. Uranium solution-mineral equilibria at low temperatures with applications to sedimentary ore deposits. *Geochim. Cosmochim. Acta* 42, 547–569.
- Langmuir, D., Herman, J.S., 1980. The mobility of thorium in natural waters at low temperatures. *Geochim. Cosmochim. Acta* 44, 1753–1766.
- Latham, A.G., Schwarcz, H.P., 1987a. On the possibility of determining rates of removal of uranium from crystalline igneous rocks using U-series disequilibria – 1: a U-leach model, and its applicability to whole-rock data. *Appl. Geochem.* 2, 55–65.
- Latham, A.G., Schwarcz, H.P., 1987b. On the possibility of determining rates of removal of uranium from crystalline igneous rocks using U-series disequilibria – 2: applicability of a U-leach model to mineral separates. *Appl. Geochem.* 2, 67–71.
- Lebedeva, M.I., Fletcher, R.C., Balashov, V.N., Brantley, S.L., 2007. A reactive diffusion model describing transformation of bedrock to saprolite. *Chem. Geol.* 244, 624–645.
- Lin, H.S., 2006. Temporal stability of soil moisture spatial pattern and subsurface preferential flow pathways in the Shale Hills Catchment. *Vadose Zone J.* 5, 317–340.
- Lin, H., Kogelmann, W., Walker, C., Bruns, M.A., 2006. Soil moisture patterns in a forested catchment: a hydropedological perspective. *Geoderma* 131, 345–368.
- Littke, R., Klusmann, U., Krooss, B., Leythaeuser, D., 1991. Quantification of loss of calcite, pyrite, and organic matter due to weathering of Toarcian black shales and effects on kerogen and bitumen characteristics. *Geochim. Cosmochim. Acta* 55, 3369–3378.
- Lynch, J.A., 1976. Effects of Antecedent Soil Moisture on Storm Hydrographs. University Park, Pennsylvania State University.
- Lynch, J.A., and Corbett, E.S. (1985). Source-area variability during peak flow, edited by E.B. Jones and T.J. Ward, J. Irrig. Drain. Div. Am. Soc. Civ. Eng., pp. 300–307., in *Watershed Management in the 1980s*, E. Jones and T. Ward, Editors. ASCE: Reston, VA. p. 300–307.
- Maher, K., 2010. The dependence of chemical weathering rates on fluid residence time. *Earth Planet. Sci. Lett.* 294, 101–110.
- Maher, K., DePaolo, D.J., Lin, J.C.F., 2004. Rates of silicate dissolution in deep-sea sediment: in situ measurement using U-234/U-238 of pore fluids. *Geochim. Cosmochim. Acta* 68, 4629–4648.
- Mathieu, D., Bernat, M., Nahon, D., 1995. Short-lived U and Th isotope distribution in a tropical laterite derived from Granite (Pitinga river basin, Amazonia, Brazil): application to assessment of weathering rate. *Earth Planet. Sci. Lett.* 136, 703–714.
- Minasny, B., McBratney, A.B., 1999. A rudimentary mechanistic model for soil production and landscape development. *Geoderma* 90, 3–21.
- Montgomery, D.R., 2007. Soil erosion and agricultural sustainability. *Proc. Natl. Acad. Sci. U. S. A.* 104 (33), 13268–13272.
- Murphy, S.F., Brantley, S.L., Blum, A.E., White, A.F., Dong, H., 1998. Chemical weathering in a tropical watershed, Luquillo Mountains, Puerto Rico: II. Rate and mechanism of biotite weathering. *Geochim. Cosmochim. Acta* 62, 227–243.
- National Oceanographic and Atmospheric Administration (NOAA) (2007), U.S. divisional and station climatic data and normals: Asheville, North Carolina, U.S. Department of Commerce, National Oceanic and Atmospheric Administration, National Environmental Satellite Data and Information Service, National Climatic Data Center, <http://cdo.ncdc.noaa.gov/CDO/cdo>.
- Pelt, E., Chabaux, F., Innocent, C., Navarre-Sitchler, A.K., Sak, P.B., Brantley, S.L., 2008. Uranium–thorium chronometry of weathering rinds: rock alteration rate and paleo-isotopic record of weathering fluids. *Earth Planet. Sci. Lett.* 276, 98–105.
- Petsch, S.T., Eglinton, T.J., Edwards, K.J., 2001. <sup>14</sup>C-dead living biomass: evidence for microbial assimilation of ancient organic carbon during shale weathering. *Science* 292, 1127–1131.
- Pierson-Wickmann, A., Reisberg, L., France-Lanord, C., 2002. Behavior of Re and Os during low temperature alteration: results from Himalayan soils and altered black shales. *Geochim. Cosmochim. Acta* 66, 1539–1548.
- Plater, A.J., Ivanovich, M., Dugdale, R.E., 1992. Uranium series disequilibrium in river sediments and waters: the significance of anomalous activity ratios. *Appl. Geochem.* 7, 101–110.
- Plater, A.J., Dugdale, R.E., Ivanovich, M., 1994. Sediment yield determination using uranium-series radionuclides: the case of the Wash and Fenland drainage basin, eastern England. *Geomorphology* 11, 41–56.
- Porcelli, D., Andersson, P.S., Baskaran, M., Wasserburg, G.J., 2001. Transport of U- and Th- series nuclides in a Baltic Shield watershed and the Baltic Sea. *Geochim. Cosmochim. Acta* 65, 2439–2459.
- Porder, S., Vitousek, P.M., Chadwick, O.A., Page Chamberlin, C., Hilley, G.E., 2007. Uplift, erosion, and phosphorus limitation in terrestrial ecosystems. *Ecosystems* 10, 158–170.
- Price, J.R., Velbel, M.A., Patino, L.C., 2005. Rates and time scales of clay-mineral formation by weathering in saprolitic regoliths of the southern Appalachians from geochemical mass balance. *Geol. Soc. Am. Bull.* 117, 783–794.
- Qu, T., Duffy, C.J., 2007. A semi-discrete finite volume formation for multiprocess watershed simulation. *Water Resour. Res.* 43. doi:10.1029/2006WR005752.
- Reuter, J., Bierman, P., Pavich, M., Gellis, A., Larsen, J., Finkel, R., 2004. Erosion of the Susquehanna River Basin: assessing relations between <sup>10</sup>Be-derived erosion rates and basin characteristics. *Geological Society of America programs with abstracts*.
- Riebe, C.S., Kirchner, J.W., Granger, D.E., Finkel, R.C., 2001. Strong tectonic and weak climatic control of long-term chemical weathering rates. *Geology* 29, 511–514.
- Riebe, C., Kirchner, J.W., Finkel, R.C., 2003. Long-term rates of chemical weathering and physical erosion from cosmogenic nuclides and geochemical mass balance. *Geochim. Cosmochim. Acta* 67, 4411–4427.
- Riebe, C.S., Kirchner, J.W., Finkel, R.C., 2004a. Erosional and climatic effects on long-term chemical weathering rates in granitic landscapes spanning diverse climate regimes. *Earth Planet. Sci. Lett.* 224, 547–562.
- Riebe, C.S., Kirchner, J.W., Finkel, R.C., 2004b. Sharp decrease in long-term chemical weathering rates along an altitudinal transect. *Earth Planet. Sci. Lett.* 218, 421–434.
- Roden, M.K., Miller, D.S., 1989. Apatite fission-track thermochronology of the Pennsylvania Appalachian Basin. *Geomorphology* 2, 39–51.
- Roering, J., Almond, P., Tonkin, P., McKean, J., 2002. Soil transport driven by biological processes over millennial time scales. *Geology* 30, 1115–1118.
- Rosholt, J., Doe, B., Tatsumoto, M., 1966. Evolution of the isotopic composition of uranium and thorium in soil profiles. *Geol. Soc. Am. Bull.* 77, 987–1004.
- Scott, R.D., MacKenzie, A.B., Alexander, W.R., 1992. The interpretation of <sup>238</sup>U–<sup>234</sup>U–<sup>230</sup>Th–<sup>226</sup>Ra disequilibria produced by rock–water interactions. *J. Geochem. Explor.* 45, 323–343.
- Shirvington, P.J., 1983. Fixation of radionuclides in the <sup>238</sup>U decay series in the vicinity of mineralized zones: 1. The Austatom Uranium Prospect, Northern Territory, Australia. *Geochim. Cosmochim. Acta* 47, 403–412.
- Small, E.E., Anderson, R.S., Hancock, G.S., 1999. Estimates of the rate of regolith production using <sup>10</sup>Be and <sup>26</sup>Al from an Alpine hillslope. *Geomorphology* 27, 131–150.
- Stallard, R.F., 1992. Tectonic processes, continental freeboard, and the rate-controlling step for continental denudation. In: *Butcher, S.S., Charlson, R.J., Orians, G.H., Wolfe, G.V. (Eds.), Global Biogeochemical Cycles*. Academic Press, London, pp. 93–121.
- Steefel, C.I., 2008. Geochemical kinetics and transport. In: *Brantley, S.L., Kubicki, J.D., White, A.F. (Eds.), Kinetics of Water–Rock Interaction*. Springer, New York, pp. 545–589.
- Taylor, A., Blum, J.D., 1995. Relation between soil age and silicate weathering rates determined from the chemical evolution of a glacial chronosequence. *Geology* 23, 979–982.
- Tuttle, M.L.W., Breit, G.N., 2009. Weathering of the New Albany Shale, Kentucky, USA: I. weathering zones defined by mineralogy and major-element composition. *Appl. Geochem.* 24, 1549–1564.
- Tuttle, M.L.W., Breit, G.N., Goldhaber, M.B., 2009. Weathering of the New Albany Shale, Kentucky: II. Redistribution of minor and trace elements. *Appl. Geochem.* 24, 1565–1578.
- Viers, J., Dupre, B., Polve, M., Schott, J., Dandurand, L., Braun, J.J., 1997. Chemical weathering in the drainage basin of a tropical watershed (Nsimi-Zoetele site, Cameroon): comparison between organic-poor and organic-rich waters. *Chem. Geol.* 140, 181–206.
- Vigier, N., Bourdon, B., Turner, S., Allegre, C.J., 2001. Erosion timescales derived from U-decay series measurements in rivers. *Earth Planet. Sci. Lett.* 193, 485–499.
- Vigier, N., Bourdon, B., Turner, S., Van Calsteren, P., Subramanian, V., Dupre, B., Allegre, C.J., 2005. Parameters influencing the duration and rates of weathering deduced from U-series measured in rivers: the Deccan trap region (India). *Chem. Geol.* 219, 69–91.
- Vigier, N., Burton, K.W., Gislason, S.R., Rogers, N.W., Duchene, S., Thomas, L., Hodge, E., Schaefer, B., 2006. The relationship between riverine U-series disequilibria and erosion rates in a basaltic terrain. *Earth Planet. Sci. Lett.* 249, 258–273.
- Von Blanckenburg, F., 2005. The control mechanisms of erosion and weathering at basin scale from cosmogenic nuclides in river sediment. *Earth Planet. Sci. Lett.* 237, 462–479.
- Von Blanckenburg, F., Hewawasam, T., Kubik, P., 2004. Cosmogenic nuclide evidence for low weathering and denudation in the wet tropical Highlands of Sri Lanka. *J. Geophys. Res.* 109, F03008. doi:10.1029/2003JF000049.
- White, A.F., Blum, A.E., 1995. Effects of climate on chemical weathering in watersheds. *Geochim. Cosmochim. Acta* 59, 1729–1747.

- White, A.F., Blum, A.E., Marjorie, S., Schulz, M.S., Bullen, T.D., Harden, J.W., Peterson, M.L., 1996. Chemical weathering rates of a soil chronosequence on granitic alluvium: I. Quantification of mineralogical and surface area changes and calculation of primary silicate reaction rates. *Geochim. Cosmochim. Acta* 60, 2533–2550.
- White, A.F., Blum, A.E., Schlz, M.S., Vivit, D.V., Stonestrom, D.A., Larsen, M., Murphy, S.F., Eberl, D., 1998. Chemical weathering in a tropical watershed, Luquillo Mountains, Puerto Rico: I. long-term versus short-term weathering fluxes. *Geochim. Cosmochim. Acta* 62, 209–226.
- White, A.F., Brantley, S.L., 2003. The effect of time on the weathering of silicate minerals: why do weathering rates differ in the laboratory and field? *Chem. Geol.* 202, 479–506.
- Wilkinson, B.H., McElroy, B.J., 2007. The impact of humans on continental erosion and sedimentation. *Geol. Soc. Am. Bull.* 119, 140–156.
- Yoo, K., Amundson, R., Heimsath, A.M., Dietrich, W.E., Brimhall, G.H., 2007. Integration of geochemical mass balance with sediment transport to calculate rates of soil chemical weathering and transport on hillslopes. *J. Geophys. Res.* 112, F02013. doi:10.1029/2005JF000402.

		ISSN 0016-7037 Volume 74, Number 13 July 1, 2010	
<h1>Geochimica et Cosmochimica Acta</h1> <p>JOURNAL OF THE GEOCHEMICAL SOCIETY AND THE METEORITICAL SOCIETY</p>			
EXECUTIVE EDITOR: FRANK A. PODOSEK		EDITORIAL BOARD: LINDA THORPE EDITORIAL ASSISTANT: KAREN KLUG KARIN SVENDE	
ASSOCIATE EDITORS: ROBERT C. ALLEN ROBERT C. ALP YUKI ANDO CAROL AMOBI MICHAEL BIRNBAUM LIONEL G. BIRCH TAMARA S. BIRCH JAY A. BRAND ALAN D. BRANSON DAVID J. BRIDGER ROBERT H. BRINE WILLIAM H. CARR TAMARA CHANG JON COOPER JANE COOPER CHRISTOPHER J. DALRYMPLE		ZORAN DRAK JAMES FARQUHAR FRANÇOISE A. FAY EDWARD GARLAND SILVIA GILBERT EDITHA N. GORMON EDWARD R. HALE H. ROSEAN HARVEY GORDON R. HELL SYLVIE R. HODSON GREGORY F. HOLLAND JAMES HURT TOMAS JELAND JUNICHIRO ISHIZUKA KARIN JARANDSON CLAIRE JARNOOK	
CHRISTIAN KÖRBER RASHI KORTUM SPENCER M. KRAEMER S. KRISHNAMURTHY ALEXANDER N. KUBITZ GREGORY A. LARSON JOSÉ LÓPEZ THOMAS J. LUDWIG MICHAEL L. MACHUGA BERNARD MATHY TAMI MCCLELLAN ANDRZEJ MARCINI MARTIN A. MARIOTT JACK J. MARSHALL ALVARO MONTI BIRKA MUYER		HERIBERTO NABARRA MARTIN NIEVEK PATRYA A. OTTAVI ERIC H. OXBURGH DINO DI PASTORIS SUSANNA PIZZARIELLO MARC ROBERTSON W. LINDA RICHARDS PETER W. RICHARDS EDWARD M. RILEY KEVIN W. RYAN SARA S. RYDHELL E. J. RYAN EDWIN A. SCHAEFER DAVID SCHULTZ THOMAS J. SHARP	
WERNER R. ROBERTS, JR. PRODUCTION MANAGER: CHRIS ACERS		JULIE S. SPINRAD-DAMME DENISE L. SPARKS DANIEL A. SUDARSKY MICHAEL J. TAYLOR PETER ULLICH DERRICK VANCE DAVID J. VANDERKAM RICHARD J. WALKER LINDA A. WALKER JOHN WILSON ROY A. WOODRICK CHIN ZHU	
Volume 74, Number 13		July 1, 2010	
<b>Articles</b>			
L. JON, R. RAYELLA, B. KITCHUM, P. R. BIRMAN, P. HEANEY, T. WHITE, S. L. BRANTLEY: Mineral weathering and elemental transport during hillslope evolution at the Susquehanna/Shale Hills Critical Zone Observatory ..... 3669			
A. OKAMOTO, H. SAEKI, N. HIRANO, N. TSUCHIYA: Mineralogical and textural variation of silica minerals in hydrothermal flow-through experiments: Implications for quartz vein formation ..... 3692			
A. VAN DAMME, F. DINGYI, E. SIEDERER, G. SARRIT, J. DOWIT, R. SWENSON, A. MANCIAU: Zinc speciation in mining and smelter contaminated overbank sediments by EXAFS spectroscopy ..... 3707			
P. LARRE-CASANOVA, S. B. HADJILEON, A. KAPPLER: Biomineralization of lepidocrocite and goethite by nitrate-reducing Fe(II)-oxidizing bacteria: Effect of pH, bicarbonate, phosphate, and humic acids ..... 3721			
L. M. REYNARD, G. M. HENDERSON, R. E. M. HEDGER: Calcium isotope ratios in animal and human bone ..... 3735			
T. S. PERKINZ, J. M. ZACHARA, D. W. KENNEDY, J. K. FREDRICKSON, B. W. ARRY, J. P. MCKINLEY, C. M. WANG, A. C. DONALDSON, Y. XIA: Ferrous phosphate surface precipitates resulting from the reduction of intragrain 6-line ferrihydrite by <i>Shewanella oneidensis</i> MR-1 ..... 3751			
M. P. BHATIA, S. B. DAK, K. LONGNECKER, M. A. CHARFET, E. B. KOJAWINSKI: Molecular characterization of dissolved organic matter associated with the Greenland ice sheet ..... 3768			
C. T. MILES, Y. ANASO, G. F. SLATER, R. F. DRAS, T. IWATSUBI, K. W. MANDERNACK: Microbial carbon cycling in oligotrophic regional aquifers near the Tono Uranium Mine, Japan as inferred from $\delta^{13}\text{C}$ and $\Delta^{14}\text{C}$ values of <i>in situ</i> phospholipid fatty acids and carbon sources ..... 3785			
S. SCHOUTEN, J. J. MIDDORF, E. C. HOPMANN, J. S. SONSINGH DAMITE: Fossilization and degradation of intact polar lipids in deep subsurface sediments: A theoretical approach ..... 3806			
H. A. N. ARSULLA, E. C. MING, R. F. DRAS, P. G. HATCHER: Changes in the compound classes of dissolved organic matter along an estuarine transect: A study using FTIR and $^{13}\text{C}$ NMR ..... 3815			
<i>Continued on outside back cover</i>			

This article appeared in a journal published by Elsevier. The attached copy is furnished to the author for internal non-commercial research and education use, including for instruction at the authors institution and sharing with colleagues.

Other uses, including reproduction and distribution, or selling or licensing copies, or posting to personal, institutional or third party websites are prohibited.

In most cases authors are permitted to post their version of the article (e.g. in Word or Tex form) to their personal website or institutional repository. Authors requiring further information regarding Elsevier's archiving and manuscript policies are encouraged to visit:

<http://www.elsevier.com/copyright>

# Mineral weathering and elemental transport during hillslope evolution at the Susquehanna/Shale Hills Critical Zone Observatory

Lixin Jin<sup>a,\*</sup>, Ramesh Ravella<sup>a</sup>, Blake Ketchum<sup>a</sup>, Paul R. Bierman<sup>b</sup>, Peter Heaney<sup>c</sup>, Timothy White<sup>d</sup>, Susan L. Brantley<sup>a</sup>

<sup>a</sup> Center for Environmental Kinetics Analysis, Earth and Environmental Systems Institute, The Pennsylvania State University, University Park, PA 16802, USA

<sup>b</sup> Department of Geology and School of Natural Resources, University of Vermont, Burlington, VT 05405, USA

<sup>c</sup> Department of Geosciences, The Pennsylvania State University, University Park, PA 16802, USA

<sup>d</sup> Earth and Environmental Systems Institute, The Pennsylvania State University, University Park, PA 16802, USA

Received 17 June 2009; accepted in revised form 31 March 2010; available online 7 April 2010

## Abstract

Located in the uplands of the Valley and Ridge physiographic province of Pennsylvania, the Susquehanna/Shale Hills Critical Zone Observatory (SSHO) is a tectonically quiescent, first-order catchment developed on shales of the Silurian Rose Hill Formation. We used soil cores augered at the highest point of the watershed and along a subsurface water flowline on a planar hillslope to investigate mineral transformations and physical/chemical weathering fluxes. About 25 m of bedrock was also drilled to estimate parent composition. Depletion of carbonate at tens of meters of depth in bedrock may delineate a deep carbonate-weathering front. Overlying this, extending from ~6 m below the bedrock–soil interface up into the soil, is the feldspar dissolution front. In the soils, depletion profiles for K, Mg, Si, Fe, and Al relative to the bedrock define the illite and chlorite reaction fronts. When combined with a cosmogenic nuclide-derived erosion rate on watershed sediments, these depletion profiles are consistent with dissolution rates that are several orders of magnitudes slower for chlorite ( $1\text{--}5 \times 10^{-17}$  mol m<sup>-2</sup> s<sup>-1</sup>) and illite ( $2\text{--}9 \times 10^{-17}$  mol m<sup>-2</sup> s<sup>-1</sup>) than observed in the laboratory. Mineral reactions result in formation of vermiculite, hydroxy-interlayered vermiculite, and minor kaolinite. During weathering, exchangeable divalent cations are replaced by Al as soil pH decreases.

The losses of Mg and K in the soils occur largely as solute fluxes; in contrast, losses of Al and Fe are mostly as downslope transport of fine particles. Physical erosion of bulk soils also occurs: results from a steady-state model demonstrate that physical erosion accounts for about half of the total denudation at the ridgetop and midslope positions. Chemical weathering losses of Mg, Na, and K are higher in the upslope positions likely because of the higher degree of chemical undersaturation in porewaters. Chemical weathering slows down in the valley floor and Al and Si even show net accumulation. The simplest model for the hillslope that is consistent with all observations is a steady-state, clay weathering-limited system where soil production rates decrease with increasing soil thickness.

© 2010 Elsevier Ltd. All rights reserved.

## 1. INTRODUCTION

The Earth's surface comprises a weathering engine that solubilizes and disaggregates rock to form regolith. Regolith formation contributes to important processes such as nutrient cycling, carbon sequestration, erosion, and acid rain mitigation; thus, it is important that we learn to predict

\* Corresponding author. Tel.: +1 814 865 9384.  
E-mail address: [luj10@psu.edu](mailto:luj10@psu.edu) (L. Jin).

the rates and mechanism of such regolith formation. Over the long term, the rates of weathering and erosion also combine to control the evolution of landscapes and define the access, rates of motion, and time scales of water and energy movement within the Critical Zone (CZ) (Stallard, 1992; White et al., 1996, 2001, 2005; Riebe et al., 2003; Amundson, 2004; Heimsath et al., 2005; Brantley et al., 2006; Yoo et al., 2007; Anderson et al., 2007; Brantley and White, 2009). An understanding of the coupled processes that control regolith formation on all important parent lithologies is required to predict how the CZ will change in response to anthropogenic and climate perturbation. To understand such phenomena, watersheds are utilized to investigate intensively the relevant chemical, physical, and biological aspects of weathering on specific lithologies (e.g., White and Blum, 1995; Chadwick et al., 1999; Gaillardet et al., 1999; Jacobson et al., 2003; West et al., 2005; Williams et al., 2007).

As a ubiquitous lithology that covers about 25% of continental land mass (Amiotte-Suchet et al., 2003), shale has been the focus of some pioneering weathering studies (Little et al., 1991; Kolowith and Berner, 2002; Piersson-Wickmann et al., 2002; Amiotte-Suchet et al., 2003; Copard et al., 2007). However, quantitative models to predict rates of shale weathering are still unavailable. Partly in response to the need for such models, an observatory to study the inter-relationships among hydrology, geochemistry, ecology, and geomorphology has been established at the Shale Hills catchment in central Pennsylvania (hereafter termed the Susquehanna/Shale Hills Observatory or SSHO), developed largely on shale in the Rose Hill Formation. Importantly, Rose Hill Formation represents the oxidized end-member in the continuum of compositions observed for shales worldwide. The full range of shale compositions, including organic-rich endmembers, may be important in determining global fluxes of C, heavy metals and P worldwide (e.g., Petsch et al., 2001; Kolowith and Berner, 2002). The goals of this study are to: (1) identify mineral transformations during weathering of the Rose Hill shale; (2) attribute soil elemental depth profiles to mineral reaction fronts; and (3) use models of hillslope evolution to understand chemical weathering and physical erosion along a planar hillslope. The relatively limited variation in parent lithology at SSHO provides a well-constrained system to investigate relationships among weathering and erosion in a first-order catchment within a tectonically quiescent setting.

## 2. METHODS

### 2.1. Site description

The Susquehanna/Shale Hills observatory is an 8-hectare catchment located within the Valley and Ridge Physiographic Province of the Appalachian Mountains in central Pennsylvania (Fig. 1A). At SSHO, the mean annual temperature is 10 °C and the mean annual precipitation is 107 cm (NOAA, 2007). Within this forested catchment, a 1st-order ephemeral stream within the catchment flows to Shavers Creek, which eventually joins the Susquehanna

River via the Juniata River. The catchment is characterized by a stream channel which is aligned roughly east-west between narrow ridges (Fig. 1A). The average local relief from the valley floor to the ridge top is 30 m and the average channel gradient is 4.5% (Lynch, 1976). The gradients of the south-facing and north-facing slopes are 23° and 28°, respectively.

The geologic structure in the region is characterized by tight plunging folds in Silurian-aged strata. The catchment overlies shales of the Rose Hill Formation of the Clinton Group (Folk, 1960; Lynch, 1976; Lynch and Corbett, 1985). Strike and dip measured on an extremely limited exposure of bedrock at one point along the catchment floor are N54°E and 76°NW, respectively (Fig. 1A). Strike and dip measured stratigraphically and geographically proximal to the catchment range from 60° to 80°. However, borehole televue studies near the entrance of the catchment indicate more gentle dips of approximately 25°, consistent with results from three-point calculations on the regional geologic map (Hoskins, 1976). Tight meter-scale kink folds have been observed nearby in the Rose Hill Formation (Rose, 1973). These combined observations suggest that the structural setting below SSHO is complex with gently to steeply dipping and faulted strata. Characteristic erosion rates in the Appalachian Mountain region range from 8 to 29 m/Myrs with northern shale units (e.g., the SSHO) near the lower limit of this range (Roden and Miller, 1989; Blackmer et al., 1994; Reuter et al., 2004).

The 700-foot-thick Silurian-age Rose Hill Formation consists of olive-pink, grayish-buff shales with a few interbedded limestones (Lynch, 1976). Soil thickness, surveyed by augering and ground penetrating radar, averages 1.4 m in the catchment but varies from shallower at the ridge top to much deeper in the valley floor and swales (Lin et al., 2006). Soils show evidence of bioturbation and tree throw (Lin et al., 2006). As delineated by topography, location, soil thickness, and redox features, five soil series have been previously mapped in the catchment (Lin, 2006; Lin et al., 2006; Lin and Zhou, 2008). Soils on the ridge are mapped as Weikert series whereas planar and convex hillslope soils belong to the Berks series. All are loamy-skeletal, mixed, active, mesic Dystrudepts according to the US Soil Taxonomy (Lin and Zhou, 2008).

The SSHO has experienced at least two major perturbations in the geologically recent past: a perturbation from peri-glacial to modern conditions at approximately 15 kya (Gardner et al., 1991), and a perturbation due to clearing of forests during colonial occupation. Extensive data sets are available at SSHO from forestry field experiments: geographic information surveys, 1-m digital elevation model data (DEM), soil moisture synoptic sampling, soil mapping, streamflow monitoring, and preliminary ground penetration radar and gravity measurements from 1996-present (Lynch, 1976; Lynch and Corbett, 1985; Duffy and Cusumano, 1998; Lin et al., 2006; Qu and Duffy, 2007). The site is presently managed as a Pennsylvania State University experimental forest.

To characterize weathering of this catchment, pedons and catenas were chosen to investigate the propagation rates of weathering for sites representing different patterns

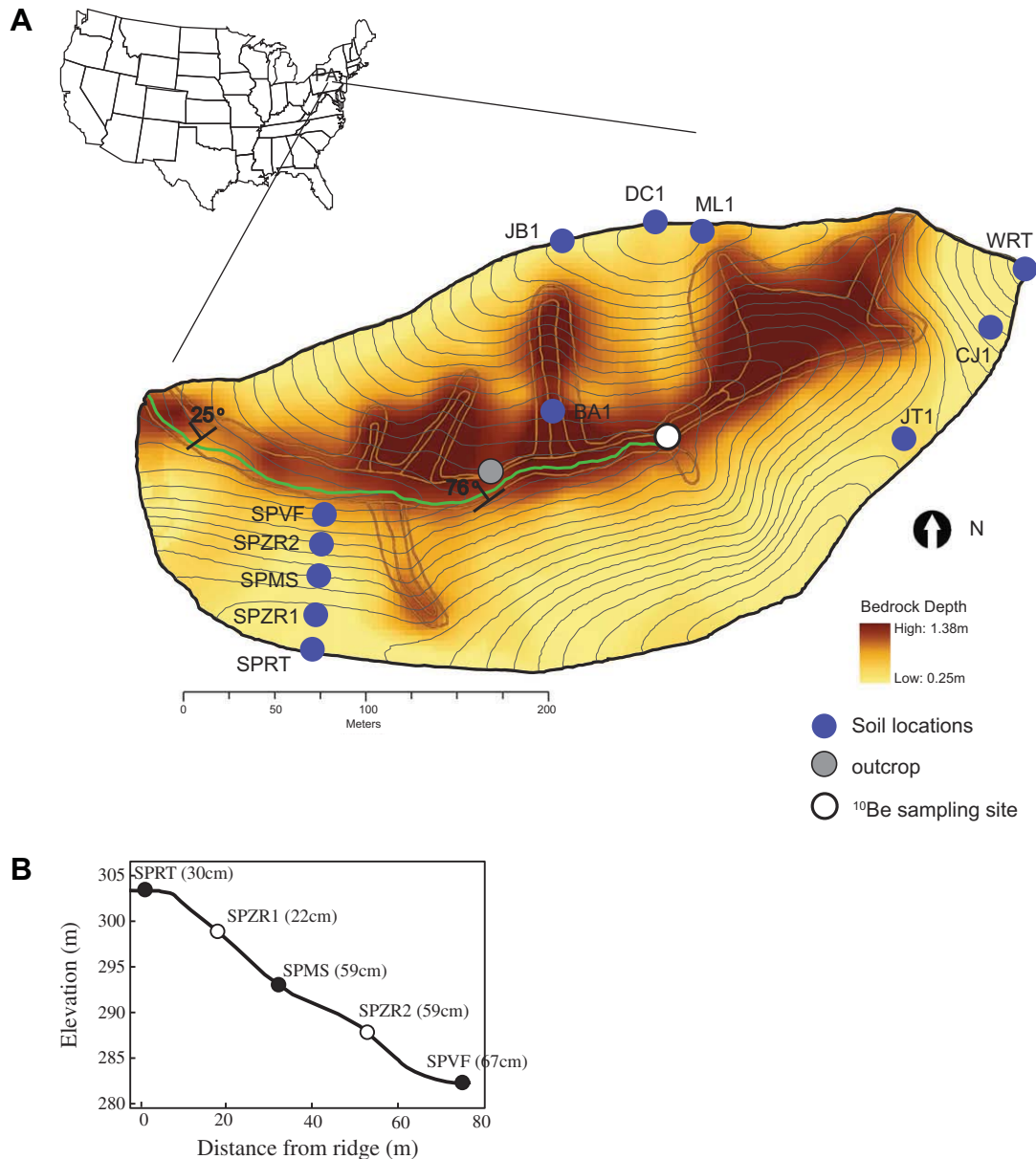


Fig. 1. Soil sampling locations in the Shale Hills catchment (A; modified from Lin et al., 2006). Background color indicates soil thickness. DC1 is the drill core site, where 25 m of parent shale was sampled as chips and powder. Soil core WRT represents the 1D site. Soil cores SPRT (SPRT2), SPMS (SPMS2) and SPVF (SPVF2) comprise the 2D planar transect. Two more cores are sampled along the 2D transect for bulk density analysis (SPZR1 and SPZR2). The strike and dip were measured from an outcrop (grey circle) and near the entrance. Five other cores were collected as shown in other sites of the SSHO and chemically analyzed for the deepest sample to constrain the parent composition. One stream sediment was collected near the headwater of the stream (white circle) and analyzed for meteoric  $^{10}\text{Be}$  to estimate erosion rates. (B) Cross section of the planar transect illustrates shape of the hillslope. Numbers in parentheses are soil thickness in centimeters. Notice that the hillslope is flat at SPRT, concave at SPVF, and planar at SPMS.

of sediment erosion, accumulation and water flow. These sites were selected where subsurface fluid flow in the regolith is largely one-dimensional (“1D”) and vertical (ridge top), two-dimensional (“2D”) downslope (planar hillslope), and three-dimensional (“3D”) downslope (convergent hillslope, swale). The overall strategy of the approach is to quantify weathering rates at each of these types of sites in order to integrate patterns over the entire watershed. In recognition of the effects of aspect as well as underlying

geological structure, two 2D and two 3D sites were each identified in the catchment, one on the north-facing slope and one on the south-facing slope.

The 1D-weathering site comprises the highest point in the catchment. Due to its location, this site does not include the effects of sedimentation but only losses through weathering and erosion. Interpretation of weathering at this site follows the approach described previously in the literature for other such 1D sites (Murphy et al., 1998; White et al.,

2001). In contrast to the 1D-site, the 2D- and 3D-weathering sites include not only the effects of propagation of the weathering front but also the effects of downslope regolith transport, i.e., the sites experience input/output of sediments and thus require more complex models for weathering (Yoo et al., 2007; Burke et al., 2007; Green et al., 2006). In this paper, we focus on chemical and mineralogical observations for the 1D site and the 2D planar hillslope (catena) on the southern slope (north-facing).

## 2.2. Drill core

Using a rotary air drill, we drilled 25 m deep into bedrock at the northern ridge and recovered disaggregated shale chips (site labeled as DC1 on Fig. 1A). Chips were used to characterize parent shale. Due to the steep dip of the bedding inferred from the outcrop at the valley floor, these samples may only correspond to about 6 m of the Rose Hill Formation. Soil samples (labeled DC1-1 (depth from surface = 0.18 m) and DC1-2 (depth from surface = 0.3 m)) were also collected at this location before drilling.

A rough estimate of the bulk densities of rock chips from drilling was determined by weighing chips dry and then measuring volume by displaced water using a graduated cylinder. Grain densities of representative DC1 samples were also measured with higher sensitivity using a pycnometer after grinding the samples to fine particles using a shatter box.

## 2.3. Augered soil cores

Soil profiles were sampled at SSHO using a 2-in. diameter auger. In this study, “soil” is operationally defined to be all regolith that can be sampled with a hand auger until the point of refusal. The zero depth was defined as the bottom of the organic layer or, equivalently, the top of the mineral soil. For each soil sample, an interval of about 10 cm was collected but the sample itself is labeled by the mid-point of this depth range.

One profile at the highest point of the catchment (WRT) was chosen as the 1D site (Fig. 1A). A roughly planar hillslope in the south side of the catchment was chosen as the southern 2D catena site (Fig. 1B). Duplicate soil profiles were collected at three sites down this hillslope: the South Planar Ridge Top (SPRT, SPRT2), Middle Slope (SPMS, SPMS2) and Valley Floor (SPVF, SPVF2) (Fig. 1). The two profiles at each location were only a few meters apart at the same elevation along the hillslope: one was characterized extensively while the other analyzed for chemistry only. Sample site SPVF is located ~5 m from the stream, i.e., in the footslope. Thus, the water table and the redox conditions in the deeper soil fluctuate seasonally.

We also report the chemistry of the bottom-most samples from five other soil profiles (BA1, JB1, ML1, CJ1, JT1) collected throughout the SSHO (Fig. 1A). These relatively unweathered materials were used to evaluate the heterogeneity of the parent shale as discussed further below.

Grain densities of representative weathered soil samples were measured with a pycnometer. Two more cores (SPZR1 and SPZR2, Fig. 1A and B) were also collected along the

planar hillslope for bulk density measurement following the method of Blake and Hartge (1986). For these, we used a sampler of known volume attached to our auger. Samples were then transferred to polyethylene bags, dried at 105 °C in the laboratory, and weighed after drying. Bulk density was computed using the known volume of the sampler and the mass after drying.

## 2.4. Sample preparation and elemental analysis

Soil pH values were measured in a slurry of soil and deionized water (1:1) (USDA, 2004). The remainder of each sample was air-dried immediately after sampling, homogenized and stored in resealable bags. Bulk samples, including rock fragments, were ground to pass through a 100-mesh sieve (<150 µm). Elemental abundances were measured by SGS Canada Inc. (Minerals Services Laboratory at Toronto, Ontario; method ICP95A). In this analysis, 1 g of ground sample was combusted at 950 °C for 1 h, and the difference in sample weight before and after combustion was reported as loss on ignition (LOI). The samples were further fused with lithium metaborate at 950 °C and re-dissolved in dilute nitric acid. Resultant solutions were analyzed by inductively coupled plasma optical emission spectrometer (ICP-OES) for major elements and inductively coupled plasma mass spectrometer (ICP-MS) for Zr. All analyses reported here are estimated to have precision of ±3%. Soil samples from WRT, SPZR1, SPZR2, SPRT2, SPMS2 and SPVF2 were analyzed at the Materials Characterization Laboratory (MCL) of Pennsylvania State University using the same lithium metaborate fusion method but without measuring LOI and then analyzed using ICP-OES for major elements. To investigate rock fragment chemistry in one location, elongated centimeter-sized shale chips from three depths of the augered SPRT core were also analyzed for elemental chemistry at Penn State. An inter-laboratory comparison was performed by running two standard reference materials (soils SRM2709 and SRM2711 from NIST) at SGS and MCL for major elements. The chemistry data by the two laboratories are within reasonable ranges of the certified values (Appendix Table 1).

## 2.5. Separation of clay fraction

For some samples, clay fractions were separated from bulk soils following the method of White and Dixon (2003) and Poppe et al. (2002). To start, 15–30 g of sample was weighed into a 250-ml glass beaker. A dilute acetic acid solution was prepared (1:4 acid to water ratio) and 50–75 ml portions were added to the samples to remove carbonate minerals. The sample and acid mixture were allowed to react for 2 h and additional 50 ml aliquots of acid was added and left to react overnight. Supernatant was decanted without loss of sample. A 3% H<sub>2</sub>O<sub>2</sub> solution was prepared and 50–75 ml aliquots were added to each sample. Samples were then heated and maintained for 30 min below 100 °C to facilitate oxidative removal of any organic matter in the samples. An additional 10 ml of 30% H<sub>2</sub>O<sub>2</sub> was added to samples rich in organic matter along with 50 ml of 3% H<sub>2</sub>O<sub>2</sub> to all the samples until frothing subsided. These solutions were transferred to 250-ml Teflon bottles

and centrifuged at 2000 rpm for 5 min. Supernatant was decanted and the soil was transferred into wide-mouthed 1-L glass bottles using distilled water. A small quantity (about 10 mg) of sodium hexametaphosphate dispersant was added to each sample and bottles were filled with distilled water to a height of ~10 cm. The bottles were shaken vigorously, then magnetically stirred for 20–30 s.

After stirring, the bottles were allowed to settle for 3 h 50 min at 22 °C so that only clay fractions remained suspended. Supernatant from the top 5 cm was then removed using a syringe. Successive extractions of clay fraction were accomplished by re-suspending the samples in distilled water. After each suspension, the supernatant was collected: this process was repeated until the solution in the top 5 cm was clear, indicating that the entire clay fraction was removed. The solutions were collected in 250-ml beakers and dried at 60 °C. After oven drying, samples were ground to fine powders using a mortar and pestle and stored in air-tight glass bottles for further analysis.

## 2.6. XRD and SEM analysis

Minerals in DC1 samples, selected soils, and in the clay fraction of soils were identified using X-ray diffraction (XRD). Samples were mounted onto a holder by a side loading technique (Moore and Reynolds, 1997) to achieve random orientation. Using a Scintag PAD-V powder X-ray diffractometer, samples were scanned from 2° to 70° 2 $\theta$  at 35 kV voltage and 30 mA current with Cu-K $\alpha$  radiation ( $\lambda = 1.54178 \text{ \AA}$ ) and a Ge solid state detector. Diffraction patterns were collected with a step size of 0.020° 2 $\theta$  at 1° 2 $\theta$  per minute. XRD patterns were analyzed using JADE software.

In addition to mineral identification, mineral abundances were also quantified for selected DC1, SPRT, SPMS, and SPVF bulk samples. XRD patterns were obtained and analyzed using the USGS program RockJock (Eberl, 2003).

Because chemical and thermal treatments can shift clay peaks in XRD patterns allowing differentiation of individual clay minerals, sample clay fractions were further treated sequentially by (i) Mg-saturation with 1 N MgCl<sub>2</sub> solution; (ii) Mg-saturation followed by treatment with ethylene glycol; (iii) K-saturation with 1 N KCl solution; (iv) K-saturation followed by heat treatments at 400 °C and 550 °C, respectively (complete methodologies are summarized in Moore and Reynolds (1997) and White and Dixon (2003)). Slides were prepared at room temperature by spreading powdered samples on zero-background quartz slides with a drop of water and then were left to dry. XRD patterns were obtained for each sample following treatments (i) through (iv).

A few samples from the DC1 core were also placed on conductive sample holders for observation with FEI Quanta 200 Environmental scanning electron microscopy (SEM).

## 2.7. Cation exchange characterization

To define the clay mineralogy and occupancy of cations in the interlayers, a cation exchange experiment was carried out following the methods of Amacher et al. (1990) and

White et al. (2005). Specifically, representative DC1 and bulk soil samples were sieved so that only particles less than 2 mm were analyzed. About 2.5 g of a sample were weighed into a 50-ml centrifuge tube and 25 ml of 0.1 M BaCl<sub>2</sub>–0.1 M NH<sub>4</sub>Cl solution was added. Samples were shaken for 15 min at 180 oscillation/min, then centrifuged at 2500 rpm for 20 min. The solution was filtered, weighed and analyzed by ICP-OES for major elements at MCL of the Pennsylvania State University. ICP standards were prepared in 0.1 M BaCl<sub>2</sub>–0.1 M NH<sub>4</sub>Cl solution to ensure matrix matching.

Soil residue was washed with de-ionized water, and 10 ml of 4 M acetic acid was added to dissolve carbonate minerals if present (Jacobson et al., 2003). The mixture was shaken for 6 h at 180 oscillation/min, then centrifuged at 2500 rpm for 20 min. The solution was filtered, weighed, and analyzed by ICP-OES for major elements at MCL of the Pennsylvania State University.

## 2.8. Stream water samples

Stream water was sampled near the mouth of the SSOH catchment from October 2006 to October 2008 (approximately 25 samples). Samples were filtered through 0.45  $\mu\text{m}$  Nylon syringe filters, and then acidified with a few drops of high purity HNO<sub>3</sub> for cation analysis. Measurements were completed for Ca, Mg, K, Na, Al, Si, and Fe using ICP-OES at MCL of the Pennsylvania State University.

## 2.9. Sampling and characterization of stream sediment for meteoric <sup>10</sup>Be

To estimate a catchment-specific rate of erosion, meteoric <sup>10</sup>Be was extracted from a sample of fluvial sediment (sand fraction) collected from the channel of the ephemeral stream (Fig. 1A). The sediment was powdered and 0.499 g of the powder, along with 299  $\mu\text{g}$  of SPEX <sup>9</sup>Be carrier, was processed using the method of Stone (1998) at the University of Vermont and analyzed at Lawrence Livermore National Laboratory using accelerator mass spectrometry. The <sup>10</sup>Be/<sup>9</sup>Be ratio of a full process blank was subtracted from the measured sample ratio.

# 3. RESULTS

## 3.1. Parent shale

At the DC1 site (Fig. 1A), the soil is very shallow (~0.1 m); thus, all samples deeper than 0.1 m at this site are shale bedrock. These DC1 samples were mostly olive or olive grey in color. However, two grey samples (the deepest two samples from 23 m and 24.5 m, respectively) and one olive brown sample at 4.5 m depth were observed. Loss on ignition (LOI) of the DC1 samples averaged 6 wt. %, but was higher at the shallow depths, at ~4.5 m, and also in the bottom-most sample.

DC1 samples (Table 1; Fig. 2A) are generally constant in elemental concentration except for the olive grey sample that showed very high Fe and low Al content at ~4.5 m

Table 1  
Elemental concentrations of drill core samples from Shale Hills catchment (DC1-longitude: W077°54.241'; latitude: N40°39.948').

Sample number	Depth range (m)	LOI (%)	Al (%)	Ca (%)	Fe (%)	K (%)	Mg (%)	Mn (%)	Na (%)	P (%)	Si (%)	Ti (%)	Zr (ppm)
DC1-1	0–0.18	7.20	10.43	0.11	5.08	3.41	0.78	0.12	0.40	0.07	27.02	0.68	204
DC1-2	0.18–0.30	6.88	11.96	0.29	5.66	4.24	0.96	0.06	0.33	0.27	27.25	0.70	152
DC1-3	0.30–0.49	7.14	10.80	0.13	5.47	3.64	0.87	0.18	0.36	0.07	26.08	0.65	165
DC1-4	0.49–0.61	6.40	10.69	0.14	5.36	3.65	0.86	0.09	0.27	0.07	26.79	0.67	171
DC1-5	0.61–0.79	6.17	10.74	0.14	5.44	3.74	0.92	0.05	0.44	0.05	26.93	0.65	194
DC1-8	1.1–1.2	6.13	11.33	0.14	5.44	3.98	0.92	0.05	0.42	0.06	26.83	0.67	179
DC1-11	1.5–1.7	6.84	10.90	0.11	5.60	3.69	0.86	0.09	0.30	0.06	26.88	0.66	186
DC1-14	2.4–2.6	5.83	10.69	0.12	5.57	3.73	0.92	0.06	0.50	0.06	26.79	0.65	195
DC1-17	3.4–3.5	5.81	10.32	0.11	5.46	3.63	0.90	0.05	0.36	0.04	25.94	0.62	173
DC1-20	4.3–4.5	7.68	9.16	0.14	12.17	2.47	1.03	0.64	0.37	0.07	24.40	0.52	171
DC1-23	5.2–5.4	5.63	9.84	0.11	5.26	3.46	0.89	0.05	0.33	0.05	26.55	0.61	203
DC1-26	6.1–6.3	5.84	11.06	0.11	5.97	3.93	1.05	0.09	0.28	0.06	27.25	0.67	172
DC1-29	10.7–10.9	6.11	11.01	0.09	5.67	3.88	0.95	0.10	0.36	0.05	26.97	0.63	170
DC1-32	15.2–15.4	5.73	10.58	0.11	5.42	3.88	1.10	0.08	0.35	0.05	26.41	0.57	172
DC1-35	19.8–20.0	5.57	11.01	0.13	5.36	3.95	1.12	0.02	0.32	0.04	26.93	0.62	155
DC1-37	22.9–23.0	5.29	10.74	0.48	5.20	3.87	1.29	0.05	0.37	0.05	26.37	0.58	153
DC1-38	24.4–24.6	8.16	7.73	1.85	5.85	2.60	1.33	0.19	0.28	0.05	27.67	0.46	231
Average <sup>a</sup>			10.75	0.12	5.50	3.76	0.95	0.08	0.36	0.06	26.70	0.64	178
Standard deviation <sup>b</sup>			0.38	0.02	0.19	0.16	0.09	0.04	0.07	0.01	0.38	0.03	14

The average values are used as the chemical composition of the parent shales for  $\tau$  calculations.

LOI and oxides for each sample add up to about  $100 \pm 2\%$ .

<sup>a</sup> Average of elemental concentrations, for samples between 0.30 and 20.0 m excluding 4.3–4.5 m.

<sup>b</sup> Standard deviation of elemental concentrations, for samples between 0.30 and 20.0 m excluding 4.3–4.5 m.

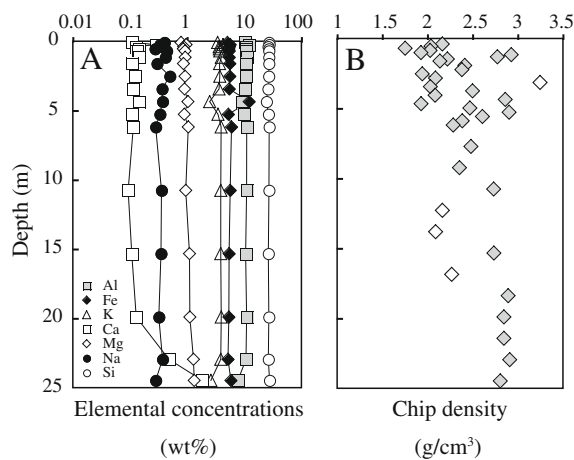


Fig. 2. Major element concentrations (A) and bulk density (B) measured in the 25-m drill core at DC1 site. A relatively high Fe content is observed at 4.5 m depth, above which a large variation in bulk density is also observed. Below 18 m, shale chips recovered from the drill core are smaller, and bulk density is almost constant. The bottom two samples are high in Fe, Ca and Mg, due to the presence of ankerite.

(Fe and Al values differed by more than  $1\sigma$  from the mean of the DC1 data). In addition, the two deepest grey samples are characterized by relatively high concentrations of Ca, Fe and Mn but lower concentrations of K and Al, i.e., these concentrations are more than one standard deviation higher than the mean of the DC1 sample set.

The average composition of shale bedrock was calculated to determine an inferred parent material composition

by averaging the concentrations of DC1 samples between 0.3 m and 20 m, excluding the topmost two soil samples, the sample at 4.5 m, and the deepest two samples. To assess heterogeneity of this parent material, the standard deviation around the mean was calculated: the values ranged from 0.01 to 0.38 wt.% for major elements to about 14 ppm for Zr (Table 1). The standard deviations are observed to be relatively low for elements present at more than 3 wt.% but much higher for elements present at less than 1 wt.%. The average compositions of the deepest, least weathered soils from five cores (BA1, CJ1, ML1, JB1, JT1) were also observed to be similar to the parent material within  $\pm 1\sigma$  (Table 1 and Appendix Table 2). Based on these observations, the averaged DC1 composition (where some samples were excluded as defined above) was used as the composition of the parent material for the following discussion.

Quantitative XRD of several parent samples (DC1) show that the analyzed section of Rose Hill shale is composed predominantly of illite (58 wt.%), quartz (30 wt.%), “chlorite” (either chlorite itself or a mineral exhibiting the same XRD peaks as chlorite; 11 wt.%), and trace amounts of feldspar (plagioclase and K-feldspar) and Fe-oxides (magnetite and hematite) (Table 2). “Chlorite”, as determined from quantitative XRD, is a term that here encompasses chlorite, vermiculite, hydroxy-interlayered vermiculite (HIV), and/or mixtures of these phases (Moore and Reynolds, 1997). Ankerite (Fe- and Mn-rich carbonate) was identified in the two deepest samples (1.4 wt.% and 7.1 wt.%, respectively), consistent with the higher Fe, Mn, Ca and LOI contents and the grey color of those samples. However, carbonate minerals were absent in all shallower samples.

Table 2  
Mineralogy of Shale Hills bedrock and soils, with corresponding  $\tau_{Zr,j}$  values.

Sample and depth (cm)	Quartz		Illite		Chlorite		Fe-oxides	Peat	Disordered kaolinite	Carbonate	Feldspar (wt.%)	Quartz/Zr <sup>b</sup>
	wt.%	$\tau_{Zr,j}$	wt.%	$\tau_{Zr,j}$	wt.%	$\tau_{Zr,j}$						
SPRT 0–10	49.9	0.02	29.6	-0.62	5.5	-0.55	2.5	9.8	2.8	–	4.2	0.18
SPRT 20–30	55.7	0.15	30.1	-0.61	8.1	-0.32	2.0	3.6	0.5	–	5.0	0.23
SPMS 0–10	55.1	-0.20	25.4	-0.77	4.8	-0.72	2.1	9.8	2.7	–	5.2	0.16
SPMS 20–30	60.7	0.05	26.7	-0.71	6.1	-0.58	1.9	3.2	1.4	–	6.6	0.21
SPMS 50–59	53.6	0.02	35.5	-0.58	7.1	-0.46	1.7	1.3	0.9	–	5.6	0.20
SPVF 0–10	63.3	-0.08	22.6	-0.80	3.5	-0.79	1.9	7.7	0.9	–	6.2	0.18
SPVF 30–40	43.4	0.01	47.5	-0.31	8.3	-0.23	0.4	0.0	0.4	–	2.8	0.20
SPVF 60–67	36.3	-0.03	54.4	-0.10	9.3	0.00	0.0	0.0	0.0	–	1.2	0.19
DC1-17	30.5		60.8		5.9		2.1	–	–	0	0.3	0.18
DC1-26	30.1		60.3		6.9		1.6	–	–	0	0.5	0.18
DC1-30	31.7		57.1		10.1		0.4	–	–	0	0	–
DC1-37	29.8		55.6		12.2		0	–	–	1.6	0	0.19
DC1-38	45.8		36.0		9.2		0.2	–	–	7.8	0.2	0.20
Average <sup>a</sup>	33.6		54.0		8.8							
Standard deviation <sup>a</sup>	6.9		10.3		2.5							

<sup>a</sup> Averaged from five drill core samples, and used as the parent shale mineralogy for  $\tau_{Zr,j}$  calculation.

<sup>b</sup> Quartz (in %) to Zr (ppm) ratios of bedrock and soils are close, indicating the immobile nature of both phases.

Under SEM, bedrock samples showed relatively homogeneous clay particle morphologies. Most grains appeared to be aggregates of individual particles. Using energy dispersive X-ray analysis (EDX), qualitative chemical analysis was completed. Most samples contained some Fe. EDX analysis was consistent with Fe oxides, clays, and occasional feldspar and zircon grains.

The grain densities of the DC1 chip samples average  $2.62 \pm 0.08 \text{ g/cm}^3$  ( $1\sigma$ ,  $n = 6$ ). The bulk densities determined for chips in the upper 4.5 m show high variability from 1.8 to  $3.3 \text{ g/cm}^3$ . In contrast, from 4.5 to 18 m depth, the densities only vary between 2 and  $2.8 \text{ g/cm}^3$ . Rock chips (generally several centimeters in dimension) recovered during drilling were also observed to be larger in the upper 17 m compared to deeper samples. Below 18 m, the bulk densities are consistently  $2.8\text{--}2.9 \text{ g/cm}^3$  (Appendix Table 3 and Fig. 2B). Bulk density can only be greater than grain density if material is lost during measurement. We conclude that some Fe oxides may have been lost during grinding for grain density measurement; furthermore, the bulk density measurements can only be seen as rough values. Despite this, a general trend is observed that chip density increased with depth.

### 3.2. Soils

Soil thickness varies significantly among the studied locations, depending on elevation and topographic features. Soils near the ridge tops are thin (WRT, SPRT, DC1, JB1, ML1), varying from 20 cm at DC1 and WRT to 30 cm at SPRT, 40 cm at JB1 and 28 cm at ML1. At DC1 and WRT, broken shale chips lie within the organic layer and are occasionally visible on the ground surface. Along the 2D-planar transect, soil thickness increases downslope from 30 cm at the ridge top (SPRT) to 59 cm at the middle slope (SPMS) and 67 cm at the valley floor (SPVF) (Fig. 1B).

Although the hillslope is nonconvergent and thus largely planar when considered along the east-west axis of the SSHO channel, when considered along a downslope axis, it is slightly convex at the ridgetop (SPRT) and slightly concave at the footslope position, SPVF.

Soil pH, ranging from 3.5 to 5.0, generally increases with depth, except for the ridge top site where pH is nearly constant at  $\sim 4$  (Table 3). The bulk density of soils increases from less than  $1.0 \text{ g/cm}^3$  in the organic-rich surface soils to about  $1.8 \text{ g/cm}^3$  in the deepest soil, where it is similar to shallow drill core samples (Appendix Table 3 and Fig. 3A). The grain densities of soil samples average  $2.63 \pm 0.05 \text{ g/cm}^3$  ( $1\sigma$ ;  $n = 5$ ), similar to that of the parent shale ( $2.60 \pm 0.08 \text{ g/cm}^3$ ) ( $1\sigma$ ;  $n = 6$ ), except for the topmost soil ( $0.69 \text{ g/cm}^3$ ), which contains significant amounts of organic matter (Appendix Table 3).

The minerals in the parent shale dominate the mineralogy of all the bulk soil samples, with addition of kaolinite (0–3 wt%) and organic matter (Table 2). Detailed clay characterization confirms the absence of smectite and the presence of kaolinite in the soil clay fractions. Kaolinite is inferred to be a secondary phase because it is observed in the soils but not in bedrock, and its abundance decreases with depth. The LOI values of the soils are higher than those observed in the DC1 samples, with a maximum in the topsoils (12–15%, Table 4A).

Clay characterization is consistent with the “chlorite” fraction consisting of chlorite, vermiculite and HIV in all soils from the planar transect (Appendix Tables 4 and 5). The mineral chlorite is absent from the topmost soils at SPRT and from one sample in the middle section of soil profile SPVF.

Major elements (except for Ca) show little variation with depth for the ridge top soils, but at the middle slope and valley floor sites, concentrations of major elements such as Al, Fe, Mg and K increase with depth while Si

Table 3  
Cations in the CEC of Shale Hills parent and soils along the planar transect.

Sample depth (cm)	Soil pH	Al (mmol/kg)	Ca (mmol/kg)	K (mmol/kg)	Mg (mmol/kg)	Na (mmol/kg)	Si (mmol/kg)	Mn (mmol/kg)	CEC (+) (meq/kg)	Al/CEC <sup>a</sup> (%)
<i>Ridge top (SPRT)</i>										
0–10	3.99	7.22	5.60	2.04	1.61	0.17	0.08	2.66	43.9	49.3
10–20	4.10	6.09	5.71	1.91	1.66	0.32	0.07	1.66	38.9	47.0
20–30	3.84	8.00	2.70	1.48	0.93	0.16	0.09	0.53	34.3	69.9
<i>Middle slope (SPMS)</i>										
0–10	3.79	7.91	4.40	1.35	0.92	0.17	0.11	3.37	43.1	55.0
10–20	3.72	7.08	4.30	1.09	0.98	0.20	0.10	0.83	35.2	60.4
20–30	3.80	6.36	5.25	0.92	1.49	0.16	0.09	0.24	34.5	55.3
30–40	3.72	8.04	5.18	1.03	1.75	0.22	0.12	0.36	40.5	59.6
40–50	4.46	8.60	6.04	1.33	2.71	0.35	0.15	0.33	46.3	55.8
50–59	4.38	7.35	4.96	1.18	2.61	0.13	0.13	0.44	39.9	55.2
<i>Valley floor (SPVF)</i>										
0–10	4.42	5.22	11.98	1.34	9.68	0.22	0.08	1.60	64.1	24.4
10–20	4.44	2.70	11.04	1.47	9.49	0.19	0.10	0.54	52.3	15.5
20–30	4.84	1.08	13.44	1.90	10.88	0.19	0.13	0.48	55.4	5.8
30–40	4.81	0.74	16.06	2.28	12.25	0.31	0.17	0.41	62.9	3.5
40–50	4.40	0.48	18.37	2.19	13.38	0.28	0.17	0.39	68.9	2.1
50–60	4.72	0.21	19.12	2.22	14.18	0.31	0.21	0.26	71.1	0.9
60–67	4.97	0.15	19.20	2.23	14.07	0.36	0.22	0.18	70.8	0.6
<i>Parent Shale</i>										
DC1 17		0.17	22.36	1.84	16.03	1.58	0.26	0.13	82.0	0.6
DC1 22		0.23	22.72	1.92	18.93	0.65	0.38	0.41	88.9	0.8
DC1 26		0.01	16.56	1.76	19.79	0.73	0.25	0.05	76.4	0.1
DC1 29		0.04	14.04	1.20	22.32	0.26	0.21	0.06	75.2	0.1
DC1 32		0.00	10.27	1.45	17.70	3.52	0.00	0.03	61.0	0.0

<sup>a</sup> Al/CEC ratio on an equivalent basis.

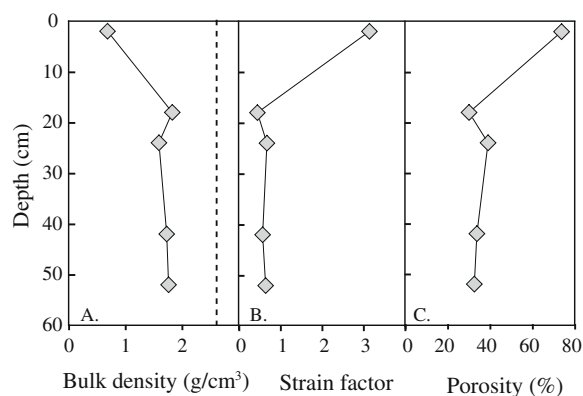


Fig. 3. (A) Bulk density measured at SPZR1 and SPZR2 cores along the planar transect. The soil grain density averages about 2.63 g/cm<sup>3</sup> (dashed line). (B) Strain factor calculated from bulk density for same cores. Positive values of strain indicate volume expansion during soil formation at SSHO. Ti instead of Zr was used as the immobile element for this calculation, which may overestimate the strain factor as discussed in text. (C) Total porosity calculated from bulk density and grain density. See text for details.

concentrations decrease (Table 4). The chemical composition of the duplicate cores (SPRT2, SPMS2, SPVF2, reported in Appendix Table 6) do not display significant variations from the primary core analyses. For the SPRT auger core, the rock fragment chips have higher Al, Fe,

Mg, K but lower Si, Zr, Ti concentrations than the corresponding bulk soils. Overall, the chemical composition of the chips is similar to that of the bedrock, except for Ca and Na.

Total Ca in SSHO soils and DC1 above 20 m is only about 0.1 wt.% and Ca concentrations are generally higher in surface soils. Relatively insignificant Mg and Ca concentrations were leached by 4 M acetic acid (<1 mmole/kg soil), consistent with little to no carbonate minerals (<0.01 wt.%) present in the soils.

### 3.3. Exchangeable cations

Cation concentrations in the exchangeable sites of five drill core samples and samples from three soil profiles along the 2D planar transect are presented in Table 3 and Fig. 4. The cation exchange capacity (CEC) of the parent shale ranges from 61 to 89 meq/kg dry soil with exchangeable sites dominantly occupied by Ca and Mg. The CEC of the three soil profiles, ranging from 34 to 71 meq/kg dry soil, increases downslope from the ridge top (SPRT), to middle slope (SPMS), to valley floor (SPVF) along the 2D planar transect (Fig. 4A–C). The deeper SPVF soils are similar to the parent shale with respect to capacity and composition of cation exchange sites, while the shallower soils have lower CEC. In the SPVF soils, the relative proportion of Al in the exchangeable sites is higher and the proportions of Mg and Ca decrease towards the surface (Table 3 and Fig. 4C). Cations in the exchangeable sites

Table 4A  
Elemental concentrations of Shale Hills soils, with corresponding Tau values, using Zr as an immobile element ( $\tau_{Zr,j}$ ).

Depth (cm)	Elemental concentrations														$\tau_{Zr,j}$ values										
	LOI (%)	Al (%)	Ca (%)	Fe (%)	K (%)	Mg (%)	Mn (%)	Na (%)	P (%)	Si (%)	Ti (%)	Zr (ppm)	Al	Ca	Fe	K	Mg	Mn	Na	P	Si	Ti			
<i>SPRT</i>																									
0-10	15.3	7.20	0.12	3.76	1.98	0.51	0.46	0.38	0.10	27.49	0.62	273	-0.56	-0.34	-0.56	-0.66	-0.65	2.81	-0.31	0.13	-0.33	-0.37			
10-20	11.3	7.36	0.17	4.00	2.13	0.56	0.36	0.39	0.13	28.98	0.64	275	-0.56	-0.08	-0.53	-0.63	-0.62	1.95	-0.29	0.53	-0.30	-0.35			
20-30	7.66	7.41	0.06	4.28	2.35	0.59	0.12	0.25	0.07	31.13	0.67	246	-0.50	-0.61	-0.44	-0.55	-0.55	0.15	-0.49	-0.14	-0.16	-0.25			
<i>SPMS</i>																									
0-10	12.6	6.51	0.15	2.98	1.74	0.43	0.31	0.49	0.12	29.96	0.71	351	-0.69	-0.37	-0.73	-0.77	-0.77	1.01	-0.31	0.12	-0.43	-0.43			
10-20	7.21	6.93	0.09	3.25	2.07	0.49	0.10	0.28	0.05	32.86	0.71	329	-0.65	-0.58	-0.68	-0.70	-0.72	-0.30	-0.57	-0.53	-0.33	-0.40			
20-30	6.65	7.20	0.11	3.60	2.22	0.55	0.05	0.48	0.08	32.07	0.65	295	-0.60	-0.43	-0.61	-0.64	-0.65	-0.58	-0.19	-0.14	-0.28	-0.38			
30-40	7.22	7.62	0.08	3.97	2.32	0.62	0.07	0.44	0.05	31.60	0.64	288	-0.56	-0.60	-0.55	-0.62	-0.60	-0.45	-0.24	-0.46	-0.27	-0.39			
40-50	7.77	8.10	0.10	4.26	2.57	0.66	0.06	0.47	0.08	31.46	0.64	277	-0.52	-0.47	-0.50	-0.56	-0.55	-0.49	-0.15	-0.09	-0.24	-0.36			
50-59	7.01	8.63	0.06	4.55	2.82	0.71	0.09	0.47	0.04	30.71	0.64	266	-0.46	-0.64	-0.45	-0.50	-0.50	-0.27	-0.12	-0.47	-0.23	-0.33			
<i>SPVF</i>																									
0-10	11.7	5.28	0.15	2.50	1.64	0.36	0.09	0.39	0.08	31.88	0.70	349	-0.75	-0.36	-0.77	-0.78	-0.80	-0.39	-0.44	-0.23	-0.39	-0.45			
10-20	7.51	6.88	0.11	3.31	2.24	0.52	0.07	0.35	0.03	31.83	0.68	318	-0.64	-0.50	-0.66	-0.67	-0.69	-0.50	-0.45	-0.65	-0.33	-0.41			
20-30	7.67	8.63	0.13	4.08	2.80	0.72	0.08	0.37	0.06	30.20	0.65	258	-0.45	-0.26	-0.49	-0.49	-0.47	-0.32	-0.28	-0.24	-0.22	-0.29			
30-40	7.56	9.05	0.11	4.45	3.05	0.78	0.07	0.35	0.04	28.33	0.62	219	-0.32	-0.23	-0.34	-0.34	-0.33	-0.27	-0.21	-0.36	-0.14	-0.21			
40-50	7.53	9.74	0.13	4.79	3.22	0.85	0.08	0.42	0.04	28.70	0.64	208	-0.22	-0.08	-0.25	-0.27	-0.23	-0.15	0.01	-0.39	-0.08	-0.15			
50-60	7.25	10.21	0.12	5.04	3.35	0.89	0.08	0.30	0.04	27.67	0.61	182	-0.07	-0.01	-0.10	-0.13	-0.08	-0.03	-0.19	-0.31	0.01	-0.07			
60-67	6.84	10.32	0.11	5.22	3.50	0.92	0.07	0.37	0.04	26.93	0.61	191	-0.11	-0.11	-0.12	-0.13	-0.09	-0.17	-0.03	-0.26	-0.06	-0.12			
<i>Chips from SPRT</i>																									
0-10		10.27	0.06	5.88	3.59	0.87		0.19	0.09	27.81	0.57	180	-0.06	-0.53	0.06	-0.06	-0.09		-0.49	0.56	0.03		-0.12		
10-20		11.75	0.05	5.04	4.37	0.99		0.22	0.06	26.79	0.61	150	0.30	-0.51	0.09	0.38	0.24		-0.26	0.22	0.19		0.13		
20-30		11.11	0.04	5.20	4.03	0.95		0.20	0.05	27.95	0.59	165	0.12	-0.62	0.02	0.15	0.08		-0.40	0.02	0.13		-0.01		

Table 4B

Elemental concentrations of Shale Hills soils, with corresponding Tau values, using Ti as an immobile element ( $\tau_{Ti,j}$ ).<sup>a</sup>

Depth (cm)	Elemental concentrations										$\tau_{Ti,j}$ values							
	Al (%)	Ca (%)	Fe (%)	K (%)	Mg (%)	Mn (%)	Na (%)	Si (%)	Ti (%)	Ti* (%)	Al	Ca	Fe	K	Mg	Mn	Na	Si
<i>WRT</i>																		
0–11	10.00	0.02	5.78	3.34	0.71	0.15	0.15	27.26	0.62	0.89	–0.33	–0.89	–0.25	–0.36	–0.46	0.37	–0.70	–0.27
11–15	9.47	0.03	5.25	3.05	0.65	0.14	0.15	27.38	0.64	0.98	–0.43	–0.86	–0.38	–0.47	–0.55	0.17	–0.73	–0.33
15–19	8.79	0.03	5.43	2.76	0.65	0.11	0.13	28.42	0.62	0.82	–0.36	–0.84	–0.23	–0.43	–0.46	0.14	–0.72	–0.17
19	10.85	0.01	5.56	3.88	0.80	0.04	0.16	27.30	0.62	0.62	0.04	–0.91	0.04	0.06	–0.14	–0.52	–0.54	0.05
<i>SPZR1</i>																		
6–0	2.37	0.52	1.06	0.36	0.13	0.40	0.09	7.33	0.15	0.25	–0.44	10.01	–0.51	–0.76	–0.64	12.21	–0.36	–0.30
12–22	7.57	BDL	3.95	2.08	0.49	0.07	0.12	29.17	0.61	0.76	–0.40	–1.00	–0.39	–0.53	–0.56	–0.25	–0.72	–0.08
<i>SPZR2</i>																		
0–3	5.88	BDL	2.93	1.44	0.31	0.25	0.15	26.51	0.56	1.02	–0.66	–1.00	–0.67	–0.76	–0.80	1.00	–0.74	–0.38
20–23	7.20	0.03	3.57	2.23	0.47	0.02	0.24	30.80	0.60	0.85	–0.50	–0.78	–0.51	–0.55	–0.63	–0.78	–0.50	–0.13
38–41	8.95	BDL	4.44	2.95	0.62	0.02	0.24	29.03	0.59	0.74	–0.28	–1.00	–0.30	–0.32	–0.44	–0.74	–0.41	–0.06
48–51	8.84	BDL	4.52	2.81	0.60	0.03	0.21	29.03	0.60	0.70	–0.25	–1.00	–0.25	–0.32	–0.42	–0.64	–0.47	–0.01
54–59	9.21	0.01	4.76	3.21	0.63	0.02	0.20	26.46	0.55	0.60	–0.08	–0.88	–0.07	–0.08	–0.28	–0.68	–0.40	0.06

BDL, below detection limit; 0.01% for Ca.

<sup>a</sup> Zr concentrations were not measured in these soils. Assuming similar proportions of Ti were lost at the same depth between WRT and SPRT, between SPZR1 and SPMS, and between SPZR2 and SPVF, we reconstructed Ti concentrations (Ti\*) and used these for  $\tau$  calculations.

of the SPRT and SPMS are mainly comprised of Al (about 60%), with moderate amounts of Ca and Mg. Contributions of Na, K and Si to overall CEC remain relatively constant as a function of depth and position as compared to parent shale (DC1).

Cation exchange sites account for about 20% of the total Ca in the soils at SPRT and SPMS, and nearly 50% in the SPVF soils and DC1 shale samples (Total Ca in SSSH soils and DC1 above 20 m is only about 0.1 wt.%). In contrast, Al and Mg on the CEC sites are negligible compared to their contents in the bulk soils.

### 3.4. Stream water chemistry

Concentrations of major elements varied seasonally in stream waters, ranging from 20 to 45  $\mu\text{M}$  for K, 12 to 60  $\mu\text{M}$  for Na, 60 to 600  $\mu\text{M}$  for Ca, 70 to 200  $\mu\text{M}$  for Mg, and 70 to 130  $\mu\text{M}$  for Si. In comparison, the dissolved Fe and Al concentrations are much lower (0.1 to 1  $\mu\text{M}$  for Fe, and 0.5 to 5  $\mu\text{M}$  for Al). The stream pH values range from 5 to 6.5. The average molar ratios of element concentrations over the two year period for Mg:Si:K:Fe:Al equal approximately 1.5:1:0.35:0.005:0.01.

### 3.5. Basin-scale erosion rate

The  $^{10}\text{Be}$  concentration of the sediment,  $3.33 \times 10^8$  atoms  $\text{g}^{-1}$ , was interpreted as a basin scale erosion rate of 39 tons  $\text{km}^{-2} \text{y}^{-1}$  (15 m/Myrs) assuming steady state, the site-specific rock density of 2.6  $\text{g cm}^{-3}$ , and an integrated  $^{10}\text{Be}$  delivery rate of  $1.3 \times 10^6$  atoms  $\text{g}^{-1} \text{y}^{-1}$  (Bierman et al., 2008; 2009). This site-specific erosion rate is indistinguishable from the average rate of denudation for the entire Appalachian Mountain range ( $17 \pm 9$  m/Myrs) calcu-

lated using over 250 in-situ measurements of  $^{10}\text{Be}$  in catchment sediments sampled over the entire Appalachian region (Bierman et al., 2007).

## 4. DISCUSSION

### 4.1. Bedrock transformation and weathering fronts

Major elements such as K, Mg, Fe, Al, and Si are relatively homogeneous within 25 m of the drill core samples (Table 1; Fig. 2A). However, Ca concentrations in the drill core samples are relatively low from the surface to 20 m depth, and then increase as high as 1.8% below that depth. DC1 samples also show less variability in chip density with depth below 20 m. This transition at 20 m may be related to either a lithologic shift between a carbonate-poor and a carbonate-rich unit in the Rose Hill Formation or may be indicative of the reaction front for dissolution of carbonate. Due to its reactivity,  $\text{Ca} \pm \text{Fe} \pm \text{Mg} \pm \text{Mn}$  carbonate (e.g., ankerite) is expected to be one of the first minerals to dissolve.

Brantley and White (2009) have argued that carbonate minerals can be profile-controlling minerals in that dissolution of these fast-dissolving phases often precedes weathering of other minerals and promotes deep influx of water into bedrock at the base of the weathering zone. For example, White et al. (1999) have documented that dissolution of calcite occurs at 10 m depth in granite in Panola, Georgia. According to those authors, calcite dissolution controls dissolution of plagioclase such that the plagioclase reaction front exactly parallels the calcite front but lies at shallower depths. Although we cannot rule out a lithological change as an alternate explanation, the simplest interpretation of the Ca profile in DC1 is therefore that loss of Ca above

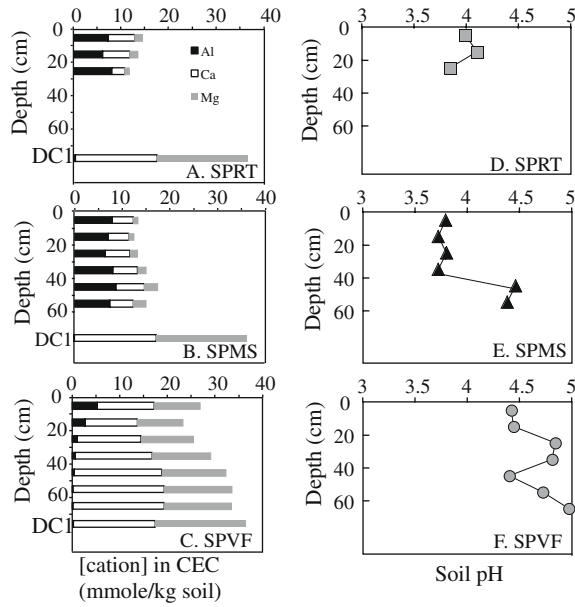


Fig. 4. Cation concentrations within the exchangeable sites at SPRT (A), SPMS (B) and SPVF (C) are plotted versus depth. Soil pH is plotted versus depth at SPRT (D), SPMS (E) and SPVF (F). The exchangeable cation concentrations averaged for DC1 site (bedrock) were plotted at the bottom of (A), (B) and (C) for comparison.

20 m depth represents dissolution of a carbonate mineral. If that is the case, the Ca profile in Fig. 2 thus represents the reaction front for ankerite in the system.

Likewise, the large variability in density above 6 m in the drilled shale chips may also be related to chemical factors. The similar chemistry observed between chips collected from SPRT and from drilled bedrock suggests that chips experience little chemical weathering with respect to K, Al, Fe, and Mg. Therefore, the loss of Ca and Na from the chips is attributed to feldspar dissolution that occurs before the clay mineral dissolution (Table 4). Most likely, the high Fe at 4.8 m and the change in chip size at about 17 m is related to the dissolution of feldspar and carbonate respectively and may correlate with the changes in density. Specifically, this uppermost zone demonstrates significant variability in Na and Ca chip concentrations, consistent with varying degrees of dissolution of feldspar.

The bottom-most soil bulk densities are similar to those measured in shallow drill core samples, consistent with our inference that DC1 samples can be considered as parent material. In the soils, clay minerals start to dissolve as described below and the bulk density decreases towards the ground surface (Fig. 3). Thus, the reaction fronts inferred at depth for carbonate (20 m) and feldspar (6 m) are overlain by weathering fronts for clay minerals. We have no evidence to suggest that these clay reactions extend into bedrock.

#### 4.2. Strain and element immobility

Our analysis of SSHO soils relies on the determination of elements that are mobilized from the soil and those that remain immobile. Elements that are commonly immobile in

soils include Zr, Ti, and Nb (Brimhall and Dietrich, 1987; Chadwick et al., 1990; Taylor and Blum, 1995; White et al., 1996; Price et al., 2005), although the mobility depends upon mineralogy and porewater composition (Kurtz et al., 2000; Neaman et al., 2006). In the soils at SSHO, Ti/Zr ratios decrease towards the land surface to values consistent with up to 45% loss of Ti. SiO<sub>2</sub> in quartz is also commonly used as a conservative component in sedimentary environments (White et al., 1996, 2008). At SSHO, quartz/Zr ratios are similar between bedrock shale and soils, consistent with little mobility of either quartz or Zr (Table 2). Thus, Zr, which we have only observed to be present as the relatively insoluble mineral zircon, is assumed to be the most immobile element in the analyzed soils.

The ratios of the volume of the soil ( $V_w$ ) to that of parent ( $V_p$ ) were assessed at SSHO by calculating the strain factor  $\varepsilon_{i,w}$  (Brimhall and Dietrich, 1987; Anderson et al., 2002):

$$\varepsilon_{i,w} = \frac{V_w}{V_p} - 1 = \frac{\rho_p}{\rho_w} \frac{C_{i,p}}{C_{i,w}} - 1 \quad (1)$$

Here,  $\rho$  refers to bulk density of parent (subscript  $p$ ) or weathered material ( $w$ ), and  $C$  refers to concentration of immobile or mobile elements ( $i, j$ , respectively). Positive  $\varepsilon$  values indicate expansion, a value of zero indicates iso-volumetric soil formation, and negative values indicate compaction. For example, deep regolith commonly develops iso-volumetrically on granite, i.e., soil thickness is equivalent to the initial thickness of parent material (White et al., 2005). Soils in karst regions, in contrast, collapse significantly due to preferential dissolution of carbonate minerals (Jin et al., 2008).

The calculated value of  $\varepsilon_{i,w}$  depends upon choice of immobile element. Given that we only measured bulk density of a few soil samples but did not measure Zr concentrations in those samples, to investigate strain we here only assess values of  $\varepsilon_{Ti,w}$ . Using 2.6 g/cm<sup>3</sup> as  $\rho_p$ , the calculated values of  $\varepsilon_{Ti,w}$  are positive for SPZR1 and SPZR2, ranging from 0.5 to 3.5, consistent with expansion of soils (Fig. 3B). These reported strain values based on Ti are presumed to be larger than  $\varepsilon_{Zr,w}$ , given the significant amount of Ti that has been lost. If we correct  $\varepsilon$  by assuming 45% loss of Ti, this yields strain values from 0 (no volume change) to 2 (doubling in soil volume). Therefore, soil expands during development.

Another calculation that can be made and which does not depend upon immobile elements is the calculation of total porosity  $\phi_t$  from bulk and grain density:

$$\phi_t = \left(1 - \frac{\rho_w}{\rho_g}\right) * 100\% \quad (2)$$

The porosity in the surface layer is as high as 70% and decreases with depth to 40% (Fig. 3C).

#### 4.3. Elemental changes along the planar transect

We use the assumption of immobility of Zr or Ti to also calculate relative loss or gain of elements. The behavior of elemental concentrations as a function of depth in regolith

and bedrock can be categorized with respect to simple end-member types (Brantley et al., 2007, 2008; Brantley and White, 2009). The end-member types relevant to SSHO are immobile profiles that show concentrations close to parent at all depths and depletion profiles wherein the elements are depleted at the surface but approach parent concentration at depth.

To assess the elemental profiles, it is necessary to first correct for the effects of expansion/compaction and for relative changes in concentrations due to changes in other elements in the soils. The value of  $\tau$ , the mass transfer coefficient, is therefore calculated according to the following equation (Brimhall and Dietrich, 1987; Anderson et al., 2002):

$$\tau_{i,j} = \frac{C_{j,w}}{C_{j,p}} \frac{C_{i,p}}{C_{i,w}} - 1 \quad (3)$$

Positive  $\tau_{i,j}$  values indicate enrichment of element  $j$ , negative values mean depletion and zero means element  $j$  is immobile in the weathered soils ( $w$ ) with respect to parent ( $p$ ). In fact,  $\tau_{i,j}$  equals the fraction of element  $j$  that was lost from the soil for  $\tau_{i,j} < 0$  and the relative enrichment factor for element  $j$  when  $\tau_{i,j} > 0$ . The  $\tau_{i,j}$  values computed for all profiles are reported in Table 4.

Fe, K, Mg, Si and Al show depletion profiles in the 1D site (WRT) and in all five soils along the planar 2D transect (Fig. 5). However, in contrast to SPVF, the deepest soils of the WRT, SPRT, SPZR1 and SPMS sites do not reach parent composition. The shallow soils at the upslope sites may have been homogenized by physical and biological mixing such as animal burrowing and tree throw. If mixing is the major reason for subvertical  $\tau_{i,j}$  plots (Fig. 5), then mixing processes are almost as fast as chemical weathering in the shallow ridgetop soils but are slower than such weathering in the thicker soils at SPMS and SPVF. However, bioturbation has been shown to be ineffective in mixing the soils in New England where snow cover can be significant (Kaste et al., 2007). Given the relatively similar climate between PA and New England, we argue that the subvertical  $\tau$  plots are not well explained simply by mixing. The chips recovered from the SPRT site are depleted with respect to Na, Ca but not other major elements such as K, Mg, Al and Fe, suggesting feldspar dissolution is prior to clay weathering (Fig. 5G).

Given our observations of leaching of elements such as Ca and Na in the bedrock, the best explanation for subvertical  $\tau$  plots is probably that unweathered bedrock has not been reached at the layer of augering refusal at the WRT, SPRT, SPZR1 and SPMS sites. As stated previously, these bottom-most samples lie within  $1\sigma$  of the mean for DC1; however, this relative error in estimation of parent composition is large enough to explain the discrepancy in Fig. 5. To exemplify this idea, we have drawn two horizontal lines on Fig. 5B, one to indicate the depth of refusal of augering (physical definition of bedrock) and one to indicate the inferred depth of chemically unaltered bedrock (chemical definition of bedrock). The latter was defined by visually extrapolating the  $\tau$  plots to  $\tau = 0$ .

Within each soil profile on the planar transect, the relative proportions of depletion are similar among Al, Fe, K,

and Mg. For example, the SPRT site has lost 55% of K and Mg, 50% of Al and about 44% of Fe. As Al, Fe, Mg and K occur in the chlorite and illite (see next section), similar fractional depletion for these elements is consistent with congruent dissolution of these two minerals, as discussed later. This conclusion is also consistent with similar grain densities observed for the soils and the parent shale.

Due to the presence of inert quartz, Si shows less depletion than K and Mg. Similarly, Na and Ca are depleted to a lesser extent than K and Mg (e.g., by about 30%) at all three sites, presumably due to feldspar dissolution (Table 4). Values of  $\tau_{Mg}$ , contoured based on the five soil profiles along the planar transect using Origin software (Fig. 5H), document that the extent of Mg depletion is higher in the upper hillslope, decreasing towards the valley floor.

#### 4.4. Mineral transformations

Soil mineralogy was compared to the parent shale to understand weathering reactions as a function of depth and landscape location (e.g., White et al., 1996; Murphy et al., 1998; White et al., 2001; Burke et al., 2007; Brantley and White, 2009). Depletions or enrichments of the dominant minerals illite and “chlorite” ( $j$ ) were evaluated by calculating  $\tau_{Zr,j}$  from Eq. (2), using mineral abundances instead of elemental concentrations. Uncertainty in mineral  $\tau_{Zr,j}$  was evaluated in the same fashion as for elemental  $\tau_{Zr,j}$  values by assuming that relative error in mineral quantification is 5%. Both “chlorite” and illite showed depletion profiles, indicating significant loss of “chlorite” and illite especially from the shallow soils (Fig. 6A–C). This observation is consistent with the significant depletion of K, Mg, Al, Si, and Fe in soils (Fig. 5). Quartz remains relatively immobile (Fig. 6A–C).

Previous studies in a variety of climates and soil types have demonstrated that chlorite and illite weathering generally occurs through a series of clay transformation reactions (e.g., Klute, 1986; Bain et al., 1993; Lee et al., 2003; Wilson, 2004; Hseu et al., 2007). For example, Lee et al. (2003) showed that chlorite transformed into interstratified vermiculite–chlorite and vermiculite with progressive release of Mg and Fe from the brucite-layer of the chlorite structure in serpentinitic soils of northern California. Detailed clay characterization at SSHO showed vermiculite and HIV in all soils of the planar transect. Both phases share XRD peaks with chlorite (Appendix Tables 4 and 5), making it difficult to distinguish primary mineral phases from weathering products. However, because the charge and identity of the interlayer cations in chlorite, vermiculite, and HIV are different, we used the CEC of the soil and parent shale samples to characterize the clay transformations as described in the next section.

The shale bedrock (DC1) and soils at the valley floor (SPVF) have similar cation exchange capacity and composition, with  $Mg^{2+}$  and  $Ca^{2+}$  dominating exchange sites (Fig. 4C). The occurrence of vermiculite in the soils of the valley floor, especially the deepest soils, is consistent with the interpretation that the chlorite in the parent Rose Hill shale has a vermiculite component, i.e., “vermiculited” chlorite. At SPVF,  $Al^{3+}$  concentrations in the cation ex-

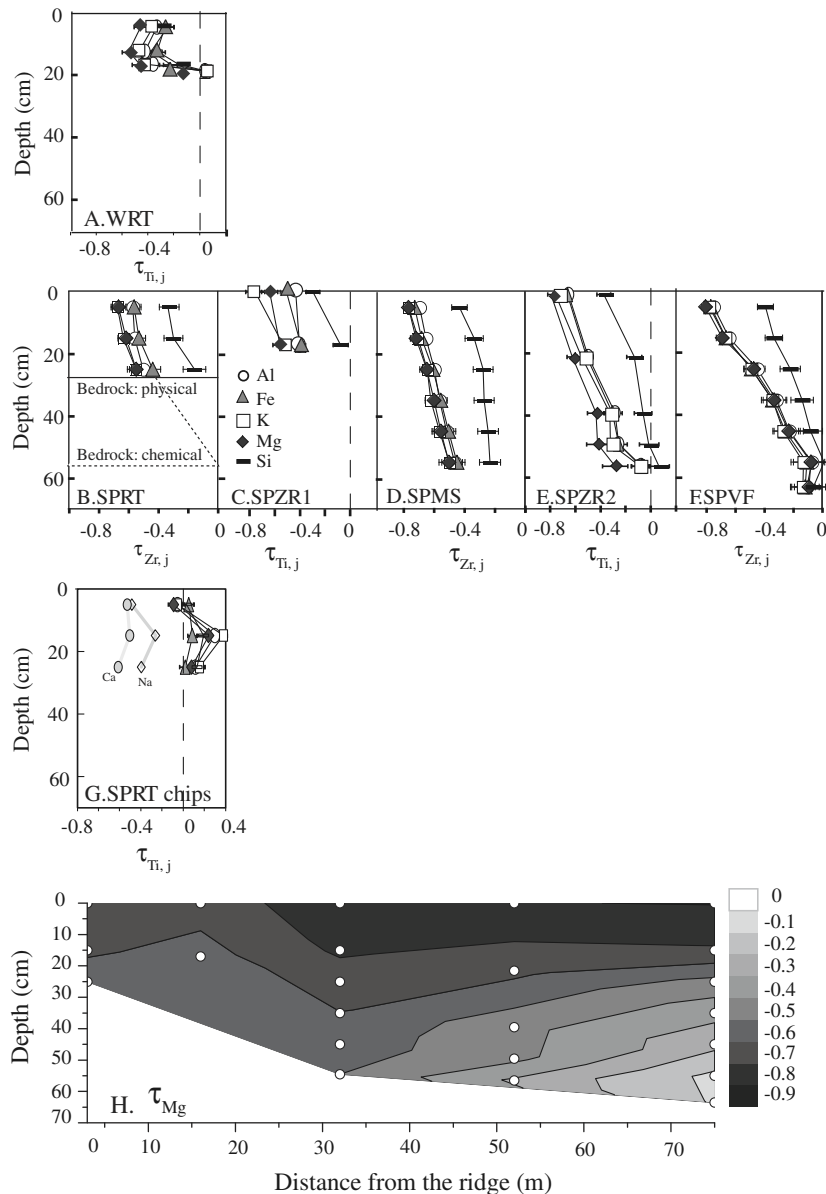


Fig. 5. Depletion of major elements in the 1D site sampled at the highest point in the catchment (A.WRT) and in five soil profiles along the 2D planar transect (B – SPRT at ridge top; C – SPZR1; D – SPMS at middle slope; E – SPZR2; F – SPVF at valley floor). Error bars indicate uncertainties in  $\tau$  calculation. Ti was used as the immobile element for (A), (C) and (E) (see Table 4 for details). In Figure 5B, one horizontal line indicates the depth of refusal of augering (physical definition of bedrock) and one indicates the inferred depth of chemically unaltered bedrock (chemical definition of bedrock). The latter was defined by visually extrapolating the  $\tau$  plots to  $\tau = 0$ . A contour map was made for  $\tau_{Mg}$  based on the 5 soil profiles along the 2D transect (H).

change sites increase upward in the soil profile while  $Mg^{2+}$  and  $Ca^{2+}$  concentrations decrease. In contrast, the CEC and its composition at SPRT and SPMS vary little with depth but differ significantly with DC1 samples, consistent with the previous conclusion that the soils at these two sites have not been sampled to the parent shale.

Importantly,  $Al^{3+}$  content in CEC becomes significant as weathering progresses, occupying up to 60% of the exchange sites at SPRT and SPMS. This is consistent with the observation that the soil pH showed an increase of pH with depth (Fig. 4D and E). A value of  $Al/CEC$  ratio of 60% (Table 3) as observed at SPRT and SPMS has been

described as the threshold value where Al starts to play a greater role in buffering acidity (Chadwick and Chorover, 2001). The high Al composition of the CEC also reflects the inferred hydrolysis and polymerization of Al in interlayers of vermiculite in acid soils such as those at SSHO (Graham et al., 1989).

Vermiculite formation generally reflects a structural inheritance from illite and chlorite. In contrast, when precipitation of kaolinite occurs during such clay transformations, it forms after the complete destruction of the 2:1 clay structure. Kaolinite, not detected in the parent bedrock, is present in concentrations up to 2.8 wt.% in the soils,

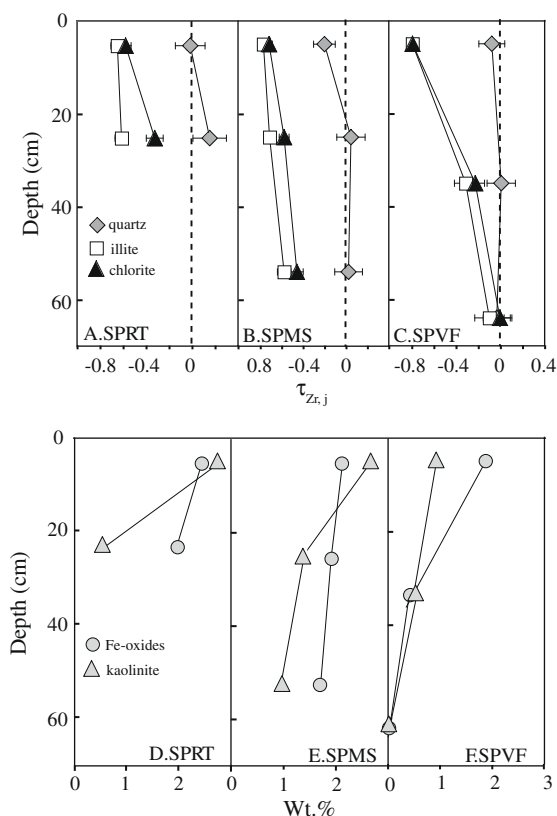


Fig. 6. Variation of primary mineral abundances relative to parent (dashed lines) at ridge top (A), middle slope (B), and valley floor (C); absolute abundances of kaolinite and Fe-oxides at ridge top (D), middle slope (E), and valley floor (F) along the planar transect. “Chlorite” and illite show depletion while quartz remains relatively unchanged versus depth. The fraction attributed to “chlorite” is assumed to be composed of chlorite, vermiculite and HIV, as described in the text.

increasing in abundance upward to the surface (Table 2; Fig. 6D, E, F). All of these characteristics are consistent with its presence as a weathering product. Kaolinite may also form due to feldspar dissolution, as negative values of  $\tau_{Na}$  are observed in all soils (Table 4). Kaolinite is known to be a stable secondary phase in temperate regions such as SSHO (Klute, 1986; Berner and Berner, 1996; Jin et al., 2008). The absence of smectite at Shale Hills is consistent with the fact that the catchment is well-drained and experiences a temperate climate (Helgeson et al., 1969; Berner and Berner, 1996; Price et al., 2005).

The sequence of mineral transformations in the soils developed on Rose Hill shale can be summarized in the following five reactions:

- (i) feldspars  $\rightarrow$  kaolinite
- (ii) illite  $\rightarrow$  vermiculite
- (iii) chlorite  $\rightarrow$  vermiculite
- (iv) vermiculite  $\rightarrow$  hydroxy interlayered vermiculite (HIV)
- (v) hydroxy interlayered vermiculite  $\rightarrow$  kaolinite + Fe-oxhydroxide.

The similarity of K and Mg depletion profiles is suggestive of congruent dissolution of illite and chlorite (Fig. 5). However, dissolved Al and Fe concentrations in filtered stream waters averaged over 24 months at Shale Hills are less than  $5 \mu\text{M}$  and  $1 \mu\text{M}$ , respectively, not high enough to account for stoichiometric release of these elements from chlorite and illite dissolution. Thus, Fe and Al are not significantly lost from the SSHO soils as solutes that pass a  $0.45 \mu\text{m}$  filter. Instead, micron-sized Al- and Fe-rich particles are inferred to be lost from the soils. Since no accumulation of Al and Fe was observed at the soil–bedrock interface, these particles must be translocated downslope by flowing water.

Consistent with the inference of translocation, previous field studies and soil column experiments in France, Denmark, and Virginia have revealed that particles can be mobilized vertically in soil profiles by shear stresses in macropores at rates of about 10–100 mg particle/L (Laegdsmand et al., 1999; El-Farhan et al., 2000; Rousseau et al., 2004). The mobilized particles are generally several microns in size and consist of clay minerals (kaolinite), organic matter, and Fe-oxide/hydroxides (Kaplan et al., 1997). Particle transport is favored by high infiltration rate, high soil moisture content, and the presence of continuous macropores in the soil structures (Rousseau et al., 2004), all of which have been observed through soil moisture studies at SSHO (Lin, 2006).

Given that shales are characterized initially by fine grain size, particle translocation should be an important player once chemical dissolution has disaggregated the bedrock. Thus, we conclude that mobilization of Al- and Fe-bearing particles, especially secondary phases such as kaolinite and Fe-oxhydroxide, is a very significant contributor to elemental mobility at SSHO. Given that Fe and Al accumulation was observed in SPVF, we also conclude that this particle transport occurs down the hillslope through the soil.

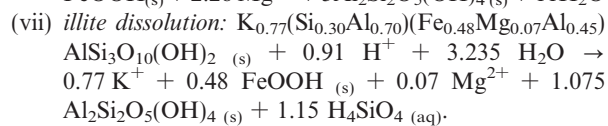
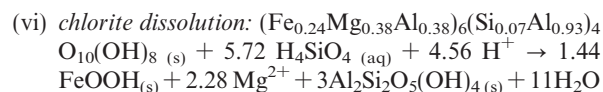
#### 4.5. Stoichiometric reactions

It is impossible to physically separate or quantitatively partition the two dominant minerals in the SSHO, “chlorite” and illite, because their physical and chemical properties are similar. In this section, a normative model of mass balance is therefore developed that is consistent with all observations – and especially the quantitative XRD information. The model is constructed to partition major elements into identified mineral phases. Samples used to constrain this exercise are soils from the planar transects and DC1 samples where carbonate minerals are known to be absent (above 20 m).

First, all of the measured Na and Ca concentrations were allocated to albite and anorthite, respectively. The K was then allocated to potassium feldspar until the total wt.% feldspar (albite + anorthite + K feldspar) equaled the feldspar fraction estimated from quantitative XRD (Table 2). Si was also allocated in the requisite amounts to feldspar. Next, the remaining Si was allocated to quartz until the wt.% of that phase equaled that measured by XRD. When kaolinite was observed using quantitative XRD, the appropriate amount of Al and Si was allocated to

kaolinite. Some Fe was allocated to Fe-oxide assuming a stoichiometry of FeOOH. Last, the remaining major cations (as K, Mg, Fe, Al, and Si oxides) were allocated to illite and chlorite to achieve the fraction observed for each clay with XRD. For this calculation, Fe was assumed to be Fe(III) in the illite and chlorite structure because the Rose Hill Formation is relatively oxidized, as evidenced by the presence of hematite and magnetite (Folk, 1960). A multiple-dimension linear regression was applied using a standard mineral composition (Kudrat et al., 2000) for “chlorite”,  $(\text{Fe}_a\text{Mg}_b\text{Al}_{1-a-b})_6(\text{Si}_{1.5b-0.5}\text{Al}_{1.5-1.5b})_4\text{O}_{10}(\text{OH})_8$ , and illite,  $\text{K}_{1+y-z}(\text{Si}_z\text{Al}_{1-z})(\text{Fe}_x\text{Mg}_y\text{Al}_{1-x-y})\text{AlSi}_3\text{O}_{10}(\text{OH})_2$ . The following stoichiometric coefficients were determined as best fits:  $a = 0.24$ ,  $b = 0.38$ ,  $c = 0.07$ ;  $x = 0.48$ ,  $y = 0.07$ ,  $z = 0.30$ .

Importantly, the “chlorite” phase discussed here is a model mineral that includes contributions from vermiculite and HIV. For this reason, Al is calculated to be present in greater abundance than in a typical chlorite (Kudrat et al., 2000). Using this mineral formula, the following stoichiometric weathering reactions were written as composite reactions describing reaction (i) through (iv) above:



In summary, dissolution of illite and chlorite forms more stable kaolinite through intermediate phases, followed by translocation of Fe-oxides and kaolinite as particles. Overall, Al and Fe are lost mostly as secondary phase particulates while  $\text{Mg}^{2+}$  and  $\text{K}^+$  were lost as solutes into the stream. Based on average streamwater chemistry and reactions (vi), and (vii), chlorite dissolution contributes 98% of the dissolved Mg; illite dissolution contributes 2% of dissolved Mg and almost 100% of dissolved K. Loss of Na and Ca also occurs as feldspar dissolution as shown in reaction (iv) above.

#### 4.6. Hillslope evolution along a planar transect

Soil development and the overall hillslope evolution are controlled by the soil production rate at the bedrock–soil interface ( $P$ ,  $\text{g m}^{-2} \text{y}^{-1}$ ), and the total denudation rate ( $D$ ,  $\text{g m}^{-2} \text{y}^{-1}$ ) (e.g., Fernandes and Dietrich, 1997; Anderson et al., 2002; Heimsath et al., 2005; Green et al., 2006; Yoo et al., 2007; Anderson et al., 2007). The denudation rate includes three components, the loss of mass as solutes, the loss of mass as fine particles throughout the soil profile, and the loss of bulk mineral particles due to erosion at the land surface. In the model we develop below, we define only two components, namely the “chemical” weathering rate  $W$  ( $\text{g m}^{-2} \text{y}^{-1}$ ) and physical erosion rate  $E$  (in  $\text{g m}^{-2} \text{y}^{-1}$ ). According to our definitions below, physical erosion removes weathered soil grains that have element ratios *identical* to bulk soil while “chemical” weathering as we define it

below removes some elements more rapidly than others. However, this latter transport includes both losses as solutes and fine particles.

To develop the model for the 2D transect, we make assumptions about erosion and soil production rates with respect to time. The margin of the last glacial advance lies approximately 60 km north of Shale Hills (Sevon and Braun, 1997). Periglacial features and deposits are observed in the SSHO and in central Pennsylvania (Ciolkosz et al., 1990; Gardner et al., 1991). The glacial advance boundary divides less well-developed soils to the north in Pennsylvania from thick, well-developed soils to the south (Ciolkosz et al., 1990). Periglacial activity has been hypothesized to be more effective in shaping the Appalachian landscape around the SSHO than temperate fluvial processes (Braun, 1989).

For example, studies in central Pennsylvania have shown that soils developed on slopes, especially south-facing slopes, have experienced downslope transport driven by intensive freezing and thawing (Carter and Ciolkosz, 1986). In some settings, unconsolidated fragments form a stratification of rhythmically layered deposits, interpreted as Grezes Litees (Clark and Ciolkosz, 1988). Grezes Litees on hillslope and riverine terraces have been identified to occur throughout Pennsylvania in the periglacial region (Clark and Ciolkosz, 1988), including the area occupied by the SSHO. However, such mixing and inverting of soils due to periglacial activity probably does not describe the ridgetop sites such as WRT or SPRT where little movement from upslope is likely. Furthermore, the chemistry-depth curves for the SPMS and SPVF sites (Fig. 5) document no evidence for mixing other than downslope creep. Thus, such a “mixed soils” scenario is not considered further here for the 1D or north-facing 2D transect.

Two other hypotheses are introduced here as end-member scenarios for geomorphological development of the north-facing planar transect at SSHO. In the “steady state” scenario, the hillslope, hypothesized to have been perturbed by the last glacial advance, has achieved a new steady state. With this hypothesis, the rate of bedrock to soil transformation equals the rate of chemical and physical erosion so that soils now maintain a time-independent thickness and chemistry (e.g., Roering et al., 2001). Under this scenario, the soil residence time at SSHO is estimated to  $\approx 20,000$  years by dividing the soil thickness at the ridge top (30 cm), by the denudation rate (15 m/Myrs from  $^{10}\text{Be}$  analysis). As expected, this residence time is much shorter than the time since deposition of the Rose Hill Formation (i.e., in the Silurian).

In the second “transient” scenario, soils may have been stripped or otherwise significantly perturbed during the most recent peri-glacial period, leaving behind exposed bedrock or very thin soils that began weathering 13,000 years ago in the warming climate. This scenario is consistent with the relatively high erosion rates of 150–300 m/Myrs that have been determined near the ancient ice margin in Pennsylvania: such a rate could have thinned soils significantly 13,000 years ago (Braun, 1989). In this scenario, the soils remain today in a transient condition and have not reached a new steady state thickness. As discussed below, we cannot

refute the transient hypothesis but we show that the system can be modeled as if it is in steady state without any significant contradictions.

We therefore first assume that soils are at steady state and test a mass-balance model for the three planar transect sites, following Yoo et al. (2007). In this treatment, the soil profile at the ridge top (SPRT site) is modeled as a 1D system, where water flows downward and soil material is lost both through chemical weathering and physical erosion. Input of sediment to the SPRT site is assumed negligible, given that the slope of the southern east-west ridgeline near SPRT is less than 5%. In contrast, at other locations along the planar transect (e.g., the middle slope SPMS site and valley floor SPVF site) water flowpaths are largely 2D, downward and along the slope. Although we cannot dismiss the possibility entirely, contributions from down-channel transport of sediments or solutes to the soils at SPVF are thought to be minimal given the relatively high position of this site. As shown below, no contradictions are encountered with this assumption.

Instead of using chemistry fitting-iteration methods used by previous researchers (Yoo et al. 2007), we assume that sediment transport occurs in steps between three boxes (e.g., SPRT → SPMS → SPVF; Fig. 1B). The sediment erosion and weathering rates are assumed to be the same within each box. Given that the distance between SPRT and SPVF is roughly 75 m, we thus set the length of each box to be 25 m (denoted as  $L$ ).

Biota can significantly take up nutrients such as K, thereby affecting their loss from a system as solutes (e.g., Taylor and Velbel 1991; Amundson et al., 2007). However, given the long time-scale (thousands of years) of soil formation at SSHO, we can assume that biota exists at steady state, i.e., uptake of nutrients into biota are balanced by outputs from biota as fresh litter. In the model, biota therefore do not represent net sources or sinks.

If the thickness of soils along the hillslope is at steady state, then the total denudation rate  $D$  equals the soil production rate  $P$  for the transect:

$$P = D = W + E \quad (4)$$

The average soil chemistry for each site (SPRT, SPMS, SPVF) was calculated by averaging the compositions for each sampled soil interval weighted by soil density and thickness ( $C_{j,SPRT}$ ,  $C_{j,SPMS}$ ,  $C_{j,SPVF}$ , as summarized in

Table 5A). At the ridge top, no sediment from above was assumed to be added to the soil, so mass balance equations can be written for immobile ( $i$ ) (5) and mobile elements ( $j$ ) (6):

$$P^{\text{SPRT}} C_{i,p} = E^{\text{SPRT}} C_{i,SPRT} \quad (5)$$

$$P^{\text{SPRT}} C_{j,p} = E^{\text{SPRT}} C_{j,SPRT} + W_j^{\text{SPRT}} \quad (6)$$

Rearranging Eqs. (4)–(6), the total chemical weathering rates,  $W$ , and weathering rates of each element,  $W_j$  (in  $\text{g m}^{-2} \text{y}^{-1}$ ), are calculated based on average soil chemistry at the ridge top:

$$W^{\text{SPRT}} = P^{\text{SPRT}} \left( 1 - \frac{C_{i,p}}{C_{i,SPRT}} \right) \quad (7)$$

$$\begin{aligned} W_j^{\text{SPRT}} &= P^{\text{SPRT}} \left( C_{j,p} - \frac{C_{i,p}}{C_{i,SPRT}} C_{j,SPRT} \right) \\ &= -P^{\text{SPRT}} C_{j,p} \tau_{j,SPRT} \end{aligned} \quad (8)$$

As seen from Eq. (9),  $W_j$  is a function of the depletion factor  $\tau_j$ . The sum of  $W_j$  for all elements equals  $W$  for each site. The fraction of chemical weathering relative to the total denudation flux is defined as the chemical depletion factor (CDF) (Riebe et al., 2003):

$$\text{CDF}^{\text{SPRT}} \equiv \frac{W^{\text{SPRT}}}{P^{\text{SPRT}}} = \frac{W^{\text{SPRT}}}{D^{\text{SPRT}}} = 1 - \frac{C_{i,p}}{C_{i,SPRT}} \quad (9)$$

The CDF can also be defined on an elemental basis, i.e.,  $\text{CDF}_j$  is the fraction of loss of element  $j$  due to chemical weathering to overall production rate of  $j$  and is related to  $\tau$  (Table 4):

$$\text{CDF}_j^{\text{SPRT}} = -\tau_{j,SPRT} \quad (10)$$

The physical erosion  $E^{\text{SPRT}}$  ( $\text{g m}^{-2} \text{y}^{-1}$ ) and sediment flux out of the ridge top site,  $Q^{\text{SPRT}}$  ( $\text{g m}^{-1} \text{y}^{-1}$ ), can be calculated as:

$$E^{\text{SPRT}} = P^{\text{SPRT}} \frac{C_{i,p}}{C_{i,SPRT}} \quad (11)$$

$$Q^{\text{SPRT}} = E^{\text{SPRT}} L \quad (12)$$

Here  $L$  is the length of the box, i.e., 25 m.

For the middle slope site, net physical erosion is defined as the gradient of the sediment flux:

Table 5A  
Averaged soil chemistry at each site along the hillslope.

	Ridge top SPRT	SPZR1	Middle slope SPMS	SPZR1	Valley floor SPVF
Al (%)	7.35	7.36	7.59	8.34	8.85
Ca (%)	0.12	0.02	0.09	0.01	0.12
Fe (%)	4.08	3.83	3.85	4.21	4.33
K (%)	2.19	2.01	2.34	2.69	2.92
Mg (%)	0.56	0.48	0.59	0.56	0.75
Na (%)	0.33	0.12	0.43	0.22	0.36
Si (%)	29.63	28.27	31.63	28.57	29.19
Zr (ppm)	263		296		238
Fe/Al (molar)	0.27		0.24		0.24
K/Al (molar)	0.21		0.21		0.23
Mg/Al (molar)	0.09		0.09		0.10
Si/Al (molar)	3.89		4.02		3.18

$$E^{\text{SPMS}} = (Q^{\text{SPMS}} - Q^{\text{SPRT}})/L \quad (13)$$

$$P^{\text{SPMS}} = E^{\text{SPMS}} + W^{\text{SPMS}} \quad (14)$$

This can be written for immobile (*i*) and mobile elements (*j*):

$$P^{\text{SPMS}} C_{i,p} = (Q^{\text{SPMS}} C_{i,\text{SPMS}} - Q^{\text{SPRT}} C_{i,\text{SPRT}})/L \quad (15)$$

$$P^{\text{SPMS}} C_{j,p} = (Q^{\text{SPMS}} C_{j,\text{SPMS}} - Q^{\text{SPRT}} C_{j,\text{SPRT}})/L + W_j^{\text{SPMS}} \quad (16)$$

By rearranging Eqs. (14)–(17), we derive:

$$W^{\text{SPMS}} = P^{\text{SPMS}} \left(1 - \frac{C_{i,p}}{C_{i,\text{SPMS}}}\right) + E^{\text{SPRT}} \left(1 - \frac{C_{i,\text{SPRT}}}{C_{i,\text{SPMS}}}\right) \quad (17)$$

$$E^{\text{SPMS}} = P^{\text{SPMS}} \frac{C_{i,p}}{C_{i,\text{SPMS}}} - E^{\text{SPRT}} \left(1 - \frac{C_{i,\text{SPRT}}}{C_{i,\text{SPMS}}}\right) \quad (18)$$

$$Q^{\text{SPMS}} = \left(P^{\text{SPMS}} \frac{C_{i,p}}{C_{i,\text{SPMS}}} + E^{\text{SPRT}} \frac{C_{i,\text{SPRT}}}{C_{i,\text{SPMS}}}\right) L \quad (19)$$

$$W_j^{\text{SPMS}} = P^{\text{SPMS}} C_{j,p} \left(1 - \frac{C_{j,\text{SPMS}} C_{i,p}}{C_{j,p} C_{i,\text{SPMS}}}\right) + E^{\text{SPRT}} C_{j,\text{SPRT}} \left(1 - \frac{C_{j,\text{SPMS}} C_{i,\text{SPRT}}}{C_{j,\text{SPRT}} C_{i,\text{SPMS}}}\right) \quad (20)$$

$$\text{CDF}^{\text{SPMS}} \equiv \frac{W^{\text{SPMS}}}{P^{\text{SPMS}}} = 1 - \frac{C_{i,p}}{C_{i,\text{SPMS}}} + \frac{E^{\text{SPRT}}}{P^{\text{SPMS}}} \left(1 - \frac{C_{i,\text{SPRT}}}{C_{i,\text{SPMS}}}\right) \quad (21)$$

The same equations can be written for the SPVF site, with sediment transport from the SPMS site defining input to the valley floor site. For both the SPMS and SPVF sites, we have assumed only downslope nonconvergent transport

of sediments and solutes along the hillslope. However, for the SPVF site we further assume no input of sediments or solutes except from the 2D transect (i.e., the site is high enough above the alluvial channel that no inputs were derived from the channel). In using this formulation of the model, the value of  $W_j$  is the net loss or gain of element *j* attributed to weathering processes from each site along the hillslope. The weathering flux,  $F_j$  ( $\text{g m}^{-1} \text{y}^{-1}$ ) out of each box can be calculated by integrating weathering rates calculated with Eq. (9) or Eq. (21) over distance:

$$F_j^{\text{SPRT}} = W_j^{\text{SPRT}} L \quad (22)$$

$$F_j^{\text{SPMS}} = W_j^{\text{SPMS}} L + F_j^{\text{SPRT}} \quad (23)$$

$$F_j^{\text{SPVF}} = W_j^{\text{SPVF}} L + F_j^{\text{SPMS}} \quad (24)$$

The denudation rate of 15 m/Myrs was measured at SSHO by meteoric  $^{10}\text{Be}$ . The soil production rate ( $P$ ) can be set equal to 15 m/Myrs for the whole transect assuming this is a steady-state system. Thus, with soil chemistry and soil production rate known for each site, erosion ( $E$ ), weathering rates (both  $W$  and  $W_j$ ), sediment fluxes ( $Q$ ) and weathering fluxes ( $F_j$ ) are calculated (Table 5B). Importantly, 30–50% (CDF) of the total elemental loss is due to chemical dissolution from the ridge top and the middle slope sites (Fig. 7A). Of this total major elemental loss at these two sites, Si and Al together account for almost 70% of chemical weathering loss, followed by Fe (13%), K (7%) and Mg oxides (3%).

In contrast to the soils at ridge and midslope, chemical processes led to both accumulation and outfluxes at the valley floor site, SPVF. The outfluxes of Al, K, Fe and Mg from the SPVF can be considered as the chemical contribution of the planar transect as a whole to the catchment:

Table 5B  
Mass-balance model results.

	$P = 15 \text{ m/Myrs}$			$P \text{ decays}^a$		
	Ridge top	Middle slope	Valley floor	Ridge top	Middle slope	Valley floor
$P$ ( $\text{g m}^{-2}\text{yr}^{-1}$ )	37.2	37.2	37.2	37.2	19.7	16.5
$W$ ( $\text{g m}^{-2}\text{yr}^{-1}$ )	12.0	17.7	−1.5	12.0	10.7	−4.2
$E$ ( $\text{g m}^{-2}\text{yr}^{-1}$ )	25.2	19.5	38.7	25.2	9.0	20.7
CDF <sup>b</sup>	0.3	0.5	0.0	0.3	0.5	−0.3
$F$ ( $\text{g m}^{-1}\text{yr}^{-1}$ )	300	742	704	300	567	463
$Q$ ( $\text{g m}^{-1}\text{yr}^{-1}$ )	630	1118	2086	630	854	1371
$F_{\text{Al}}^c$ ( $\text{g m}^{-1}\text{yr}^{-1}$ )	54	115	115	54	88	76
$F_{\text{Ca}}$ ( $\text{g m}^{-1}\text{yr}^{-1}$ )	0.4	1.2	0.8	0.4	0.9	0.5
$F_{\text{Fe}}$ ( $\text{g m}^{-1}\text{yr}^{-1}$ )	26	59	63	26	45	42
$F_{\text{K}}$ ( $\text{g m}^{-1}\text{yr}^{-1}$ )	21	44	44	21	33	29
$F_{\text{Mg}}$ ( $\text{g m}^{-1}\text{yr}^{-1}$ )	5	11	11	5	8	7
$F_{\text{Na}}$ ( $\text{g m}^{-1}\text{yr}^{-1}$ )	1.2	1.8	2.5	1.2	1.4	1.6
$F_{\text{Si}}$ ( $\text{g m}^{-1}\text{yr}^{-1}$ )	62	143	136	62	109	89
Fe/Al <sup>d</sup> (molar)	0.23	0.25	0.26	0.23	0.25	0.26
K/Al (molar)	0.27	0.26	0.26	0.27	0.26	0.26
Mg/Al (molar)	0.11	0.11	0.10	0.11	0.11	0.10
Si/Al (molar)	1.1	1.2	1.1	1.1	1.2	1.1

<sup>a</sup>  $P = 15 \text{ m/Myrs}$  at the ridge top, and decays exponentially with soil thickness along the transect.

<sup>b</sup> CDF (chemical depletion factor) =  $W/P$  (see text for details).

<sup>c</sup>  $F_j$  is the outflux of element *j*; thus,  $F_{j,\text{SPMS}} = F_{j,\text{SPRT}} + W_{\text{SPMS}} L$ ,  $F_{j,\text{SPVF}} = F_{j,\text{SPMS}} + W_{\text{SPVF}} L$ , and  $F_{\text{SPRT}} = W_{\text{SPRT}} L$ , where  $L$  is 25 m, the length of the box along the hillslope.

<sup>d</sup> Molar ratio of chemical weathering fluxes  $F_j$ , very similar to those in the soils except for Si.

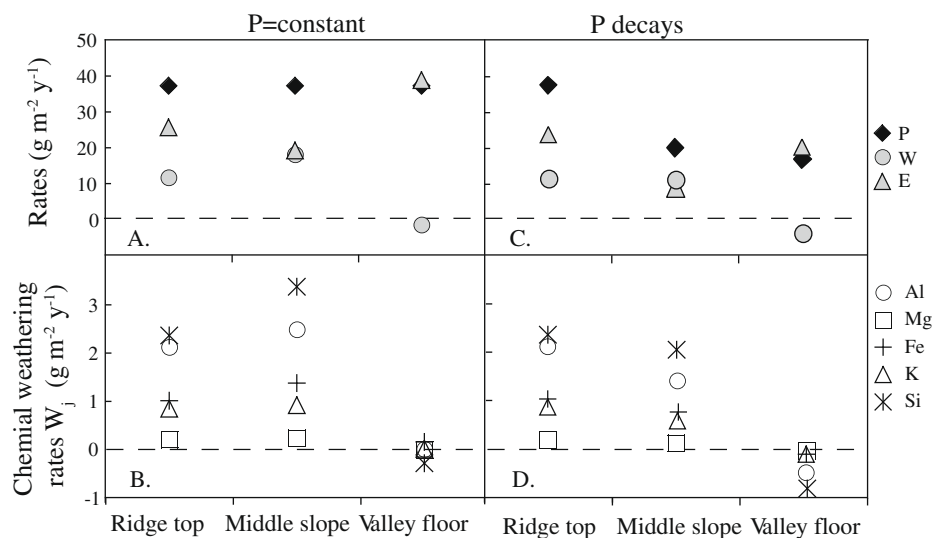


Fig. 7. Model results for relative contributions of net chemical weathering fluxes ( $W$ ) and net physical erosion fluxes ( $E$ ) to the overall soil production rate assuming the latter is constant (A;  $P = 15 \text{ m/Myrs} = 37.2 \text{ g m}^{-2} \text{ y}^{-1}$ ) or is variable (C;  $P = 37.2 \text{ g m}^{-2} \text{ y}^{-1}$  at ridge top but decreases exponentially with increasing soil thickness). Notice the negative chemical weathering rates, or accumulation instead of loss, in valley floor. Chemical weathering rates of individual elements ( $W_j$ ) as a function of topographic position are also plotted for the two modeling scenarios (B, D).

importantly, the chemical losses are proportional among these elements, with relative ratios similar to stoichiometry of average soil chemistry (Table 5B). In contrast, the ratio of  $F_{Si}$  to  $F_j$  for  $j = \text{K, Mg, Fe, Na}$  does not match the stoichiometric ratios in the shale, presumably because Si mainly occurs as the unreactive mineral quartz in the shale. As discussed previously, the molar ratios of the gradients in Al, K, Fe and Mg versus depth in the SPVF profile are equal to the ratios of those elements in illite and chlorite. These two lines of evidence are consistent with congruent dissolution of illite and chlorite according to reactions (vi) and (vii).

As formalized in the equations above, this mass balance calculation depends greatly on the accurate determination of Zr concentrations in the parent and weathered materials. Furthermore, erosion ( $E$ ) is considered to be loss of soil particles, i.e., particles that contain Zr, while chemical weathering ( $W$ ) is considered to be loss of mass that is chemically distinct from the average soil – this latter is either loss of solutes or loss of particles that do not contain Zr. In effect, we rely upon the observation from SEM analysis that Zr is present as zircons in the shale, and we assume that zircons with density of  $4.6 \text{ g/cm}^3$  are not lost as subsurface particle transport of kaolinite and Fe-oxyhydroxide particles throughout the profiles. These largely Zr-free particle fluxes are described by the  $W$  and  $W_j$  terms rather than by  $E$  in our model. For this reason,  $W$  is referred to as the nonstoichiometric or the “chemical” weathering term.

As mentioned previously, relatively high concentrations of K, Si and Mg are measured in stream water; thus, transport of these elements is attributed primarily to soluble loads. In contrast, stream water Al and Fe concentrations are so low that transport of these elements is attributed predominantly to particle loss. Loss of Si is from both soluble and particle loads. It is expected from soil chemistry at the

2D sites that both illite and chlorite dissolve congruently: therefore, during illite and chlorite dissolution, Mg, Si and K are released to solution while Al and Fe form secondary phases – kaolinite, Fe oxyhydroxides, Si–Al amorphous material, and Fe-coated primary materials – which are then lost as fine particles.

These “chemical” or “nonstoichiometric” weathering losses correlate to landscape position as indicated by the net elemental fluxes  $W_j$  illustrated in Fig. 7B. For example, the net fluxes of Mg,  $W_{Mg}$ , are  $0.2 \text{ g m}^{-2} \text{ y}^{-1}$  at the SPRT site,  $0.2 \text{ g m}^{-2} \text{ y}^{-1}$  at the SPMS site, and 0 at the SPVF site. A similar trend is observed for K at SPRT, SPMS, and SPVF:  $0.8 \text{ g m}^{-2} \text{ y}^{-1}$  to  $1.0 \text{ g m}^{-2} \text{ y}^{-1}$  to  $0 \text{ g m}^{-2} \text{ y}^{-1}$ , respectively. It has been suggested that geomorphic features (e.g., slope, soil thickness) can control chemical weathering reactions through availability of water (e.g., Lin et al., 2006; Burke et al., 2007). At the ridge top in SSSH, the chemical weathering is very intensive, presumably because a larger proportion of rainfall penetrates through the soil, moving downward to the bedrock instead of being lost through evapotranspiration (Graham et al., 1990). Furthermore, the soil waters in contact with minerals at the ridge top are expected to be dilute and far from chemical equilibrium. All these conditions favor faster reaction kinetics at the ridgetop. Consistent with these assumptions, the chemical weathering rates calculated at the middle slope site and ridge top are similar and higher than those calculated at the valley floor.

Consistent with these conclusions, the model yields negative chemical weathering rates for Si at the valley floor, indicating net accumulation instead of dissolution at that site for that element. As a secondary phase, kaolinite is observed at all three sites (Fig. 6D–F). We suggest that kaolinite particles are deposited or precipitated in the valley site. Net weathering losses of K and Mg are around zero at

the valley floor. Therefore, the solubilization of the primary minerals illite and chlorite is insignificant in the valley floor, as demonstrated by the similar CECs observed for SPVF soil and parent shale. In contrast, the CEC observed at the ridge top and middle slope sites are much lower, documenting loss of Mg during dissolution of chlorite and illite (SPRT and SPMS).

Overall dissolution of minerals near a ridge top and accumulation of major elements further along the flow path were also observed in a catena in New South Wales, Australia developed on granodiorite (Yoo et al., 2007). That transect, covered with soils whose average residence time was estimated as 1 ka, has a similar slope gradient but much higher CDF values ( $\sim 0.6$ ) compared to the transect here. As expected, granodiorite thus reacts faster than shale. Furthermore, in that system, subsurface translocation was not thought to be significant.

The model so far has been based upon the assumption of constant  $P$  with soil depth. In many cases,  $P$  has been inferred to vary with soil depth exponentially (e.g., Riebe et al., 2003; Heimsath et al., 2005). To investigate this possibility, we applied the same mass transport model as discussed above, but assumed that  $P$  decays as a function of soil thickness at different locations along the 2D transect:

$$p = p_0 e^{-\alpha h} \quad (25)$$

Here,  $\alpha$  is an empirical constant. We set this constant equal to  $0.022 \text{ cm}^{-1}$  following Heimsath et al. (2005), where  $h$  is soil thickness (cm).  $P_0$ , a reference soil production rate, is set equal to  $48 \text{ g m}^{-2} \text{ y}^{-1}$  by assuming  $P$  at the ridge top ( $h=30 \text{ cm}$ ) equals  $15 \text{ m/Myrs}$  ( $39 \text{ g m}^{-2} \text{ y}^{-1}$ ). For these assumptions, trends are observed to be similar to the previous depth-independent model (Table 5B and Fig. 7C, D), demonstrating that the major conclusions are consistent with either varying or non-varying  $P$ .

For both models, the net sediment fluxes ( $E$ ) decline from the ridge top to middle slope. Under the assumption of constant soil production rate,  $E$  values increase again at the valley floor site, becoming even higher at SPVF than at the ridge top. As seen in Fig. 1B, the transect is flat at the ridge and concave at the valley floor. The gentle slope at the valley floor should lead to lower net sediment flux, contradicting the model results. Therefore, the system is best described by the model where soil production rates vary with soil thickness: for that model,  $E$  at the valley floor is not as large as predicted for the other model.

#### 4.7. Mineral weathering rates

The calculated values of  $W_j$  for the SPRT site are essentially the extent of depletion of each element  $j$  divided by the residence time of the soil per unit geographical area. This rate can be converted to mineral surface-area based weathering rates ( $R$ , in mole mineral  $\text{m}^{-2} \text{ s}^{-1}$ ):

$$R = W_j / (M_j \rho S \beta h) \quad (26)$$

where  $M_j$  is atomic mass of element  $j$  ( $\text{g/mol}$ ),  $\rho$  is bulk density ( $\text{g/m}^3$ ),  $S$  is specific surface area of the reacting mineral ( $\text{m}^2/\text{g}$ ) and  $\beta$  is the stoichiometric factor describing the number of atoms of element  $j$  in the reacting mineral for-

mula. The specific surface area, measured on SSHO soil samples (BA1 core in Fig. 1A) by nitrogen adsorption and the Brunauer–Emmett–Teller (BET) isotherm (Gregg and Sing, 1967), equals  $22\text{--}30 \text{ m}^2/\text{g}$ . This BET surface area value for bulk soil ( $\sim 25 \text{ m}^2/\text{g}$ ) was partitioned into illite and chlorite according to the mass ratio of these minerals (5:1). It was assumed that quartz did not contribute significantly because of its relatively low BET surface area (e.g., Klute, 1986). The mineral weathering rates for illite and chlorite calculated from Eq. (26) were then estimated at the ridge top from K and Mg data respectively after correcting for the appropriate stoichiometric factor:  $9 \times 10^{-17}$  and  $5 \times 10^{-17} \text{ mol m}^{-2} \text{ s}^{-1}$ .

These weathering rates are based on a calculation that is roughly equivalent to previous calculations based on mass balance used at other sites (Murphy et al., 1998; White, 2002; Brantley and White, 2009). Of course, in those previous approaches, the estimate of  $R$  was based on the observation of a gradient in the soil elemental profile measured for a ridgetop site that was interpreted to be at steady state. To implement that method following White (2002), we fitted our data at SPRT to a straight line, and these linear gradients were then used to derive mineral weathering rates for illite ( $2 \times 10^{-17} \text{ mol m}^{-2} \text{ s}^{-1}$ ) and chlorite ( $1 \times 10^{-17} \text{ mol m}^{-2} \text{ s}^{-1}$ ). These rates, like those discussed in the previous paragraph based on calculated values of  $W$ , are much slower than those from the laboratory. Indeed, for illite at the same pH conditions ( $\sim 4.5$ ), dissolution rates measured in laboratory experiments are much higher, varying from  $10^{-13.5}$  to  $10^{-14.5} \text{ mol m}^{-2} \text{ s}^{-1}$  (e.g., Kohler et al., 2005; Lowson et al., 2005). Such discrepancies between field and laboratory dissolution rates are common (White, 2008).

Incomplete depletion (i.e.,  $\tau$  not equal to  $-1$ ) at the land surface is observed for major elements and for the major minerals illite and chlorite. Depending on the relative contributions to the overall denudation from “chemical” weathering ( $W$ ,  $\text{g m}^{-2} \text{ y}^{-1}$ ) and physical erosion ( $E$ ,  $\text{g m}^{-2} \text{ y}^{-1}$ ), weathering systems have been in the past considered to be limited either by kinetics or transport (Stallard, 1992; West et al., 2005; Brantley and White, 2009; Lebedeva et al., 2010). In a transport-limited system, soils are relatively thick, reactive minerals tend to be leached completely from shallow horizons ( $\tau$  equals  $-1$ ), and the rate of denudation is limited by the rate of sediment transport out of the system. In kinetically limited systems, soils remain relatively thin, reactive minerals are not as highly leached near the surface, and the rate of denudation is limited by the rate of mineral dissolution. Based on the elemental profiles, carbonate weathering at SSHO is inferred to be transport-limited. In contrast, clay mineral profiles are controlled by slow dissolution kinetics, operating as a weathering-limited system (Lebedeva et al., 2010).

## 5. CONCLUSIONS

We studied weathering processes of the Rose Hill Formation at the SSHO with 25-m drill core samples and soils in sites located at ridgetops (“1D” sites where fluid flow is predominantly downward and thus one-dimensional) and on planar hillslopes (“2D” sites where flow of fluid and

sediment is predominantly two-dimensional downslope). The first weathering front where ankerite is dissolved may be as deep as 22 m below ground surface at the northern ridgetop. Shallower in the bedrock at this ridgetop site (~6 m), feldspar dissolution starts, followed by clay dissolution which initiates within the soil itself. Clay transformations during chemical weathering follow a complex pattern wherein the parent minerals illite and chlorite weather to vermiculite, HIV, and to kaolinite. Accompanying these transformations of mineralogy, Mg and K are released to streams as soluble loads and Al and Fe are transported through the subsurface as fine particles, especially as secondary kaolinite and Fe-oxyhydroxide. Both chemical weathering reactions and particle transport contribute to mass loss from the soils, forming depletion profiles for all major elements (Mg, K, Al, Fe, and Si). The incomplete depletion profiles of major elements and clay minerals are consistent with weathering limitation of these reactions, i.e., loss of Mg and K is controlled by slow mineral dissolution kinetics of clays (Stallard, 1992; Lebedeva et al., 2010).

A mass transport model applied to this transect is consistent with the inference that at ridge top and middle slope, chemical weathering can explain only about half of the elemental loss from the soils: the rest is lost by fine sediment transport throughout the soil profiles. However, chemical precipitation and/or physical accumulation are important at the valley floor due to transport from upslope. These model results are based upon an assumption that soils are maintained at steady state thickness, with a decrease of soil production rates from ridge top to valley floor along the 2D transect. This steady state assumption leads to no significant contradictions despite the fact that peri-glacial conditions 15 ky ago presumably accelerated erosion fluxes for some transient period.

The relatively limited number of major minerals present in the parent shale allows important observations to be made about weathering and erosion of this lithology. By emphasizing an investigation of 1D, 2D, and 3D sites on this monolithologic catchment, it is possible to constrain rates of weathering and erosion: ongoing research efforts on shales in other climate regimes are using similar approaches to enable comparison across climate. Other efforts should be pursued similarly on other lithologies to make lithologic comparisons as well.

#### ACKNOWLEDGMENTS

We thank those who helped with fieldwork, especially Z. Ruge, J. Flemming and J. Williams for sampling soil cores. We thank L. Liermann, H. Gong, M. Jungers, L. Reusser, A. Matmon, and R. Finkel for assistance in the lab. This work benefitted greatly from discussions with A. Blum, J. Peters, F. Pazzaglia, D. Eberl and the SSHO team, especially H. Lin, K. Singha, E. Kirby and R. Slingerland. Financial support is provided by National Science Foundation under Grant No. CHE-0431328 for Center for Environmental Kinetics Analysis and under Grant No. EAR-0725019 to Chris Duffy (PSU) for the Susquehanna/Shale Hills Critical Zone Observatory. Logistical support and/or data were provided by the NSF-supported Shale Hills Susquehanna Critical Zone Observatory. We thank Art White, Kyungsoo Yoo, and an anonymous reviewer for

constructive comments and Associate Editor Jon Chorover for handling of the manuscript.

#### APPENDIX A. SUPPLEMENTARY DATA

Supplementary data associated with this article can be found, in the online version, at doi:10.1016/j.gca.2010.03.036.

#### REFERENCES

- Amacher M. C., Henderson R. E., Breithaupt M. D., Sele C. L. and LaBauve J. M. (1990) Unbuffered and buffered salt methods for exchangeable cations and effective cation-exchange capacity. *Soil Sci. Soc. Am. J.* **54**, 1036–1042.
- Amiotte-Suchet P., Probst J. L. and Ludwig W. (2003) Worldwide distribution of continental rock lithology: implications for the atmospheric/soil CO<sub>2</sub> uptake by continental weathering and alkalinity river transport to the oceans. *Global Biogeochem. Cycles* **17**, 1038. doi:10.1029/2002GB001891.
- Amundson, R. (2004) Soil formation. In *Treatise on Geochemistry* (eds. H. D. Holland and K.K. Turekian). Elsevier Press, Amsterdam, Chap. 5.01, pp. 1–35.
- Amundson R., Richter D. D., Humphreys G. S., Jobbage E. G. and Gaillardet J. (2007) Coupling between biota and earth materials in the Critical Zone. *Elements* **3**, 327–332.
- Anderson S. P., Dietrich W. E. and Brimhall G. H. (2002) Weathering profiles, mass-balance analysis, and rates of solute loss: linkage between weathering and erosion in a small, steep catchment. *Geol. Soc. Am. Bull.* **114**, 1143–1158.
- Anderson S. P., von Blanckenburg F. and White A. F. (2007) Physical and chemical controls on the Critical Zone. *Elements* **3**, 315–319.
- Bain D. C., Mellor A., Robertson-Rintoul M. S. E. and Buckland S. T. (1993) Variations in weathering processes and rates with time in a chronosequence of soils from Glen Feshie, Scotland. *Geoderma* **57**, 275–293.
- Berner E. K. and Berner R. A. (1996) *Global Environment: Water, Air and Geochemical Cycles*. Prentice-Hall, Inc., Upper Saddle River, New Jersey, 07458.
- Bierman, P. R., Reusser, L. and Pavich, M. (2009) New ways of using an old isotopic system – meteoric 10-Be is back and ready to do geomorphology. *Geophys. Res. Abstracts*, **11**, EGU2009-0.
- Bierman, P. R., Jungers, M., Reusser, L. and Pavich, M. (2008) Look again: meteoric 10-Be is a useful tracer of hillslope and basin-scale process. *Geol. Soc. Am. Abstracts Program*. pp. 165–166.
- Bierman, P., Reusser, L., Sullivan, C., Duxbury, J., Jungers, M., Reuter, J., Larsen, J., Pavich, M. and Finkel, R. (2007) A geochronologic glimpse into how ancient mountain ranges erode. *Geol. Soc. Am. Abstracts Program*.
- Blackmer G. C., Omar G. I. and Gold D. P. (1994) Post-Alleghanian unroofing history of the Appalachian Basin, Pennsylvania, from apatite fission trace analysis and thermal models. *Tectonics* **13**, 1259–1276.
- Blake, G. R. and Hartge, K. H. (1986) Bulk density. *Methods of Soil Analysis, Part 1-I, Physical and Mineralogical Methods*, Ch. 13, second ed. (ed. Arnold Klute). pp. 363–375.
- Brantley S. B. and White A. F. (2009) Approaches to modeling weathered regolith. *Rev. Mineral. Geochem.* **70**, 435–484.
- Brantley, S. B., White, T. S., White, A. F., Sparks, D., Richter, D., Prigitz, K., Derry, L., Chorover, J., Chadwick, O., April, R., Anderson, S. and Amundson, R. (2006) Frontiers in explora-

- tion of the Critical Zone: Report of a workshop sponsored by the National Science Foundation (NSF), October 24–26, 2005, Newark, DE, p. 30.
- Brantley S. B., Godhaber M. B. and Ragnarsdottir K. V. (2007) Crossing disciplines and scales to understand the Critical Zone. *Elements* **3**, 307–314.
- Brantley S. B., Banstra J., Moore J. and White A. F. (2008) Modelling chemical depletion profiles in regolith. *Geoderma* **145**, 494–504.
- Braun D. D. (1989) Glacial and periglacial erosion of the Appalachians. *Geomorphology* **2**, 233–256.
- Brimhall G. H. and Dietrich W. E. (1987) Constitutive mass balance relations between chemical composition, volume, density, porosity, and strain in metasomatic hydrochemical systems: results on weathering and pedogenesis. *Geochim. Cosmochim. Acta* **51**, 567–587.
- Burke B. C., Heimsath A. M. and White A. F. (2007) Coupling chemical weathering with soil production across soil-mantled landscapes. *Earth Surf. Proc. Land.* **32**, 853–873.
- Carter B. J. and Ciolkosz E. J. (1986) Sorting and thickness of waste mantle material on a sandstone spur in central Pennsylvania. *Catena* **13**, 241–256.
- Chadwick O. A., Brimhall G. H. and Hendricks D. M. (1990) From a black to a grey box – a mass balance interpretation of pedogenesis. *Geomorphology* **3**, 369–390.
- Chadwick O. A. and Chorover J. (2001) The chemistry of pedogenic thresholds. *Geoderma* **100**, 321–353.
- Chadwick O. A., Derry L. A., Vitousek P. M., Huebert B. M. and Hedin L. O. (1999) Changing sources of nutrients during four million years of ecosystem development. *Nature* **397**, 491–497.
- Ciolkosz E. J., Carter B. J., Hoover M. T., Cronce R. C., Waltman W. J. and Dobos R. R. (1990) Genesis of soils and landscapes in the Ridge and Valley province of central Pennsylvania. *Geomorphology* **3**, 245–261.
- Clark G. M. and Ciolkosz E. J. (1988) Periglacial geomorphology of the Appalachian highlands and interior highlands south of the glacial border—a review. *Geomorphology* **1**, 191–220.
- Copard Y., Amiotte-Suchet P. and Di-Giovanni C. (2007) Storage and release of fossil organic carbon related to weathering of sedimentary rocks. *Earth Planet. Sci. Lett.* **258**, 345–357.
- Duffy C. J. and Cusumano J. M. (1998) A low-dimensional model for concentration-discharge in groundwater-stream systems. *Water Resour. Res.* **34**, 2235–2247.
- Eberl, D. D. (2003) User's guide to RockJock – a program for determining quantitative mineralogy from powder X-ray diffraction data. U.S. Geological Survey, Open-file Report 03-78.
- El-Farhan Y. H., DeNovio N. M., Herman J. S. and Hornberger G. M. (2000) Mobilization and transport of soil particles during infiltration experiments in an agricultural field, Shenandoah Valley, Virginia. *Environmental Science & Technology* **34**, 3555–3559.
- Fernandes N. F. and Dietrich W. E. (1997) Hillslope evolution by diffusive processes: the timescale for equilibrium adjustments. *Water Resour. Res.* **33**, 1307–1318.
- Folk R. L. (1960) Petrography and origin of the Tuscarora, Rose Hill, and Keefer formations, Lower and Middle Silurian of eastern west Virginia. *J. Sed. Petrol.* **30**, 1–58.
- Gaillardet J., Dupré B., Louvat P. and Allègre C. J. (1999) Global silicate weathering and CO<sub>2</sub> consumption rates deduced from the chemistry of large rivers. *Chem. Geol.* **159**, 3–30.
- Gardner T. W., Ritter J. B., Shuman C. A., Bell J. C., Sasowsky K. C. and Pinter N. (1991) A periglacial stratified slope deposit in the valley and ridge province of central Pennsylvania, USA: sedimentology, stratigraphy, and geomorphic evolution. *Permafrost Periglac. Process.* **2**, 141–162.
- Graham R. C., Weed S. B., Bowen L. H., Amarasiriwardena D. D. and Buol S. W. (1989) Weathering of iron-bearing minerals in soils and saprolite on the North Carolina Blue Ridge front: II. Clay mineralogy. *Clay Clay Mineral.* **37**, 29–40.
- Graham R. C., Daniels R. B. and Buol S. W. (1990) Soil-geomorphic relations on the Blue Ridge front: I. Regolith types and slope processes. *Soil Sci. Soc. Am. J.* **54**, 1362–1367.
- Green E. G., Dietrich W. E. and Banfield J. F. (2006) Quantification of chemical weathering rates across an actively eroding hillslope. *Earth Planet. Sci. Lett.* **242**, 155–169.
- Gregg S. J. and Sing K. S. W. (1967) *Adsorption, Surface Area and Porosity*. Academic Press, London, p. 370.
- Heimsath A. M., Furbish D. J. and Dietrich W. E. (2005) The illusion of diffusion: field evidence for depth dependent sediment transport. *Geology* **33**, 949–952.
- Helgeson H. C., Garrels R. M. and Mackenzie F. T. (1969) Evaluation of irreversible reaction in geochemical processes involving minerals and aqueous solutions II: applications. *Geochim. Cosmochim. Acta* **33**, 455–482.
- Hoskins, D. M. (1976) Pine Grove Mills Quadrangle Pennsylvania (7.5 min series, topographic). This map is from Map 61 – Atlas of Preliminary Geologic Quadrangle maps of Pennsylvania 1981, PA Geological Survey.
- Hseu Z. Y., Tsai H., Hsi H. C. and Chen Y. C. (2007) Weathering sequences of clay minerals in soils along a serpentinitic topequence. *Clay Clay Miner.* **55**, 389–401.
- Jacobson A. D., Blum J. D., Chamberlain C. P., Craw D. and Koons P. O. (2003) Climatic and tectonic controls on chemical weathering in the New Zealand Southern Alps. *Geochim. Cosmochim. Acta* **67**, 29–46.
- Jin L., Hamilton S. K. and Walter L. M. (2008) Mineral weathering rates in glacial drift soils (SW Michigan, USA): new constraints from seasonal sampling of waters and gases at soil monoliths. *Chem. Geol.* **249**, 129–154.
- Kaplan I., Bertsch P. M. and Adriano D. C. (1997) Mineralogical and physicochemical differences between mobile and nonmobile colloidal phase in reconstructed pedons. *Soil Sci. Soc. Am. J.* **61**, 641–649.
- Kaste J. M., Heimsath A. M. and Bostick B. C. (2007) Short-term mixing quantified with fallout radionuclides. *Geology* **35**(3), 234–246.
- Klute, A. (1986) *Methods of Soil Analysis. Part I: Physical and Mineralogical Methods*, second ed. SSSA Book Series 9 (Part 1). Soil Science Society of America, Madison, Wisconsin.
- Kohler S. J., Bosbach D. and Oelkers E. H. (2005) Do clay mineral dissolution rates reach steady state? *Geochim. Cosmochim. Acta* **69**, 1997–2006.
- Kolowith L. C. and Berner R. A. (2002) Weathering of phosphorus in black shales. *Global Biogeochem. Cycles* **16**, 1140. doi:10.1029/2001GB001887.
- Kudrat M., Varadachari C. and Ghosh K. (2000) Application of the improved regression method to derive  $\Delta G$  of non-stoichiometric clay minerals and their correlations with compositional parameters. *Chem. Geol.* **168**, 225–238.
- Kurtz A. C., Derry L. A., Chadwick O. A. and Alfano M. J. (2000) Reflectory element mobility in volcanic soils. *Geology* **28**, 683–686.
- Laegdsmand M., Villholth K. G., Ullum M. and Jensen K. H. (1999) Processes of colloid mobilization and transport in macroporous soil monoliths. *Geoderma* **93**, 33–59.
- Lebedeva M. I., Fletcher R. C. and Brantley S. L. (2010) A mathematical model for steady-state regolith production at constant erosion rate. *Earth Surf. Proc. Land.* **35**, 508–524.
- Lee B. D., Sears S. K., Graham R. C., Amrhein C. and Vali H. (2003) Secondary mineral genesis from chlorite and serpentine

- in an ultramafic soil toposequence. *Soil Sci. Soc. Am. J.* **67**, 1309–1317.
- Lin H. S. (2006) Temporal stability of soil moisture spatial pattern and subsurface preferential flow pathways in the Shale Hills Catchment. *Vadose Zone J.* **5**, 317–340.
- Lin H., Kogelmann W., Walker C. and Bruns M. A. (2006) Soil moisture patterns in a forested catchment: a hydrogeological perspective. *Geoderma* **131**, 345–368.
- Lin H. and Zhou X. (2008) Evidence of subsurface preferential flow using soil hydrologic monitoring in the Shale Hills catchment. *Eur. J. Soil Sci.* **59**, 34–49.
- Littke R., Klussmann U., Krooss B. and Leythaeuser D. (1991) Quantification of loss of calcite, pyrite, and organic matter due to weathering of Toarcian black shales and effects on kerogen and bitumen characteristics. *Geochim. Cosmochim. Acta* **55**, 3369–3378.
- Lowson R. T., Comarmond M.-C. J., Rajaratnam G. and Brown P. L. (2005) The kinetics of dissolution of chlorite as a function of pH and at 25 °C. *Geochim. Cosmochim. Acta* **69**, 1687–1699.
- Lynch J. A. and Corbett E. S. (1985) Source-area variability during peak flow. In *Drain. Div. Am. Soc. Civ. Eng.* (eds. E. B. Jones, T. J. Ward and J. Irrig) (eds. E. Jones and T. Ward). ASCE, Reston, VA, pp. 300–307.
- Lynch, J. A. (1976) Effects of antecedent soil moisture on storm hydrographs. PhD Dissertation. Pennsylvania State University, University Park, PA.
- Moore, M. D. and Reynolds, Jr., C. R. (1997) *X-Ray Diffraction and the Identification and Analysis of Clay Minerals*, second ed. Oxford University Press, Oxford, New York.
- Murphy S. F., Brantley S. L., Blum A. E., White A. F. and Dong H. (1998) Chemical weathering in a tropical watershed, Luquillo Mountains, Puerto Rico: II. Rate and mechanism of biotite weathering. *Geochim. Cosmochim. Acta* **62**, 227–244.
- National Oceanographic and Atmospheric Administration (NOAA) (2007) U.S. divisional and station climatic data and normals: Asheville, North Carolina, U.S. Department of Commerce, National Oceanic and Atmospheric Administration, National Environmental Satellite Data and Information Service, National Climatic Data Center. <http://cdo.ncdc.noaa.gov/CDO/cdo>.
- Neaman A., Chorover J. and Brantley S. L. (2006) Effects of organic ligands on granite dissolution in batch experiments at pH 6. *Am. J. Sci.* **306**, 451–473.
- Petsch S. T., Eglinton T. I. and Edwards K. J. (2001) 14C-dead living biomass: evidence for microbial assimilation of ancient organic carbon during shale weathering. *Science* **292**, 1127–1131.
- Pieresson-Wickmann A., Reisberg L. and France-Lanord C. (2002) Behavior of Re and Os during low-temperature alteration: results from Himalayan soils and altered black shales. *Geochim. Cosmochim. Acta* **66**, 1539–1548.
- Poppe, L. J., Paskevich, V. F., Hathaway, J. C. and Blackwood, D. S. (2002) A laboratory manual for X-ray powder diffraction. U.S. Geological Survey Open File Report 01–041. U.S. Geological Survey, MA.
- Price J. R., Velbel M. A. and Patino L. C. (2005) Rates and time scales of clay–mineral formation by weathering in saprolitic regoliths of the southern Appalachians from geochemical mass balance. *Geol. Soc. Am. Bull.* **117**, 783–794.
- Qu Y. and Duffy C. J. (2007) A semidiscrete finite volume formation for multiprocess watershed simulation. *Water Resour. Res.* **43**. doi:10.1029/2006WR005753.
- Reuter, J., Bierman, P., Pavich, M., Gellis, A., Larsen, J. and Finkel, R. (2004) Erosion of the Susquehanna River Basin: assessing relations between <sup>10</sup>Be-derived erosion rates and basin characteristics. *Geol. Soc. Am. Program. Abstracts*.
- Riebe C. S., Kirchner J. W. and Finkel R. C. (2003) Long-term rates of chemical weathering and physical erosion from cosmogenic nuclides and geochemical mass balance. *Geochim. Cosmochim. Acta* **67**, 4411–4427.
- Roering J. J., Kirchner J. W. and Dietrich W. E. (2001) Hillslope evolution by nonlinear, slope-dependent transport: steady-state morphology and equilibrium adjustment timescales. *J. Geophys. Res.* **106**, 16499–16514.
- Roden M. K. and Miller D. S. (1989) Apatite fission-track thermochronology of the Pennsylvania Appalachian Basin. *Geomorphology* **2**, 39–51.
- Rose, A.W. (1973) Structure and Silurian and Devonian stratigraphy of the Valley and Ridge Province in Central Pennsylvania. In *The 38th Annual Field Conference of Pennsylvania Geologists*.
- Rousseau M., Di Pietro L., Angulo-Jaramillo R., Tessier D. and Cabibel B. (2004) Preferential transport of soil colloidal particles: physicochemical effects on particle mobilization. *Vadose Zone J.* **3**, 247–261.
- Sevon, W. D. and Braun, D. D. (1997) Glacial deposits of Pennsylvania map. Bureau of Topographic and Geological Survey, Department of Conservation and Natural Resources, Map 59, second ed.
- Stallard, R.F. (1992) Tectonic processes, continental freeboard, and the rate-controlling step for continental denudation. In *Global Biogeochemical Cycles* (eds. S. S. Butcher, R. J. Charlson, G. H. Orians, G. V. Wolfe). Academic Press, London, pp. 93–121.
- Stone, J. (1998) A rapid fusion method for separation of beryllium-10 from soils and silicates. *Geochim. Cosmochim. Acta* **62**, 555–561.
- Taylor A. and Blum J. D. (1995) Relation between soil age and silicate weathering rates determined from the chemical evolution of a glacial chronosequence. *Geology* **23**, 979–982.
- Taylor A. and Velbel M. A. (1991) Geochemical mass balances and weathering rates in forested watersheds of the southern Blue Ridge II. Effects of botanical uptake terms. *Geoderma* **51**, 29–50.
- United States Department of Agriculture, Natural Resources Conservation Service (2004). Soil survey laboratory methods manual. Version No. 4.0. Soil Survey Investigations Report No. 42.
- West A. J., Galy A. and Bickle M. (2005) Tectonic and climatic controls on silicate weathering. *Earth Planet. Sci. Lett.* **235**, 211–228.
- White A. F. (2002) Determining mineral weathering rates based on solid and solute weathering gradients: application to biotite weathering in saprolites. *Chem. Geol.* **190**, 69–89.
- White A. F. (2008) Quantitative approaches to characterizing natural chemical weathering rates. In *Kinetics of Water-Rock Interaction* (eds. S. L. Brantley, J. D. Kubicki and A. F. White). Springer, New York, pp. 469–544.
- White A. F. and Blum A. E. (1995) Effects of climate on chemical weathering in watersheds. *Geochim. Cosmochim. Acta* **59**, 1729–1747.
- White A. F., Blum A. E., Marjorie S., Schulz M. S., Bullen T. D., Harden J. W. and Peterson M. L. (1996) Chemical weathering rates of a soil chronosequence on granitic alluvium: I. Quantification of mineralogical and surface area changes and calculation of primary silicate reaction rates. *Geochim. Cosmochim. Acta* **60**, 2533–2550.
- White A. F., Bullen T. D., Vivit D. V., Schulz M. S. and Clow D. W. (1999) The role of disseminated calcite in the chemical weathering of granitoid rocks. *Geochim. Cosmochim. Acta* **63**, 1939–1953.

- White A. F., Bullen T. D., Schulz M. S., Blum A. E., Huntington T. G. and Peters N. E. (2001) Differential rates of feldspar weathering in granitic regoliths. *Geochim. Cosmochim. Acta* **65**, 847–869.
- White A. F., Schulz M. S., Vivit D. V., Blum A. E., Stonestrom D. A. and Harden J. W. (2005) Chemical weathering rates of a soil chrono-sequence on granitic alluvium: III. Hydrochemical evolution and contemporary solute fluxes and rates. *Geochim. Cosmochim. Acta* **69**, 1975–1996.
- White A. F., Schulz M. S., Vivit D. V., Blum A. E., Stonestrom D. A. and Anderson S. P. (2008) Chemical weathering of a marine terrace chronosequence, Santa Cruz, California I: interpreting rates and controls on soil concentration-depth profiles. *Geochim. Cosmochim. Acta* **72**, 36–68.
- White, G. N. and Dixon, J. B. (2003) *Soil Mineralogy Laboratory Manual, ninth ed. Department of Soil and Crop Sciences*. Texas A&M University, College Station, TX77843.
- Williams E. L., Szramek K. J., Jin L., Ku T. C. W. and Walter L. M. (2007) The carbonate system geochemistry of shallow ground water–surface water systems in temperate glaciated watersheds (Michigan, USA): significance of open-system dolomite weathering. *Geol. Soc. Am. Bull.* **119**, 515–528.
- Wilson M. J. (2004) Weathering of primary rock forming minerals: processes, products, and rates. *Clay Mineral.* **39**, 233–266.
- Yoo K., Amundson R., Heimsath A. M., Dietrich W. E. and Brimhall G. H. (2007) Integration of geochemical mass balance with sediment transport to calculate rates of soil chemical weathering and transport on hillslopes. *J. Geophys. Res.* **112**, F02013. doi:10.1029/2005JF000402.

Associate editor: Jon Chorover

Appendix 1: Interlaboratory comparison in soil chemistry measurements of two certified soil reference materials (unit: wt.%).

	Al <sub>2</sub> O <sub>3</sub>	CaO	Fe <sub>2</sub> O <sub>3</sub>	K <sub>2</sub> O	MgO	MnO	Na <sub>2</sub> O	SiO <sub>2</sub>	TiO <sub>2</sub>
MCL <sup>a</sup>	14.57	2.82	5.36	2.49	2.62	0.08	1.56	65.54	0.58
SGS <sup>b</sup>	13.60	2.52	4.61	2.32	2.33	0.06	1.45	59.10	0.52
2709 <sup>c</sup>	14.17	2.65	5.00	2.45	2.50		1.56	63.45	0.57
MCL <sup>a</sup>	12.34	4.04	4.13	2.95	1.74	0.07	1.54	64.26	0.51
SGS <sup>b</sup>	12.30	3.88	3.93	2.93	1.68	0.07	1.54	63.20	0.49
2711 <sup>c</sup>	12.28	3.98	4.25	2.97	1.73	0.08	1.51	65.28	0.51

<sup>a</sup> Data from Material Characterization Laboratory at Penn State University.

<sup>b</sup> Data from Minerals Service Lab at SGS Canada Inc.

<sup>c</sup> Certified values of the two soil reference materials.

Appendix 2: Parent composition calculated from Shale Hills unweathered soils <sup>a</sup>.

Sample name	Depth (cm)	Al (%)	Ca (%)	Fe (%)	K (%)	Mg (%)	Mn (%)	Na (%)	P (%)	Si (%)	Ti (%)	Zr (%)
BA1	290-300	10.69	0.11	5.65	3.61	0.92	0.09	0.31	0.04	27.11	0.63	202
CJ1	40-50	11.27	0.02	5.67	3.54	0.62	0.05	0.41	0.06	26.55	0.58	148
ML1	28	10.21		5.41	3.60	0.65	0.09	0.25		26.18		
JB1	30-40	10.58	0.04	5.70	3.40	0.71	0.03	0.33	0.06	25.85	0.60	180
JT1	61-66	10.37	0.11	5.10	3.85	0.81	0.06	0.27	0.04	26.37	0.58	178
Average		10.63	0.07	5.51	3.60	0.74	0.07	0.31	0.05	26.41	0.59	177
Stdev		0.41	0.05	0.26	0.16	0.12	0.02	0.06	0.01	0.47	0.03	22
<b>DC1<sup>b</sup></b>												
average		10.75	0.12	5.50	3.76	0.95	0.08	0.36	0.06	26.70	0.64	178
Stdev		0.38	0.02	0.19	0.16	0.09	0.04	0.07	0.01	0.38	0.03	14

<sup>a</sup> The chemical composition of the deepest sample from each core was averaged. As these samples experience very little to no weathering, they represent parent composition.

<sup>b</sup> Parent composition from DC1 core is similar to that calculated from unweathered soils.

Appendix 3: Bulk and grain density of Shale Hills bedrock and soils.

Sample Number	Depth <sup>a</sup> (m or cm)	Bulk Density (g/cm <sup>3</sup> )	Grain Density (g/cm <sup>3</sup> )
DC1-3	0.40	2.16	
DC1-4	0.55	2.04	
DC1-5	0.70	1.75	
DC1-6	0.85	2.03	
DC1-7	1.01	1.93	
DC1-8	1.16	2.93	
DC1-9	1.31	2.77	
DC1-10	1.46	2.22	2.65
DC1-11	1.62	2.14	
DC1-12	1.92	2.41	
DC1-13	2.23	2.38	
DC1-14	2.53	1.94	
DC1-15	2.83	2.09	
DC1-16	3.14	3.25	
DC1-17	3.44	2.03	
DC1-18	3.75	2.50	
DC1-19	4.05	2.08	
DC1-20	4.36	2.86	
DC1-21	4.66	1.93	
DC1-22	4.97	2.47	
DC1-23	5.27	2.90	
DC1-24	5.58	2.61	
DC1-25	5.88	2.38	2.47
DC1-26	6.19	2.28	
DC1-27	7.71	2.48	2.57
DC1-28	9.24	2.35	
DC1-29	10.76	2.73	
DC1-30	12.28	2.16	
DC1-31	13.81	2.09	2.69
DC1-32	15.33	2.74	
DC1-33	16.86	2.27	2.60
DC1-34	18.38	2.89	2.65
DC1-35	19.90	2.85	
DC1-36	21.43	2.85	
DC1-37	22.95	2.91	
DC1-38	24.48	2.81	
SPZR1	-3 - 0	0.13	
SPZR1	17-20	1.83	
SPZR2	0-3	0.69	
SPZR2	23-26	1.59	
SPZR2	41-44	1.73	
SPZR2	51-54	1.76	
SPRT	0-10		2.19
SPRT	10-20		2.66
SPRT	20-30		2.66
SPVF	20-30		2.64
SPVF	40-50		2.53
SPVF	60-67		2.66

<sup>a</sup> Depth m is for DC1 samples and depth cm is for soil samples

Appendix 4: Shifts of clay mineral peaks in XRD at different conditions (Å).

	Kaolinite <sup>b</sup>	Mica/illite <sup>c</sup>	HIV <sup>d</sup>	Vermiculite <sup>e</sup>	Smectite <sup>f</sup>	Chlorite <sup>g</sup>
Mg 25°C	7	10	14	14	14	14
Mg EG <sup>a</sup>	7	10	14	14	18	14
K 25°C	7	10	14	10-12	10-14	14
K 400°C	7	10	10-14	10	10	14
K 550°C	-	10	10-14	10	10	14

<sup>a</sup> Mg saturated then dried in ethylene glycol;

<sup>b</sup> Kaolinite is confirmed by peak at 7 Å at all treatment except for K saturation and 550 °C heating;

<sup>c</sup> Presence of mica/illite is confirmed by a peak at 10 Å at all treatments;

<sup>d</sup> Hydroxy interlayered vermiculite is confirmed by a peak shift from 14 Å to 10-14 Å at K saturation;

<sup>e</sup> Vermiculite is confirmed by a peak at 14 Å at Mg saturation but at 10 Å at K saturation;

<sup>f</sup> Smectite peak will shift from 14 Å when dried in air to 18 Å when dried in EG, after Mg saturation;

<sup>g</sup> Chlorite has a peak at 14 Å at all treatments.

Appendix 5: Peaks observed after different treatments between 4 and 20 Å and minerals identified at Shale Hills soils.

				Kaolinite	Illite	HIV	Vermiculite	smectite	Chlorite
<b>SPRT (0-10cm)</b>									
Mg 25°C	6.99	9.78	13.68						
Mg EG	6.95	9.82	13.56						
K 25°C	7.03	10.00	13.73						
K 400°C	7.12	9.94	12.28						
K 550°C	10.05	11.70		Y	Y	Y	Y	N	N
<b>SPRT (20-30cm)</b>									
Mg 25°C	7.02	9.78	13.60						
Mg EG	7.00	9.76	13.64						
K 25°C	7.12	10.00	13.90						
K 400°C	7.12	9.94	12.28						
K 550°C	10.00	11.60	13.98	Y	Y	Y	Y	N	Y
<b>SPMS (0-10cm)</b>									
Mg 25°C	7.09	10.05	14.12						
Mg EG	7.03	9.94	13.99						
K 25°C	7.11	9.96	13.73						
K 400°C	7.11	9.94	12.02						
K 550°C	10.21	11.45		Y	Y	Y	Y	N	N
<b>SPMS (20-30cm)</b>									
Mg 25°C	7.12	9.98	14.17						
Mg EG	7.11	9.93	14.08						
K 25°C	7.12	9.96	13.90						
K 400°C	7.11	9.96	12.12						
K 550°C	10.00	11.37	13.95	Y	Y	Y	Y	N	Y
<b>SPMS (50-59cm)</b>									
Mg 25°C	7.12	9.98	14.17						
Mg EG	7.11	9.93	14.03						
K 25°C	7.12	10.00	13.69						
K 400°C	7.13	9.96	10.89	11.69					
K 550°C	10.00	13.74		Y	Y	Y	Y	N	Y
<b>SPVF (0-10cm)</b>									
Mg 25°C	7.10	9.93	13.99						
Mg EG	7.09	9.89	13.95						
K 25°C	7.13	10.00	13.56						
K 400°C	7.14	10.00							
K 550°C	10.04	14.04		Y	Y	Y	Y	N	Y
<b>SPVF (30-40cm)</b>									
Mg 25°C	7.10	9.91	13.99						
Mg EG	7.04	9.85	13.78						
K 25°C	7.12	10.00	13.65						
K 400°C	7.11	9.93							
K 550°C	10.00			Y	Y	Y	Y	N	N
<b>SPVF (60-67cm)</b>									
Mg 25°C	7.02	9.91	13.86						
Mg EG	7.10	9.89	13.94						
K 25°C	7.12	9.96	13.90						
K 400°C	7.12	9.93							
K 550°C	9.93	13.76		Y	Y	Y	Y	N	Y

Appendix 6: Elemental concentrations of Shale Hills soils, with corresponding Tau values, using Ti as an immobile element ( $\tau_{Ti,j}$ )

Depth (cm)	Elemental Concentrations													$\tau_{Ti,j}$ values												
	Al (%)	Ca (%)	Fe (%)	K (%)	Mg (%)	Mn (%)	Na (%)	P (%)	Si (%)	Ti (%)	Al (%)	Ca (%)	Fe (%)	K (%)	Mg (%)	Mn (%)	Na (%)	P (%)	Si (%)							
<b>SPRT2</b>																										
0-11	8.84	0.10	4.41	2.38	0.63	0.33	0.26	0.07	33.33	0.73	-0.28	-0.27	-0.29	-0.44	-0.41	2.67	-0.36	0.18	0.10							
11-16	9.26	0.06	4.97	2.64	0.66	0.26	0.20	0.07	32.76	0.70	-0.21	-0.57	-0.18	-0.36	-0.37	1.98	-0.49	0.15	0.12							
16-22	9.32	0.04	4.50	2.74	0.63	0.12	0.24	0.06	33.56	0.71	-0.22	-0.68	-0.27	-0.35	-0.40	0.33	-0.39	-0.08	0.13							
<b>SPMS2</b>																										
0-13	8.36	0.17	3.83	2.17	0.56	0.78	0.26	0.10	34.12	0.76	-0.35	0.20	-0.42	-0.52	-0.50	7.41	-0.39	0.52	0.07							
13-21	7.67	0.16	4.02	2.28	0.59	0.17	0.30	0.04	34.49	0.70	-0.34	0.26	-0.33	-0.44	-0.43	1.01	-0.22	-0.35	0.19							
21-27	8.73	0.14	4.66	2.83	0.72	0.09	0.29	0.03	32.44	0.64	-0.18	0.20	-0.15	-0.24	-0.23	0.20	-0.19	-0.44	0.22							
27-32	10.22	0.14	4.68	3.46	0.83	0.07	0.30	0.02	30.52	0.64	-0.05	0.13	-0.15	-0.08	-0.12	-0.11	-0.17	-0.61	0.14							
32-33	9.90	0.14	4.74	3.26	0.82	0.12	0.29	0.03	31.08	0.65	-0.10	0.16	-0.16	-0.15	-0.15	0.55	-0.21	-0.46	0.14							
<b>SPVF2</b>																										
0-6	6.25	0.09	2.90	2.08	0.37	0.12	0.33	0.03	36.92	0.78	-0.52	-0.42	-0.57	-0.55	-0.68	0.22	-0.23	-0.48	0.13							
6-14	6.30	0.07	3.02	2.13	0.38	0.07	0.29	0.03	36.46	0.76	-0.50	-0.50	-0.54	-0.52	-0.66	-0.24	-0.31	-0.60	0.16							
14-22	6.46	0.07	2.95	2.17	0.45	0.0	0.32	0.01	36.46	0.71	-0.46	-0.47	-0.52	-0.48	-0.58	-0.64	-0.20	-0.79	0.22							
22-28	7.04	0.07	3.41	2.33	0.51	0.0	0.31	0.02	35.06	0.68	-0.39	-0.44	-0.42	-0.42	-0.49	-0.54	-0.18	-0.70	0.23							
28-36	7.83	0.07	4.11	2.52	0.59	0.0	0.31	0.01	34.35	0.66	-0.29	-0.42	-0.28	-0.35	-0.39	-0.62	-0.15	-0.77	0.25							
36-41	8.63	0.06	4.52	2.85	0.65	0.0	0.30	0.02	33.28	0.66	-0.22	-0.54	-0.20	-0.27	-0.33	-0.62	-0.19	-0.69	0.21							
41-46	8.73	0.06	4.22	2.96	0.66	0.0	0.30	0.02	33.05	0.67	-0.23	-0.55	-0.27	-0.25	-0.34	-0.72	-0.21	-0.70	0.18							
53-59	9.21	0.06	4.46	3.13	0.69	0.0	0.26	0.02	31.36	0.66	-0.17	-0.54	-0.22	-0.19	-0.29	-0.52	-0.30	-0.69	0.14							
59-62	10.43	0.06	4.85	3.61	0.78	0.0	0.24	0.03	31.32	0.68	-0.08	-0.55	-0.17	-0.09	-0.22	-0.53	-0.37	-0.55	0.11							
62-66	10.32	0.06	4.76	3.61	0.77	0.03	0.23	0.02	30.71	0.68	-0.09	-0.50	-0.18	-0.09	-0.24	-0.63	-0.39	-0.63	0.09							

These were duplicate soil cores at the SPRT, SPMS and SPVF sites. As no Zr was measured, Ti was assumed immobile in the  $\tau$  calculation. Compared to data presented at Table 4, the  $\tau$  values in this table are more positive, e.g. Si, due to the loss of Ti in the soil profiles.

# Dynamical modelling of concentration–age–discharge in watersheds

Christopher J. Duffy\*

*Department of Civil and Environmental Engineering, Penn State University, University Park, PA, USA*

## Abstract:

There is now a wide literature on the use of tracer age and transit time distributions to diagnose transport in environmental systems. Theories have been proposed using idealized tracer age modelling for ocean ventilation, atmospheric circulation, soil, stream and groundwater flow. Most approaches assume a steady flow regime and stationarity in the concentration (tracer) distribution function for age, although recent work shows that this is not a necessary assumption. In this paper, dynamic model for flow, concentration, and age in volume-averaged and a spatially distributed watershed system are derived in terms of the moments of the underlying distribution function for tracer age, time, and position. Several theoretical and practical issues are presented: (1) The low-order moments of the age distribution function are sufficient to construct a dynamical system for the mean age and concentration under steady or transient flow conditions. (2) Solutions to the coupled system of equations for flow, concentration and age show that ‘age’ of solutes stored within the watershed or leaving the watershed is a dynamic process which depends on flow variations as well as the solute or tracer dynamics. (3) Intermittency of wetting and drying cycles leads to an apparent increase in the tracer age in proportional to the duration of the ‘dry’ phase. (4) The question of how mobile/immobile flow may affect the age of solutes is examined by including a low permeable, passive store that relaxes the well-mixed assumption. (5). A spatially distributed advective and dispersive transport solution for age evolution over a simple 1-D hillslope is developed to demonstrate the age theory for a distributed source of water and tracer, and the solution is shown to have very similar input–output behaviour when compared to the volume-average model for comparable parameters. Copyright © 2010 John Wiley & Sons, Ltd.

KEY WORDS watershed modelling; age of tracers; dynamical systems

*Received 23 September 2009; Accepted 17 March 2010*

## INTRODUCTION

The concept of ‘age’ in terrestrial watersheds and river basins has long been a useful quantity for the analysis of process timescales (Phillip, 1995) and resource assessment (Allison and Holmes, 1973), and recent reviews of the modelling and experimental strategies have greatly organized our approach to the problem of age of waters (IHP-V, 2001; Kazemi *et al.*, 2006; Brooks *et al.*, 2010). Many authors have noted that the interpretation of ‘age’ of waters is complicated by the fact that age depends on the fluid path (Botter *et al.*, 2008; Darracq *et al.*, 2010), physical and chemical interactions along the path (Destouni and Graham, 1995; Fiori and Russo, 2008), and the forcing or watershed inputs (Maloszewski and Zuber, 1982).

In this paper equations for the age of solutes in subsurface flow in watersheds governed by transient flow dynamics are investigated. The theory is based on the early work of Nauman (1969), Eriksson (1971), Bolin and Rodhe (1973), Goode (1996) for groundwater, and the recent work for transient systems of Delhez *et al.* (1999) and Gourgue *et al.* (2006). This paper shows that the coupled dynamical system for transient flow,

concentration and age can be derived without assuming the particular form of the age distribution function. Several solutions are presented that illustrate the theory and shed some light on the questions of ‘old water’, such as the role of mobile–immobile tracer flow, the implications of constant, intermittent and random flow and tracer inputs, and the role of advection–dispersion on water ‘age’ at the hillslope scale.

## THE CONCENTRATION–AGE SYSTEM

Solute ‘age’ is an extensive property which is defined here as the elapsed time since the solute or tracer of interest entered the system, and that the tracer or solute in question has the usual properties of a neutrally buoyant fluid particle (Bolin and Rodhe, 1973). For the watershed, the age might be defined as the time since the tracer entered the soil surface as precipitation. Or in the case of groundwater, the time since the solute entered the aquifer. In general, ‘age’ is a function of space and time  $A(x, t)$  and depends on the particular transport processes, physical and chemical interactions, the boundaries and initial conditions of the watershed. In 1972 Rotenberg proposed a theory for age-dependent biological species that is relevant here. Following Rotenberg’s development, we define a joint age–time concentration distribution function  $c(\mathbf{x}, t, \tau)$ , position vector  $\mathbf{x}$ , which describes the

\* Correspondence to: Christopher J. Duffy, Department of Civil and Environmental Engineering, Penn State University, University Park, PA, USA. E-mail: cxd11@psu.edu

number of dissolved particles that exist within a specified sub-volume in the time interval  $\{t, t + dt\}$  and the age interval  $\{\tau, \tau + d\tau\}$ . In general, the particular form of  $c(x, t, \tau)$  would be required to develop information on the joint age–time characteristics of the system. However, as has been shown by Nauman (1969), Rotenberg (1972), and more recently by Delhez *et al.* (1999), it is straightforward to examine moments of  $c(x, t, \tau)$  which generally are more accessible for analysis. We assume that the joint age–time distribution is from a population of particles in any sub-volume that is sufficiently large that a continuous distribution exists, and that the time and age correlation of particles in the volume is small relative to other timescales of the system (e.g. statistical independence). From the usual rules of probability, the  $n$ th moment of  $c(x, t, \tau)$  with respect to  $\tau$  is written as

$$\mu_n(x, t) = \int_0^\infty \tau^n c(x, \tau, t) d\tau \quad (1)$$

The tracer concentration  $C(x, t)$  for one dimensional flow in  $x$  is given by the zeroth moment:

$$C(x, t) = \int_0^\infty c(x, \tau, t) d\tau \quad (2)$$

Now following Delhez *et al.* (1999) the mean age  $A(x, t)$  of our tracer is conveniently defined as the ratio of the first and zeroth moments:

$$A(x, t) = \frac{\int_0^\infty \tau c(x, \tau, t) d\tau}{\int_0^\infty c(x, \tau, t) d\tau} = \frac{\alpha(x, t)}{C(x, t)} \quad (3)$$

where  $\alpha(x, t)$ , the first moment of Equation (1), is referred to as the age–concentration function and the denominator is the tracer concentration  $C(x, t)$  or zeroth moment. From Equation (3) we see that the mean age  $A(x, t)$  is an explicit function of position and time. The purpose of this representation, as we shall see, is to put the mean age in terms of moments of the tracer distribution function  $c(x, t, \tau)$  which is developed next for general transport.

Assuming the tracer distribution function is subject to the processes of solute transport and reaction, Rotenberg (1972) and later Delhez *et al.* (1999) show that  $c(x, t, \tau)$  satisfies a conservation equation in terms of time, age and position:

$$\frac{\partial c}{\partial t} + \frac{\partial c}{\partial \tau} = \Gamma_c - L(c) \quad (4)$$

where the left-hand represents the total derivative for particles that are allowed to age,  $L(c)$  is a general operator for transport (advection, diffusion and dispersion or bulk transport) and the term  $\Gamma_c$  represents sources and sinks. Figure 1 shows the particle control volume within our conceptual watershed. The importance of Equation (4) is that even if the distribution function  $c(x, t, \tau)$  is not known explicitly, it provides a means of forming transport equations for the individual moments of the process. The necessary properties of Equation (4) are:

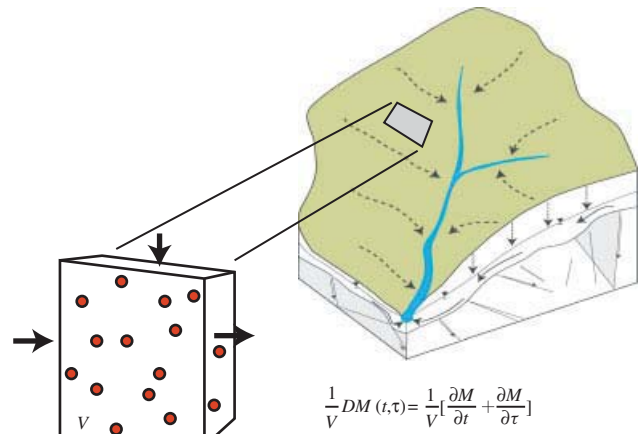


Figure 1. A control volume within the watershed showing the hypothetical distribution of particles of mass  $M$  that are allowed to evolve in time and age.  $dM(t, \tau)$  is the total derivative for tracer mass with respect to age and time

$c(x, t, \tau)$  is a continuous density for the time and age distribution of particles in any sub-volume of the system; that the time correlation among the particles in the sub-volume is small relative to other timescales of the system and that  $c(x, t, \tau)$  can be approximately described by its first few moments. To calculate the moments for age, we multiply Equation (4) by  $\tau^n$  and integrate over  $\tau$ :

$$\int_0^\infty \tau^n \frac{\partial c}{\partial t} d\tau + \int_0^\infty \tau^n \frac{\partial c}{\partial \tau} d\tau = \int_0^\infty \tau^n [\Gamma_c - L(c)] d\tau \quad (5)$$

which yields, after some manipulation, a general equation for the tracer moments:

$$\frac{\partial \mu_n}{\partial t} = n \mu_{n-1} + \Gamma_{\mu_n} - L(\mu_n) \quad (6)$$

The term  $n \mu_{n-1}$  is found from integration by parts for the second term on the left-hand side of Equation (6), and making the assumption that the moments of the distribution function for concentration and age have the property (Delhez *et al.*, 1999)

$$\lim_{\tau \rightarrow 0} \tau^n c(x, \tau, t) = \lim_{\tau \rightarrow \infty} \tau^n c(x, \tau, t) = 0 \quad (7)$$

Evaluating Equation (6) for moments  $n = \{0, 1\}$  yields

$$n = 0 \quad \frac{\partial C}{\partial t} = \Gamma_c - L(C) \quad (8)$$

$$n = 1 \quad \frac{\partial \alpha}{\partial t} = C + \Gamma_{\alpha_1} - L(\alpha) \quad (9)$$

$$A(x, t) = \frac{\int_0^\infty \tau c(x, t, \tau) d\tau}{\int_0^\infty c(x, t, \tau) d\tau} = \frac{\alpha(x, t)}{C(x, t)} \quad (10)$$

Note that Equation (8) is the transport equation for the tracer concentration  $C(x, t)$  and Equation (9) represents transport of age concentration  $\alpha(x, t)$  which are related by  $A(x, t) = \alpha(x, t)/C(x, t)$ . Together, Equations (8)–(10) form a coupled system of partial differential equations

for concentration and age. Boundary and initial conditions will depend on the particular transport assumed in the model. One implication of the system above is that the mean age can be directly determined using the same transport and reaction operator  $L(\alpha)$  as the concentration equation (8). In the following sections, we examine a range of solutions for flow and tracer transport applicable to small watershed settings similar to models developed by Duffy and Cusumano (1998) and Duffy and Lee (1992).

CONCENTRATION-AGE-DISCHARGE FOR A VOLUME-AVERAGED SYSTEM

An elementary model of an upland watershed assumes that the fluid reservoir (e.g. the watershed) has fluid storage volume  $V(t)$ , input volumetric flow rate  $Q_i(t)$  and output flux  $Q(t)$ . The flow through the reservoir satisfies a balance equation:

$$\frac{dV}{dt} = Q_i - Q \tag{11}$$

where the outflow is some function of the storage  $Q = Q(V)$  defined later. The tracer concentration for the input  $C_i(t)$  and the output concentration  $C(t)$  have the material balance

$$\frac{d(VC)}{dt} = Q_i C_i - QC + V\Gamma_c \tag{12}$$

where  $\Gamma_c$  is an internal source or sink of the tracer including any physical or chemical reactions. Equations (11) and (12) can be simplified by expanding Equation (12) and combining with Equation (11) to yield

$$\begin{aligned} \frac{dV}{dt} &= Q_i - Q \\ \frac{dC}{dt} &= \frac{Q_i}{V}(C_i - C) + \Gamma_c \end{aligned} \tag{13}$$

If we assume that our tracer has the concentration distribution function  $c(t, \tau)$  for time and age, then following the previous development we can immediately write down our dynamical system to include transient flow and tracer age:

$$\begin{aligned} \frac{dV}{dt} &= Q_i - Q \\ \frac{dC}{dt} &= \frac{Q_i}{V}(C_i - C) + \Gamma_c \\ \frac{d\alpha}{dt} &= C - \frac{Q_i}{V}\alpha + \Gamma_\alpha \\ A(t) &= \alpha(t)/C(t) \end{aligned} \tag{14}$$

where it is assumed that  $\alpha_i(t) = A_i(t) = 0$ , or the tracer input is specified to be of zero age as it enters the system. The zero-age input is of course an arbitrary assumption for the purpose of setting a base condition. The initial conditions for age concentration and age,  $\alpha(0) = A(0) = 0$ , can also be set to zero but again

this is arbitrary. The flow-concentration-age dynamical system (14) is a stable, nonlinear system with the exception of the singularity at  $V(t) \rightarrow 0$ . This nonphysical situation is avoided by adding a small constant to  $V(t)$  which assures that  $\lim_{V \rightarrow 0} \frac{Q(t)}{V(t)} = \text{finite}$ . The system (14) represents a fully coupled model of the tracer mixing process with the addition of the equation for the scalar  $\alpha(t)$ , the age concentration, and the auxiliary equation for age  $A(t)$ . Solutions to the system (14) follow.

CLOSED-FORM SOLUTION FOR STEADY FLOW

The system (14) admits a closed-form solution for steady flow conditions ( $Q_i = Q$ ), constant input ( $C_o$ ) and initial conditions ( $C_i$ ):

$$\begin{aligned} C(t) &= C_i e^{-kt} + C_o(1 - e^{-kt}) \\ \alpha(t) &= k^{-1} C_o(1 - e^{-kt}) + t C_i e^{-kt} - t C_o e^{-kt} \\ A(t) = \frac{\alpha(t)}{C(t)} &= \frac{k^{-1} C_o(1 - e^{-kt}) + t(C_i - C_o)e^{-kt}}{C_i e^{-kt} + C_o(1 - e^{-kt})} \end{aligned} \tag{15}$$

The steady-state solution  $A(t \rightarrow \infty) = A^*$  shows that the age depends on  $C_o$ :

$$\begin{aligned} C_o \neq 0, \quad A^*(\infty) &= k^{-1} = V/Q \\ C_o = 0, \quad A(\infty) &= t \end{aligned} \tag{16}$$

As expected, for large time, the age of the solute tends to a constant value defined by the steady-state age or steady-state residence time ( $V/Q$ ) of the system. While for  $C_o = 0$ , the age of the solute grows in proportional to time, a simple clock. The implications of these two solutions will be discussed further in the next section.  $A^*$  will also serve as a comparison for other solutions developed in the paper.

NUMERICAL SOLUTIONS FOR TRANSIENT FLOW AND TRACER INPUTS

Next, we examine numerical solutions for the system (14) for unsteady flow with step, pulse and random inputs for the tracer and flow with particular attention paid to the tracer mean age  $A(t)$ . In Figure 2, the solution is given for a unit step input  $Q_i = C_i = 1$  ( $t > 0$ ), with  $\Gamma_{c,\alpha} = 0$  and initial conditions  $Q(0) = C(0) = A(0) = 0$ . The figure shows that age  $A(t)$  for constant inputs evolves to the expected result, the mean residence time or the steady-state age. As the age of the tracer tends to a constant value, the ‘ageing process’ stops as the flow and the tracer approach steady state. For this case and subsequent cases, the volume-discharge relation is assumed to have the form:

$$Q = a(V - V_0)^b \tag{17}$$

with the parameters arbitrarily assigned to be  $V_0 = 3$ ,  $a = 5$  and  $b = 1$ , which were found to be convenient

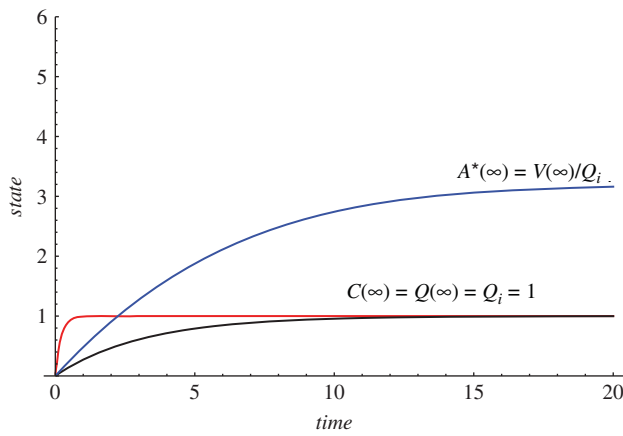


Figure 2. Numerical solution to the system (14) for unit step inputs  $Q_i$  and  $C_i$  and zero-state initial conditions. Note that  $A^*(\infty) = V(\infty)/Q_i$  is the steady-state age or residence time.  $A^*(\infty)$  with constant input is used as a reference for later results

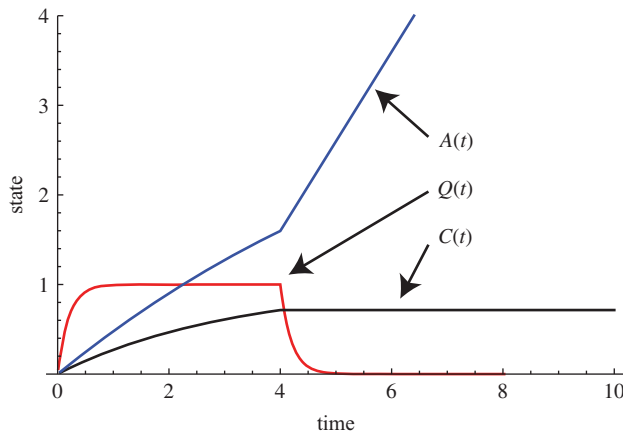


Figure 3. The evolution of solute age  $A(t)$  for a finite duration pulse input for  $Q_i$  and  $C_i$ . Note that during the drying phase  $A(t) \sim t$

for illustrating the results.  $V_0$  can be thought of as the residual storage volume in the system under static or no-flow conditions.

Figure 3 shows a solution to Equation (14) for discrete pulse inputs of flow and solute, and represents the case when the ageing process of the tracer is intermittent due to an abrupt change in the hydrological forcing. The inputs are defined as

$$C_i = Q_i = 1, \quad (0 < t \leq 4) \\ = 0, \quad \text{otherwise} \quad (18)$$

The initial conditions are the same as for the continuous unit step input. During the transient period, the flow, tracer and age all tend to an equilibrium value governed by the forcing as before. As the flow relaxes to no flow, the concentration remains constant, and the age increases as linear function of time.

The important point here is that, as the flow stops the tracer age evolves in time, a simple clock, or  $A(t) \sim t$ . The implications for watershed systems that have extended periods without hydrological inputs (e.g. arid regions or extended drought conditions) is that

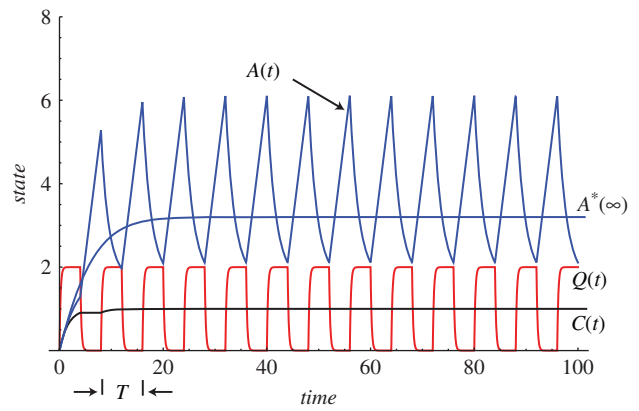


Figure 4. The evolution of solute age  $A(t)$  for an intermittent pulse input of  $Q_i$  and  $C_i$ . Note that the intermittency increases the age of the tracer over the steady state for constant inputs  $A^*(\infty)$  (Figure 2). Also note that the concentration  $C(t)$  is almost unaffected by the intermittent inputs as compared to the age in this example, suggesting the importance of transient flow on tracer ages

no-flow conditions will increase the tracer age in proportion to the duration of the dry period, until wetter conditions return and the ‘clock’ slows as shown in Figure 1.

Figure 4 shows the ‘clock’ effect for periodic pulse inputs of wet–dry or on–off cycles for the flow and the tracer. The first observation is that even though the tracer is subject to intermittent pulses just like the flow, the longer time constant for the solute produces very little fluctuation in  $C(t)$ . So, age fluctuations are almost entirely due to the intermittency in the flow. The second point is the age of the system  $A(t)$  is on-average greater than the steady-state age  $A^*(t)$ . This simulation suggests that the age of tracers in upland ephemeral channels or arid zone ephemeral streams will increase in proportion to the duration of the seasonal drought or the length of the dry period.

Next, we examine the role of stationary random inputs  $Q_i(t)$  and  $C_i(t)$  to illustrate the effect of continuous variation in forcing conditions on flow, concentration and age dynamics (Figure 5). In this case  $A(t)$  is sensitive to variability in both the flow and the tracer concentration.  $A(t)$  tends to increase during dry periods and to slow down during wet cycles but with a phase lag that depends on both the flow and the tracer. It was found that even when the input concentration was constant, the output age can have fairly large variations due to the flow dynamics alone. Once the initial conditions wear off, fluctuations in tracer and flow vary about a constant value as does the age. In general, the amplitudes of  $A(t)$  are large in comparison to the concentration. Although the results discussed above will depend on the timescale for mixing in the system, they suggest the importance of transient flow conditions in estimating the age of waters in the field. Note that all simulations use the same mean parameters to allow the above comparisons.

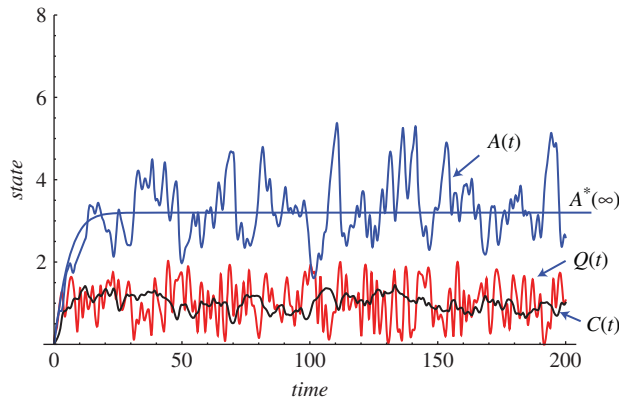


Figure 5. Age evolution of  $C(t)$  and  $Q(t)$  due to stationary random inputs  $Q_i(t)$  and  $C_i(t)$  and initial condition  $Q(0)=C(0)=0$ . The inputs are generated from a uniform distribution with range  $\{0, 2\}$ . It was found that even when the input concentration is relatively constant, the age can exhibit significant time fluctuations due to the flow dynamics

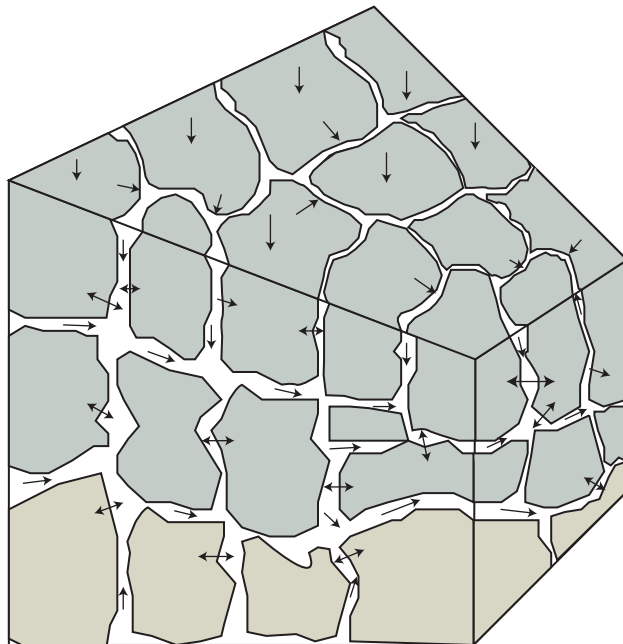


Figure 6. Conceptual model for mobile-immobile flow and tracer transport

CONCENTRATION-DISCHARGE-AGE DYNAMICS FOR MOBILE-IMMOBILE FLOW SYSTEMS

In a recent paper by Brooks *et al.* (2010) the authors present experimental stable isotope data that bring into question the assumption of complete mixing (or volume averaging) as developed in the previous section. The authors show that a significant fraction of tightly bound water stored in the soil does not participate in the advective component of stormflow during precipitation-runoff events. The conceptual model applied here (Figure 6) allows for a linear exchange between the immobile and mobile solute states. The goal of this section is to examine the age dynamics when the solute is partitioned into mobile and immobile components. The formulation follows the development of Gerke and van Genuchten

(1993); however, we apply their approach to a volume-average system. The resulting dynamical system, derived in the same way as Equation (14), is given by:

$$\begin{aligned} \frac{dV_m}{dt} &= Q_i - Q \\ \frac{dC_m}{dt} &= \frac{Q_i}{V_m}(C_i - C_{im}) - k_1 \frac{V_{im}}{V_m}(C_m - C_{im}) \\ \frac{dC_{im}}{dt} &= k_1(C_m - C_{im}) \\ \frac{d\alpha_m}{dt} &= C_m - \frac{Q_i}{V_m}\alpha_m - k_1 \frac{V_{im}}{V_m}(\alpha_m - \alpha_{im}) \\ \frac{d\alpha_{im}}{dt} &= C_{im} + k_1(\alpha_m - \alpha_{im}) \\ A_m(t) &= \alpha_m(t)/C_m(t) \\ A_{im}(t) &= \alpha_{im}(t)/C_{im}(t) \end{aligned} \tag{19}$$

where  $C_m, C_{im}, \alpha_m, \alpha_{im}$  are the mobile and immobile tracers and age concentration respectively, and  $A_m$  and  $A_{im}$  are the mobile and immobile water ages.  $k_1$  in this case is the rate constant for exchange between the mobile and immobile solute states. Note that the system of equations (19) has seven state variables, five dynamic and two algebraic states. The assumption of an immobile fluid volume implies  $\dot{V}_{im} = 0$ , and the volume ratio is defined as

$$\frac{V_{im}}{V_m} = \frac{(1 - \beta)nV_0}{\beta nV(t)} \tag{20}$$

where  $\beta$  is the fraction of the porosity  $n$  that is occupied by the mobile storage volume, and  $V_0$  is the mean residual saturated volume of the system. Figure 7 shows the unit step input case for the age of mobile and immobile flows. The asymptotic value for mobile and immobile ages is given by:

$$\begin{aligned} A_m(\infty) &= \frac{V_m(\infty) + V_{im}}{Q_i} \\ A_{im}(\infty) &= \frac{V_m(\infty) + V_{im}}{Q_i} + \frac{1}{k} \end{aligned} \tag{21}$$

It is interesting to note that the age of the mobile fraction is increased by the magnitude of the immobile volume (21) as compared to the well-mixed case, and that the age of the immobile fraction is further increased by  $k^{-1}$ . The implications for watershed systems may be significant where immobile storage volume represents an adequate model and  $k^{-1}$  is large enough. In this case  $k = 0.1$  (time units<sup>-1</sup>) and the mobile volume fraction is  $\beta = 0.8$ . Clearly, the simple model proposed here for immobile/mobile tracer storage cannot entirely explain the apparent ‘old water’ often observed in upland watersheds. However, combined with the transient hydrology effects described earlier, it does provide useful insight into the path to a more complete understanding of the contributing processes.

The solution for age was extended to cyclic wet-dry input sequences. In Figure 8 we see that the on-off flow

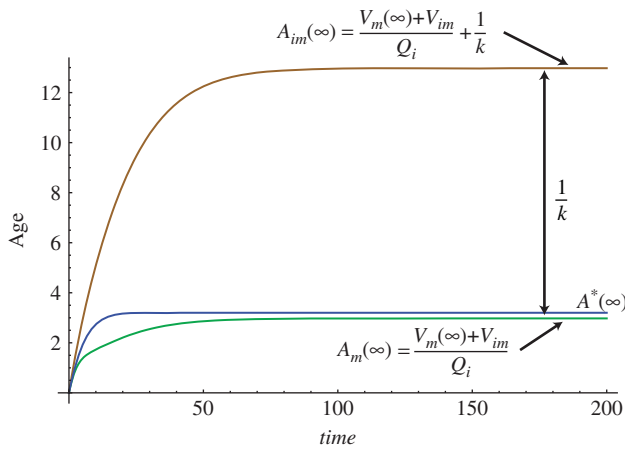


Figure 7. Numerical solution for the mobile-immobile flow and tracer transport system (Equation 19) for unit step inputs  $Q_i$  and  $C_i$  and the corresponding steady-state age for mobile and immobile storage (shown). Note that both  $A_m(\infty)$  and  $A_{im}(\infty)$  are larger than the steady-state age for constant inputs  $A^*(\infty)$  by constant factors given in Equation (21)

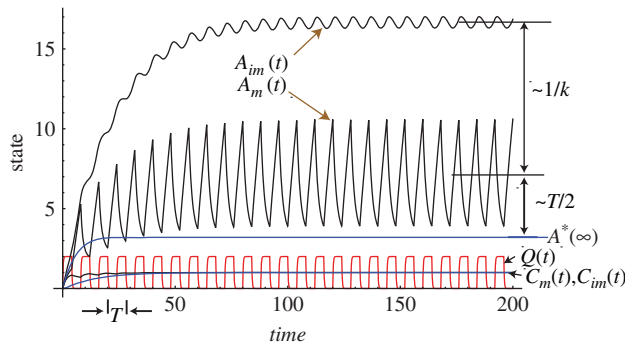


Figure 8. Numerical solution for the mobile-immobile flow, tracer and age for the system (19) for an intermittent sequence (wet-dry) of unit step inputs  $Q_i$  and  $C_i$ . The corresponding age for mobile and immobile storage fractions are very sensitive to the input fluctuations, while the mobile and immobile concentrations are not. It was estimated that the time-averaged age of mobile and immobile tracers were larger than  $A^*(\infty)$  by the factors  $\sim T/2$  and  $k^{-1}$  respectively

cycle has only a small effect on the concentration but a very large effect on the age of mobile and immobile solutes. The solution shows that although a dynamic steady state is reached, during the drying cycle, the age of the mobile state increases in proportion to clock time, and both mobile and immobile states are significantly older than the steady-state age  $A^*(\infty)$ .

The case of random inputs with mobile-immobile solute storage was simulated and the results are shown in Figure 9. The inputs were chosen to fluctuate about unit values with the same assumptions and parameters as for the earlier case (Figure 5). The results are consistent with the previous interpretations; however, we note that the immobile solute concentration has filtered the high-frequency solute fluctuations observed in the mobile volume.

The commentary by Kirchner (2003) is relevant here in that, this simple model provides one explanation for the ‘rapid mobilization of old water’, where the immobile storage of solute increases the age of the mobile state in proportion to  $k^{-1}$ . We also notice that the age of solutes in

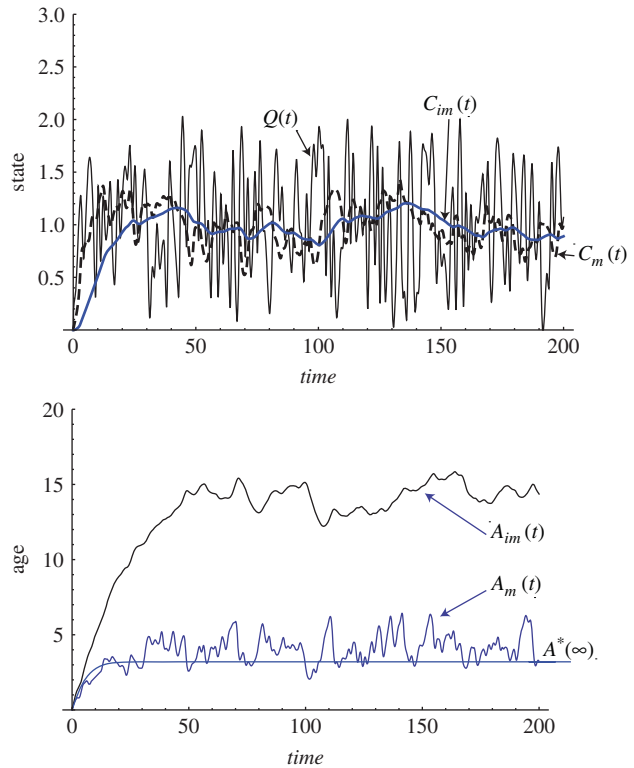


Figure 9. Solution to the mobile-immobile flow system (19) for uniform random inputs for  $Q_i$  and  $C_i$  showing the evolution of age for the mobile and immobile storage volume (lower graph) under fluctuating input conditions. The inputs were generated from a uniform distribution in the range  $\{0, 2\}$ . The initial conditions are zero-state as in the previous cases. The steady-state age for constant inputs (Figure 2) is also shown for reference

runoff will depend on the fluctuations in  $Q(t)$ . Overall, the simple model provides useful insight into the behaviour for field settings where immobile storage is suspected, and the approach could provide a tool for estimating the immobile volume and the rate constant  $k^{-1}$ .

### CONCENTRATION-AGE FOR A DISTRIBUTED SOURCE WITH ADVECTION AND DISPERSION

The final example is motivated by an attempt to extend the age solution to spatially distributed inputs over a hillslope, and the setting is shown in Figure 10. Following the same strategy outlined earlier, the transport operator  $L(C)$  in Equation (8) is now defined in terms of the advective and dispersive flux. The limited goal of this section is to demonstrate that the age-simulation strategy also applies to advective-dispersive systems, and to compare these solutions to the volume-average system (14) results given earlier. Assuming a steady flow, the 1-D hillslope system is given by (Bear, 1972; Duffy and Cusumano, 1998):

$$\begin{aligned} \nabla \cdot (Kh\nabla h) + \varepsilon &= 0 \\ \theta_s \frac{\partial(C_h)}{\partial t} + \nabla \cdot F &= \varepsilon C_i \\ F &= QC - hJ \\ J &= -\theta_s D \nabla C \end{aligned} \tag{22}$$

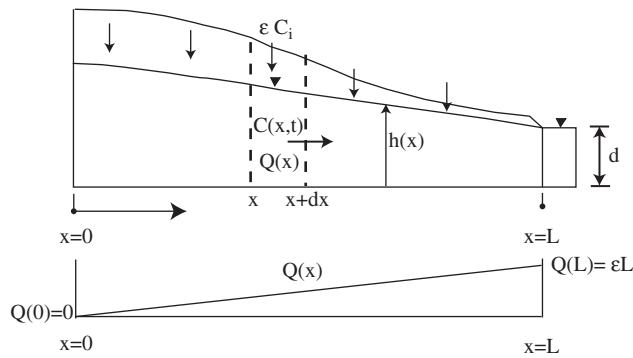


Figure 10. A distributed tracer and recharge in a steady, 1-D non-uniform flow. The constant recharge rate produces the advective flux  $Q(x) = \epsilon x$  which varies linearly along the flow path. The parameters were assigned such that the spatially distributed solution could be compared to the volume-average solutions developed earlier

where  $C(x, t)$  is the solute concentration,  $h(x)$  is the saturated thickness,  $K$  is the hydraulic conductivity and  $\epsilon$  is the recharge rate to the aquifer. In Equation (8)  $L[C] = \nabla \cdot F$  is the advective-dispersive flux term and  $D$  is the dispersion coefficient. Expanding the transport equation in (22) and including the age concentration equation (9) lead to the following system for concentration and age in a steady 1-D flow with recharge:

$$\begin{aligned} \frac{\partial C}{\partial t} + u(x)\frac{\partial C}{\partial x} - D(x)\frac{\partial^2 C}{\partial x^2} &= K(C_i - C) \\ \frac{\partial \alpha}{\partial t} + u(x)\frac{\partial \alpha}{\partial x} - D(x)\frac{\partial^2 \alpha}{\partial x^2} &= C - k\alpha \end{aligned} \quad (23)$$

where for steady flow the lateral flux of groundwater and the parameters are given by:

$$\begin{aligned} Q(x) &= -Kh\frac{\partial h}{\partial x} = qh = \epsilon x \\ k &= \frac{\epsilon}{\theta_s d}; \quad u(x) = k(x - a_L) \\ D(x) &= kxa_L \end{aligned} \quad (24)$$

As before, the age concentration is assumed to have the initial condition  $\alpha(0) = 0$ , and the external source or the recharge age concentration is taken to be  $\alpha_i = 0$ , which states that the input of solute is zero age as it enters the system as before. Figure 11 shows the space-time solution for constant inputs. It is clear that the depth-averaged model (23) has a nearly constant solution in space. In fact, we get essentially the same solution at any location along the flow as we do for the volume-averaged case. To demonstrate this point, the unit step solution for volume-averaged age and concentration are superimposed in Figure 11 with almost no difference between 1-D advective-dispersive transport with unit inputs. Duffy and Lee (1992) found a similar result for a more general 2-D flow system with stationary spatial variability in  $K(x, z)$ ,  $\epsilon(x)$  and  $C_i(x, z)$ . We see in this comparison that the age and concentration for well-mixed and spatial inputs are essentially the same for comparable conditions. One practical implication is that the simple

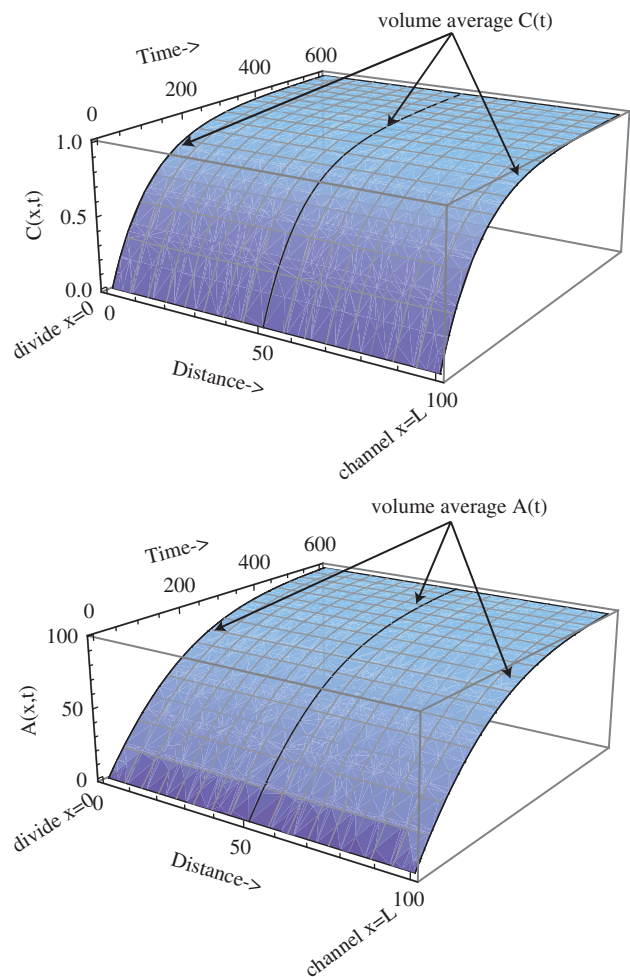


Figure 11. The space and time distribution of tracer concentration (upper) and age (lower) for the system (23) including the effects of non-uniform flow and advective-dispersive transport, with uniform constant  $\epsilon_i$  and  $C_i$ . The solutions for  $C(x, t)$  and  $A(x, t)$  are nearly constant in space as shown by Duffy and Lee (1992). The solid lines are superimposed from the volume-average solution from Equation (14) shown in Figure 2

volume-average model has very similar dynamics and input-output behaviour to the spatially distributed flow along a hillslope, and that simple models continue to have an important role to play in watershed studies. It must be noted that in real field settings, the processes encountered will be more complex including the role of bedrock slope, displacement dynamics, transient contributing area, etc. The comparisons made here can only serve as a step towards a more comprehensive theory that includes these processes.

CONCLUSIONS

A theoretical interpretation of tracer and solute ages for a transient hydrological systems is developed based on constructing the moments of the underlying concentration age distribution function  $c(x, t, \tau)$ . The results are applicable to spatially distributed and volume-averaged systems and the method requires limited assumptions on the particular form of the distribution function. Particular examples or numerical experiments are conducted

using *Mathematica* simulation software (Wolfram, 2010) which demonstrate a number of points: (1) The first two moments of the age distribution function are sufficient to construct a dynamical system for the mean age and concentration under steady or transient flow conditions. (2) Solutions to the coupled system of equations for flow, concentration and age show that 'age' of solutes stored within the watershed or leaving the watershed is a dynamic process which depends on flow variations as well as the solute or tracer dynamics. (3) Intermittency of wetting and drying cycles leads to an apparent increase in the tracer age in proportional to the duration of the 'dry' phase. It is noted that transient effects may be a particular problem for regions where intermittent rainfall–runoff has long periods of no flow. This would be the case in arid regions or for small upland humid watersheds where vegetation tends to consume all the summer precipitation. (4) The question of how mobile/immobile flow may affect the age of solutes is examined by including a low permeable, passive store that drops the well-mixed assumption in the first model. In this case, we see explicitly how an immobile storage of tracer will increase the age of the stored or exiting waters as compared to the steady-state age often used. The presence of immobile storage in the watershed serves to increase these time constants in a predictable way based on the magnitude of the rate constant  $k$ . (5) Comparison of the volume-averaged model with spatially distributed advective–dispersive transport along a 1-D hillslope trajectory is shown to compare well with the volume-average results for similar hydraulic parameters. The comparisons extend earlier work (Duffy and Lee, 1992; Duffy and Cusumano, 1998) by including age in the comparison. Finally, the paper shows that relatively few additional parameters are necessary to include dynamic hydrology in age modelling. In general, including transient flow added additional information that complements steady-state age results widely used in the literature.

#### ACKNOWLEDGEMENT

This research was funded by the National Science Foundation EAR 0725019 Shale Hills-Susquehanna Critical Zone Observatory at Penn State. This support is gratefully acknowledged.

#### REFERENCES

- Allison G, Holmes J. 1973. The environmental tritium concentration of under ground water and its hydrological interpretation. *Journal of Hydrology* **19**(2): 131–143.
- Bear J. 1972. *Dynamics of fluids in porous media*, Elsevier pub.; 764 p.
- Bolin B, Rodhe H. 1973. A note on the concepts of age distribution and transit time in natural reservoirs. *Tellus* **25**(1): 58–62.
- Botter G, Peratoner F, Putti M, Zuliani A, Zonta R, Rinaldo A, Marani M. 2008. Observation and modeling of catchment-scale solute transport in the hydrologic response: a tracer study. *Water Resources Research* **44**(5): W05409. DOI: 10.1029/2007WR006611.
- Brooks J, Barnard H, Coulombe R, McDonnell J. 2010. Ecohydrologic separation of water between trees and streams in a Mediterranean climate. *Nature Geoscience* **3**: 100–104.
- Darracq A, Destouni G, Persson K, Prieto C, Jarsjö J. 2010. Quantification of advective solute travel times and mass transport through hydrological catchments. *Environmental Fluid Mechanics* **10**(1–2): 103–120.
- Delhez EJM, Campin J-M, Hirst AC, Deleersnijder E. 1999. Toward a general theory of the age in ocean modeling. *Ocean Modelling* **1**(1): 17–27.
- Destouni G, Graham W. 1995. Solute transport through an integrated heterogeneous soil groundwater system. *Water Resources Research* **31**(8): 1935–1944.
- Duffy CJ, Cusumano J. 1998. A low-dimensional model for concentration-discharge dynamics in groundwater stream systems. *Water Resources Research* **9**(34): 2235–2247.
- Duffy CJ, Lee DH. 1992. Baseflow response from nonpoint source contamination: simulated spatial uncertainty in source, structure and initial condition. *Water Resources Research* **28**(3): 905–914.
- Eriksson E. 1971. Compartment models and reservoir theory. *Annual Reviews Ecological Systems* **2**: 67–84.
- Fiori A, Russo D. 2008. Travel time distribution in a hillslope: insight from numerical simulations. *Water Resources Research* **44**(12): W12426. DOI: 10.1029/2008WR007135.
- Gerke HH, van Genuchten MTh. 1993. Evaluation of a first order water transfer term for variably saturated dual-porosity models. *Water Resources Research* **29**(4): 1225–1238.
- Goode D. 1996. Direct simulation of groundwater age. *Water Resources Research* **32**(2): 289–296.
- Gourgou O, Deleersnijder E, White L. 2006. Toward a generic method for studying water renewal, with application to the epilimnion of Lake Tanganyika, Estuarine. *Coastal and Shelf Science* **74**(4): 628–640.
- IHP-V. 2001. *Environmental Isotopes in the Hydrological Cycle*, Mook W (ed). IHP Technical Documents in Hydrology, No. 39 Unesco: Paris, Vol. VI, 117 p.
- Kazemi A, Lehr J, Perrochet P. 2006. *Groundwater Age*. Wiley: New Jersey USA; 325 p.
- Kirchner JW. 2003. A double paradox in catchment hydrology and geochemistry. *Hydrologic Processes* **17**: 871–874.
- Maloszewski P, Zuber A. 1982. Determining the turnover time of groundwater systems with the aid of environmental tracers. I. Models and their applicability. *Journal of Hydrology* **57**(3–4): 207–231.
- Nauman E. 1969. Residence time distribution theory for unsteady stirred tank reactors. *Chemical Engineering Science* **24**(9): 1461–1470.
- Phillip F. 1995. The use of isotopes and environmental tracers in subsurface hydrology. *Reviews in Geophysics* **33**: 1029–1033 (Supplement, July 1995, U.S. Nat. Rept. To Int. Union Geod. Geophys. 1991–1994).
- Rotenberg M. 1972. Theory of population transport. *Journal of Theoretical Biology* **37**(2): 291–305.
- Wolfram Research, 2010. *Mathematica 7.0*, (software) www.wolfram.com.



Tree Physiology 00, 1–10  
doi:10.1093/treephys/tpr050



## Research paper

# Hydraulic patterns and safety margins, from stem to stomata, in three eastern US tree species

D.M. Johnson<sup>1,5</sup>, K.A. McCulloh<sup>2</sup>, F.C. Meinzer<sup>3</sup>, D.R. Woodruff<sup>3</sup> and D.M. Eissenstat<sup>4</sup>

<sup>1</sup>Department of Environmental and Plant Biology, Ohio University, Athens, OH 45701 USA; <sup>2</sup>Department of Wood Science and Engineering, Oregon State University, Corvallis, OR 97331, USA; <sup>3</sup>USDA Forest Service, Pacific Northwest Research Station, Corvallis, OR 97331, USA; <sup>4</sup>Department of Horticulture, Penn State University, University Park, PA 16802, USA; <sup>5</sup>Corresponding author (johnsod6@ohio.edu)

Received December 8, 2010; accepted May 10, 2011; handling Editor Nathan Phillips

Adequate water transport is necessary to prevent stomatal closure and allow for photosynthesis. Dysfunction in the water transport pathway can result in stomatal closure, and can be deleterious to overall plant health and survival. Although much is known about small branch hydraulics, little is known about the coordination of leaf and stem hydraulic function. Additionally, the daily variations in leaf hydraulic conductance ( $K_{\text{leaf}}$ ), stomatal conductance and water potential ( $\Psi_L$ ) have only been measured for a few species. The objective of the current study was to characterize stem and leaf vulnerability to hydraulic dysfunction for three eastern US tree species (*Acer rubrum*, *Liriodendron tulipifera* and *Pinus virginiana*) and to measure in situ daily patterns of  $K_{\text{leaf}}$ , leaf and stem  $\Psi$ , and stomatal conductance in the field. Sap flow measurements were made on two of the three species to compare patterns of whole-plant water use with changes in  $K_{\text{leaf}}$  and stomatal conductance. Overall, stems were more resistant to hydraulic dysfunction than leaves. Stem  $P_{50}$  ( $\Psi$  resulting in 50% loss in conductivity) ranged from  $-3.0$  to  $-4.2$  MPa, whereas leaf  $P_{50}$  ranged from  $-0.8$  to  $-1.7$  MPa. Field  $\Psi_L$  declined over the course of the day, but only *P. virginiana* experienced reductions in  $K_{\text{leaf}}$  (nearly 100% loss). Stomatal conductance was greatest overall in *P. virginiana*, but peaked midmorning and then declined in all three species. Midday stem  $\Psi$  in all three species remained well above the threshold for embolism formation. The daily course of sap flux in *P. virginiana* was bell-shaped, whereas in *A. rubrum* sap flux peaked early in the morning and then declined over the remainder of the day. An analysis of our data and data for 39 other species suggest that there may be at least three distinct trajectories of relationships between maximum  $K_{\text{leaf}}$  and the %  $K_{\text{leaf}}$  at  $\Psi_{\text{min}}$ . In one group of species, a trade-off between maximum  $K_{\text{leaf}}$  and %  $K_{\text{leaf}}$  at  $\Psi_{\text{min}}$  appeared to exist, but no trade-off was evident in the other two trajectories.

**Keywords:** cavitation, embolism, photosynthesis, transpiration, xylem.

## Introduction

Water transport from plant stems into and throughout leaves is critical for maintenance of adequate leaf water status. To prevent stomatal closure, and to permit photosynthetic carbon gain, this water pathway must remain functional. However, during periods of drought stress, dysfunction in this hydraulic pathway may occur. Reductions in leaf and stem hydraulic capacity can result in reduced photosynthesis and even plant mortality via carbon starvation, desiccation or some combination of both (e.g., McDowell et al. 2008). In stems, it appears that the

primary source of hydraulic dysfunction is xylem embolism (e.g., Tyree and Sperry 1989). There is some debate in the literature as to the mechanism of this dysfunction in leaves, although most evidence points to leaf xylem embolism as the cause of loss of leaf hydraulic conductance ( $K_{\text{leaf}}$ ; Nardini et al. 2001, 2003, Bucci et al. 2003, Woodruff et al. 2007, Johnson et al. 2009a). Partial collapse of leaf xylem has also been proposed as another mechanism responsible for reductions in  $K_{\text{leaf}}$  during dehydration (Cochard et al. 2004, Brodribb and Cochard 2009, Blackman et al. 2010). Additionally, reductions in extra-xylary

conductance (e.g., membrane permeability and aquaporin expression) could also impact  $K_{\text{leaf}}$  (Cochard et al. 2007, Kaldenhoff et al. 2008, Voicu et al. 2008, Heinen et al. 2009).

Although much research has been done on the hydraulic parameters of small-diameter stems and roots in various species from a variety of habitats, little is known about how plant hydraulic parameters are coordinated throughout the entire plant hydraulic continuum from root to leaf (Meinzer et al. 2009, 2010). Even the coordination of hydraulic properties at the terminal portion of the pathway, at the level of stem and leaf, is poorly understood, although there has been some previous work dealing with the subject (Salleo et al. 2001, Choat et al. 2005). It has been proposed that rapidly reversible diurnal changes in  $K_{\text{leaf}}$  may constitute part of an essential hydraulic signal that enables stomata to maintain stem and leaf water potential at set points that ensure the integrity of the stem water transport system upstream (Brodribb and Holbrook 2003, Meinzer et al. 2004, 2008, 2009, Woodruff et al. 2007). Failure of stomata to respond quickly to rapid increases in transpiration could result in sharp increases in stem xylem tension and loss of conductivity from embolism. However, the fact that many species operate so close to the threshold of declining stem hydraulic conductance (Meinzer et al. 2009) suggests that there are mechanisms (stomatal regulation or stem capacitance) that regulate minimum stem water potentials and prevent substantial losses in hydraulic function. Although these are critical processes governing carbon capture and survival in plants, diurnal coordination of leaf and stem water potential, stomatal conductance and  $K_{\text{leaf}}$  have only been explored in a few species (e.g., Woodruff et al. 2007, Meinzer et al. 2008, Johnson et al. 2009b).

The objective of this study was to evaluate leaf and stem vulnerability to embolism and to determine the degree of embolism experienced in situ by leaves and stems of three tree species that occur naturally in the eastern USA. Two of the three species were also selected for sap flow measurements to compare patterns of whole-plant water use with changes in  $K_{\text{leaf}}$  and stomatal conductance. In addition, the relationship between maximum  $K_{\text{leaf}}$  and the portion of  $K_{\text{leaf}}$  remaining at midday was explored because in an earlier survey of 31 species we found that they tended to fall into one of two groups: species that maintained near-maximal  $K_{\text{leaf}}$  at their minimum daily  $\Psi_L$  and species that lost >50% of their maximum  $K_{\text{leaf}}$  at their minimum daily  $\Psi_L$  (Johnson et al. 2009b). We hypothesized that there would be a trade-off of maximum leaf hydraulic capacity against the ability to maintain leaf hydraulic capacity throughout the day.

## Materials and methods

### Field sites and species

The field site used for this study was a common garden plot planted in 1996 near State College, PA, USA (40.79 N, 77.86 W).

All plants measured were within 20 m of each other. All measurements were carried out during July of 2010, with the addition of measurements of stem and leaf water potentials, and hydraulic vulnerability on a subset of *Pinus virginiana* and *Liriodendron tulipifera* stems carried out in July of 2009 (see below). In order to represent different plant functional groups, we selected two deciduous broadleaf species (*Acer rubrum* L. and *L. tulipifera* L.) and one evergreen conifer (*P. virginiana* Mill.). Diameters at breast height for the three species were 5.6 ( $\pm 0.3$  cm), 7.7 ( $\pm 0.4$  cm) and 7.7 ( $\pm 0.2$  cm) for *A. rubrum*, *L. tulipifera* and *P. virginiana*, respectively. Individual tree heights ranged from 8.1 to 12.4 m.

### Stem hydraulic conductivity and vulnerability

Branches ~50 cm long were collected in the field, bagged and transported back to the lab (~30 min in transit). Segments of branches (~20 cm in length and 5.5–7 mm in diameter with bark removed) were cut under water and were flushed with filtered, distilled water at pH 2 before hydraulic measurements. Embolisms were removed by submerging the stem segments in filtered, distilled (pH 2) water in a vacuum chamber overnight. To measure maximum hydraulic conductivity, a hydrostatic pressure head (~70 cm) was used to induce flow through the segments. The resulting volume flow rate was measured by timing the intervals for water to reach successive gradations on a pipette attached with tubing to the distal end of the segment. Hydraulic conductivity ( $k_h$ ) was calculated by dividing the volume flow rate of water flowing through the stem by the hydrostatic pressure gradient along the stem.

Vulnerability curves were constructed using the air injection method (Sperry and Saliendra 1994). Briefly, after measurement of maximum hydraulic conductivity ( $k_{h\text{max}}$ ), stems were placed in a pressure sleeve, and were pressurized to 1 MPa for 2 min. The stem was then removed from the pressure sleeve and  $k_h$  was measured using the same method used for maximum conductivity. This process was repeated at 1 MPa increments of increasing pressure until  $k_h$  had fallen to <10% of its maximum value. The percentage loss in hydraulic conductivity (PLC) was calculated as

$$\text{PLC} = 100 \times \left( 1 - \left( \frac{k_h}{k_{h\text{max}}} \right) \right)$$

### Leaf hydraulic conductance and vulnerability

Leaf hydraulic conductance ( $\text{mmol m}^{-2} \text{s}^{-1} \text{MPa}^{-1}$ ) was determined using a timed rehydration method described in Brodribb and Holbrook (2003), which is based on an analogy between rehydrating a leaf and recharging a capacitor:

$$K_{\text{leaf}} = C \ln(\Psi_o / \Psi_f) / t$$

where  $C$  = capacitance,  $\Psi_0$  = leaf water potential prior to partial rehydration,  $\Psi_t$  = leaf water potential after partial rehydration and  $t$  = duration of rehydration. Branches ~30–50 cm long were collected from trees early in the morning prior to significant transpirational water loss and were transported to the lab, re-cut under water and allowed to rehydrate for at least 4 h. Shoots were dried on the bench top for varying lengths of time, placed in a plastic bag and sealed and then kept in the dark for at least 1 h to equilibrate. Measurements of leaf rehydration kinetics were conducted over the next 3 days (shoots kept in the dark at 4 °C, unless measured on the same day as they were dehydrated) on excised leaves/fascicles for initial values ( $\Psi_0$ ) and for final values after a period of rehydration of  $t$  seconds ( $\Psi_t$ ), which was between 60 and 120 s. Adjacent or paired leaves/fascicles were used for each  $K_{\text{leaf}}$  measurement and a total of 34–63 leaf/fascicle pairs were used to construct each  $K_{\text{leaf}}$  vulnerability curve. Distilled water was used for rehydration of  $K_{\text{leaf}}$  samples and water temperature was maintained between 21 and 23 °C.

Values of  $C$  were estimated from pressure–volume curves (Scholander et al. 1965, Tyree and Hammel 1972) using the methods described by Brodribb and Holbrook (2003). Briefly, the  $\Psi_L$  corresponding to turgor loss was estimated as the inflection point of the graph of  $\Psi_L$  vs. relative water content (RWC). The slope of the curve prior to, and following, turgor loss provided  $C$  in terms of RWC ( $C_{\text{RWC}}$ ) for pre-turgor loss and post-turgor loss, respectively. Five to six leaves of each species were used to construct pressure–volume curves and estimate  $C$ .

Pressure–volume curves were conducted on individual leaves for the broadleaf species and on fascicles of two needles for *P. virginiana*. Branch samples of ~30–50 cm, from the same individuals that were used for rehydration and measurement of  $K_{\text{leaf}}$ , were excised early in the morning and re-cut under water in the lab. Branches were allowed to rehydrate for at least 4 h before pressure–volume analyses were performed. Pressure–volume curves were created by plotting the inverse of  $\Psi_L$  against RWC with alternate determinations of fresh mass and  $\Psi_L$  repeated during slow dehydration of the twig on the laboratory bench until values of  $\Psi_L$  exceeded the measuring range of the pressure chamber (–4.0 MPa). Leaf water potential was measured using a pressure chamber (PMS Instrument Company, Albany, OR, USA). For normalizing  $C$  on a leaf area basis, leaf areas for the broadleaf species were obtained with a scanner and ImageJ version 1.27 image analysis software (Abramoff et al. 2004, National Institute of Mental Health, Bethesda, MD, USA) and needle areas for *Pinus* were determined by multiplying mean needle lengths and circumferences ( $n = 6$  leaves/needles per species).

For measurement of  $K_{\text{leaf}}$  in the field, branches (~10–20 cm in length) were collected from trees, and leaves were then excised for determination of  $\Psi_0$ , with no equilibration time

( $\Psi$  for leaves on the same shoot typically varied by <0.1 MPa). Leaf samples from the same branch were then rehydrated for a period of  $t$  seconds and  $\Psi_t$  was measured. Distilled water was used for rehydration of  $K_{\text{leaf}}$  samples and all measurements took place in the shade. These measurements (both field and lab) were performed on individual leaves of *Acer* and *Liriodendron* and fascicles (two needles each) of *Pinus*.

Field measurements of  $K_{\text{leaf}}$  along with corresponding measurements of  $\Psi_L$  (predawn and midday), stem water potential and stomatal conductance were performed over 4 days in July of 2010 (20, 22, 24 and 25 July). Additionally, predawn and midday (stem and leaf) water potentials for *Pinus* and *Liriodendron* were measured on 12 and 13 July 2009 and were not significantly different from those measured in 2010 (although 2009 *Liriodendron* predawn values were slightly more negative than 2010 values, by ~0.04 MPa). All measurements were made on three to six leaves from five preselected individuals approximately every 120 min from 530–600 h (predawn) until 1600–1630 h Eastern Daylight Time. All individuals were in open areas and fully sunlit branches/leaves were chosen for measurement (with the exception of predawn measurements).

### Leaf and stem water potentials and stomatal conductance

Stomatal conductance ( $g_s$ ) was measured with a steady-state porometer (LI-1600; Li-Cor, Lincoln, NE, USA) and leaf temperatures were measured concomitantly with a fine-wire thermocouple (located in the LI-1600 chamber). One-sided leaf areas of foliage from the porometer measurements were obtained with a scanner and ImageJ. Leaf water potential was measured using a pressure chamber on individual leaves of *Acer* and *Liriodendron* and fascicles (two needles each) of *Pinus*. Measurements of  $g_s$  and  $\Psi_L$  were conducted on the same dates and over the same time intervals as  $K_{\text{leaf}}$  measurements, and on three to five leaves of each species (per time interval). Additionally, measurements of stem water potential were performed in order to estimate the amount of embolism that occurred in stems of the measured trees. Large disequilibria can exist between stem and leaf water potentials, especially at midday (Bucci et al. 2004). Therefore, it was necessary to bag and cover shoots (with a sealable plastic bag covered in aluminum foil) before dawn and then measure the midday water potential of bagged leaves to get an estimate of stem water potential.

### Sap flow

Heat dissipation sap flow probes with heated and reference sensors 20 mm in length (Granier 1985) were used to determine sap flux in *A. rubrum* and *P. virginiana*. For probe installation, two holes separated axially by 10 cm were drilled into the sapwood (2 cm depth) and the heated sensor installed above the reference sensor. The sensors were coated with thermally conductive silicone heat sink compound prior to

insertion. All probes were protected from ambient radiation by reflective insulation. Signals from the sap flow probes were scanned every minute and 10-min means were recorded by a data logger (CR10X; Campbell Scientific Corp., Logan, UT, USA) equipped with a 32-channel multiplexer (AM416; Campbell Scientific). Differential voltage measurements between the heated and reference sensors were converted to a temperature difference ( $\Delta T$ ), which was converted to sap flux ( $v$ ;  $\text{g m}^{-2} \text{s}^{-1}$ ) using the empirical calibration of Granier (1985):

$$v = 119 k^{1.231}$$

where  $k = (\Delta T_m - \Delta T)/\Delta T$ , and where  $\Delta T_m$  is the temperature difference when sap flux is assumed to be zero. Sap flux values were averaged over five clear days for three individuals of each species.

Our primary interest was in the temporal dynamics of sap flow as opposed to actually quantifying total water use, or the spatial variability of sap flow, in these trees. Although there is likely to be sap flow inwards of 2 cm on these trees, the majority of water use in these stems should be captured by the 2 cm probes due to the fact that the outermost regions of sapwood typically represent the area where sap flow is highest and due to the fact that these stems were relatively small in diameter.

#### Comparison of maximum $K_{\text{leaf}}$ and remaining $K_{\text{leaf}}$ at midday

Absolute maximum values of  $K_{\text{leaf}}$  were obtained from multiple sources, including the current study, previous studies by our research group and published data from other researchers (see Table 2). Values of  $K_{\text{leaf}}$  were converted to relative values by dividing each species' maximum value by the overall maximum  $K_{\text{leaf}}$  out of all species in the study (*Myrsine guianensis*, maximum  $K_{\text{leaf}} = 75.5 \text{ mmol m}^{-2} \text{ s}^{-1} \text{ MPa}^{-1}$ ). Then, the percentage of maximum  $K_{\text{leaf}}$  remaining at that species' lowest water potential (typically midday) was calculated, based on published vulnerability curves and minimum leaf water potential, or reported as measured (as in the current study). The relative maximum  $K_{\text{leaf}}$  and the percentage of maximum  $K_{\text{leaf}}$  remaining at midday were then compared to determine whether there was a trade-off between maximum conductance and vulnerability to hydraulic dysfunction. To ensure that there was no bias due to differences in measurement techniques, data obtained by using bulk leaf capacitance in combination with rehydration kinetics were plotted as a comparison.

## Results

Precipitation during the month of July 2010 was only 8.2 cm, below the average of 10.9 cm. The daily maximum temperature for the four measurement days was 31.8 °C, which was

much greater than the historical mean maximum July temperature of 27.1 °C.

Overall, stems were much less vulnerable to embolism than leaves (Figure 1). *Acer* stems showed a 50% loss in conductivity ( $P_{50}$ ) at  $-3.9 \text{ MPa}$ , whereas leaves from the same species had a  $P_{50}$  of  $-1.7 \text{ MPa}$ . *Liriodendron* had stem and leaf  $P_{50}$ s of  $-3.0$  and  $-1.2 \text{ MPa}$ , respectively, and *Pinus* had a stem  $P_{50}$  of  $-4.2 \text{ MPa}$  and a leaf  $P_{50}$  of  $-0.8 \text{ MPa}$ . The largest difference in stem and leaf  $P_{50}$  was 3.4 MPa, in *Pinus*. *Pinus* and *Acer* had high maximum  $K_{\text{leaf}}$  values (Table 1; 32.8 and 29.2  $\text{mmol m}^{-2} \text{ s}^{-1} \text{ MPa}^{-1}$ ,

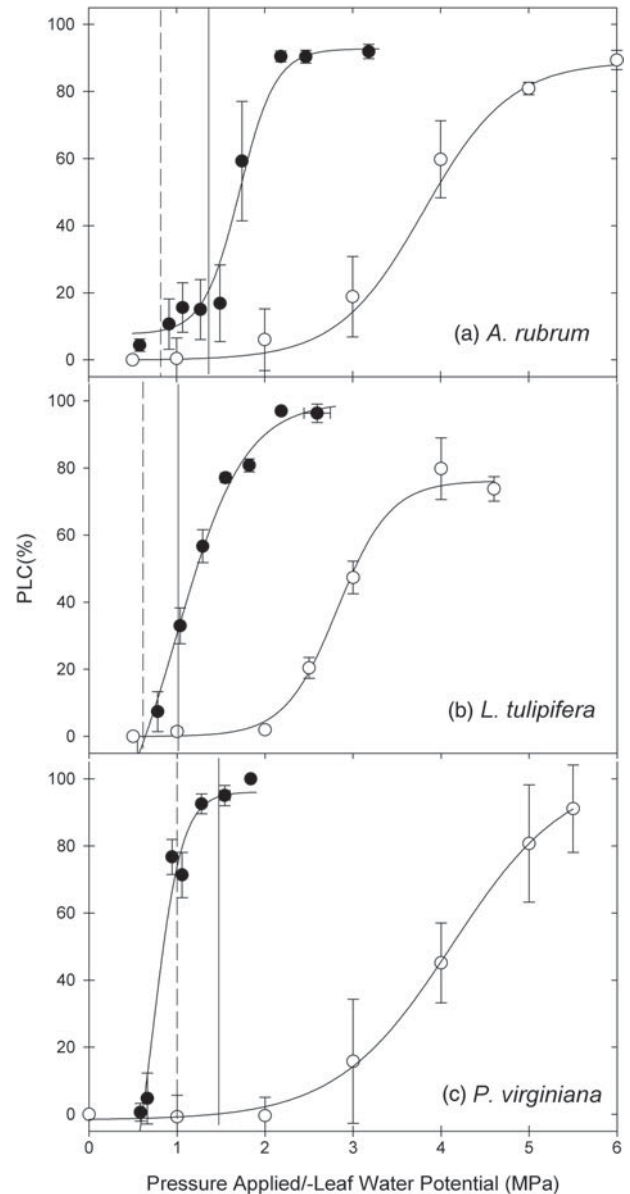


Figure 1. PLC of leaf hydraulic conductance (closed circles) and stem hydraulic conductivity (open circles) across a range of water potentials for (a) *A. rubrum*, (b) *L. tulipifera* and (c) *P. virginiana*. Midday minimum leaf water potentials and stem water potentials are indicated by vertical solid and dashed lines, respectively. Error bars represent standard error.

Table 1. Leaf turgor loss point (TLP), pre- and post-turgor loss point capacitance (C) and maximum leaf hydraulic conductance ( $K_{leaf}$ ). TLP and C values from pressure–volume analyses. Numbers in parentheses are standard errors.

Species	TLP (MPa)	Pre-TLP C (mol m <sup>-2</sup> MPa <sup>-1</sup> )	Post-TLP C (mol m <sup>-2</sup> MPa <sup>-1</sup> )	Maximum $K_{leaf}$ (mmol m <sup>-2</sup> s <sup>-1</sup> MPa <sup>-1</sup> )
<i>A. rubrum</i>	-1.59 (0.03)	0.87 (0.15)	3.06 (0.54)	29.2 (0.7)
<i>L. tulipifera</i>	-1.13 (0.08)	0.35 (0.05)	1.31 (0.08)	9.8 (0.5)
<i>P. virginiana</i>	-1.98 (0.18)	1.38 (0.31)	2.50 (0.97)	32.8 (1.2)

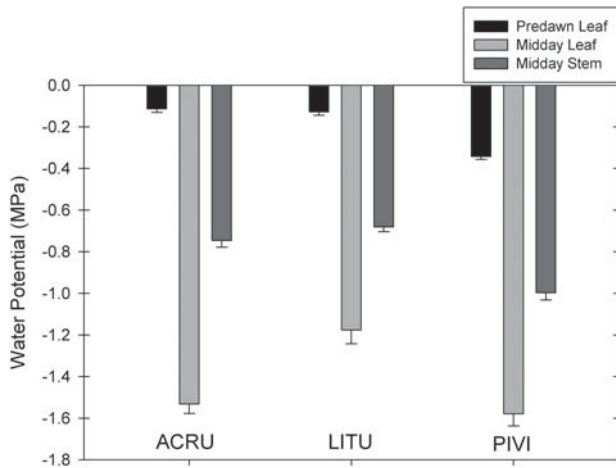


Figure 2. Measured water potential of leaves predawn, midday and stem water potential measured midday. ACRU is *A. rubrum*, LITU is *L. tulipifera* and PIVI is *P. virginiana*. Vertical error bars represent standard error.

respectively) whereas *Liriodendron* had a much lower maximum  $K_{leaf}$  (9.8 mmol m<sup>-2</sup> s<sup>-1</sup> MPa<sup>-1</sup>).

Predawn leaf water potentials were between -0.1 and -0.4 MPa in all three species and declined to minima of -1.2 to -1.8 MPa by midday (Figure 2). Midday stem water potentials varied from -0.6 to -1.0 MPa. *Pinus* had the lowest predawn and midday leaf and stem water potentials. No daily reductions in  $K_{leaf}$  were observed in either *Acer* or *Liriodendron* (Figure 3). However, *Pinus* had a complete loss of  $K_{leaf}$  by late afternoon but recovered slightly by the end of the measurement period (1600). Based on the stem vulnerability curves and midday stem water potentials, no loss in stem hydraulic conductivity was predicted for any of the three species.

Stomatal conductance was greater in *Pinus* than either *Acer* or *Liriodendron* and declined by midday for all species (Figure 4). Although *Pinus* lost the greatest percentage (~65% reduction) of its maximum measured stomatal conductance, it still remained higher than either *Acer* or *Liriodendron* throughout most of the day. On the other hand, *Acer* and *Liriodendron* had lower absolute maximum stomatal conductance, but their percentage reduction in stomatal conductance (52% and 35% for *Acer* and *Liriodendron*, respectively) was less than for *Pinus*.

Diurnal courses of sap flux differed in *Acer* and *Pinus* (Figure 5). In *A. rubrum* sap flow peaked early in the day (by

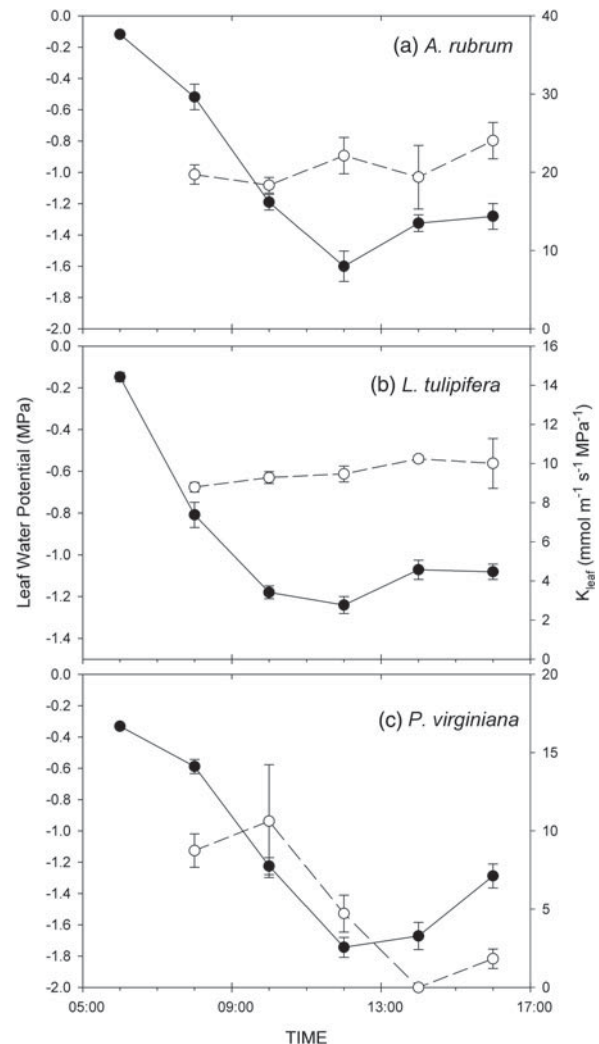


Figure 3. Leaf water potential ( $\Psi_{leaf}$ , closed circles) and leaf hydraulic conductance ( $K_{leaf}$ , open circles) measured in the field for (a) *A. rubrum*, (b) *L. tulipifera* and (c) *P. virginiana*.

0800 h), was reduced by an average of 38% by mid-afternoon, and then fell to near zero at the end of the day. In *P. virginiana* sap flux followed a more bell-shaped trajectory, reaching a maximum between 1000 and 1300 h. Daily courses of sap flux for these two species were consistent with their daily courses of stomatal conductance (cf. Figure 4). Mean maximum values of sap flux were somewhat greater for *Pinus* (31 g m<sup>-2</sup> s<sup>-1</sup>) than for *Acer* (23 g m<sup>-2</sup> s<sup>-1</sup>), although this difference was not significant ( $P = 0.18$ ).

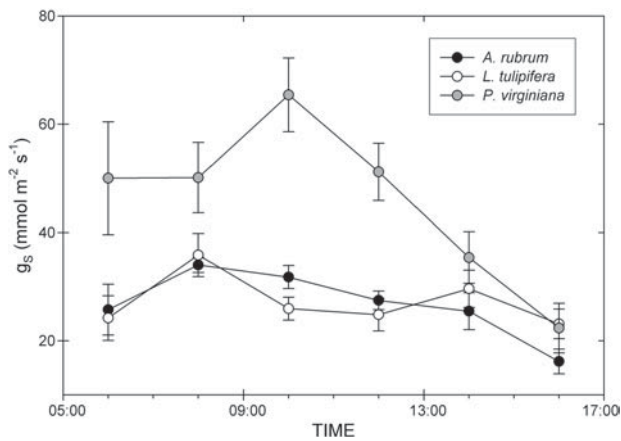


Figure 4. Stomatal conductance ( $g_s$ ) measured in the field for *A. rubrum*, *L. tulipifera* and *P. virginiana*. Vertical error bars represent standard error.

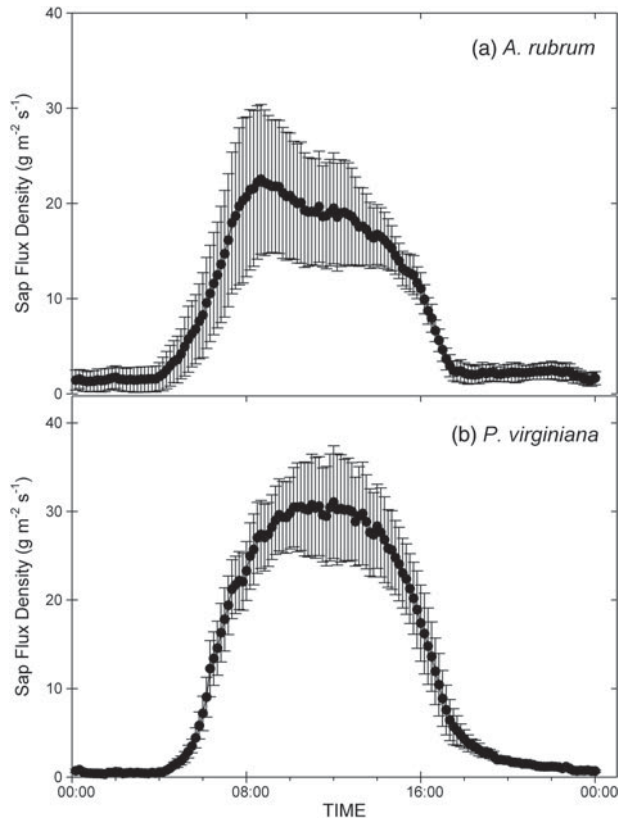


Figure 5. Sap flux measurements for three individuals of each (a) *A. rubrum* and (b) *P. virginiana*. Each plot is an average of five sunny days during the measurement period and vertical bars represent standard error.

The 42 species assessed for the relationship between relative maximum  $K_{leaf}$  and the percentage of maximum  $K_{leaf}$  remaining at midday appeared to fall into three groups based on their trajectories of this relationship (Figure 6, see Table 2 for groupings). Species in Group A showed relatively small losses of  $K_{leaf}$  at midday, and the trajectory of a linear fit through these data

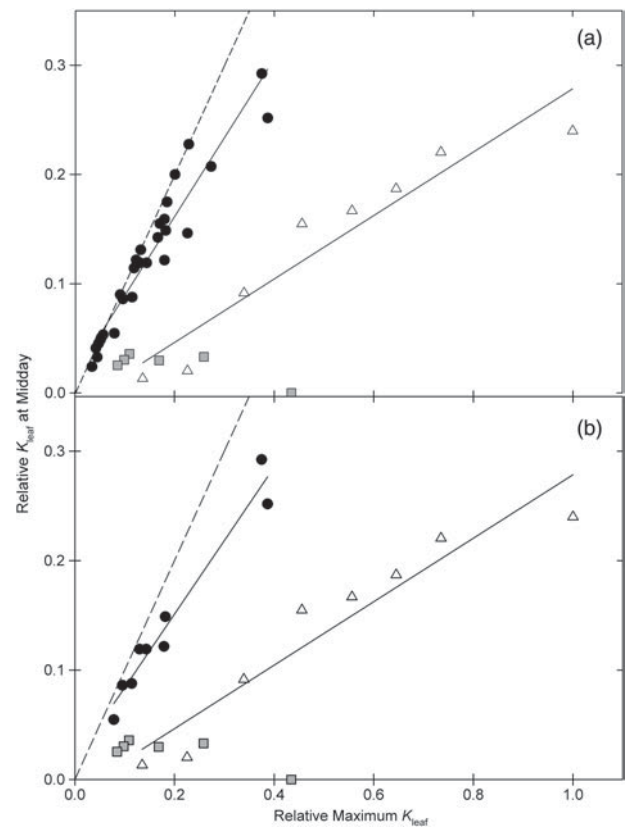


Figure 6. Relative maximum  $K_{leaf}$  (as compared with maximum values found in the literature; see the text for references) and the relative remaining  $K_{leaf}$  at midday. The 1:1 line (dashed line) indicates where a leaf would have lost no leaf hydraulic conductance at midday. Closed circles represent Group A, open triangles represent Group B and gray squares represent Group C (see Table 2 for groupings). Solid lines represent best-fit linear regressions through Groups A and B. For regression parameters, see the text. Panel (a) includes all data from Table 2 and panel (b) includes only data from the rehydration kinetics method using bulk leaf capacitance.

( $R^2 = 0.92$ ,  $P < 0.0001$ ) did not differ significantly from that of a 1:1 relationship even though its slope was 0.72. In contrast, species in Group B tended to have greater relative maximum  $K_{leaf}$  and experienced greater loss of  $K_{leaf}$  at midday (linear fit: slope = 0.29,  $R^2 = 0.91$ ,  $P = 0.0002$ ). Finally, species in Group C (Pinaceae and Cupressaceae) had overall low values of maximum  $K_{leaf}$  and all six species in this group lost the majority of their  $K_{leaf}$  at midday (linear fit through data not significant;  $R^2 = 0.64$ ,  $P = 0.0545$ , slope =  $-0.08$ ).

## Discussion

### Coordination of leaf and stem vulnerabilities

Although considerable research has been performed on stem and leaf hydraulics, few studies have addressed either the coordination of stem and leaf hydraulic vulnerability or the daily variation of leaf hydraulics in situ. In the current study, stems of each species were more resistant to embolism than were

Table 2. Species maximum  $K_{\text{leaf}}$  and percent of maximum  $K_{\text{leaf}}$  at daily  $\Psi_{\text{min}}$ . Species were grouped based on the percentage of  $K_{\text{leaf}}$  remaining at midday and whether the species was a gymnosperm or an angiosperm.

Species	$K_{\text{leaf}}$ max mmol m <sup>-2</sup> s <sup>-1</sup> MPa <sup>-1</sup>	% remaining at $\Psi_{\text{min}}$	Reference
Group A			
<i>Vochysia ferruginea</i>	28.3	78	FCM, unpublished
<i>Protium panamense</i>	13.5	68	Johnson et al. (2009b)
<i>Q. garryana</i>	8.6	77	Johnson et al. (2009b)
<i>Arbutus menziesii</i>	13.7	82	Johnson et al. (2009b)
<i>Alnus rubra</i>	5.9	70	Johnson et al. (2009b)
<i>A. rubrum</i>	29.2	65	Current study
<i>L. tulipifera</i>	9.8	92	Current study
<i>Byrsonima crassifolia</i>	17.2	100	Brodribb and Holbrook (2006)
<i>Rehdera trinervis</i>	20.6	76	Brodribb and Holbrook (2006)
<i>Genipa americana</i>	17.0	65	Brodribb and Holbrook (2006)
<i>Cercis siliquastrum</i>	12.5	86	Nardini et al. (2003)
<i>Anacardium excelsum</i>	10.8	83	DMJ and KAM, unpublished
<i>Miconia argentea</i>	7.2	90	DMJ and KAM, unpublished
<i>Orites diversifolus</i>	9.9	100	Blackman et al. (2010)
<i>Gaultheria hispida</i>	6.8	100	Blackman et al. (2010)
<i>Richea scoparia</i>	3.8	97	Blackman et al. (2010)
<i>Atherospermum moschatum</i>	3.1	100	Blackman et al. (2010)
<i>Nothofagus gunnii</i>	13.5	89	Blackman et al. (2010)
<i>Tasmannia lanceolata</i>	3.5	98	Blackman et al. (2010)
<i>Lomatia polymorpha</i>	4.2	96	Blackman et al. (2010)
<i>Telopea truncata</i>	9.2	100	Blackman et al. (2010)
<i>Nothofagus cunninghamii</i>	3.9	98	Blackman et al. (2010)
<i>Olearia pinifolia</i>	2.5	73	Blackman et al. (2010)
<i>Pittosporum bicolor</i>	3.3	75	Blackman et al. (2010)
<i>Coprosma nitida</i>	12.8	92	Blackman et al. (2010)
<i>Eucalyptus coccifera</i>	8.9	97	Blackman et al. (2010)
<i>Hakea lissosperma</i>	13.9	95	Blackman et al. (2010)
<i>Hakea microcarpa</i>	15.1	100	Blackman et al. (2010)
Group B			
<i>Simarouba glauca</i>	42.0	30	Brodribb and Holbrook (2004)
<i>Hymenea stignocarpa</i>	55.5	30	Hao et al. (2008)
<i>Aegiphila lhotzkiana</i>	34.4	34	Hao et al. (2008)
<i>Myrsine guianensis</i>	75.5	24	Hao et al. (2008)
<i>S. ferrugineus</i>	48.7	29	Hao et al. (2008)
<i>Tapirira guianensis</i>	17.0	9	Hao et al. (2008)
<i>Tachigalia versicolor</i>	25.6	27	Johnson et al. (2009b)
<i>Quercus rubra</i>	10.2	10	DMJ and KAM, unpublished
Group C			
<i>P. virginiana</i>	32.8	0	Current study
<i>P. ponderosa</i>	8.2	33	Johnson et al. (2009b)
<i>P. menziesii</i>	7.4	31	Johnson et al. (2009b)
<i>P. taeda</i>	6.4	30	Domec et al. (2009)
<i>Tsuga heterophylla</i>	19.5	13	DMJ and KAM, unpublished
<i>Thuja plicata</i>	12.7	18	DMJ and KAM, unpublished

leaves, consistent with the findings of Hao et al. (2008) for 10 forest and savanna tree species and Chen et al. (2010) in *Hevea brasiliensis*. Interestingly, Chen et al. (2009) found that leaves were significantly more vulnerable to embolism than stems in three evergreen members of the Euphorbiaceae, but that leaf and stem vulnerabilities were not different in three deciduous members of the same family. It was hypothesized by Chen et al. (2010) that leaf embolism may serve as a 'safety

valve' to isolate and protect the upstream hydraulic pathway, although this may not be the case in those species where stem and leaf vulnerability was similar. It would seem reasonable that emboli in leaf xylem, due to its proximity to living tissue, would be more easily refilled than air-filled conduits in stems (e.g., Zwieniecki and Holbrook 2009). Additionally, leaves should also be more 'disposable' due to their lower construction cost as compared with branches so sacrificing one or more

leaves may protect the stem (and other associated leaves) from runaway xylem embolism and possible stem dieback. This is consistent with earlier studies that have proposed that leaf xylem embolism may serve as a trigger to induce stomatal closure (e.g., Sperry 1986) to protect branches and other upstream components from embolism.

### Daily patterns of $K_{leaf}$ , water potential and stomatal conductance

Although several studies have reported declines and partial or complete recovery of  $K_{leaf}$  over the course of a day (Bucci et al. 2003, Brodribb and Holbrook 2004, Meinzer et al. 2004, Johnson et al. 2009b), it is becoming apparent that this is not the case for all species (Blackman et al. 2010). In species that experience declines in  $K_{leaf}$  on a daily basis, there seems to be one or more mechanisms for repair of the dysfunction by the next day even when water in adjacent functional conduits is under considerable tension (e.g., Bucci et al. 2003, Nardini et al. 2008, Johnson et al. 2009b, Zwieniecki and Holbrook 2009).

In the current study, leaves of *P. virginiana* lost nearly 100% of their  $K_{leaf}$  but began to recover late in the day, while water potentials were still more negative than  $-1.0$  MPa. Leaves of *Pinus ponderosa* and *Pseudotsuga menziesii* also lost large percentages of  $K_{leaf}$  but began to recover in the late afternoon while leaf water potentials were still highly negative (Johnson et al. 2009b). However, *Acer* and *Liriodendron* (from the current study) lost none or very little of their  $K_{leaf}$  as previously observed in *Quercus garryana* and *Arbutus menziesii* (Johnson et al. 2009b) and 16 other species from Tasmania (Blackman and Brodribb 2010). In fact, there was a slight increase in  $K_{leaf}$  in both *Acer* and *Liriodendron* between early morning and noon. Increases in  $K_{leaf}$  with increasing temperature and light have been previously reported for several species (Sack et al. 2004, Scoffoni et al. 2008, Sellin et al. 2008, Voicu et al. 2008).

In the current study, overall values of stomatal conductance were low, which is likely due to lower than average July rainfall (~25% less than average). In addition, the data from the current study were in contrast to earlier work showing a close relationship between maximum  $K_{leaf}$  and maximum stomatal conductance (Brodribb et al. 2005). The most plausible explanation for this is that the data in the current study were not representative of maximum stomatal conductance due to higher than normal temperatures or lower than average rainfall.

*Acer* and *Liriodendron* exhibited much more conservative behavior than did *Pinus* in that their stomatal conductance was low early in the day and then gradually decreased, avoiding low values of  $\Psi_L$  that would have provoked substantial embolism. In contrast, *Pinus* had high stomatal conductance until it began to show loss of  $K_{leaf}$  at which point stomatal conductance began to decline, although only by ~60% (cf. Figures 4 and 5).

These two different approaches are mirrored in the sap flow profiles for *Acer* and *Pinus* (Figure 5), where *Acer* displayed a reduction in sap flow early in the morning and *Pinus* sap flow did not slow until late afternoon. *Pinus ponderosa* exhibited behavior similar to that of *P. virginiana*:  $K_{leaf}$  was reduced to ~40% of its maximum value, but stomatal conductance only decreased by ~40% and only after initial decreases in  $K_{leaf}$  (Johnson et al. 2009b). This behavior is in contrast to a hypothesis put forth by Zwieniecki et al. (2007) which predicts that needle-leaved species like *Pinus* may close their stomata early (before reaching the water potential resulting in embolism), to protect the mesophyll cells, since they are not well irrigated by the xylem.

### Potential trade-offs between maximum $K_{leaf}$ and $K_{leaf}$ at $\Psi_{min}$

Although there is evidence for a hydraulic safety vs. efficiency trade-off in other plant organs (Sperry and Saliendra 1994, Domec and Gartner 2003, Wheeler et al. 2005, Domec et al. 2006, Hacke et al. 2006), such as stems and roots, this is a topic of ongoing debate (e.g., Meinzer et al. 2010). To our knowledge, no trade-off between leaf hydraulic vulnerability and maximum  $K_{leaf}$  has been previously described. It should be noted that absolute maximum  $K_{leaf}$  values can vary based on the method used (e.g., Blackman and Brodribb 2011), and although multiple methods were used in measuring the maximum  $K_{leaf}$  values in Figure 6, this should not change the overall results or groupings in the three trajectories. In fact, using only the data from the rehydration kinetics method and bulk leaf capacitance resulted in the same groupings (see Figure 6b). Although using bulk leaf capacitance for the rehydration kinetics method tends to overestimate  $K_{leaf}$  as compared with other methods, it does so in a systematic nature across a wide range of leaf types. For example, Blackman and Brodribb (2011), when using bulk leaf capacitance as compared with flow-based estimates of capacitance, overestimated  $K_{leaf}$  by 59% on average (SE = 10.2% when one outlier, greater than four standard deviations from the mean was removed; 76% overestimation with outlier not removed and SE = 13.5%).

In a recent study by Blackman et al. (2010), none of the 16 species measured lost even 30% of  $K_{leaf}$  at the minimum seasonal leaf water potential, which would place them in Group A (Table 2, Figure 6) of the current study. Of the six conifers represented in Figure 6, all lose the majority of their  $K_{leaf}$  at midday. For example, Domec et al. (2009) observed 70–77% losses of  $K_{leaf}$  at midday for *Pinus taeda*, depending on the treatment (e.g., elevated carbon dioxide or fertilization). The reason for the observed large daily declines and recovery of  $K_{leaf}$  in conifer species may be related to the limited hydraulic connections between different tissues inside conifer leaves (Zwieniecki et al. 2007) or the observed delay in *P. taeda*, *P. ponderosa*, *P. virginiana* and *P. menziesii* stomatal conductance

reductions in response to losses of  $K_{\text{leaf}}$  (Domec et al. 2009, Johnson et al. 2009b and the current study). It is also feasible that xylem embolism in small, needle-type leaves may be easier or less costly to refill than that in larger broadleaves. This may also be related to the occurrence of transfusion tissue in the Pinaceae, and its ability to store solutes that could be released into adjacent tracheids, prompting refilling (Canny 1993, Zwieniecki and Holbrook 2009, Liesche et al. 2011).

An explanation of the differences in trajectory of Groups A and B in Figure 6 may be related to differences in leaf anatomy or stomatal responsiveness to changes in leaf water status. For example, *Styrax ferrugineus* (Group B) leaf water potential dropped to  $-1.7$  MPa (corresponding to  $\sim 70\%$  reduction in  $K_{\text{leaf}}$ ) before stomata began to close (Bucci et al. 2004). Even when stomata began to close, the resulting decline in stomatal conductance was only  $\sim 30\%$ . In *Simarouba glauca* (Group B, Brodribb and Holbrook 2004), reductions in stomatal conductance occurred only after  $K_{\text{leaf}}$  declined during the wet season, and although stomatal conductance decreased earlier in the day in the dry season, it still did not prevent massive ( $\sim 65\%$ ) losses of  $K_{\text{leaf}}$ . The fact that there are many evergreen and sclerophyllous species in Group A (little loss of  $K_{\text{leaf}}$ ) may reflect the investment in those tissues and the need for a more conservative strategy as opposed to a less conservative strategy where (i) large losses of  $K_{\text{leaf}}$  could lead to leaf death or (ii) large losses in  $K_{\text{leaf}}$  must be repaired by what is likely an energetically expensive process (e.g., Bucci et al. 2003, Zwieniecki and Holbrook 2009).

## Acknowledgments

The authors would like to thank Cecile Perrineau, Katie Gaines, Jane Wubbels and Tom Adams for their helpful assistance with field data collection. The authors are also grateful to Dr Barbara Lachenbruch and the AvH plant biology group for critical discussion of ideas.

## Funding

This research was supported by NSF IOS-0919871 and NSF EAR 07-25019.

## References

- Abramoff, M.D., P.J. Magelhaes and S.J. Ram. 2004. Image processing with image. *J. Biophotonics Int.* 11:36–42.
- Blackman, C.J. and T.J. Brodribb. 2011. Two measures of leaf capacitance: insights into the water transport pathway and hydraulic conductance in leaves. *Funct. Plant Biol.* 38:118–126.
- Blackman, C.J., T.J. Brodribb and G.J. Jordan. 2010. Leaf hydraulic vulnerability is related to conduit dimensions and drought resistance across a diverse range of woody angiosperms. *New Phytol.* 188:1113–1123.
- Brodribb, T.J. and H. Cochard. 2009. Hydraulic failure defines the recovery and point of death in water-stressed conifers. *Plant Physiol.* 149:575–584.
- Brodribb, T.J. and N.M. Holbrook. 2003. Stomatal closure during leaf dehydration, correlation with other leaf physiological traits. *Plant Physiol.* 132:2166–2173.
- Brodribb, T.J. and N.M. Holbrook. 2004. Diurnal depression of leaf hydraulic conductance in a tropical tree species. *Plant, Cell Environ.* 27:820–827.
- Brodribb, T.J., N.M. Holbrook, M.A. Zwieniecki and B. Palma. 2005. Leaf hydraulic capacity in ferns, conifers and angiosperms: impacts on photosynthetic maxima. *New Phytol.* 165:839–846.
- Brodribb, T.J. and N.M. Holbrook. 2006. Declining hydraulic efficiency as transpiring leaves desiccate: two types of response. *Plant, Cell Environ.* 29:2205–2215.
- Bucci, S.J., F.G. Scholz, G. Goldstein, F.C. Meinzer and L. Da S.L. Sternberg. 2003. Dynamic changes in hydraulic conductivity in petioles of two savanna tree species: factors and mechanisms contributing to the refilling of embolized vessels. *Plant, Cell Environ.* 26:1633–1645.
- Bucci, S.J., F.G. Scholz, G. Goldstein, F.C. Meinzer, J.A. Hinojosa, W.A. Hoffmann and A.C. Franco. 2004. Processes preventing nocturnal equilibration between leaf and soil water potential in tropical savanna woody species. *Tree Physiol.* 24:1119–1127.
- Canny, M.J. 1993. Transfusion tissue of pine needles as a site of retrieval of solutes from the transpiration stream. *New Phytol.* 123:227–232.
- Chen, J-W., Q. Zhang, X-S. Li and K-F. Cao. 2009. Independence of stem and leaf hydraulic traits in six Euphorbiaceae tree species with contrasting leaf phenology. *Planta* 230:459–468.
- Chen, J-W., Q. Zhang, X-S. Li and K-F. Cao. 2010. Gas exchange and hydraulics in seedlings of *Hevea brasiliensis* during water stress and recovery. *Tree Physiol.* 30:876–885.
- Choat, B., E.C. Lahr, P.J. Melcher, M.A. Zwieniecki and N.M. Holbrook. 2005. The spatial pattern of air-seeding thresholds in mature sugar maple trees. *Plant, Cell Environ.* 28:1082–1089.
- Cochard, H., F. Froux, S. Mayr and C. Coutand. 2004. Xylem wall collapse in water-stressed pine needles. *Plant Physiol.* 134:401–408.
- Cochard, H., J-S. Vénisse, T.S. Barigah, N. Brunel, S. Herbette, A. Guilliot, M.T. Tyree and S. Sakr. 2007. Putative role of aquaporins in variable hydraulic conductance of leaves in response to light. *Plant, Physiol.* 143:122–133.
- Domec, J-C. and B.L. Gartner. 2003. Relationship between growth rates and xylem hydraulic characteristics in young, mature and old-growth *Ponderosa* pine trees. *Plant, Cell Environ.* 26:471–483.
- Domec, J-C., B. Lachenbruch and F.C. Meinzer. 2006. Bordered pit structure and function determine patterns of air-seeding thresholds in xylem of Douglas fir (*Pseudotsuga menziesii*; Pinaceae) trees. *Am. J. Bot.* 93:1588–1600.
- Domec, J-C., S. Palmroth, E. Ward, C.A. Maier, M. Therezien and R. Oren. 2009. Acclimation of leaf hydraulic conductance and stomatal conductance of *Pinus taeda* (loblolly pine) to long-term growth in elevated  $\text{CO}_2$  (free-air  $\text{CO}_2$  enrichment) and N-fertilization. *Plant, Cell Environ.* 32:1500–1512.
- Granier, A. 1985. Une nouvelle methode pour la mesure du flux de seve brute dans le tronc des arbres. *Ann. Sci. For.* 42:193–200.
- Hacke, U.G., J.S. Sperry, J.K. Wheeler and L. Castro. 2006. Scaling of angiosperm xylem structure with safety and efficiency. *Tree Physiol.* 26:689–701.
- Hao, G., W.A. Hoffmann, F.G. Scholz, S.J. Bucci, F.C. Meinzer, A.C. Franco, K. Cao and G. Goldstein. 2008. Stem and leaf hydraulics of congeneric tree species from adjacent tropical savanna and forest ecosystems. *Oecologia* 155:405–415.

- Heinen, R.B., Q. Ye and F. Chaumont. 2009. Role of aquaporins in leaf physiology. *J. Exp. Bot.* 60:2971–2985.
- Johnson, D.M., F.C. Meinzer, D.R. Woodruff and K.A. McCulloh. 2009a. Leaf xylem embolism, detected acoustically and by cryo-SEM, corresponds to decreases in leaf hydraulic conductance in four evergreen species. *Plant Cell Environ.* 32:828–836.
- Johnson, D.M., D.R. Woodruff, K.A. McCulloh and F.C. Meinzer. 2009b. Leaf hydraulic conductance, measured in situ, declines and recovers daily: leaf hydraulics, water potential and stomatal conductance in four temperate and three tropical tree species. *Tree Physiol.* 29:879–887.
- Kaldenhoff, R., M. Ribas-Carbo, J. Flexas Sans, C. Lovisolo, M. Heckwolf and N. Uehlein. 2008. Aquaporins and plant water balance. *Plant, Cell Environ.* 31:658–666.
- Liesche, J., H.J. Martens and A. Schulz. 2011. Symplasmic transport and phloem loading in gymnosperm leaves. *Protoplasma* 248:181–190.
- McDowell, N., W.T. Pockman, C.D. Allen et al. 2008. Mechanisms of plant survival and mortality during drought: why do some plants survive while others succumb to drought? *New Phytol.* 178:719–739.
- Meinzer, F.C., S.A. James and G. Goldstein. 2004. Dynamics of transpiration, sap flow and use of stored water in tropical forest canopy trees. *Tree Physiol.* 24:901–909.
- Meinzer, F.C., D.R. Woodruff, J.-C. Domec, G. Goldstein, P.I. Campanello, M.G. Gatti and R. Villalobos-Vega. 2008. Coordination of leaf and stem water transport properties in tropical forest trees. *Oecologia* 156:31–41.
- Meinzer, F.C., D.M. Johnson, B. Lachenbruch, K.A. McCulloh and D.R. Woodruff. 2009. Xylem hydraulic safety margins in woody plants: coordination of stomatal control of xylem tension with hydraulic capacitance. *Funct. Ecol.* 23:922–930.
- Meinzer, F.C., K.A. McCulloh, B. Lachenbruch, D.W. Woodruff and D.M. Johnson. 2010. The blind men and the elephant: the impact of context and scale in evaluating conflicts between plant hydraulic safety and efficiency. *Oecologia* 164:287–296.
- Nardini, A., M.T. Tyree and S. Salleo. 2001. Xylem cavitation in the leaf of *Prunus laurocerasus* and its impact on leaf hydraulics. *Plant Physiol.* 125:1700–1709.
- Nardini, A., S. Salleo and F. Raimondo. 2003. Changes in leaf hydraulic conductance correlate with leaf vein embolism in *Cercis siliquastrum* L. *Trees* 17:529–534.
- Nardini, A., M. Ramani, E. Gortan and S. Salleo. 2008. Vein recovery from embolism occurs under negative pressure in leaves of sunflower (*Helianthus annuus*). *Physiol. Plant.* 133:755–764.
- Sack, L., C.M. Streeter and N.M. Holbrook. 2004. Hydraulic analysis of water flow through leaves of sugar maple and red oak. *Plant Physiol.* 134:1824–1833.
- Salleo, S., M.A. Lo Gullo, F. Raimondo and A. Nardini. 2001. Vulnerability to leaf cavitation of leaf minor veins: any impact on leaf gas exchange? *Plant, Cell Environ.* 24:851–859.
- Scholander, P.F., H.T. Hammel, E.D. Bradstreet and E.A. Hemmington. 1965. Sap pressure in vascular plants. *Science* 148:339–346.
- Scoffoni, C., A. Pou, K. Aasamaa and L. Sack. 2008. The rapid light response of leaf hydraulic conductance: new evidence from two experimental methods. *Plant, Cell Environ.* 31:1803–1812.
- Sellin, A., E. Öunapuu and P. Kupper. 2008. Effects of light intensity and duration on leaf hydraulic conductance and distribution of resistance in shoots of silver birch (*Betula pendula*). *Physiol. Plant.* 134:412–420.
- Sperry, J.S. 1986. Relationship of xylem embolism to xylem pressure potential, stomatal closure, and shoot morphology in the palm *Rhapis excelsa*. *Plant Physiol.* 80:110–116.
- Sperry, J.S. and N.Z. Saliendra. 1994. Intra- and inter-plant variation in xylem cavitation in *Betula occidentalis*. *Plant, Cell Environ.* 17:1233–1241.
- Tyree, M.T. and H.T. Hammel. 1972. The measurement of the turgor pressure and the water relations of plants by the pressure-bomb technique. *J. Exp. Bot.* 23:267–282.
- Tyree, M.T. and J.S. Sperry. 1989. Vulnerability of xylem to cavitation and embolism. *Ann. Rev. Plant, Physiol. Mol. Biol.* 40:19–38.
- Voicu, M.C., J.J. Zwiazek and M.T. Tyree. 2008. Light response of hydraulic conductance in bur oak (*Quercus macrocarpa*) leaves. *Tree Physiol.* 28:1007–1015.
- Wheeler, J.K., J.S. Sperry, U.G. Hacke and N. Hoang. 2005. Inter-vessel pitting and cavitation in woody Rosaceae and other vesselless plants: a basis for a safety versus efficiency trade-off in xylem transport. *Plant, Cell Environ.* 28:800–812.
- Woodruff, D.R., K.A. McCulloh, J.R. Warren, F.C. Meinzer and B. Lachenbruch. 2007. Impacts of tree height on leaf hydraulic architecture and stomatal control in Douglas-fir. *Plant, Cell Environ.* 30:559–569.
- Zwieniecki, M.A. and N.M. Holbrook. 2009. Confronting Maxwell's demon: biophysics of xylem embolism repair. *Trends Plant Sci.* 14:530–534.
- Zwieniecki, M.A., T.J. Brodrigg and N.M. Holbrook. 2007. Hydraulic design of leaves: insights from rehydration kinetics. *Plant, Cell Environ.* 30:910–921.



February 18, 2012

Dr. Susan Brantley  
Earth and Environmental Systems Institute  
The Pennsylvania State University  
2217 Earth & Engineering Sciences Building, 225B  
University Park, PA 16802

Dear Dr. Brantley,

CUAHSI is pleased to provide this letter of commitment for the renewal proposal for the Shale Hills/Susquehanna Critical Zone Observatory. I confirm that CUAHSI will allow your CZO (and the others in the network) use of our webinar capabilities for regular scientific seminars and that we will use the CUAHSI outlets to publicize those webinars. These services will be made available to you at no cost to your project as part of our service to the critical zone research community.

Best of luck in the competition and I look forward to continuing our work together.

Sincerely,

A handwritten signature in black ink, which appears to read 'Richard P. Hooper'. The signature is written in a cursive style.

Dr. Richard P. Hooper  
President and Executive Director

**Table 5. Personnel Support Table**

Name	Educational Background	Support per year	Project Responsibility
<b><u>CoInvestigators</u></b>			
Susan Brantley	Ph.D.	1 month	Geochemistry, microbiology; supervise project; advise postdocs, students
Ken Davis	Ph.D.	1/2 month	Eddy covariance measurements; advise postdoctoral scholar + finishing students
Chris Duffy	Ph.D.	3/4 month	Sensor network, PIHM modeling; advise postdocs + finishing grad students; Steering Committee administration
Dave Eissenstatt	Ph.D.	3/4 month	Root distribution and sapflux; advise postdocs + finishing grad students; Steering Committee administration
Jason Kaye	Ph.D.	1/2 month	Organic carbon & CO <sub>2</sub> measurements; advise postdocs + finishing grad students
Eric Kirby	Ph.D.	3/4 month	Cosmogenic isotopes, erosion regime; advise postdocs + finishing grad students; Steering Committee administration
Henry Lin	Ph.D.	1/2 month	Soil moisture, soil surveys; advise postdocs + finishing grad students
Kamini Singha	Ph.D.	1/2 month	Drilling and geophysics; advise postdocs + finishing grad students
<b><u>Support Personnel</u></b>			
Jennifer Williams	M.S.	12 months	Project coordination and data management
TBD	TBD	6 months	Cyberspecialist for website and databases; 50% effort over 12 months
TBD	TBD	12 months	Watershed technician, maintaining sensors, dataloggers, eddy flux tower, taking samples
TBD	Ph.D.	12 months	Postdoctoral scholar; work on hypothesis 1 with Davis, Duffy, Lin, Eissenstatt
TBD	Ph.D.	12 months	Postdoctoral scholar; work on hypothesis 2 with Duffy, Brantley, Lin, Kaye
TBD	Ph.D.	12 months	Postdoctoral scholar; work on hypothesis 3 with Kaye, Eissenstatt, Brantley, Kirby
TBD	Ph.D.	12 months	Postdoctoral scholar; work on hypothesis 4 with Singha, Kirby, Brantley, Duffy
<b><u>Graduate Students</u></b>			
Yu Zhang		12 months	1 student, Fall, Spring & Summer Semester; dissertation adding sediment transport to PIHM
Ashlee Dere		12 months	1 student, Fall, Spring & Summer Semester; dissertation investigating shale transect sites